Title	Chemical Synthesis of Luminescent Silicon Quantum Dots for Light-Emitting Diodes
Author(s)	山田, 博之
Degree Grantor	北海道大学
Degree Name	博士(理学)
Dissertation Number	甲第15406号
Issue Date	2023-03-23
DOI	https://doi.org/10.14943/doctoral.k15406
Doc URL	https://hdl.handle.net/2115/91499
Type	doctoral thesis
File Information	YAMADA_Hiroyuki.pdf

Chemical Synthesis of Luminescent Silicon Quantum Dots for Light-Emitting Diodes

シリコン量子ドット蛍光体の化学合成と発光ダイオードへの応用

Hiroyuki Yamada

山田　博之

Graduate School of Chemical Sciences and Engineering

Hokkaido University

2023

Contents

Chapter 1 Introduction 9

1.1 Quantum Confinement Effects 11

1.1.1 For Spherical Quantum Dot 12

1.1.2 For Cubic Quantum Dot 14

1.1.3 For Realistic Semiconductor Quantum Dot 16

1.2 Advances in Display Technology 19

1.3 Advances in Colloidal Quantum Dots Light-Emitting Diodes 20

1.3.1 Type I: QLEDs Utilizing Polymer CTLs 21

1.3.2 Type II: QLEDs Incorporating Organic Small Molecule CTLs 23

1.3.3 Type III: QLEDs Featuring Inorganic CTLs 26

1.3.4 Type IV: QLEDs Incorporating Hybrid Organic-Inorganic CTLs 28

1.4 Recent Progress in Near-Infrared Light-Emitting Device Technology 30

1.5 Heavy-Metal-Free Quantum Dots Light-Emitting Diodes 34

1.5.1 Silicon Quantum Dots Light-Emitting Diodes 35

1.5.2 Challenges and Limitations in the Development of Si-QLEDs 38

1.6 Research Motivation 40

1.7 References 41

Chapter 2 Synthesis of Colloidal Silicon Quantum Dots and Characteristics of Photoluminescence Quantum Yields 48

2.1 Introduction 48

2.1.1 Synthesis of Crystalline Colloidal Silicon Quantum Dots 50

2.1.1.1 Non-Thermal Plasma Synthesis 50

2.1.1.2 Thermolysis of Silicon Sub-Oxide 52

2.2 Experimental Methods 55

2.3 Experimental Results 57

2.3.1 Synthesis and Physical Characterization of SiQDs 57

2.3.2 Manipulation of Photoluminescence Peak Wavelength in SiQDs 63

2.3.3 Investigation of the Impact of Hydrolysis Techniques on Photoluminescence Quantum Yield in Triethoxysilane-based SiQDs 67

2.4 Conclusion 73

2.5 References 74

Chapter 3 Inverted Device Architecture for Silicon Quantum Dots Light-Emitting Diodes 77

3.1 Introduction 77

3.2 Experimental Methods 80

3.3 Experimental Results 84

3.4 Conclusion 97

3.5 References 98

Chapter 4 Color-Tunable Silicon Quantum Dots Light-Emitting Diodes 103

4.1 Introduction 103

4.2 Experimental Methods 105

4.3 Experimental Results 109

4.3.1 Impact of QD Layer Thickness on Device Performance in Si-QLEDs 109

4.3.2 Pale-Orange Region Emission from Si-QLEDs 112

4.3.3 Control of EL Peak Wavelength through the 590-755 nm Range 117

4.3.4 Si-QLEDs Operating in the Near-Infrared II Spectral Window 135

4.3.5 Manipulating the Spectral Characteristics of Electroluminescence 141

4.4 Conclusion 145

4.5 References 147

Chapter 5 Manipulation of Carrier Transport Layer and Interparticle Distance in the Active Layer for Improved Performance in Si-QLEDs 151

5.1 Introduction 151

5.2 Experimental Methods 154

5.3 Experimental Results and Discussion 159

5.3.1 Manipulation of Carrier Transport Layer for Improved Performance in Si-QLEDs 159

5.3.2 Post-Production Techniques for Enhancing EQE in Si-QLEDs 166

5.3.2.1 Device Performance Results 166

5.3.2.2 Analysis of the "Post-Electric-Annealing" Mechanism 171

5.4 Conclusion 177

5.5 References 178

Chapter 6 Summary and Future Prospects 182

Summary 182

Future Prospects 186

Abstract

Silicon quantum dots (SiQDs) are particles in which silicon crystals with diamond structures are miniaturized to a size smaller than the bulk exciton Bohr radius. SiQDs exhibit a high photoluminescence quantum yield (PLQY) based on the quantum confinement effect of photoexcited carriers, and the emission wavelength can be modulated over a broad range of 535-1,050 nm, depending on the particle size. Further enhancement of the PLQY can be achieved through the hydrosilylation of 1-alkenes. Additionally, the organic termination allows for the SiQDs to be dispersed in an organic solvent and to form a film through the spin-coating method, making them suitable for developing optoelectronic devices such as photoelectrodes and light-emitting diodes (LEDs).

In 2009, the development of near-infrared (NIR) emitting SiQDs LEDs (Si-QLEDs) was reported in literature, followed by the emergence of visible red emitting Si-QLEDs in 2011, with SiQDs employed in the light-emitting layer. However, the emission wavelength was restricted to a narrow range of 850-625 nm. Furthermore, the expansion of emission colors, improvement of external quantum efficiency (EQE) of electroluminescence (EL), and blue-shift of the EL peak with increasing device driving voltage, are ongoing challenges in the field.

The purpose of this paper is to investigate the correlation between luminescence properties and quantum dots (QDs) or QDs LEDs (QLEDs) structures, with the goal of identifying the key technological elements necessary for the fabrication of Si-QLEDs with superior EL properties. This includes the synthesis of SiQDs with high PLQY, the development of stable device structures, and the optimization of carrier transport layers to improve EQE of EL.

In Chapter 1, the fabrication methods of QLEDs and the EL characteristics were presented. In particular, for Si-QLEDs, by analyzing the previously reported correlation between device structure and EL characteristics, the existing challenges in Si-QLEDs were identified and the objectives of this

study were outlined.

In Chapter 2, the synthesis of diamond-structured SiQDs via thermal disproportionation reactions and the evaluation of optical properties were studied. It was found that the photoluminescence (PL) peak wavelength of SiQDs was correlated with both the temperature during the thermal disproportionation reaction and the duration of hydrofluoric acid etching. Additionally, by carefully controlling the injection speed of an acidic solution during the hydrolysis of triethoxysilane (TES), the PLQY was improved by up to two-fold.

In Chapter 3, the fabrication and characterization of conventional structured Si-QLEDs and inverted structured Si-QLEDs (Si-iQLEDs) were investigated. As a result, it was observed that the conventional structured Si-QLEDs exhibited a significant blue-shift of the EL spectral peak under high-voltage driving, as well as emission from adjacent layers. In contrast, the Si-iQLEDs displayed minimal blue-shift of the EL peak even under high-voltage driving, and no emission from adjacent layers was detected. Additionally, the Si-iQLEDs exhibited a lifetime that was 10 times longer than that of the conventional structured Si-QLEDs under the same driving conditions. Furthermore, by substituting polyethylene terephthalate (PET) substrates for glass substrates for device film deposition, a flexible Si-iQLED was successfully developed.

In Chapter 4, the control of the EL peak wavelength and spectral shape of Si-iQLEDs was investigated. It was found that by reducing the thickness of the SiQDs film to 6 nm, emission from the adjacent layer appeared, allowing for the tuning of the EL spectral shape. The device fabricated using this result exhibited an emission peak at 620 nm, as well as emission from the zinc oxide layer, thus enabling the tuning of the emission color. Previously, the shortest emission wavelength reported for Si-QLEDs was 625 nm, with an EQE as low as 0.0006%. However, by utilizing the inverted device structure described in Chapter 3, Si-iQLEDs with an EL peak at 620 nm and an enhanced EQE of 0.036% were fabricated, which is 100 times higher than conventional Si-QLEDs. In the following investigation, the fabrication and characterization of Si-iQLEDs with tunable EL peak wavelength were studied. The tuning of the EL peak wavelength was achieved by controlling the diameter of SiQDs in the active layer. The fabricated devices exhibited EL peak wavelengths of 755 nm, 722 nm, 670 nm, 635 nm and 590 nm, respectively, with EQEs of 3.70%, 1.32%, 1.20%, 0.88% and 0.12%. Furthermore, it was found that the conventional emission color tuning range of Si-QLEDs was 625-868 nm, but with the results of this study, the short wavelength side was extended to 590 nm, corresponding to yellow emission. Subsequently, NIR emitting Si-iQLEDs were fabricated and evaluated. By synthesizing SiQDs with a PL peak in the NIR region and incorporating them into the active layer, Si-iQLEDs with an EL peak at 1,000 nm were achieved, along with an EQE of 4.84%. Additionally, by incorporating SiQDs with varying particle sizes into the active layer, the EL spectral shape was tuned. The presence of a significant Stokes shift between the absorption and PL spectra, a characteristic specific to SiQDs, minimized energy transfer between SiQDs of different sizes, resulting in the demonstration of Si-iQLEDs with a broad EL spectrum in the NIR region. These results extend the longest EL peak wavelength of Si-QLEDs to 1,000 nm.

In Chapter 5, the control of the carrier transport layer and the control of the interparticle distance were investigated. To achieve carrier balance control, the EQE of the Si-iQLEDs was enhanced to 7.44% by incorporating an electron transport blocking layer (EBL) between the electron transport layer (ETL) and the SiQDs layer. Furthermore, Si-iQLEDs with $Zn_{0.86}Mg_{0.14}O$ as the ETL and Tris(4-carbazoyl-9-ylphenyl)amine (TCTA) as the hole transport layer (HTL) showed a 12-fold increase in light output intensity compared to ZnO/4,4′-Bis(9*H*-carbazol-9-yl)biphenyl (CBP) ETL/HTL devices. Additionally, a novel approach for EQE enhancement, referred to as the “post-electric-annealing” method, was developed. By fabricating Si-iQLEDs with decane-terminated SiQDs in the active layer and applying a constant voltage to the device, it was found that the EQE and optical power density increased, with the EQE reaching a maximum of 12.2%. Observations of the device cross-sections via

Transmission Electron Microscopy (TEM) before and after voltage application revealed that the average distance between SiQDs in the device after voltage application had decreased by 0.59 nm in comparison to prior to voltage application. This suggests that the Joule heat generated during voltage application damaged the ligands of SiQDs and shortened the distance between the QDs, resulting in efficient charge injection and radiative recombination in the active layer, leading to increased EQE and optical power density.

Chapter 6 summarizes the conclusions and provides a summary and perspective on the potential and promise of Si-iQLEDs as optical devices presented by this study.

Chapter 1 Introduction

Nanomaterials characterized by precisely controlled structures, such as nanotubes [1], nanoparticles [2], nanosheets [3], nanofilms [4], and nanoporous materials [5], are driving numerous innovations in contemporary science and technology, particularly in the fields of electronics, optoelectronics and biology. Their exceptional structure and properties have spurred increased research efforts across a spectrum of disciplines. Specifically, quantum-sized materials, such as quantum dots (QDs), have garnered significant attention from the scientific community due to their potential to exhibit a range of novel functions based on well-defined physics [6–8].

The initial synthesis of QDs can be traced back to the development of lead-sulfide (PbS) QDs more than two millennia ago, through a process utilizing inexpensive natural materials such as lead monoxide (PbO), calcium hydroxide ($Ca(OH)_2$), and water [9]. These substances were utilized by the ancient *Romans* and *Greeks* as cosmetic products for hair dyeing. In more recent history, controlling the size of QDs in silicate glass has been a longstanding and widely-used technique for altering glass color. In the early 20th century, cadmium sulfide (CdS) and cadmium selenide (CdSe) were incorporated into silicate glass to achieve a red-yellow hue. In 1932, X-ray diffraction (XRD) studies conducted by *Rocksby* revealed that the precipitation of CdS and CdSe was responsible for the color of selenium glasses [10]. Historically, glasses doped with semiconductor particles have been employed as optical filters. In 1981, *Ekinov* and *Onushchenko* reported an optical spectral blue shift of nanometer-sized copper chloride (CuCl) in silicate glass [11]. In 1982, Efros *et al.*, advanced the hypothesis that the color of glass could be controlled through quantum size effects by altering the size or stoichiometry of CdS_xSe_{1-x} [12]. In 1984, Rosetti *et al.*, discussed color changes in colloidal solutions of semiconductors [13]. Throughout this period, a variety of synthetic techniques were developed, including the 1987 synthesis of highly luminescent CdS QDs through surface modification with cadmium hydroxide ($Cd(OH)_2$) by Spanhel *et al.* [14], the 1990 synthesis of composite semiconductor crystallites involving CdSe grown on a ZnS seed, and vice versa, by Kortan *et al.* [15], and the 1993 synthesis of nearly monodispersed CdS, CdSe and cadmium telluride (CdTe) based on the pyrolysis of organometallic reagents by injection into a thermally coordinating solvent, by Murray *et al* [16]. In the past three decades, experimental and theoretical studies of these nanoparticles have greatly increased [17–19], aimed at understanding the fundamental properties of QDs [20,21] and have been directed towards commercialization efforts [22,23].

1.1 Quantum Confinement Effects

Over the past three decades, significant attention has been directed towards the photoelectronic properties of nanostructured semiconductors, or QDs, due to the fact that many fundamental properties are dependent on particle size in the nanometer range. QDs are relative zero-dimensional in comparison to bulk materials, and the limited number of electrons gives rise to discrete quantization energies in the density of states (DOS) of non-aggregated, zero-dimensional structures [24]. The presence of a single electronic charge in QDs can inhibit the addition of an additional charge, resulting in a stepped current-voltage (*I-V)* curve and DOS. The step size is proportional to the inverse of the radius of the QDs. The boundaries for determining whether a substance exhibits bulk, QD, or atomic properties are contingent upon the composition and crystal structure of the compound or elemental solid. A vast range of fundamental properties can be achieved by altering the size at a constant composition.

The electrons, holes and excitons within QDs are confined three-dimensionally by the deep potential formed by the dots and matrices. The electron wave is confined in a narrow space, and the wavelength is limited to a specific one, thus the kinetic energy has a discrete value. As a result, the lowest energy states of electrons, holes and excitons are higher than the band gap energy of the bulk crystal, depending on the size of the QD. These phenomena, which occur when the size of the QD is comparable to the Bohr radius of the exciton, are referred to as “Quantum Confinement Effects”.

1.1.1 For Spherical Quantum Dot

In the following, a spherical QD is assumed. When the QD is a sphere of radius $R = a$ and is surrounded by an infinitely high potential, the Schrödinger equation for a particle of mass $\boldsymbol{m}$ confined within the QD is conveniently described using spherical coordinates, with the center of the QD as the origin, as depicted in Fig.1-1.

The wave function of a particle confined within the QD can be written in the separated form of variables, utilizing the spherical symmetry, with the radial and angular components separated as follows:

$$\boldsymbol{\psi_{n,l,m}(r,\vartheta,\varphi) = \frac{u_{n,l}(r)}{r} Y_{l,m}(\vartheta,\varphi)} \qquad \textbf{Eq. 1-1}$$

where $\boldsymbol{Y_{l,m}(\vartheta,\varphi)}$ is a spherical harmonic and defines the potential energy as $\boldsymbol{U(r)}$ satisfies the Schrödinger equation for the radial component as follows:

$$\boldsymbol{-\frac{\hbar^2}{2m}\frac{d^2u}{dr^2} + \left[U(r) + \frac{\hbar^2}{2mr^2} l(l+1)\right] u = Eu} \qquad \textbf{Eq. 1-2}$$

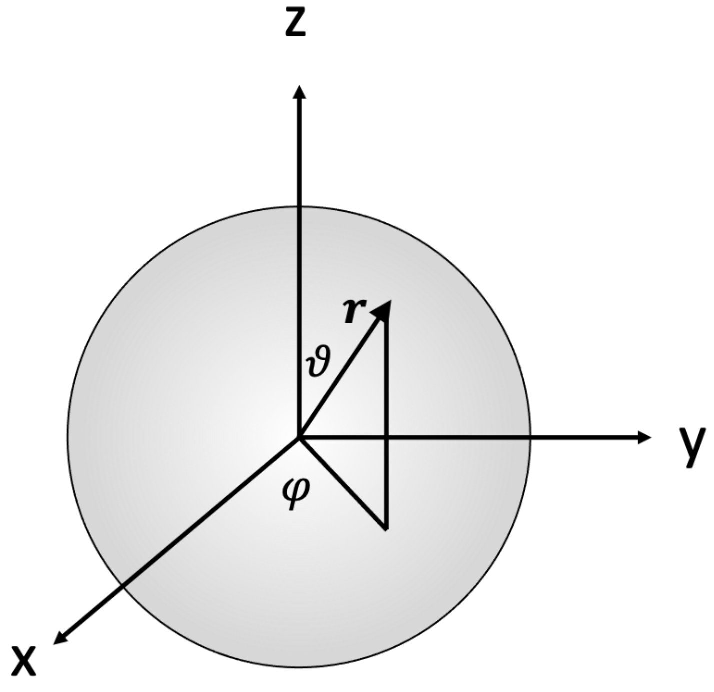

Fig.1-1 The Spherical QD and spherical coordinates.

Thus, when the QD is spherical, solving the Schrödinger equation that describes the particles confined within the dot results in solving the one-dimensional Schrödinger equation for the radial component. From this, eigenfunction and eigenvalue can be expressed in terms of the principal quantum number, $\boldsymbol{n}$, and the orbital angular momentum quantum number, $\boldsymbol{l}$, as well as the magnetic angular momentum quantum number, $\boldsymbol{m}$. Additionally, the orbital angular momentum, $\boldsymbol{L}$, can be expressed as:

$$\boldsymbol{L^2 = \hbar^2 l(l+1), \qquad l = 0, 1, 2, 3 \ldots} \qquad \textbf{Eq. 1 - 3}$$

The magnetic angular momentum is given by the z-component of the orbital angular momentum, L_z, which can be expressed as follow:

$$\boldsymbol{L_z = \hbar m, \qquad m = 0, \pm 1, \pm 2, \ldots \pm l} \qquad \textbf{Eq. 1 - 4}$$

A quantum state with an orbital angular momentum quantum number $\boldsymbol{l}$ has a degeneracy of $\boldsymbol{2l+1}$, which is the number of degrees of freedom of the magnetic angular momentum quantum number. Depending on the orbital angular momentum quantum number, they are referred to as s-state ($\boldsymbol{l} = 0$), p-state ($\boldsymbol{l} = 1$), d-state ($\boldsymbol{l} = 2$), f-state ($\boldsymbol{l} = 3$), and g-state ($\boldsymbol{l} = 4$). The region surrounding the QD is assumed to be surrounded by an infinitely high potential, thus $\boldsymbol{U(r)}$ can be expressed as follows:

$$\boldsymbol{U(r) = \begin{cases} 0 & for\, r \leq a \\ \infty & for\, r > a \end{cases}} \qquad \textbf{Eq. 1 - 5}$$

Solving the one-dimensional Schrödinger equation for the radial component under this condition, the energy eigenvalue can be obtained as follows:

$$\boldsymbol{E_{nl} = \frac{\hbar^2 \xi_{nl}^2}{2ma^2}} \qquad \textbf{Eq. 1 - 6}$$

where $\boldsymbol{\xi_{nl}}$ is the $\boldsymbol{n^{th}}$ root of the spherical Bessel function of first order. In particular, when $\boldsymbol{l} = 0$, the eigenfunction and the energy eigenvalue coincide with the case of a one-dimensional potential well. The energy eigenvalues are depicted in Fig.1-3. Thus, the energy spectrum of QD becomes discrete, similar to an atom, and possesses angular momentum. The energy can be altered by the radius.

1.1.2 For Cubic Quantum Dot

Next, consider the scenario where a QD is a cube with a side length of $\boldsymbol{a}$ as depicted in Fig.1-2. Once again, when the QD is surrounded by an infinitely high potential, it is convenient to write the Schrödinger equation for a particle of mass $\boldsymbol{m}$ confined within the dot using Cartesian coordinates $\boldsymbol{x, y, z}$ that are parallel to each side of the cube. In this case, the potential energy $\boldsymbol{U(x, y, z)}$ can be expressed as follows:

$$\boldsymbol{U(x,y,z) = \begin{cases} 0 & for\ 0 \le x,y,z \le a \\ \infty & for\ x,y, or\ z > a \end{cases}} \qquad \textbf{Eq. 1 − 7}$$

Expressing the eigenfunction in a separated form of variables as follows:

$$\boldsymbol{u_x(x)u_y(y)u_z(z)} \qquad \textbf{Eq. 1 − 8}$$

the Schrödinger equation results in three independent, one-dimensional Schrödinger equations in the $\boldsymbol{x, y,}$ and $\boldsymbol{z}$ directions as follows:

$$\boldsymbol{-\frac{\hbar^2}{2m}\frac{d^2u_x}{dx^2} = E_{n_x}u_x}$$

$$\boldsymbol{-\frac{\hbar^2}{2m}\frac{d^2u_y}{dy^2} = E_{n_y}u_y} \qquad \textbf{Eq. 1 − 9}$$

$$\boldsymbol{-\frac{\hbar^2}{2m}\frac{d^2u_z}{dz^2} = E_{n_z}u_z}$$

The total energy, $\boldsymbol{E_{total}}$, is the sum of the eigen energies of the three independent, one-dimensional Schrödinger equations in the $\boldsymbol{x, y,}$ and $\boldsymbol{z}$ directions, as follows:

$$\boldsymbol{E_{total} = E_{n_x} + E_{n_y} + E_{n_z} = \frac{(\pi\hbar n_x)^2}{2ma^2} + \frac{(\pi\hbar n_y)^2}{2ma^2} + \frac{(\pi\hbar n_z)^2}{2ma^2}} \qquad \textbf{Eq. 1 − 10}$$

Here, $\boldsymbol{n_x}$, $\boldsymbol{n_y}$, $\boldsymbol{n_z} = 1,2,3 \ldots$ are quantum numbers that define the eigenfunctions of the one-dimensional Schrödinger equation in the $\boldsymbol{x, y,}$ and $\boldsymbol{z}$ directions, respectively.

Fig.1-3 also illustrates the discrete energy spectrum of a cubic QD. Compared to the energy spectrum of a spherical QD, it possesses a distinct energy spectrum, except for the lowest energy, which is consistent with the eigen energy of the s-state in the spherical case.

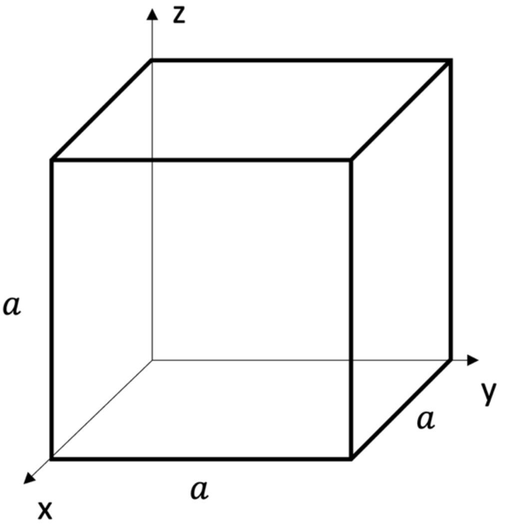

Fig.1-2 QD of a cube with a side length a in Cartesian coordinates.

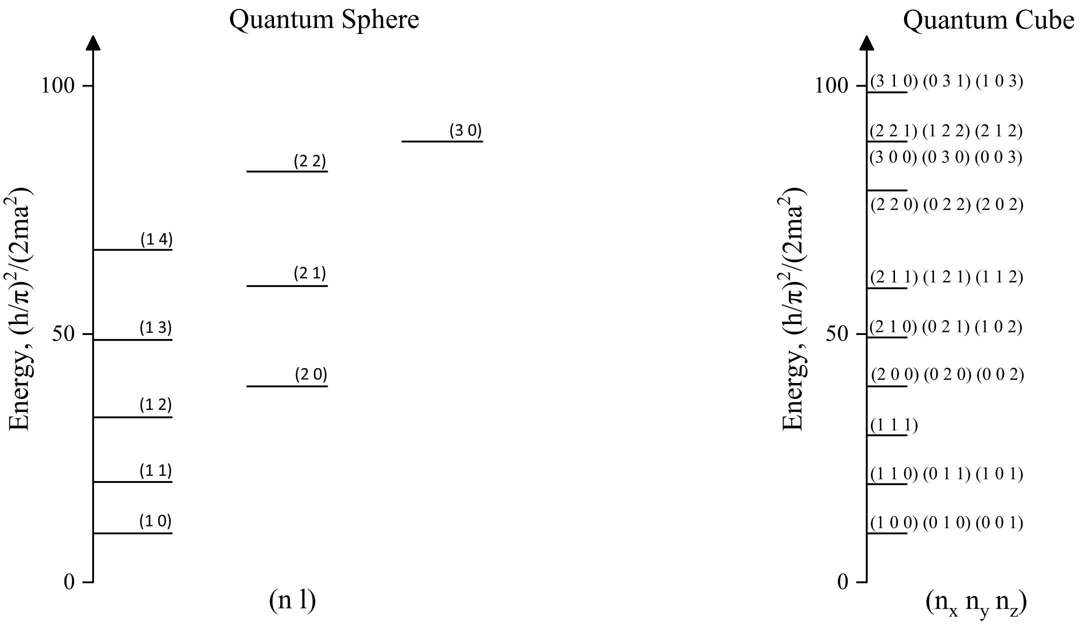

Fig.1-3 Quantum levels in a spherical QD with radius a and a cubic QD with side length a. Quantum levels in spherical QD is represented by quantum numbers (nl) using the principal quantum number n and the angular momentum quantum number l, and quantum levels in cubic QD is expressed by quantum numbers (n_x, n_y, n_z) using the quantum number n_x, n_y, n_z in the x, y and z directions. The vertical axis is normalized by the common energy $\hbar^2/(2ma^2)$.

1.1.3 For Realistic Semiconductor Quantum Dot

In the case of a realistic semiconductor QD, electrons and holes in a semiconductor possess effective masses that differ from the bare masses in a vacuum, and excitons are formed by Coulomb interactions between electrons and holes. Furthermore, the Coulomb interaction between electrons and holes is also significantly influenced by the confinement. The Hamiltonian for electrons and holes in an infinitely deep confining potential can be given by the effective mass approximation as follows:

$$\boldsymbol{H} = -\frac{\hbar^2}{2\boldsymbol{m}_e^*}\nabla_e^2 - \frac{\hbar^2}{2\boldsymbol{m}_h^*}\nabla_h^2 - \frac{\boldsymbol{e}^2}{\boldsymbol{\varepsilon}|\boldsymbol{r}_e - \boldsymbol{r}_h|} + \boldsymbol{V}(\boldsymbol{r}_e) + \boldsymbol{V}(\boldsymbol{r}_h) \qquad \textbf{Eq. 1-11}$$

Here, $\boldsymbol{m}_e^*$ and $\boldsymbol{m}_h^*$ represent the effective mass of the electron and hole, respectively, $\boldsymbol{r}_e$ and $\boldsymbol{r}_h$ represent the position of the electron and hole relative to the origin, and $\boldsymbol{\varepsilon}$ represents the dielectric constant of the semiconductor QD. The first and second terms on the right-hand side of **Eq.1-11** represent the kinetic energy of electrons and holes, respectively, and the third term represents the Coulomb energy acting between electrons and holes. The three-dimensional confinement can be divided into the following three models by the relationship between the radius $\boldsymbol{R}$ of QD and the Bohr radius $\boldsymbol{a}_B$ of excitons [25–27]. In fact, these classifications explain well the energy shift observed in actual experiments (Fig.1-4)[28].

A. $\boldsymbol{R} \gg \boldsymbol{a}_B$ (Weak Confinement)

In this region, excitons are confined within a limited spatial domain and their translational motion is quantized, hence it is referred to as exciton confinement. The energy state with the lowest energy of the exciton in this scenario is articulated as follows:

$$\boldsymbol{E} = \boldsymbol{E}_g + \frac{\hbar^2\boldsymbol{\pi}^2}{2\boldsymbol{M}(\boldsymbol{R} - \boldsymbol{\eta}\boldsymbol{a}_B)^2} - \boldsymbol{E}_R \qquad \textbf{Eq. 1-12}$$

Here, $\boldsymbol{E}_g$ represents the band gap energy of the bulk crystal, and $\boldsymbol{E}_R$ represents the Rydberg energy of the exciton. The denominator of the second term on the right-hand side denotes that the center of gravity of the exciton is confined within a radius of $\boldsymbol{R} - \boldsymbol{\eta}\boldsymbol{a}_B$. The finite size of the exciton is accounted for through the use of $\boldsymbol{\eta}$ = 0.5 [29]. A quintessential illustration of this model is provided by CuCl QDs, which possess an exciton Bohr radius of 0.68 nm (Fig.1-4).

B. $R \ll a_B$ (Strong Confinement)

In this region, electrons and holes are confined and quantized independently within the nanocrystal, hence it is referred to as electron-hole individual confinement. In this scenario, the kinetic energy of electrons and holes prevails in comparison to the Coulomb energy between the electrons and holes. The energy state with the lowest energy of the exciton in this scenario is articulated as follows:

$$E = E_g + \frac{\hbar^2\pi^2}{2\mu R^2} - \frac{1.786e^2}{\varepsilon R} - 0.248E_R \qquad \mathbf{Eq.1-13}$$

$$\frac{1}{\mu} = \frac{1}{m_e^*} + \frac{1}{m_h^*} \qquad \mathbf{Eq.1-14}$$

Here, the third term on the right-hand side of **Eq.1-13** represents the Coulomb energy resulting from the distance between electrons and holes diminishing as a consequence of confinement, and the fourth term represents the correlation energy. It is anticipated that the energy shift from the band gap of the bulk crystal will be nearly inversely proportional to $\boldsymbol{R^2}$, as the second term undergoes a greater change as $\boldsymbol{R}$ decreases in comparison to the other terms. A quintessential illustration of this model is provided by CdS QDs, which possess an exciton Bohr radius of 4.4 nm (Fig.1-4).

C. $R \sim a_B$ (Medium Confinement)

Among the electrons and holes of excitons, the lighter one, typically an electron, is restricted in its rotational motion outside, while the other one is confined within the potential created by it. An example of this model is provided by CuBr QDs, which possess an exciton Bohr radius of 1.25 nm (Fig.1-4).

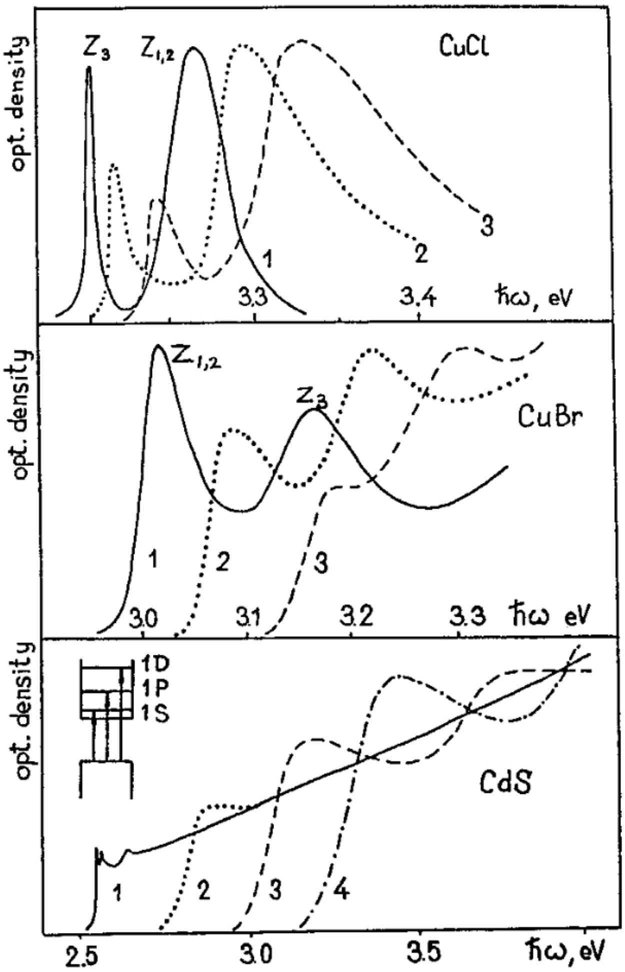

Fig.1-4 Exciton spectra at 4.2K for CuCI and CuBr microcrystallites, and excitons and electron-hole pair spectra for CdS. For CuCl, R = 31 nm (curve 1), 2.9 nm (curve 2) and 2.0 nm (curve 3); for CuBr, R = 24 nm (curve 1), 3.6 nm (curve 2) and 2.3 nm (curve 3); for CdS, R = 33 nm (curve 1), 2.3 nm (curve 2), 1.5 nm (curve 3) and 1.2 nm (curve 4). (Cited and reprinted from *Phys. Scr.* T39, 217–222 (1991) [28])

1.2 Advances in Display Technology

The recent development of information media is driven by innovations in display technology. The types of display are roughly divided into two types: non-spontaneous lighting and spontaneous lighting. The former is also called an external optical modulation method, and is represented by liquid crystal displays (LCDs) and electrochromic displays. For the latter, organic EL (Organic Light Emitting Diodes, OLEDs), plasma displays and light-emitting diodes are the main image display devices. Both displays require constant improvement in terms of higher brightness, higher efficiency, longer lifetime, higher image quality and higher resolution. In January 2017, Samsung introduced a 4K LCDs with semiconductor QDs in a color filter, amid an intensifying competition. In December of the same year, SHARP released an LCDs TV capable of 8K high-definition picture quality. Meanwhile, in January 2018, LG Display of Korea announced an OLED display supporting 8K, and in January 2020, TCL of China announced an LCD with a QDs color filter supporting 8K. Spontaneous light emitting devices are unique in that they do not require a backlight, and for example, OLED displays take advantage of this feature and are superior in display thinness, weight and design. It is expected that technological innovation of the self-luminous system will advance more and more in the future.

1.3 Advances in Colloidal Quantum Dots Light-Emitting Diodes

Colloidal quantum dots light-emitting diodes (QLEDs) are a form of spontaneous light-emitting device. They possess a similar device structure to OLEDs and employ QDs in lieu of organic compounds in the active layer. The performance of QLEDs has undergone significant improvement since their invention in 1994. Fig.1-5 illustrates the chronological progression of the maximum external quantum efficiency (EQE) (Fig.1-5(a)) and maximum brightness (Fig.1-5(b)) of orange/red-emitting QLEDs with four distinct device structures fabricated utilizing CdSe-based QDs. EQE is directly proportional to power conversion efficiency, a crucial metric for solid-state lighting (SSL) and display applications, with required brightness values of 10^3-10^4 cd m^{-2} and 10^2-10^3 cd m^{-2} for SSL and display applications, respectively. Fig.1-5 categorizes the reported QLEDs into one of four architecture types, which are described in the following section. It is evident that these four types have evolved in a nearly chronological manner. Despite scattered data, the trend indicates a steady increase in both EQE and brightness, with values approaching those of phosphorescent OLEDs.

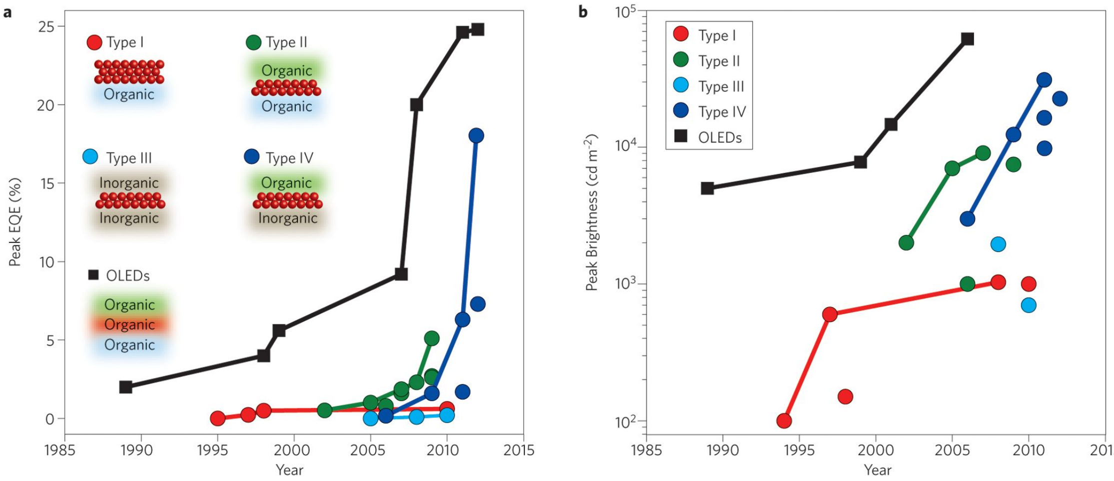

Fig.1-5 (a) Peak EQE and (b)Peak brightness. QLEDs (a substantial but non-exhaustive selection from the literature) are classified into one of four 'types' and are compared with selected orange/red-emitting (phosphorescent) OLEDs. Solid lines connect new record values. (Cited and reprinted from *Nature Photonics*. 2012, 328, Fig. 3)

1.3.1 Type I: QLEDs Utilizing Polymer CTLs

QLEDs utilizing polymer charge-transport layers, developed during the early 1990s, are among the earliest forms of QLEDs and possess structures similar to polymer LEDs [30,31]. The initial device consisted of a CdSe-core-only QD-polymer double layer or blend sandwiched between two electrodes. While electroluminescence (EL) from the QDs was achieved, the EQE was notably low (< 0.01% at approximately 100 cd m^{-2}) owing to the low PLQY of the un-shelled QDs (10% in solution). The low brightness was a consequence of the utilization of insulating QDs as both charge transport and luminescent materials, resulting in very low current densities. Subsequently, core-shell CdSe QDs were employed in type I structures to capitalize on their higher PLQY [32], and EQE values as high as 0.22% (up to 600 cd m^{-2}) were reported utilizing a CdS shell [33]. Nevertheless, these devices still exhibited significant parasitic polymer EL, indicating inefficient exciton formation within the QDs.

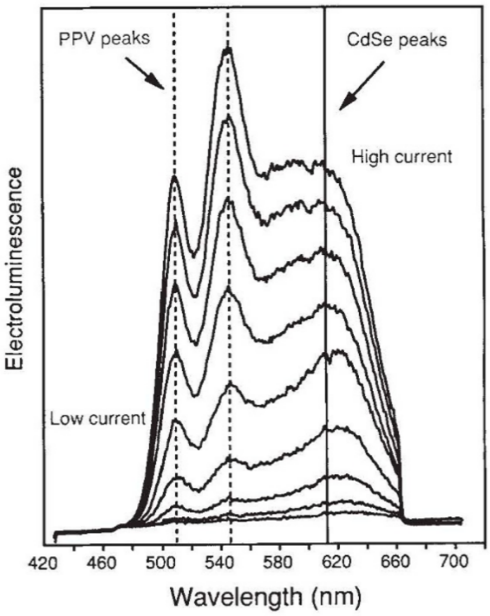

Fig.1-6 Voltage-dependent EL of CdSe/PPV samples. In samples with a very thin CdSe layer (one or two monolayers) it is possible to see significant PPV signal in addition to the CdSe signal. At lower voltages CdSe emission dominates, giving a sample with (in this case) a yellow color. As the voltage is increased the PPV emission becomes more intense, leading to distinctly green luminescence. (Cited and reprinted from *Nature*, 1994, 370, 354-357, Fig. 4)

In these early QLEDs, the mechanism of EL was theorized to be driven by either direct charge injection (Fig.1-7(b)), fluorescence resonance energy transfer (FRET) (Fig.1-7(c)), or a combination of both [34]. In the case of direct charge injection, electrons and holes are injected into the QD from the charge transport layers (CTLs), forming excitons, which subsequently recombine to emit a photon. FRET, on the other hand, is a unique mechanism that transpires when luminescent species, such as luminescent polymers, low-molecular-weight organic or inorganic semiconductors, are in close proximity to the QD layer [35–38]. FRET occurs when an exciton is formed on an emitting species and the energy of the exciton is nonradiatively transferred to the QD via dipole-dipole coupling. However, the relative contributions of direct charge injections and FRET in all four types of QLEDs are currently unknown. Therefore, a more comprehensive understanding of the mechanism, particularly as a function of the QLED architecture, is vital for the design of more efficient and brighter devices.

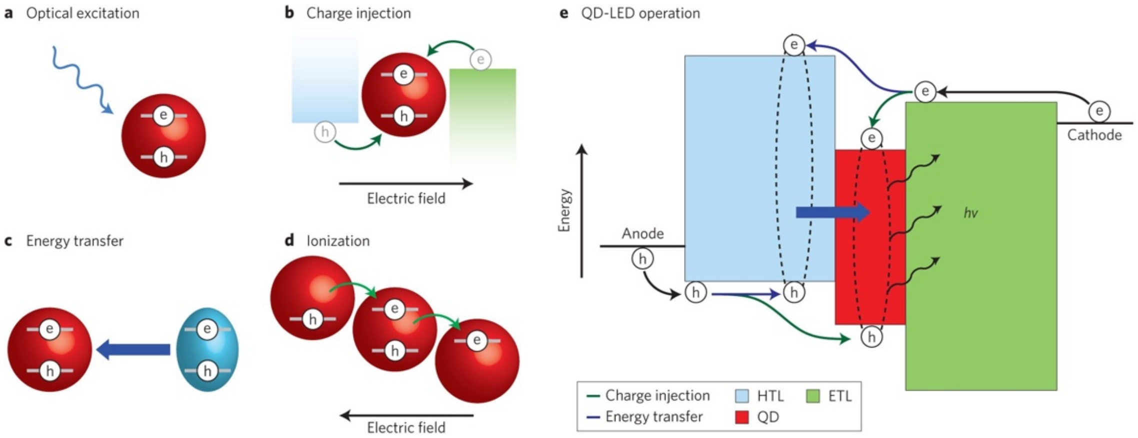

Fig.1-7 QDs excitation mechanisms. (a) Optical excitation: an exciton is formed in a QDs by absorbing a high-energy photon. (b) Charge injection: an exciton is formed by injection of an electron and a hole from neighboring CTLs. (c) Energy transfer: an exciton is transferred to a QDs via FRET from a nearby donor molecule. (d) Ionization: a large electric field ionizes an electron from one QDs to another, thereby generating a hole. When these ionization events occur throughout a QDs film, generated electrons and holes can meet on the same QDs to form excitons. (e) Energy band diagram of a typical type II QLEDs that outlines the two suspected QDs excitation mechanisms: charge injection and energy transfer. (Cited and reprinted from *Nature Photonics*. 2012, 328, Fig. 4)

1.3.2 Type II: QLEDs Incorporating Organic Small Molecule CTLs

In 2002, Coe *et al.,* introduced a type II QLEDs consisting of a monolayer of QDs at the interface of a bilayer OLEDs (Fig.1-8) and demonstrated a record EQE of up to 0.5% [39]. The improved efficiency is attributed to the utilization of a monolayer of QDs, which separates the light-emitting process from the charge transport through the organic layer [34,36,38–41]. The study demonstrated that when a mixed solution of QDs and charge-transporting organic molecules was spin-coated, a QD monolayer was spontaneously formed on the organic molecular interface through phase separation (Fig.1-8(a), inset).

As such, the fabrication and patterning of densely packed QD monolayers became crucial to enhance the efficiency and practicality of type II QLEDs. One alternative approach is microcontact printing. In this method, a QD monolayer is spin-coated on a stamp made of poly (dimethylsiloxane) (PDMS), and after drying, QDs are transferred from the stamp to the substrate through contact [40,42,43]. Microcontact printing has the advantage of avoiding the exposure of the underlying organic material to solvents during QDs deposition. Additionally, QLEDs manufactured using microcontact printing provide higher efficiency than QLEDs using phase separation, as QDs are partially embedded in the underlying organic layer during stamping [36]. Positioning a QD monolayer a few nanometers away from an organic interface is believed to reduce the charging of the QDs and the electric field across the QDs [41], which both reduce EQE due to PLQY reduction [44,45]. Anikeeva *et al.*, utilized microcontact printing to fabricate QLEDs with QDs sandwiched between two organic CTLs (Fig.1-8(b)). In this QLED, the emission wavelength was modulated across the entire visible spectrum by varying the composition of the QDs, and an EQE of up to 2.7% was achieved for orange emission [46]. Thus, the spectral purity and modularity of the QLED reported in this study clearly demonstrated its potential for EL display applications.

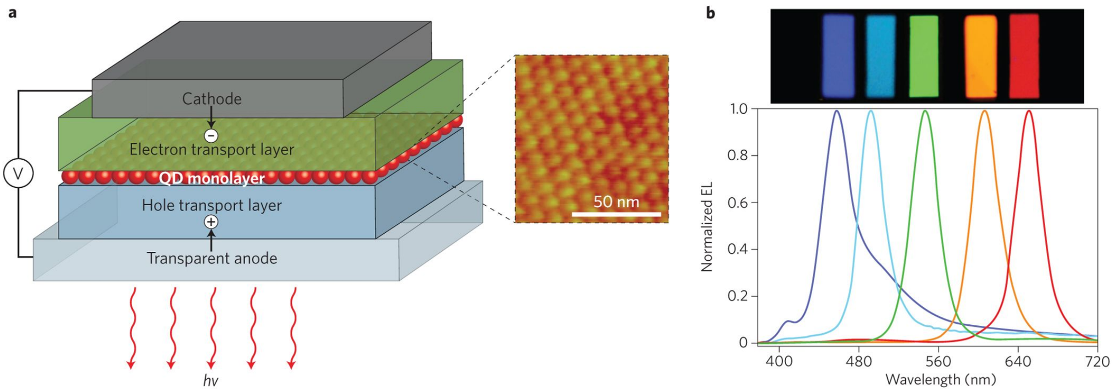

Fig.1-8 (a) The prototypical type II QLEDs structure, comprising a monolayer of QDs sandwiched between an organic hole transport layer (HTL) and an organic electron transport layer (ETL). Its corresponding energy band diagram is shown in Fig.1-7 (e). Inset: An atomic force microscope image of a monolayer of QDs on an organic HTL. (b) Photographs of EL from type II QLEDs with varying QDs compositions and their respective emission spectra. (Cited and reprinted from *Nature Photonics*. 2012, 328, Fig. 5)

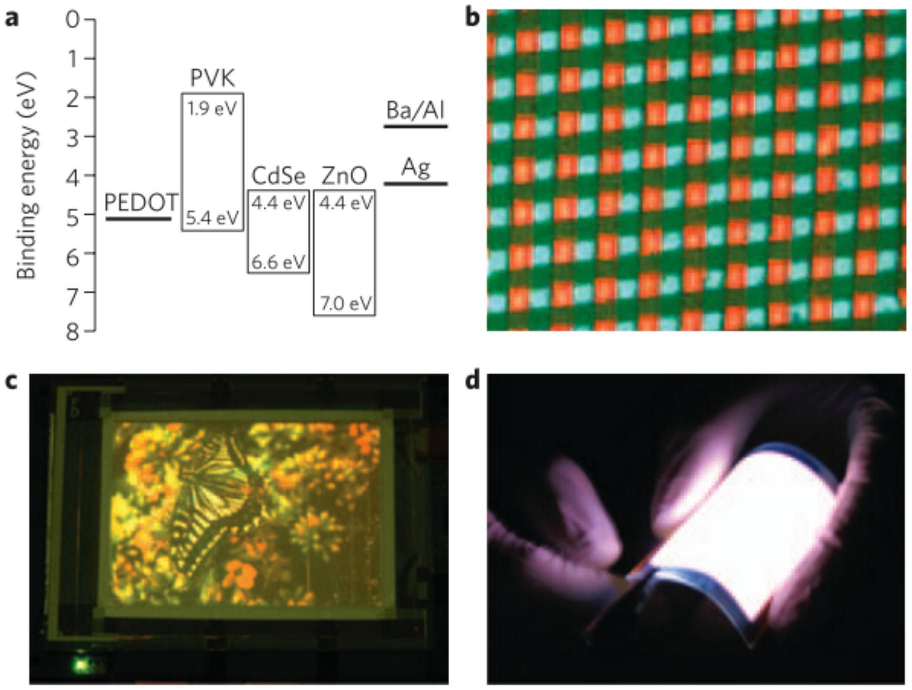

Fig.1-9 (a) Energy band diagram of the first type IV QLEDs employing ZnO [47]; the electron transport layer of choice in today's high-performance devices. PEDOT, poly(3,4-ethylenedioxythiophene); PVK, poly-N-vinyl carbazole. (b) The first demonstration of red-green-blue EL from (type II) QLEDs pixels, patterned using microcontact printing [42]. (c) This technique has been harnessed to produce a 4-inch full-color active-matrix type IV QLEDs display [48]. (d) Flexible white-emitting type II QLEDs. (Cited and reprinted from *Nature Photonics*. 2012, 328, Fig. 6)

White-light emitting QLEDs have also been demonstrated to be fabricated by mixing different compositions [49] or sizes [50] of QDs. By blending red, green, and blue, a color rendering index (CRI) of 86 was achieved. A higher CRI should be attainable by mixing a greater diversity of QD colors, indicating that white QLEDs can be implemented as sources of SSL. Furthermore, the compatibility of type II QLEDs with flexible substrates is demonstrated through the flexible white-emitting QLEDs shown in Fig.1-9(d).

Shirasaki *et al*., showed that FRET is the dominant QDs excitation mechanism, at least in some type II QLEDs geometries. However, the achievement of EQE values reaching greater than 2%, as demonstrated in QD monolayer-based devices containing organic donor materials with very low PLQY, challenges the universality of the FRET model [51]. Nonetheless, combining the OLEDs architecture with a single layer of QDs was a significant advancement in demonstrating efficient QLEDs. While these devices boast all the benefits of OLEDs, they offer the additional benefits of increased spectral purity and tunability. However, the utilization of an organic layer renders the device unstable when exposed to air [52,53]. Similar to OLEDs, commercially available QLEDs require protective encapsulation, which increases manufacturing costs and hinders applications such as flexible technology. Additionally, the relatively high insulation of organic semiconductors may limit the current density that can be achieved with QLEDs before the device breaks down, thereby limiting brightness.

1.3.3 Type III: QLEDs Featuring Inorganic CTLs

All-inorganic QLEDs utilize inorganic CTLs to improve the device's stability in air and allow for higher current densities. Mueller *et al.*, fabricated all-inorganic QLEDs by sandwiching a monolayer of QDs between epitaxially grown n-type GaN and p-type GaN [34]. They observed EL, albeit with very limited EQE (less than 0.01%). However, the epitaxial growth of GaN reduces the advantage of colloidal QDs, which can be used to inexpensively produce large-area devices. Therefore, an alternative approach is required to develop QLEDs using inorganic CTLs. One such alternative approach is the use of sputtered metal oxides as CTLs. Similar to organic materials, metal oxide and chalcogenide thin films can be deposited at room temperature by sputtering. The diverse metal oxide and chalcogenide compositions allow for fine-tuning of the energy bands required for optimal operation of QLEDs. Metal oxides are more conductive than organic oxides, and the conductivity of metal oxides can be adjusted by controlling the oxygen partial pressure during thin film growth. Caruge *et al.*, applied zinc tin oxide and NiO as n-type and p-type CTLs, respectively, for QLEDs [54]. As expected, these devices achieved high current density (up to 4 A cm^{-2}), but EQE was less than 0.1%. This low EQE was attributed to QDs damage during sputtering of the overlying oxide layer, carrier imbalance (due to a large hole injection barrier between p-type metal oxide and QDs) or PL quenching of QDs by the surrounding conductive metal oxides [55]. In 2019, Ghosh *et al.*, fabricated all-inorganic QLEDs through a solvent treatment process [56]. In this study, SiQDs was utilized as the active layer, resulting in an EQE of 0.25% and a maximum brightness of 1,400 cd m^{-2}.

Additionally, a class of all-inorganic QLEDs has emerged that utilizes distinct excitation mechanisms. These devices are composed of a capacitive structure, consisting of two contacts across a film of dielectric material with a layer of QDs at the center [55,57]. A high alternating current (AC) voltage drives these devices, which operate through field-assisted ionization of QDs to produce free carriers (Fig.1-7 (d)). This architecture obviates the need for CTLs and energy band alignment between different semiconductors. Although their brightness is limited (~10^{-3} lm W^{-1}), these devices demonstrate an alternative method for electrically exciting QDs and provide a unique platform for studying the effects of electric fields on QDs [58].

1.3.4 Type IV: QLEDs Incorporating Hybrid Organic-Inorganic CTLs

Type IV QLEDs, which are hybrid structures containing both organic and inorganic CTLs, typically use metal oxides as n-type semiconductors in one layer and organic semiconductors in the other. This device structure has garnered interest in QLEDs research due to its ability to be fabricated through a low-cost solution treatment process and its high device performance. For example, in QLEDs using CdSe-based QDs as the active layer, EQEs with red, green, and blue emissions have reached approximately 20% of the energy conversion efficiency of a mercury lamp, respectively [59,60]. Research has also been conducted on switching the anode and cathode in this device structure (Fig.1-10), and for example, the driving life in the atmosphere of an inverted OLED with a switched anode and cathode was dramatically longer than that of a conventional OLED. Furthermore, when materials that are less sensitive to oxygen and moisture were used for the electron injection layer and cathode, they did not deteriorate after exposure to air for 100 days [61]. Therefore, inverted QLEDs (iQLEDs) has a great potential because the same effect could be expected in QLEDs.

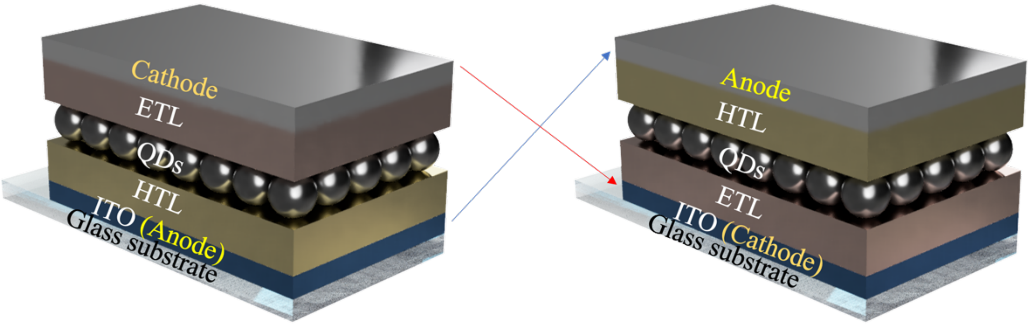

Conventional
QLEDs

Inverted
QLEDs

Fig.1-10 A schematic representation of the device structure of conventional QLEDs (left) and iQLEDs (right).

A full-color 4-inch QLEDs display (Fig.1-9(c)) utilizing a similar type IV hybrid structure has also been reported [48]. In the pixelated display structure, the QDs are patterned through microcontact printing (Fig.1-9(b)) and have a resolution of up to 1,000 pixels per inch (25 μm features) [42], which is a remarkable demonstration of the feasibility of using QLEDs in display applications. The energy transfer scheme suspected to dominate the QDs excitation in type II QLEDs requires a carrier-type transfer through the closely packed QDs of the monolayer film in order to form excitons in the adjacent donor material (Fig.1-7(e)) [41]. In contrast to type II QLEDs, which employ QD films in the form of a single layer, type III and type IV QLEDs employ QD films that are thicker than a single layer, typically around 50 nm. As a result, the operating mechanism of type IV QLEDs is more likely to rely on charge injection, as opposed to energy transfer, in comparison to type II QLEDs.

1.4 Recent Progress in Near-Infrared Light-Emitting Device Technology

Emitting the near-infrared (NIR) portion of the spectrum (700 to 2,500 nm), light-emitting diodes (called NIR-LEDs) support a wide variety of applications, including optical diagnostics and biomedical imaging [62], optical communications, remote sensing, security, night vision, and data storage [63]. The specific application field determines the desired spectral range within the NIR (Fig.1-11(a)). For in vivo bioimaging, NIR is particularly attractive for optical imaging, biomedical sensing and photodynamic therapy due to the translucency of biological tissues, which are oxygenated and deoxygenated blood in specific NIR wavelength regions, also called biological windows. In addition, in the field of optical wireless communication, it is divided into a wavelength region where the transmission loss of optical fibers is small and a correlated band [64]. NIR-LEDs are also in demand for security certification, optogenetics, crop life cycle management, optical fidelity and surveillance [65].

Common NIR-LEDs feature epitaxial heterostructures of III-V inorganic semiconductors (*e.g.*, GaAs, InGaAs, InGaAlAs) [66–68]. Commercial products also employ inorganic phosphors, compounds doped with transition metals [69] or rare earth trivalent ions [70]. The EQE of the AlGaAs/GaAs/AlGaAs III-V LED [67] is reported to be 72% at 880 nm and 44.5% at 775 nm for the LED based on $LaMgGa_{11}O_{19}$: Cr^{3+} phosphors [71]. However, III-V LEDs require the substrate to be replaced with a highly reflective mirror structure after manufacture to increase the low power output. This is due to a mismatch in refractive index between these materials (> 3.0) [68] and common substrates. Furthermore, inorganic phosphors require a sintering process at very high temperatures (over 1,000 °C). These processing requirements are roadblock to low-cost handheld portable implementations.

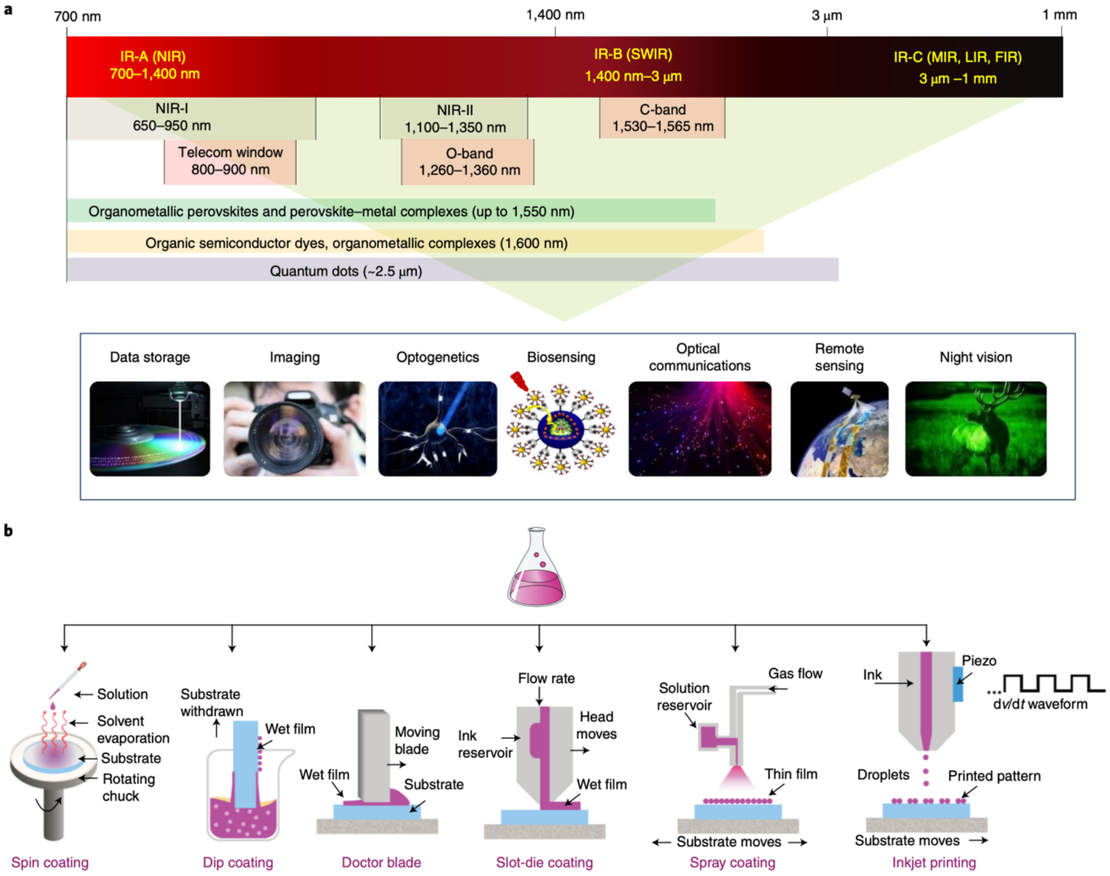

Fig.1-11 (a) The three infrared (IR) spectral regions IR-A (NIR), IR-B (SWIR) and IR-C (MIR, LIR, FIR) and illustration of selected applications. FIR, far infrared; LIR, long infrared; MIR, mid-infrared; NIR, near infrared; SWIR, short-wave infrared. NIR sources are in demand for application in biosensing, optogenetics, biometrics, night vision, data storage, surveillance and 3D imaging. Biological transparency windows are defined as follows: first (NIR-I, 650–950 nm), second (NIR-II, 1,100–1,350 nm), third (NIR-III, 1,600–1,870 nm) and fourth (NIR-IV, centered at 2,200 nm) NIR windows that allow for clearer imaging due to a scattering and absorption reduction. The telecom window between 800 nm and 900 nm was originally used for transmitting information, followed by the range 1,260–1,360 nm (or O-band) for short-distance communication, whereas today the 1,530–1,565 nm range (known as the C-band) is the most commonly used band for long-haul optical transmission. (b) Solution-processed NIR-LEDs can be processed from inks using various methods as shown. (Cited and reprinted from *Nature Photonics*. 2021, 15, 656-669, Fig. 1)

Organic semiconductor (OSC) [72], metal halide perovskite (HP) [73] and QDs [74] luminescent materials could be processed through solution-based processes such as inkjet printing, doctor blade and spray coating (Fig.1-11(b)) on a wide variety of substrates using low-cost and low-temperature methods. These properties make these thin-film LEDs a potentially cost-effective alternative to inorganic LEDs and are of interest for new applications in wearable, implantable, and portable electronics.

Fig.1-12 summarizes the EQE performance of OLEDs, perovskite LEDs (PeLEDs) and QLEDs reported in the past. At NIR-I, OLEDs and PeLEDs have been intensively studied, with some devices even exceeding 20% of EQE. However, LEDs emitting light in the wavelength range above 1,000 nm have not been developed. Therefore, QLED has great potential as an LED that emits light in the wavelength range of over 1,000 nm including NIR-II even if the EQE is less than 5%.

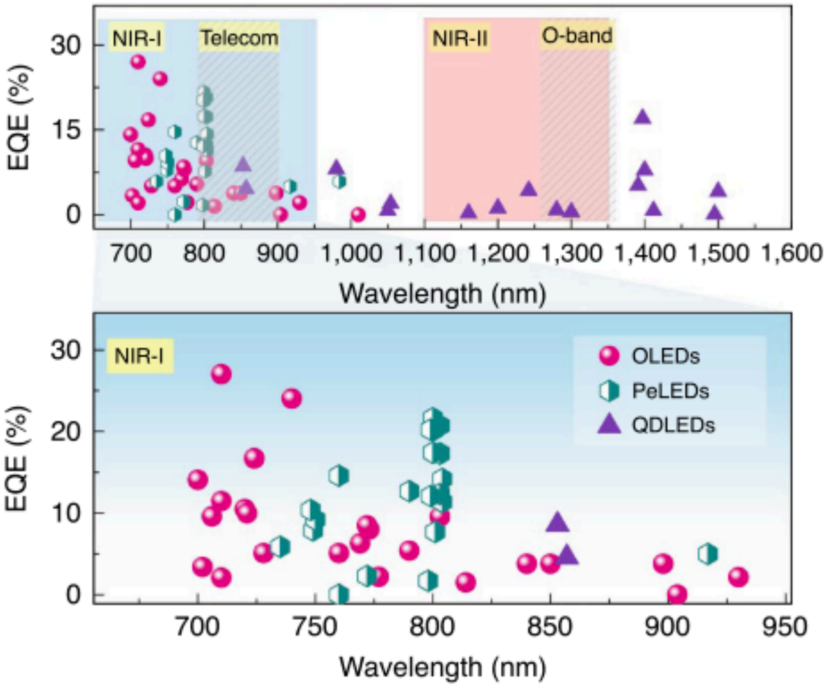

Fig.1-12 Summary of solution-processed NIR-LEDs with EQE including organic LEDs (OLEDs), perovskite LEDs (PeLEDs) and QLEDs. (Cited and reprinted from *Nature Photonics*. 2021, 15, 656-669, Fig. 5)

An early NIR-QLEDs were demonstrated using an indium arsenide-zinc selenide (InAs-ZnSe) core-shell QDs [75] or PbS QDs [76] embedded in a poly [2-methoxy-5-(2-ethylhexyloxy)-1, 4-phenylenevinylene] (MEH-PPV) matrix as the active layer. The device showed emission from 1,000 nm to 1,300 nm, although with a low EQE < 0.5. This device was driven by the formation of excitons in the organic host/surrounding interlayer and the subsequent transfer of Förster energy to the QDs via dipole-dipole interactions. However, these devices were limited in performance by the low mobility of the organic medium/surrounding interlayer and the lack of a materials with the suitable energy to enhance charge injection [75–78].

The breakthrough of NIR-QLEDs was accomplished by the realization of a device using a thick pristine QDs layer (40-50 nm) as an active layer [79]. This method improves the radiative recombination rate because excitons are generated directly in the QDs layer. Furthermore, the charge injection efficiency was individually optimized using a suitable CTLs. As a result, devices with decent PbS QDs layer showed a maximum EQE of 1.15% (at 1,200 nm). Further improvement of NIR-QLEDs performance was achieved by precise length control of organic ligands of PbS QDs [80]. By optimizing the length of ligands, the radiative recombination and carrier mobility of the QDs film could be enhanced simultaneously. A suitable interlayer injected charge directly into the QDs, allowing exciton formation in it to prevent direct contact with the electrode, thereby avoiding the quenching of the plasmon [81]. This resulted in an EQE of up to 2% (device current density, $J = 1.0$ mA cm^{-2} at 1,054 nm). An efficient heavy-metal-free NIR-QLEDs was demonstrated using SiQDs as the active layer. The device also adopted an interlayer engineering approach and showed an EQE of 8.6% ($J = 0.01$ mA cm^{-2} at 850 nm) [82]. Furthermore, QLEDs using a giant shell In(Zn)As–In(Zn)P–GaP–ZnS QDs as an active layer demonstrated EQE of 4.6% ($J = 1.5$ mA cm^{-2} at 857 nm) [83]. In particular, QLEDs based on InAs/GaAs QDs with high power (~2.6 mW) and large spectral bandwidth (1,255 nm) have also been reported at room temperature [84].

1.5 Heavy-Metal-Free Quantum Dots Light-Emitting Diodes

Previously well-developed QLEDs relied on heavy metal cations such as Cd, Pb, and mercury (Hg) that compose the core or/and shell of the colloidal QDs used in the active layer. However, concerns about the risks these substances pose to our health and the environment are growing every year. For example, the European Union's Restriction of Hazardous Substances Directive (RoHS) severely restricts the use of these substances in consumer electronic products. Therefore, if these devices could be manufactured using heavy-metal-free QDs, the commercial success of QLEDs would greatly increase.

Heavy-metal-free QLEDs using indium phosphide (InP) [85], zinc selenide (ZnSe) [86], copper indium sulfide ($CuInS_2$) [87], carbon dots [88], $(AgIn)_xZn_{2(1-x)}S_2$ (ZAIS) [89], Pb-free perovskite [90], double perovskite [91] or Si [82,92–105] QDs as their active layers are expected to be environmentally friendly and sustainable next-generation QLEDs. Notably, QLEDs utilizing InP- or ZnSe-based QDs exhibit exceptional device performance, such as high EQE beyond 20%, high brightness up to 100,000 cd m^{-2}, and low turn-on voltage (~2 V) [85,86]. Despite such remarkable progress, other alternative heavy-metal-free QLEDs still possess poor EQE characteristics, with EQEs achieved at 7.8% for $CuInS_2$ [87], 2.2% for ZAIS [89], 0.083% for carbon dots [88], 0.3% for Pb-free perovskite [90], and 0.064% for Pb-free double perovskite [91]. Despite ongoing research efforts, it remains challenging to realize high values of EQE in these QLEDs.

1.5.1 Silicon Quantum Dots Light-Emitting Diodes

The first report of colloidal silicon quantum dots light-emitting diodes (Si-QLEDs) was by Cheng *et al.*, in 2010 [101]. The device employed organic compounds for both the HTL and ETL, and exhibited an EL peak wavelength of 868 nm at a device current density of 100 mA/cm^2. However, the device also displayed an undesirable EL from the adjacent organic layer (Fig.1-13). The EQE was measured at 0.6% and the maximum optical power density was 85 μW/cm^2.

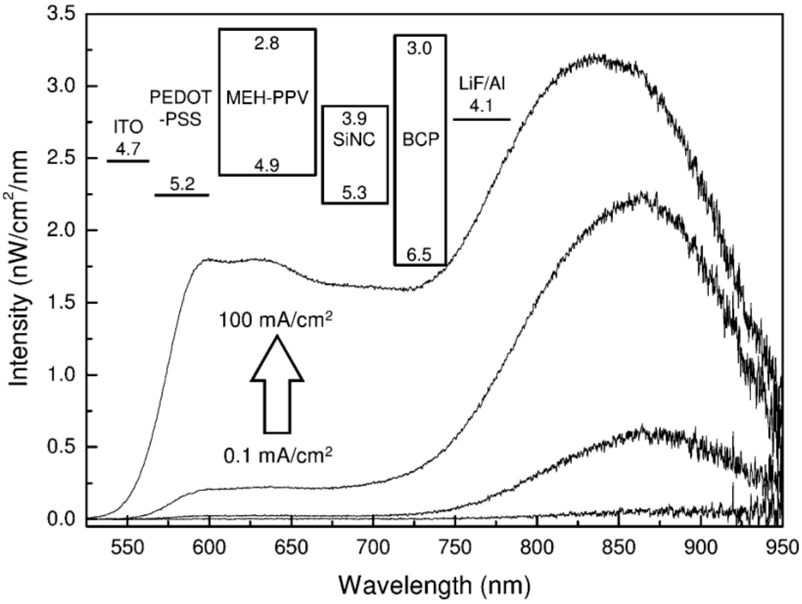

Fig.1-13 Electroluminescence spectra for the device at current densities of 0.1, 1, 10, and 100 mA/cm^2. Inset: The proposed energy level diagram for the device under applied zero bias. (Cited and reprinted from *Nano Lett.* 10, 1154–1157 (2010), Fig. 2c)

Furthermore, it was demonstrated that the device current density and EL shape are dependent on the thickness of the SiQDs (Fig.1-14). By controlling the concentration of the SiQDs solution during film fabrication, it was observed that the device current density decreased with increasing concentration, resulting in an increase in the turn-on voltage (Fig.1-14(a)). Conversely, adjacent EL emission was suppressed with increasing concentration (Fig.1-14(b)). This was attributed to the increased surface coverage of SiQDs on MEH-PPV layer, as well as the suppression of charge leakage into the adjacent layer. Additionally, the research group also demonstrated NIR emitting Si-QLEDs (λ_{EL} = 853 nm) without parasitic emission, achieving a high EQE of 8.6% by avoiding the use of a polymer emitter in the HTL and varying the ETL materials [82]. Despite this, several studies have reported red-emitting Si-QLEDs, yet the EQE remains low [102,103].

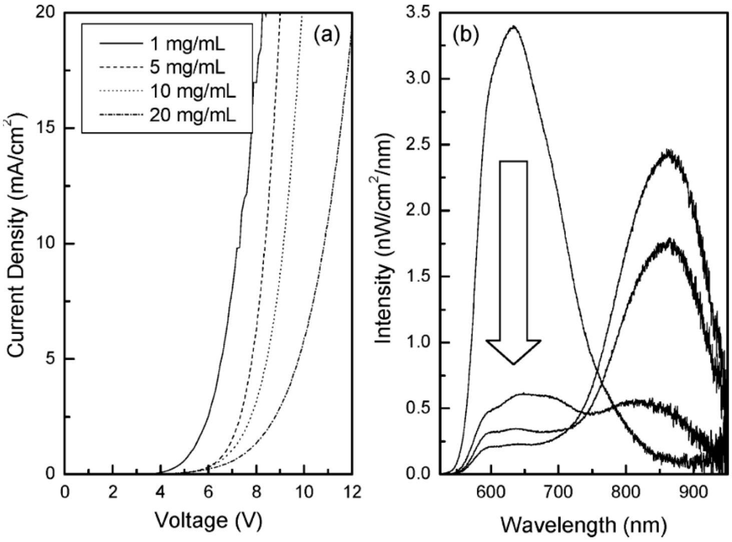

Fig.1-14 (a) Current-voltage characteristics for nanocrystal-organic light-emitting devices having emissive layers spun-cast from solutions with varying silicon nanocrystal concentration. (b) Electroluminescence spectra for the devices in (a) at an applied current density of 10 mA/cm^2. The arrow denotes the direction of increasing concentration. (Cited and reprinted from *Nano Lett.* 10, 1154–1157 (2010), Fig. 3)

In 2012, Mastronardi *et al.*, demonstrated the synthesis of SiQDs with enhanced brightness and their incorporation into hybrid OLEDs, and optimized device performance using a rational chemical approach [104]. Specifically, it was found that allylbenzene was grafted onto the surface of SiQDs via a thermally-initiated hydrosilylation reaction, which increased the packing density of SiQDs and enhanced electronic bonding between SiQDs in the device's emissive layer. These approaches enabled the construction of hybrid Si-QLEDs with a measured turn-on voltage of 4.6 V, a peak EL at 700 nm with a maximum brightness of 22.7 cd/m^2 and a maximum EQE of 0.17%. In 2013, Maier-Flaig *et al.*, demonstrated the peak wavelength modularity of EL by varying the diameter of SiQDs [105]. This study also showed that size-selective SiQDs suppressed the EL blue shift (15 nm) even in high voltage region (3.5-10 V) and enhanced the device lifetime, however, the maximum EQE was low (~1.1%). Furthermore, they reported that the undesirable emission from Poly-TPD was suppressed when the thickness of the SiQDs layer exceeded 20 nm. In 2016, Yao *et al.*, designed and demonstrated efficient Si-QLEDs with bottom cathode inverted structures. Improved carrier transport and confinement were achieved using ZnO QDs and 1,1-Bis[(di-4-tolylamino)phenyl]-cyclohexane (TAPC) as ETL and HTL, respectively. When the ITO cathode was modified using poly(ethylene imine) (PEI), the electron injection barrier between ITO and ZnO QDs was reduced to the electron well, and the electron injection current was significantly increased. Following PEI modification, the maximum EQE of the Si-QLEDs increased from 1.1% to 2.7%, indicating an improvement in the balance of carriers between electrons and holes [92]. Gu *et al.*, also adopeted this ITO modification approach into conventional device structure. By optimizing the thickness of organic compounds between ITO and the HTL, the EQE was improved from 1.1% to 2.4% [94]. In 2018, Liu *et al.*, examined how phenylpropyl- and octyl-ligands of SiQDs affected device performance. The benzene ring of the phenylpropyl ligand significantly enhanced electron transport between the QDs, thus increasing the device current density. As a result, the optical power density of phenylpropyl ligands SiQDs device was larger than that of octyl ligand SiQDs device. However, the presence of the benzene ring in the phenylpropyl ligand impeded hole transport in the QLEDs, resulting in a more pronounced imbalance in the injection of electrons and holes in the phenylpropyl ligand SiQDs device, as compared to the octyl ligand SiQDs device. Thus, the EQE of the phenylpropyl ligand of SiQDs device was actually lower (~1.1%) than that of the octyl ligand SiQDs device (~6.2%) [96].

1.5.2 Challenges and Limitations in the Development of Si-QLEDs

As previously discussed in Section 1.5.1, despite ongoing efforts by researchers to improve the performance of Si-QLEDs, the EQE has yet to surpass 10%. Fig.1-15 summarizes the EQE values in relation to the EL peak wavelength. A broad overview of Fig.1-15 reveals that there are reports in the EL peak wavelength range from 625 nm to 868 nm, but the wavelength range extending beyond 868 nm and shorter than 625 nm remains an uncharted territory. Additionally, there are no reports of Si-QLEDs surpassing 10% in any wavelength range.

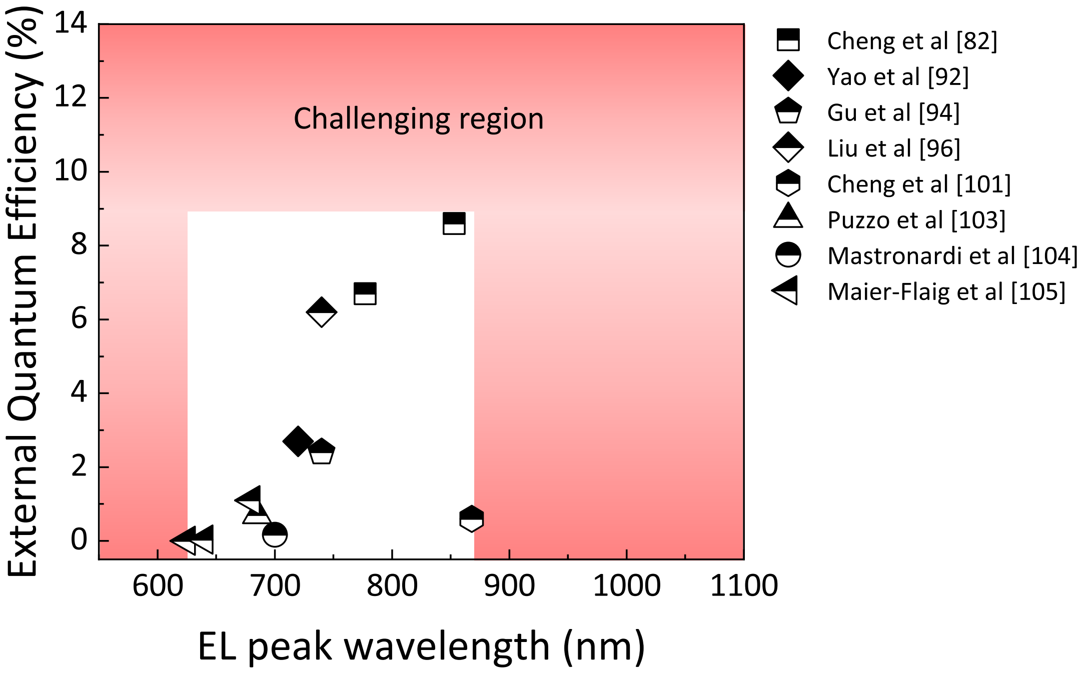

Fig.1-15 The relationship between EQE and EL peak wavelength, with data points obtained from literature sources.

In addition to the aforementioned issues, there is also the problem of EL spectral stability under high current density. As depicted in Fig.1-16, blue shifts of EL peak wavelengths have been reported in various literature. Cheng *et al.*, reported a blue shift of up to 50 nm and posited that the blue shift may reflect the size dispersion of the SiQDs and a variation of the charge injection and PL efficiency with particle diameter [82]. Liu *et al.*, also reported a blue shift of ~50 nm. In their paper, the blue shift is attributed to the band-filling effect, where charges are efficiently injected into smaller SiQDs with a larger band gap under high voltage [96]. Yao *et al.*, reported a blue shift of about 30 nm and concluded that it was due to the band-filling effect or size dispersion of the SiQDs [92]. Conversely, Maier-Flaig *et al.,* reported a suppressed blue shift of ~15 nm by applying size-separated SiQDs which reduce the size distribution of the SiQDs [105]. Furthermore, the authors have demonstrated that the size separation of SiQDs also improves device operating lifetime when compared to non-size separated ones. Therefore, these results suggest that the size separation of SiQDs is crucial to suppress the blue shift of EL and further enhance the device drive lifetime.

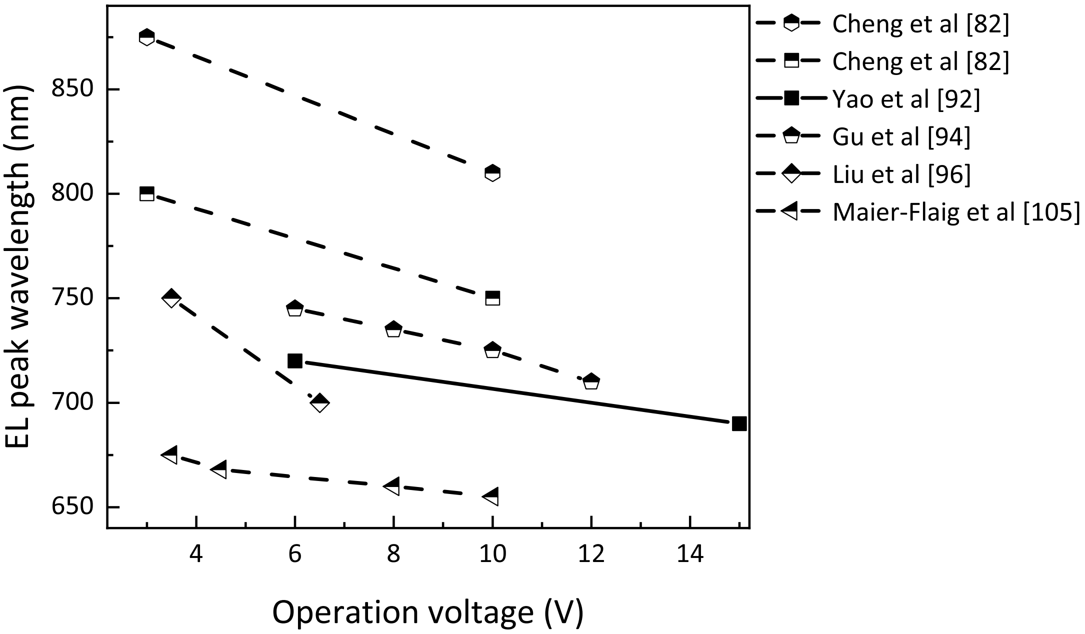

Fig.1-16 The stability of the EL peak wavelength as a function of operating voltage.

1.6 Research Motivation

In this study, “Silicon” (Si) is the focus of investigation. Being an indirect transition type semiconductor, efficient emission is not expected in bulk Si, however Si particles smaller than the exciton Bohr radius exhibit PL. Additionally, by terminating the surface of the QDs with hydrogen atoms, the emission wavelength can be modulated over a wide range of 530-1,000 nm based on the size of the QDs. The PLQY of hydrogen-terminated SiQDs is less than 5%, and it is dependent on the size of the QDs. The amorphous surface (a radiation-free deactivation source) present in hydrogen-terminated QDs can be enhanced to over 20% PLQY by terminating it with an alkyl group, which suggests that it possesses the qualities of an active layer for QLEDs. The objective of this study is to develop SiQDs synthesis technology for the enhancement of PLQY, to achieve EQE > 10% by optimizing the device structure of Si-QLEDs, and to achieve tunability of EL emission color.

1.7 References

[1] Zhai, T. *et al.* One-dimensional inorganic nanostructures: synthesis, field-emission and photodetection. *Chem. Soc. Rev.* **40**, 2986–3004 (2011)

[2] Faure, B. *et al.* Dispersion and surface functionalization of oxide nanoparticles for transparent photocatalytic and UV-protecting coatings and sunscreens. *Science and Technology of Advanced Materials* vol. 14 023001 (2013)

[3] Osada, M. & Sasaki, T. Two-Dimensional Dielectric Nanosheets: Novel Nanoelectronics From Nanocrystal Building Blocks. *Adv. Mater.* **24**, 210–228 (2012)

[4] Ariga, K., Ji, Q., Hill, J. P., Bando, Y. & Aono, M. Forming nanomaterials as layered functional structures toward materials nanoarchitectonics. *NPG Asia Materials* vol. 4 e17–e17 (2012)

[5] Ariga, K., Vinu, A., Yamauchi, Y., Ji, Q. & Hill, J. P. Nanoarchitectonics for mesoporous materials. *Bull. Chem. Soc. Jpn.* **85**, 1–32 (2012)

[6] Winnik, F. M. & Maysinger, D. Quantum dot cytotoxicity and ways to reduce it. *Acc. Chem. Res.* **46**, 672–680 (2013)

[7] Qian, H., Zhu, M., Wu, Z. & Jin, R. Quantum sized gold nanoclusters with atomic precision. *Acc. Chem. Res.* **45**, 1470–1479 (2012)

[8] Shirasaki, Y., Supran, G. J., Bawendi, M. G. & Bulović, V. Emergence of colloidal quantum-dot light-emitting technologies. *Nat. Photonics* **7**, 13–23 (2013)

[9] Walter, P. *et al.* Early Use of PbS Nanotechnology for an Ancient Hair Dyeing Formula. *Nano Lett.* **6**, 2215–2219 (2006)

[10] Rocksby, H. P. Color of selenium ruby glasses. *J. Soc. Glas. Technol.* **16**, 171–181 (1932)

[11] A.A.Onushchenko, E. Quantum size effect in three-dimensional micorscopic semiconductor crystals. *Jetp Letters* vol. 34 345–349 (1981)

[12] Efros, A. Interband light absorption in semiconductor spheres. *Sov. physics. Semicond.* **16**, 772–775 (1982)

[13] Rossetti, R., Ellison, J. L., Gibson, J. M. & Brus, L. E. Size effects in the excited electronic states of small colloidal CdS crystallites. *J. Chem. Phys.* **80**, 4464–4469 (1984)

[14] Spanhel, L., Haase, M., Weller, H. & Henglein, A. Photochemistry of colloidal semiconductors. 20. Surface modification and stability of strong luminescing CdS particles. *J. Am. Chem. Soc.* **109**, 5649–5655 (1987)

[15] Kortan, A. R. *et al.* Nucleation and Growth of CdSe on ZnS Quantum Crystallite Seeds, and Vice Versa, in Inverse Micelle Media. *J. Am. Chem. Soc.* **112**, 1327–1332 (1990)

[16] Murray, C. B., Norris, D. J. & Bawendi, M. G. Synthesis and characterization of nearly monodisperse CdE (E = sulfur, selenium, tellurium) semiconductor nanocrystallites. *J. Am. Chem. Soc.* **115**, 8706–8715 (1993)

[17] Sundaram, M., Chalmers, S. A., Hopkins, P. F. & Gossard, A. C. New Quantum Structures.

Science (80-.). **254**, 1326–1335 (1991)

[18] Cingolani, R. & Ploog, K. Frequency and density dependent radiative recombination processes in III–V semiconductor quantum wells and superlattices. *Adv. Phys.* **40**, 535–623 (1991)

[19] Alivisatos, A. P. Semiconductor Clusters, Nanocrystals, and Quantum Dots. *Science (80-.).* **271**, 933–937 (1996)

[20] Klimov, V. I. *et al.* Optical gain and stimulated emission in nanocrystal quantum dots. *Science (80-.).* **290**, 314–317 (2000)

[21] Artemyev, M. V., Woggon, U., Wannemacher, R., Jaschinski, H. & Langbein, W. Light Trapped in a Photonic Dot: Microspheres Act as a Cavity for Quantum Dot Emission. *Nano Lett.* **1**, 309–314 (2001)

[22] Graham-Rowe, D. From dots to devices. *Nat. Photonics* **3**, 307–309 (2009)

[23] Coe-Sullivan, S. Quantum dot developments. *Nat. Photonics* **3**, 315–316 (2009)

[24] Alivisatos, A. P. Perspectives on the Physical Chemistry of Semiconductor Nanocrystals. *J. Phys. Chem.* **100**, 13226–13239 (1996)

[25] Yoffe, A. D. Low-dimensional systems: quantum size effects and electronic properties of semiconductor microcrystallites (zero-dimensional systems) and some quasi-two-dimensional systems. *Adv. Phys.* **42**, 173–262 (1993)

[26] Ekimov, A. I., Efros, A. L. & Onushchenko, A. A. Quantum size effect in semiconductor microcrystals. *Solid State Commun.* **56**, 921–924 (1985)

[27] Kayanuma, Y. Quantum-size effects of interacting electrons and holes in semiconductor microcrystals with spherical shape. *Phys. Rev. B* **38**, 9797–9805 (1988)

[28] Ekimov, A. I. Optical Properties of Semiconductor Quantum Dots in Glass Matrix. *Phys. Scr.* **T39**, 217–222 (1991)

[29] Itoh, T., Iwabuchi, Y. & Kataoka, M. Study on the Size and Shape of CuCl Microcrystals Embedded in Alkali-Chloride Matrices and Their Correlation with Exciton Confinement. *Phys. status solidi* **145**, 567–577 (1988)

[30] Colvin, V. L., Schlamp, M. C. & Alivisatos, A. P. Light-emitting diodes made from cadmium selenide nanocrystals and a semiconducting polymer. *Nature* **370**, 354–357 (1994)

[31] Dabbousi, B. O., Bawendi, M. G., Onitsuka, O. & Rubner, M. F. Electroluminescence from CdSe quantum-dot/polymer composites. *Appl. Phys. Lett.* **66**, 1316–1318 (1995)

[32] Mattoussi, H. *et al.* Electroluminescence from heterostructures of poly(phenylene vinylene) and inorganic CdSe nanocrystals. *J. Appl. Phys.* **83**, 7965–7974 (1998)

[33] Schlamp, M. C., Peng, X. & Alivisatos, A. P. Improved efficiencies in light emitting diodes made with CdSe(CdS) core/shell type nanocrystals and a semiconducting polymer. *J. Appl. Phys.* **82**, 5837–5842 (1997)

[34] Mueller, A. H. *et al.* Multicolor light-emitting diodes based on semiconductor nanocrystals

encapsulated in GaN charge injection layers. *Nano Lett.* **5**, 1039–1044 (2005)

[35] Chang, T. W. F. *et al.* Efficient excitation transfer from polymer to nanocrystals. *Appl. Phys. Lett.* **84**, 4295–4297 (2004)

[36] Panzer, M. J. *et al.* Nanoscale morphology revealed at the interface between colloidal quantum dots and organic semiconductor films. *Nano Lett.* **10**, 2421–2426 (2010)

[37] Achermann, M., Petruska, M. A., Koleske, D. D., Crawford, M. H. & Klimov, V. I. Nanocrystal-based light-emitting diodes utilizing high-efficiency nonradiative energy transfer for color conversion. *Nano Lett.* **6**, 1396–1400 (2006)

[38] Achermann, M. *et al.* Energy-transfer pumping of semiconductor nanocrystals using an epitaxial quantum well. *Nature* **429**, 642–646 (2004)

[39] Coe, S., Woo, W. K., Bawendi, M. & Bulović, V. Electroluminescence from single monolayers of nanocrystals in molecular organic devices. *Nature* **420**, 800–803 (2002)

[40] Steckel, J. S. *et al.* Color-saturated green-emitting QD-LEDs. *Angew. Chemie - Int. Ed.* **45**, 5796–5799 (2006)

[41] Anikeeva, P. O., Madigan, C. F., Halpert, J. E., Bawendi, M. G. & Bulović, V. Electronic and excitonic processes in light-emitting devices based on organic materials and colloidal quantum dots. *Phys. Rev. B* **78**, 085434 (2008)

[42] Kim, L. *et al.* Contact Printing of Quantum Dot Light-Emitting Devices. *Nano Lett.* **8**, 4513–4517 (2008)

[43] Rizzo, A. *et al.* Hybrid light-emitting diodes from microcontact-printing double-transfer of colloidal semiconductor CdSe/ZnS quantum dots onto organic layers. *Adv. Mater.* **20**, 1886–1891 (2008)

[44] Empedocles, S. A. & Bawendi, M. G. Quantum-Confined Stark Effect in Single CdSe Nanocrystallite Quantum Dots. *Science (80-.).* **278**, 2114–2117 (1997)

[45] Woo, W.-K. *et al.* Reversible Charging of CdSe Nanocrystals in a Simple Solid-State Device. *Adv. Mater.* **14**, 1068 (2002)

[46] Anikeeva, P. O., Halpert, J. E., Bawendi, M. G. & Bulović, V. Quantum dot light-emitting devices with electroluminescence tunable over the entire visible spectrum. *Nano Lett.* **9**, 2532–2536 (2009)

[47] Stouwdam, J. W. & Janssen, R. A. J. Red, green, and blue quantum dot LEDs with solution processable ZnO nanocrystal electron injection layers. *J. Mater. Chem.* **18**, 1889 (2008)

[48] Kim, T. H. *et al.* Full-colour quantum dot displays fabricated by transfer printing. *Nat. Photonics* **5**, 176–182 (2011)

[49] Anikeeva, P. O., Halpert, J. E., Bawendi, M. G. & Bulović, V. Electroluminescence from a Mixed Red−Green−Blue Colloidal Quantum Dot Monolayer. *Nano Lett.* **7**, 2196–2200 (2007)

[50] Li, Y. Q., Rizzo, A., Cingolani, R. & Gigli, G. Bright White-Light-Emitting Device from Ternary

Nanocrystal Composites. *Adv. Mater.* **18**, 2545–2548 (2006)

[51] Jing, P. *et al.* Shell-dependent electroluminescence from colloidal CdSe quantum dots in multilayer light-emitting diodes. *J. Appl. Phys.* **105**, 044313 (2009)

[52] Friend, R. H. *et al.* Electroluminescence in conjugated polymers. *Nature* **397**, 121–128 (1999)

[53] Burrows, P. E. *et al.* Reliability and degradation of organic light emitting devices. *Appl. Phys. Lett.* **65**, 2922–2924 (1994)

[54] Caruge, J. M., Halpert, J. E., Wood, V., Buloví, V. & Bawendi, M. G. Colloidal quantum-dot light-emitting diodes with metal-oxide charge transport layers. *Nat. Photonics* **2**, 247–250 (2008)

[55] Wood, V. *et al.* Selection of metal oxide charge transport layers for colloidal quantum dot LEDs. *ACS Nano* **3**, 3581–3586 (2009)

[56] Ghosh, B. & Shirahata, N. All-Inorganic Red-Light Emitting Diodes Based on Silicon Quantum Dots. *Crystals* **9**, 385 (2019)

[57] Cho, S. H. *et al.* High Performance AC Electroluminescence from Colloidal Quantum Dot Hybrids. *Adv. Mater.* **24**, 4540–4546 (2012)

[58] Bozyigit, D., Wood, V., Shirasaki, Y. & Bulovic, V. Study of field driven electroluminescence in colloidal quantum dot solids. *J. Appl. Phys.* **111**, 113701 (2012)

[59] Wang, L. *et al.* Blue Quantum Dot Light-Emitting Diodes with High Electroluminescent Efficiency. *ACS Appl. Mater. Interfaces* **9**, 38755–38760 (2017)

[60] Shen, H. *et al.* Visible quantum dot light-emitting diodes with simultaneous high brightness and efficiency. *Nat. Photonics* **13**, 192–197 (2019)

[61] Fukagawa, H. & Shimizu, T. Development of Air－Stable Inverted Organic Light－Emitting Diode. *NHK技研 R&D* 48–53 (2014)

[62] Gu, Y. *et al.* High-sensitivity imaging of time-domain near-infrared light transducer. *Nature Photonics* vol. 13 525–531 (2019)

[63] Smith, A. M., Mancini, M. C. & Nie, S. Bioimaging: Second window for in vivo imaging. *Nature Nanotechnology* vol. 4 710–711 (2009)

[64] Ramaswami, R. Optical fiber communication: from transmission to networking. *IEEE Commun. Mag.* **40**, 138–147 (2002)

[65] Wu, X. *et al.* Dye-sensitized core/active shell upconversion nanoparticles for optogenetics and bioimaging applications. *ACS Nano* **10**, 1060–1066 (2016)

[66] Mokkapati, S. & Jagadish, C. III-V compound SC for optoelectronic devices. *Materials Today* vol. 12 22–32 (2009)

[67] Schnitzer, I., Yablonovitch, E., Caneau, C. & Gmitter, T. J. Ultrahigh spontaneous emission quantum efficiency, 99.7% internally and 72% externally, from AlGaAs/GaAs/AlGaAs double heterostructures. *Appl. Phys. Lett.* **62**, 131–133 (1993)

[68] Broell, M. *et al.* New developments on high-efficiency infrared and InGaAlP light-emitting

diodes at OSRAM Opto Semiconductors. in *Light-Emitting Diodes: Materials, Devices, and Applications for Solid State Lighting XVIII* (eds. Streubel, K. P., Jeon, H., Tu, L.-W. & Strassburg, M.) vol. 9003 90030L (SPIE, 2014).

[69] Mao, M. *et al.* Broadband near-infrared (NIR) emission realized by the crystal-field engineering of Y3-xCaxAl5- xSixO12:Cr3+ (x = 0-2.0) garnet phosphors. *J. Mater. Chem. C* **8**, 1981–1988 (2020)

[70] Zhong, Y. & Dai, H. A mini-review on rare-earth down-conversion nanoparticles for NIR-II imaging of biological systems. *Nano Research* vol. 13 1281–1294 (2020)

[71] Liu, S., Wang, Z., Cai, H., Song, Z. & Liu, Q. Highly efficient near-infrared phosphor LaMgGa11O19:Cr3+. *Inorg. Chem. Front.* **7**, 1467–1473 (2020)

[72] Zampetti, A., Minotto, A. & Cacialli, F. Near-Infrared (NIR) Organic Light-Emitting Diodes (OLEDs): Challenges and Opportunities. *Advanced Functional Materials* vol. 29 1807623 (2019)

[73] Kumawat, N. K., Dey, A., Narasimhan, K. L. & Kabra, D. Near infrared to visible electroluminescent diodes based on organometallic halide perovskites: Structural and optical investigation. *ACS Photonics* **2**, 349–354 (2015)

[74] Sargent, E. H. Infrared quantum dots. *Adv. Mater.* **17**, 515–522 (2005)

[75] Tessler, N., Medvedev, V., Kazes, M., Kan, S. H. & Banin, U. Efficient near-infrared polymer nanocrystal light-emitting diodes. *Science (80-.).* **295**, 1506–1508 (2002)

[76] Konstantatos, G., Huang, C., Levina, L., Lu, Z. & Sargent, E. H. Efficient Infrared Electroluminescent Devices Using Solution-Processed Colloidal Quantum Dots. *Adv. Funct. Mater.* **15**, 1865–1869 (2005)

[77] Steckel, J. S., Coe-Sullivan, S., Bulović, V. & Bawendi, M. G. 1.3 μm to 1.55 μm tunable electroluminescence from PbSe quantum dots embedded within an organic device. *Adv. Mater.* **15**, 1862–1866 (2003)

[78] Choudhury, K. R., Song, D. W. & So, F. Efficient solution-processed hybrid polymer-nanocrystal near infrared light-emitting devices. *Org. Electron.* **11**, 23–28 (2010)

[79] Bourdakos, K. N., Dissanayake, D. M. N. M., Lutz, T., Silva, S. R. P. & Curry, R. J. Highly efficient near-infrared hybrid organic-inorganic nanocrystal electroluminescence device. *Appl. Phys. Lett.* **92**, 153311 (2008)

[80] Sun, L. *et al.* Bright infrared quantum-dot light-emitting diodes through inter-dot spacing control. *Nat. Nanotechnol.* **7**, 369–373 (2012)

[81] Shimizu, K. T., Woo, W. K., Fisher, B. R., Eisler, H. J. & Bawendi, M. G. Surface-Enhanced Emission from Single Semiconductor Nanocrystals. *Phys. Rev. Lett.* **89**, 117401 (2002)

[82] Cheng, K.-Y., Anthony, R., Kortshagen, U. R. & Holmes, R. J. High-Efficiency Silicon Nanocrystal Light-Emitting Devices. *Nano Lett.* **11**, 1952–1956 (2011)

[83] Wijaya, H. *et al.* Efficient Near-Infrared Light-Emitting Diodes based on In(Zn)As–In(Zn)P–

GaP–ZnS Quantum Dots. *Adv. Funct. Mater.* **30**, 1906483 (2020)

[84] Chen, S. *et al.* InAs/GaAs Quantum-Dot Superluminescent Light-Emitting Diode Monolithically Grown on a Si Substrate. *ACS Photonics* **1**, 638–642 (2014)

[85] Won, Y.-H. *et al.* Highly efficient and stable InP/ZnSe/ZnS quantum dot light-emitting diodes. *Nature* **575**, 634–638 (2019)

[86] Kim, T. *et al.* Efficient and stable blue quantum dot light-emitting diode. *Nature* **586**, 385–389 (2020)

[87] Wang, Z. *et al.* Facile Synthesis of Cu–In–S/ZnS Core/Shell Quantum Dots in 1-Dodecanethiol for Efficient Light-Emitting Diodes with an External Quantum Efficiency of 7.8%. *Chem. Mater.* **30**, 8939–8947 (2018)

[88] Zhao, B. & Tan, Z. Fluorescent Carbon Dots: Fantastic Electroluminescent Materials for Light-Emitting Diodes. *Adv. Sci.* **8**, 2001977 (2021)

[89] Motomura, G. *et al.* Efficient quantum-dot light-emitting diodes using ZnS–AgInS 2 solid-solution quantum dots in combination with organic charge-transport materials. *Appl. Phys. Lett.* **116**, 093302 (2020)

[90] Liang, H. *et al.* High Color Purity Lead-Free Perovskite Light-Emitting Diodes via Sn Stabilization. *Adv. Sci.* **7**, 1903213 (2020)

[91] Zhang, Y. *et al.* Lead-free Double Perovskite Cs2AgIn0.9Bi0.1Cl6 Quantum Dots for White Light-Emitting Diodes. *Adv. Sci.* **9**, 2102895 (2022)

[92] Yao, L. *et al.* Efficient silicon quantum dots light emitting diodes with an inverted device structure. *J. Mater. Chem. C* **4**, 673–677 (2016)

[93] Wei Gu, Xiangkai Liu, Shuangyi Zhao, Xiaodong Pi & Deren Yang. Silicon-quantum-dot light-emitting diodes with varying emission layer thickness. in *2016 13th IEEE International Conference on Solid-State and Integrated Circuit Technology (ICSICT)* 157–159 (IEEE, 2016). doi:10.1109/ICSICT.2016.7998866

[94] Gu, W. *et al.* Silicon-Quantum-Dot Light-Emitting Diodes With Interlayer-Enhanced Hole Transport. *IEEE Photonics J.* **9**, 1–10 (2017)

[95] Zhao, S. *et al.* Al 2 O 3 -Interlayer-Enhanced Performance of All-Inorganic Silicon-Quantum-Dot Near-Infrared Light-Emitting Diodes. *IEEE Trans. Electron Devices* **65**, 577–583 (2018)

[96] Liu, X. *et al.* Light-Emitting Diodes Based on Colloidal Silicon Quantum Dots with Octyl and Phenylpropyl Ligands. *ACS Appl. Mater. Interfaces* **10**, 5959–5966 (2018)

[97] Mock, J., Groß, E., Kloberg, M. J., Rieger, B. & Becherer, M. Surface Engineering of Silicon Quantum Dots: Does the Ligand Length Impact the Optoelectronic Properties of Light-Emitting Diodes? *Adv. Photonics Res.* **2**, 2100083 (2021)

[98] Ghosh, B., Yamada, H., Chinnathambi, S., Özbilgin, İ. N. G. & Shirahata, N. Inverted Device Architecture for Enhanced Performance of Flexible Silicon Quantum Dot Light-Emitting Diode.

J. Phys. Chem. Lett. **9**, 5400–5407 (2018)

[99] Yamada, H. *et al.* Improved Brightness and Color Tunability of Solution-Processed Silicon Quantum Dot Light-Emitting Diodes. *J. Phys. Chem. C* **124**, 23333–23342 (2020)

[100] Watanabe, J. *et al.* Silicon Quantum Dots for Light-Emitting Diodes Extending to the NIR-II Window. *ACS Appl. Nano Mater.* **4**, 11651–11660 (2021)

[101] Cheng, K.-Y., Anthony, R., Kortshagen, U. R. & Holmes, R. J. Hybrid Silicon Nanocrystal−Organic Light-Emitting Devices for Infrared Electroluminescence. *Nano Lett.* **10**, 1154–1157 (2010)

[102] Tu, C.-C., Tang, L., Huang, J., Voutsas, A. & Lin, L. Y. Visible electroluminescence from hybrid colloidal silicon quantum dot-organic light-emitting diodes. *Appl. Phys. Lett.* **98**, 213102 (2011)

[103] Puzzo, D. P. *et al.* Visible Colloidal Nanocrystal Silicon Light-Emitting Diode. *Nano Lett.* **11**, 1585–1590 (2011)

[104] Mastronardi, M. L. *et al.* Silicon Nanocrystal OLEDs: Effect of Organic Capping Group on Performance. *Small* **8**, 3647–3654 (2012)

[105] Maier-Flaig, F. *et al.* Multicolor Silicon Light-Emitting Diodes (SiLEDs). *Nano Lett.* **13**, 475–480 (2013)

Chapter 2 Synthesis of Colloidal Silicon Quantum Dots and Characteristics of Photoluminescence Quantum Yields

2.1 Introduction

Silicon quantum dots (SiQDs) have received significant attention in the field of photoelectronics due to their potential for visible emission and quantum confinement effects, as demonstrated in Canham's 1991 study [1]. Early research on luminescent silicon utilized various methods, such as porous silicon [2], surface textured bulk silicon [3], silicon/silica superlattice [4–6], and various techniques for synthesizing SiQDs, including electrochemical etching and dispersion, silicon ion implantation with annealing [7], annealing of silicon oxide [8], and hydrofluoric acid (HF) etching of silicon/silica nanostructures.

Colloidal SiQDs have gained significant attention in the field of photoelectronics due to their ease of chemical processability, excellent physical and chemical stability, and tunable photoelectronic properties. The colloidal stability of QDs is achieved through surface modification and the use of various ligands. Surface-functionalized SiQDs have been investigated for dispersion in organic and aqueous solvents using synthetic strategies based on steric and charge stabilization to achieve colloidal stability [9–12]. Subsequently, many studies have reported on the synthesis and prototype applications of colloidally stable SiQDs exhibiting luminescence at room temperature. It has been demonstrated that ligand-stabilized SiQDs can be easily tuned to emit from the near-ultraviolet (NUV) to the near-infrared (NIR) region by varying the size and surface, making them suitable for solution-processable applications [13–17]. This chapter will focus on the synthesis of colloidal SiQDs and recent efforts in the synthesis approach and the unique emission characteristics that depend on various surface chemistries.

As depicted in Fig.2-1, the synthesis of colloidal SiQDs can be classified into two approaches: top-down and bottom-up. The top-down approach involves the formation of a nanostructure from a macroscopic structure, while the bottom-up approach involves the self-assembly of a nanostructure at the atomic level. Various methods for fabricating SiQDs have been reported, which can be further divided into physical and chemical methods, including both top-down and bottom-up approaches. Both physical and chemical methods are useful for fabricating silicon nanostructures, and appropriate surface chemistry provides solubility of SiQDs in colloidal suspensions.

Physical methods include ion implantation, laser ablation, magnetron sputtering, and thermal evaporation, while chemical methods include direct oxidation/reduction pathways involving silicon precursors, pyrolysis of molecular silicon precursors in supercritical fluids, laser pyrolysis, and plasma-assisted or thermal decomposition of sol-gel-derived silicon-rich oxide (SRO). The emission properties of SiQDs largely depend on the preparation process.

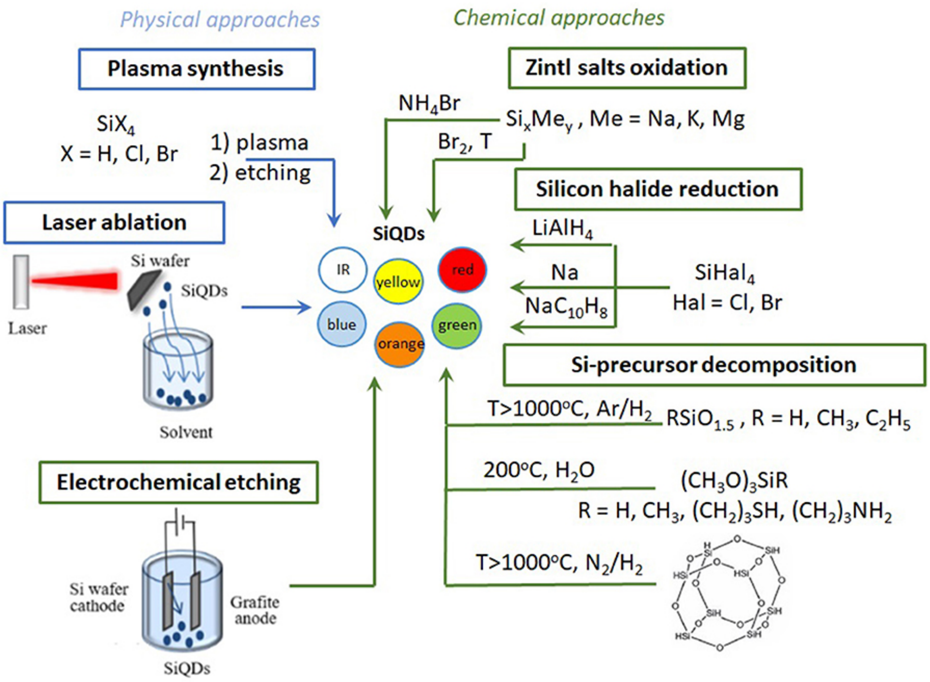

Fig.2-1 Different approaches to SiQDs synthesis. Blue lines correspond to the physical approaches for SiQD synthesis; green lines correspond to the chemical approaches. (Cited and reprinted from *Front. Chem.* 8, 1–8 (2020) [18])

2.1.1 Synthesis of Crystalline Colloidal Silicon Quantum Dots

Various methods for synthesizing SiQDs have been reported, however, the methods that have been confirmed to produce SiQDs with crystallinity via XRD are limited to non-thermal plasma synthesis [19] and thermolysis of silicon sub-oxide. The following elaborates on the specifics of these two synthesis methods.

2.1.1.1 Non-Thermal Plasma Synthesis

The synthesis of SiQDs requires a strategy utilizing silicon-containing molecules, such as silane, in which SiH_4 dissociates and nucleates to form SiQDs, followed by separate surface modifications to obtain colloidal QDs. Kortshagenra *et al.*, reported a single-step continuous non-thermal plasma process for synthesizing 2 nm and 8 nm diameter SiQDs on time scales of a few milliseconds using a specific setup schematized in Fig.2-2 [20–23]. In this study, red to NIR emitting SiQDs were prepared by utilizing a controlled flux of SiH_4/N_2 and localized irradiation with radio waves. In 2008, the group developed a novel dual plasma system by combining SiQDs synthesis and etching, with controllable size and surface functionalization, enabling a single and simple all-gas-phase process. They synthesized QDs in a SiH_4-based plasma, and CF_4-based plasma also allowed for etching and passivation by carbon and fluorine atoms. They observed emission from these SiQDs over the entire visible spectrum [24]. While many studies claim to have synthesized crystalline SiQDs, few have presented XRD results as evidence, instead relying on electron diffraction patterns obtained through transmission electron microscopy (TEM). A significant breakthrough in this area came in 2016, when Botas *et.al.*, reported the synthesis of crystalline SiQDs with XRD results (as depicted in Fig.2-3), which were synthesized via SiH_4/He precursor [19]. The red-emitting SiQDs were obtained, however, no information on PLQY was provided.

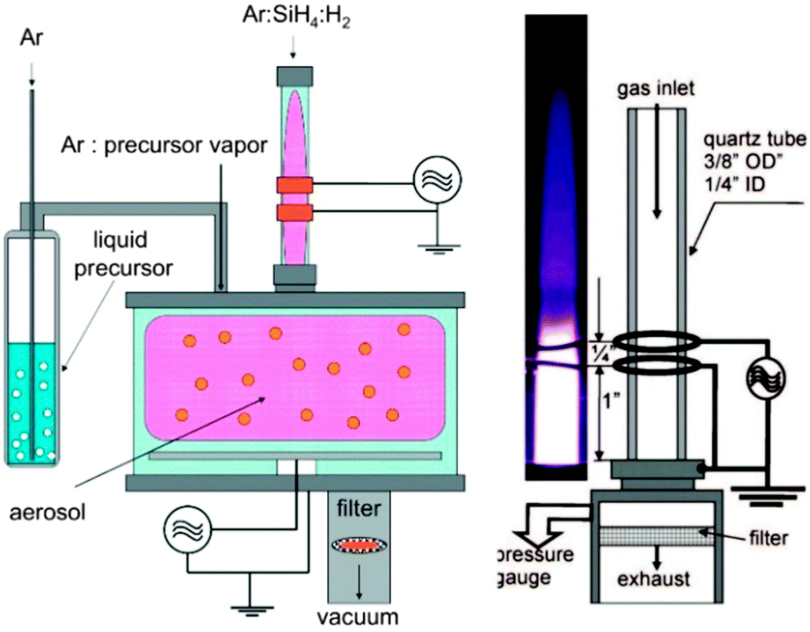

Fig.2-2 Setup for plasma-based synthesis of SiQDs. Right: plasma chamber and picture of the reacting plasma. Left: setup for on the flight functionalization of the SiQDs. (Cited and reprinted from *Chem. Soc. Rev.* 44, 4853–4921 (2015), Fig. 26)

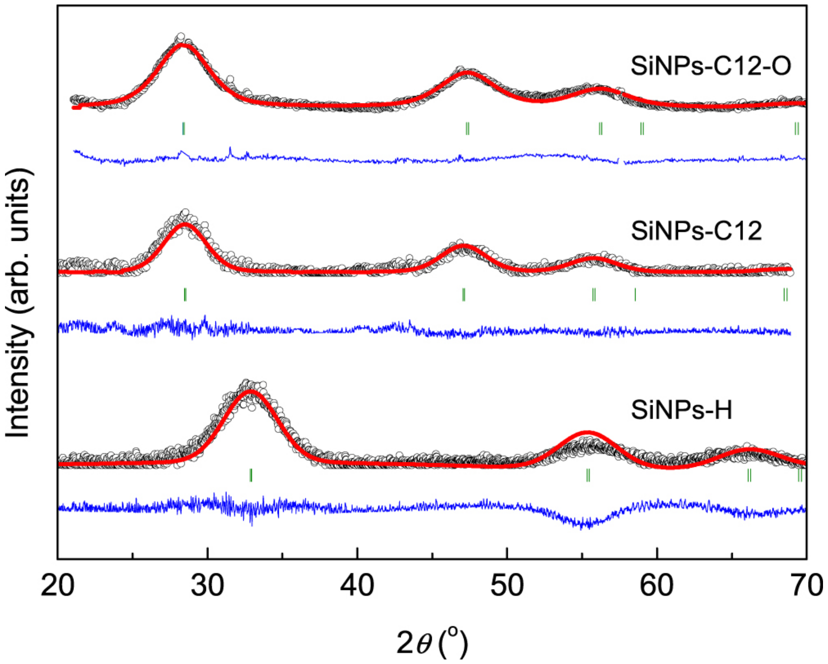

Fig.2-3 XRD patterns of SiQDs synthesized via non-thermal plasma synthesis. (Cited and reprinted from *Nanotechnology* 27, 325703 (2016), Fig. 3 [19])

2.1.1.2 Thermolysis of Silicon Sub-Oxide

The thermal decomposition of silicon suboxides is a method for synthesizing silicon-rich oxides composed of silicon nanodomains within SiO_2. To produce colloidally stable SiQDs, many researchers have investigated further etching and passivation techniques. Early studies reported that Si/SiO_2 core/shell nanostructures exhibit visible emission, with the starting precursor being a sol-gel-derived glass from triethoxysilane. In these studies, the product obtained through annealing in an argon (Ar) atmosphere at temperatures ranging from 1,000 °C to 1,200 °C was a Si/SiO_2 mixture, thus requiring fluoride etching for the liberation of QDs [26]. Liu *et al.*, used this technique to synthesize SiQDs. Thermal annealing of commercially available SiO_X ($X = 0.4$-1.8) was performed in an Ar flow at 900 °C to synthesize SiO_2 mixtures. The mixture was then etched utilizing hydrofluoric acid, resulting in the formation of fluorescent SiQDs. The product of the hydrofluoric acid etching was verified to be SiQDs with a diameter of 4.2 nm, as determined by high-resolution transmission electron microscopy (HR-TEM). Additionally, the polydispersity was determined to be approximately 12%, and the formation of a diamond cubic lattice was confirmed through XRD analysis (Fig.2-4) [27]. The Veinot group has conducted extensive research in this process, utilizing a variety of precursors. In 2006, Veinot *et al.*, utilized a commercially available hydrogenated silsesquioxane (HSQ) as a suitable molecular precursor, which was heated in an inert atmosphere containing 4% H_2 for reduction, followed by hydrofluoric acid etching to liberate the SiQDs. The emission from these SiQDs was found to be size-dependent and covered the visible spectrum. The size of the QDs can be controlled through modulation of the etching time and pyrolysis temperature [28]. A sol-gel polymer similar to that of the HSQ was synthesized from the hydrolysis of trichlorosilane ($HSiCl_3$). This polymer was employed as an efficient and cost-effective precursor in the formation of SiO_2-coated silicon nanocrystals. Since Pavesi's pioneering work in 2003, the thermolysis of sol-gel-derived polymers for the synthesis of Si/SiO_2 composites and etching processes for the synthesis of QDs have gained popularity due to their high chemical yields and cost-effectiveness [13,14,29–32]. Additionally, by roughly controlling the hydrofluoric acid etching time as illustrated in Fig.2-5, the PL spectral lines could be continuously varied from green to NIR wavelengths. Furthermore, by altering the pyrolysis temperature, it is possible to observe a different correlation between the light emission and the size change of the nanocrystal as well as the etching time. As demonstrated in Fig.2-6, variations in the pyrolysis temperature control the size of the QDs.

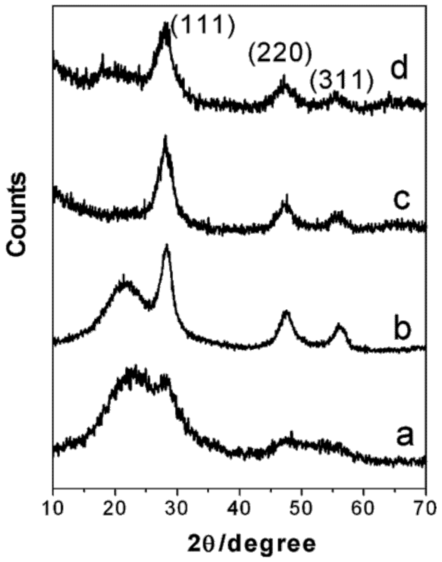

Fig.2-4 XRD patterns of (a) SiO powder, (b) 1,000 °C annealed powder, (c) HF-etched sample, and (d) octene-treated sample. (Cited and reprinted from *Chem. Mater.* 18, 637–642 (2006), Fig. 1)

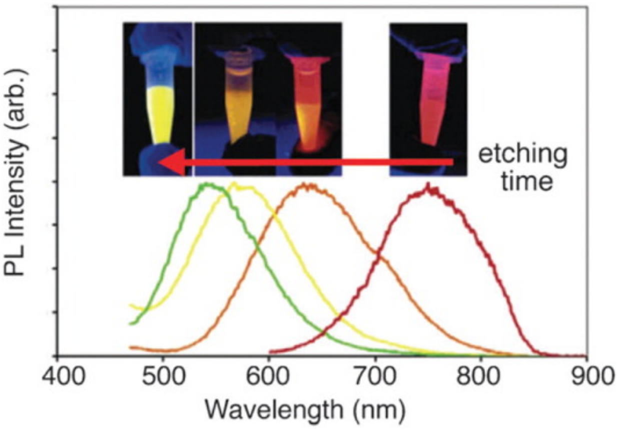

Fig.2-5 PL spectra of pentane solutions of red-, orange-, yellow- and green-emitting silicon QDs. Inset: photographs of PL observed from each pentane suspension upon exposure to UV light. (Cited and reprinted from *Science and Technology of Advanced Materials* 15, (2014), Fig. 4)

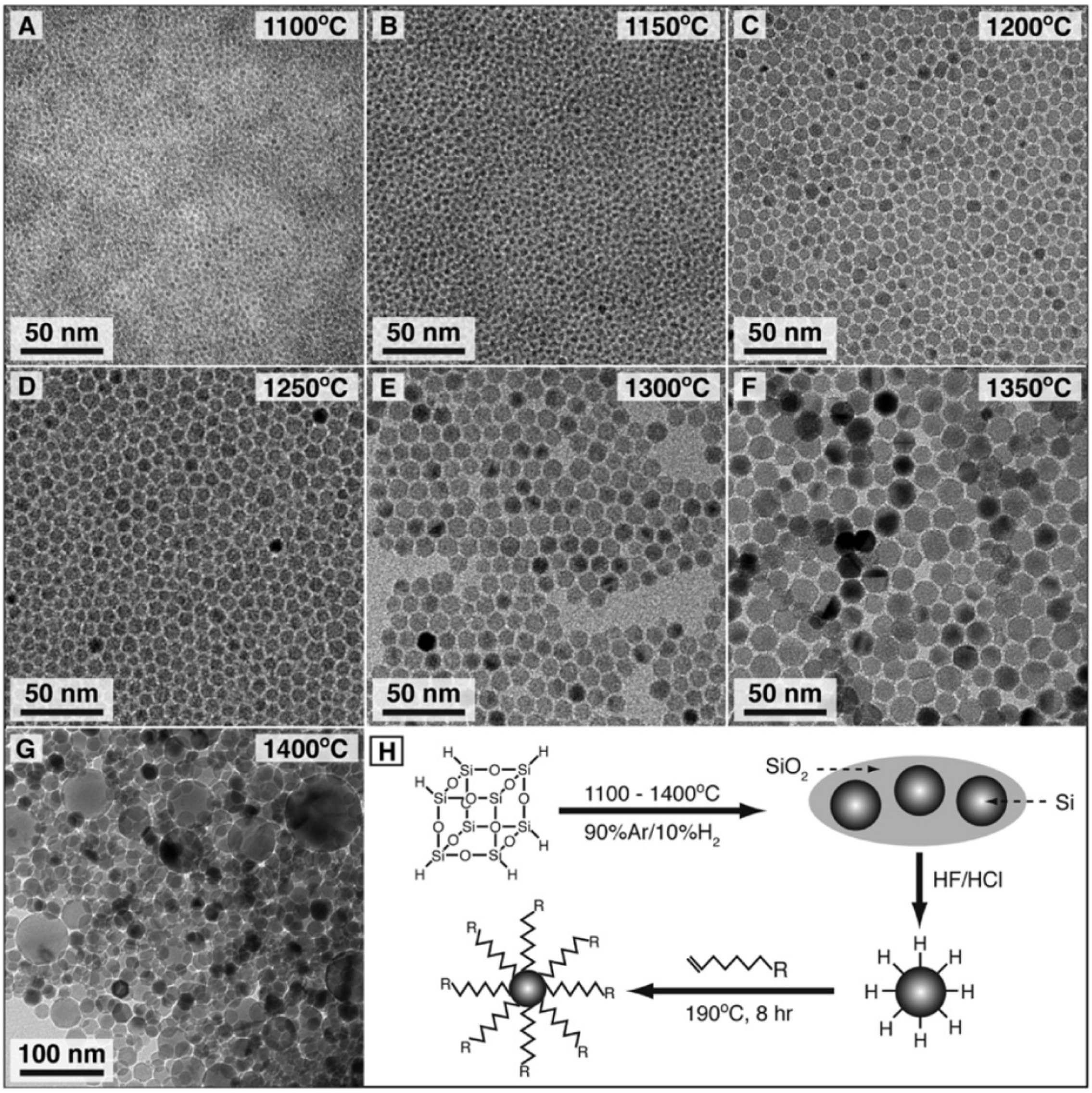

Fig.2-6 (A-G) TEM images of alkene-passivated Si nanocrystals generated by decomposition of hydrogen silsesquioxane (HSQ) at the indicated temperatures. (H) Synthetic pathway from HSQ to alkyl passivated silicon nanocrystals. (Cited and reprinted from *Chem. Mater.* 24, 393–401 (2012), Fig. 1)

2.2 Experimental Methods

Regents and Materials: Triethoxysilane (TES) was purchased from TCI chemicals. 1-Decene was purchased from Sigma-Aldrich and used as received. Electronic grade hydrofluoric acid (49% aqueous solution, Kanto Chemical), HPLC grade toluene, chloroform, ethanol and methanol were purchased from Wako chemical. Water was purified and deionized by Sartorius (arium 611 UV) water purification system.

Preparation of Colloidal SiQDs: Fig.2-7(a) illustrates a scheme for colloidal synthesis of SiQD terminated with decane monolayers (De-SiQD). Hydrogen-terminated SiQDs (H-SiQDs) were synthesized via a method reported elsewhere [33,34]. TES (16 mL) was placed in a flask, which was then kept in an ice bath and stirred in an Ar atmosphere. A hydrochloric acid solution with a pH of 3 (32 mL) was added dropwise to the TES solution while stirring vigorously under an Ar flow. The use of acidic water was crucial to prevent deprotonation of TES. The solution was filtered under reduced pressure. The obtained white powder (*i.e.*, hydrogen silsesquoxane) was washed with Milli-Q water until it reached pH 7 and dried overnight under vacuum. The dried powder was transferred to a quartz crucible and placed in a vacuum furnace. Then five gas-purging cycles were executed using a 5%-H_2/95%-Ar gas mixture. The powder underwent thermal disproportionation at a temperature of 1,190 °C for 2 hours in a 5%-H_2/95%-Ar atmosphere, resulting in a dark-brown powder composed of SiQDs dispersed within a SiO_2 matrix. The powder (300 mg) was then ground in an agate mortar using a pestle. Subsequently, the SiO_2 matrix of the fine powder was removed through stirring in an acidic solution conprising 8 mL of ethanol and 16 mL of 48% HF aqueous solution. This etching process resulted in the liberation of H-SiQDs, which were collected through centrifugation at 15,000 rpm at 10 °C. After undergoing thermal hydrosilylation with 1-decene at 180 °C, a sample consisting of decane-terminated SiQDs (De-SiQDs) was obtained. The sample displayed a broad PL spectrum, and the unreacted 1-decene was removed through evaporation. Finally, De-SiQDs were purified through high-performance liquid chromatography (HPLC, Japan Analytical Industry, Japan).

Characterization: Major crystalline planes of the SiQDs were evaluated with X-ray powder diffraction (MiniFlex600, Rigaku, Japan). Optical absorbance spectra were measured by UV–VIS spectrophotometer (JASCO V-650, Japan) with integrated sphere. PL measurement was carried out using a modular double grating Czerny–Turner monochromator and an iHR 320 emission monochromator (1,200 lines/mm of gratings) coupled to a photomultiplier tube (PMT) on a NanoLog Horiba Jovin Yvon spectrofluorometer with 450 W xenon arc lamp. The spectral resolution of the system was around 0.3 nm. To avoid scattered excitation lights, cut filters for 495-nm-light was placed in the front of monochrometer-PMT setup. The absolute PLQYs were measured at room temperature using the QY measurement system C9920-02 from Hamamatsu Photonics Co. Ltd with a 150 W xenon lamp coupled to a monochromator for wavelength discrimination, an integrating sphere as a sample chamber, and a multichannel analyzer for signal detection. The film form specimens of SiQD were used for the estimation of PLQYs.

2.3 Experimental Results

2.3.1 Synthesis and Physical Characterization of SiQDs

Fig.2-7(a) illustrates the chemical synthesis of hydrophobic, toluene-soluble SiQDs schematically. The hydrogen-terminated QDs were prepared through hydrofluoric acid etching of SiO_2-embedded SiQDs. Hydrosilylation of 1-alkenes typically yields alkane-terminated QDs. In this study, hydrogen silsesquioxane (HSQ) was prepared by hydrolyzing triethoxysilane (TES) at pH 3. Under alkaline conditions, the dehydrogenation of TES occurs in an aqueous solution. The deficiency of hydrogen results in a reduced yield of HSQ. In contrast, under highly acidic conditions ($pH \leq 2$), a rapid hydrolysis and condensation reaction is observed resulting in the formation of a white powder of HSQ. Occasionally, the presence of ethoxy groups in the powder product prepared under such highly acidic conditions is observed. It is believed that the carbon source remains as graphite after annealing during the thermal hydrosilylation reaction. To prevent such unexpected contamination, an acidic condition of pH 3 was discovered to be optimal, as it allows for the full removal of ethoxy groups from the product due to a slower hydrolysis and condensation rate. Next, the HSQ was thermally disproportionated into Si and SiO_2 at 1,190 ºC in H_2/Ar 5%/95% atmosphere for 2 hours. It is important to use a vacuum sintering furnace to ensure uniform annealing in an absolute H_2/Ar 5%/95% atmosphere. The SiO_2/Si composites were then subjected to hydrofluoric etching to liberate freestanding hydrogen-terminated QDs from the oxide. A 1-decene containing hydrogen-terminated QDs was refluxed for ~5 min in an Ar atmosphere to terminate the QD surface with decane monolayers (*i.e.*, De-SiQD). Hydrosilylation of 1-decene was completed when the solution turned transparent and brown in color. A reaction time of less than 5 min provided QDs with a high PLQY in a high yield, but increasing the reaction time reduced the synthetic yields. After vacuum evaporation of the unreacted 1-decene, the product was redispersed in chloroform and subjected to gel permeation chromatography (GPC) to extract only the strongly fluorescent QDs.

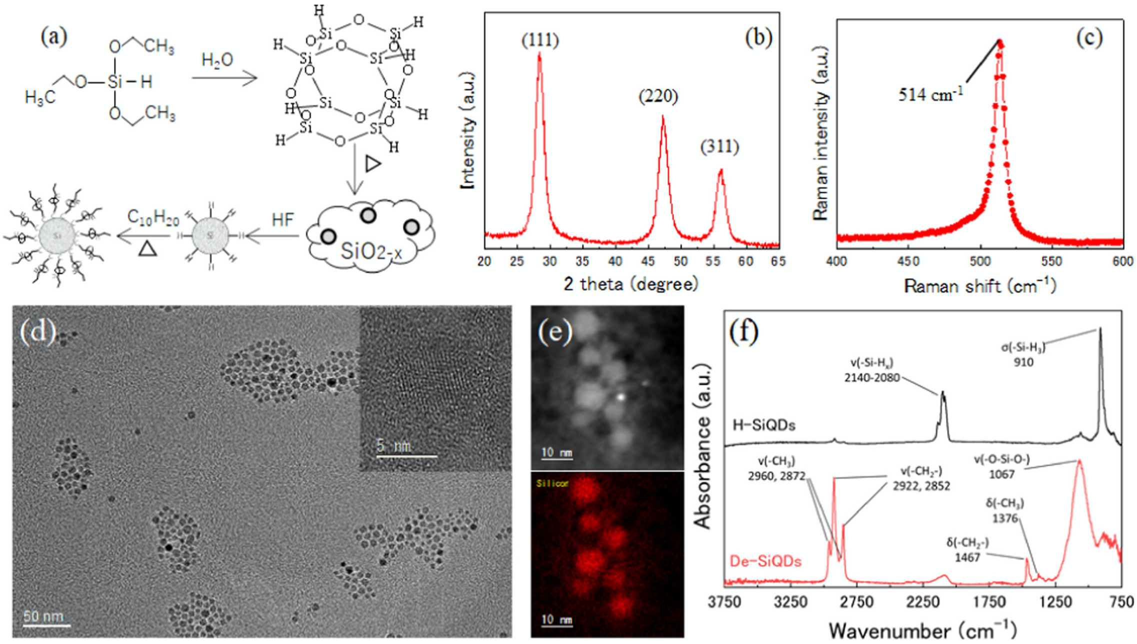

Fig.2-7 Physical properties of De-SiQDs: (a) scheme for the colloidal synthesis of De-SiQD, (b) X-ray diffraction (XRD) pattern of H-SiQD, (c) Raman spectrum of H-SiQD, (d) high-resolution transmission electron microscopy (HR-TEM) image with an inset of enlarged QDs, (e) transmission electron microscopy (TEM) and energy-dispersive X-ray spectroscopic (EDS) mapping images of De-SiQDs, and (f) attenuated total reflection Fourier transform infrared (ATR-FTIR) spectra of H-SiQD before and after hydrosilylation of 1-decene.

A typical XRD pattern of the product obtained from hydrofluoric acid etching exhibited peaks at $2\theta = 28$, 47, and 56° (as depicted in Fig.2-7(b)), which are indexed to the (111), (220), and (311) planes of the diamond cubic Si lattice structure, respectively. The estimated diameter of the product was 4.6 nm, as determined by the Williamson–Hall theory (as illustrated in Fig.2-8). Fig.2-7(c) presents a typical Raman spectrum of the product following the hydrosilylation of 1-decene. The Raman-active mode in bulk Si crystal occurs at the center of the Brillouin zone ($q = 0$), resulting in a Raman scattering peak at 520 cm^{-1}. In the spectrum, a peak at 514 cm^{-1} with a full width at half-maximum (FWHM) of 15 cm^{-1} shifts to lower wavenumbers and broadens the transverse optical (TO) phonon line due to the phonon confinement effect. The frequency downshift of the Raman peak for SiQDs can be explained by the correlation length model (as depicted in Fig.2-9) [35]. It is widely acknowledged that the size-dependence of Raman spectra can be described by a theoretical model that quantizes the phonon confinement [36]. Two representative models are expressed as follows:

$$\Delta\boldsymbol{\varpi}\,(\mathbf{D}) = -\boldsymbol{A}[\frac{\boldsymbol{a}}{\boldsymbol{D}}]^{\gamma} \qquad \mathbf{Eq.\,2-1}$$

where $\Delta\varpi\,(\mathrm{D})$ is the Raman shift as a function of the diameter (D), “*a*” is the lattice constant of diamond cubic Si (5.43 Å), and A and γ are the fitting parameters. For example, A = –47.41 cm^{-1} and γ = 1.44 for the bond-polarizability model [37], and A = –97.462 cm^{-1} and γ = 1.39 for the correlation length model [38]. As a result, the estimated diameter of 4.56 nm obtained from the relationship was consistent with the result of XRD characterization.

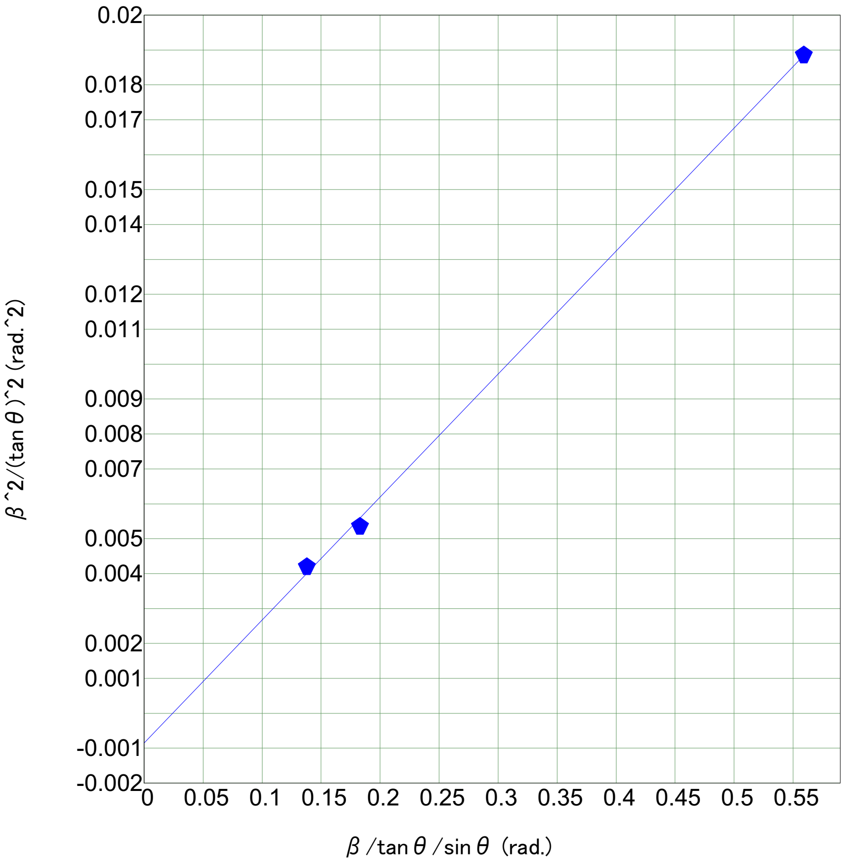

Fig.2-8 Williamson-Hall Plots for estimation of average QD size using diffraction parameters of (111), (220) and (311) planes.

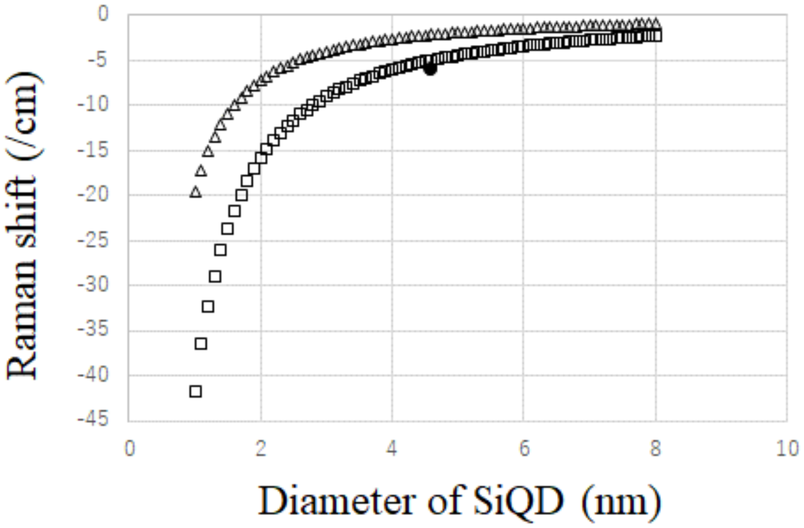

Fig.2-9 Calculated Raman shift with bond-polarizability model (open triangles) and the correlation length model (open squares), respectively. The closed circle is the Raman shift of experimental result in this study.

A representative HR-TEM image of the product is presented in Fig.2-7(d). The mean diameter of the contrasted dots was determined to be 5.25 nm with a standard deviation of approximately 1 nm (as depicted in Fig.2-10). Fig.2-7(e) illustrates the scanning transmission electron microscopy (STEM) image and the corresponding energy-dispersive X-ray (EDX) mapping analysis of Si, indicating that the contrasted dots correspond to SiQDs. The ATR-FTIR spectra of the product before and after the hydrosilylation of 1-decene are depicted in Fig.2-7(f). Prior to the hydrosilylation reaction, the spectra displayed peaks at 2,140-2,080 and approximately 910 cm^{-1}, which are associated with the SiH$_x$ stretching mode and SiH$_3$ degenerate deformation, respectively. These peaks indicated a hydrogen-terminated QD surface [39]. Following the hydrosilylation reaction, these peaks become small. Instead, strong peaks in the range 2,960–2,850 and 1,500–1,350 cm^{-1} were derived from the C–H bond of the stretching and bending/scissoring modes as the QD surface is terminated with decane monolayers (*i.e.*, De-SiQDs) [40]. The broad peak at 1,067 cm^{-1} was assigned to the stretching mode of the O–Si–O bond, which arises due to the possible oxidation during synthesis.

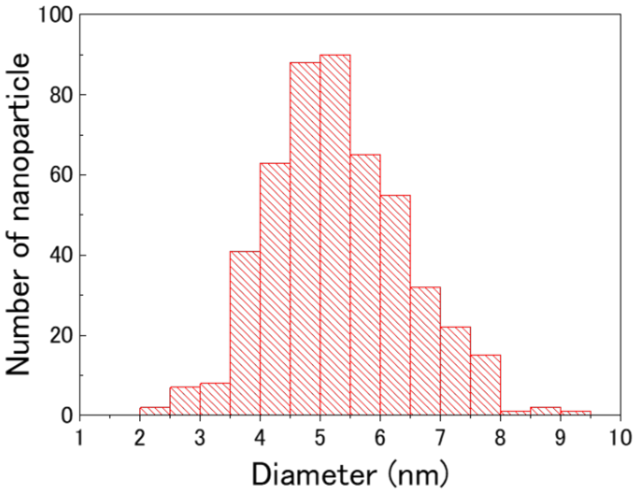

Fig.2-10 The histogram for size distribution was obtained by measuring the diameters of more than 470 De-SiQDs observed in HR-TEM images.

Fig.2-11(a) illustrates a typical pair of UV-VIS and PL spectra of the De-SiQD film coated on a quartz glass substrate. The absorption spectrum exhibited a long slope towards 1.1 eV. The monotonic increase with photon energy in the absorption spectrum reflects the indirect nature of the band gap. An absorption edge was observed around 400 nm, while the shoulder at approximately 350 nm was attributed to the direct Γ_{25}-Γ_{15} transition [41]. The PL spectrum was centered at 990 nm, featuring a Gaussian-shaped, single peak with a small FWHM of 163 nm (211 meV). There was a significant Stokes shift between the optical absorption and emission spectra. The PL decay characteristics were measured at room temperature (as illustrated in Fig.2-11(b)). The decay curve was fitted by a double exponential function ($\mathrm{Eq.}\,2-2$) where τ_1, and τ_2 are the first and second components of the PL lifetime, and B_1 and B_2 are the amplitudes of each component, respectively. The PL lifetime was on the order of milliseconds, which is a strong indication of the indirect transition-type nature of the bulk Si.

$$I(t) \approx B_1\, exp\left[-\frac{t}{\tau_1}\right] + B_2\, exp\left[-\frac{t}{\tau_2}\right] \qquad \mathrm{Eq.}\,2-2$$

$$(B_1 = 0.73,\ B_2 = 0.27,\quad \tau_1 = 0.813\ \mathrm{msec},\ \tau_2 = 1.57\ \mathrm{msec})$$

The PLQY was measured with an absolute value of 48.5%. Subsequently, the De-SiQDs was subjected to GPC for fractionation of QDs with high PLQY. The QD fraction with a retention time of 27–31 min exhibited the highest PLQY value of 53% (as depicted in Fig.2-11(c)). This fraction was used as the optically active layer in the device.

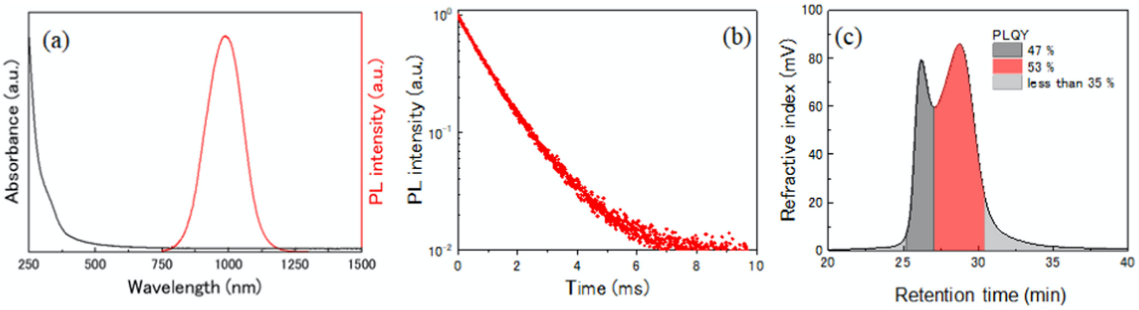

Fig.2-11 (a) Optical absorption and PL spectra of De-SiQD, (b) PL decay characteristics of De-SiQDs, and (c) gel permeation chromatography (GPC) chromatogram of De-SiQD demonstrating the separation of De-SiQDs by PLQY.

2.3.2 Manipulation of Photoluminescence Peak Wavelength in SiQDs

As previously stated in the introduction, the PL peak wavelength can be manipulated through the temperature applied during thermal disproportionation and the duration of hydrofluoric acid etching. A summary of the correlation between thermal disproportionation, etching time, PL peak wavelength, and PLQY of SiQDs synthesized in this study is presented in Table.2-1.

Table.2-1 A summary of relationship between thermal disproportionation, etching time, PL peak wavelength and PLQY.

Sample	Thermal disproportionation temperature (°C)	HF etching time (min)	PL peak wavelength (nm)	PLQY (%)
1	1190	60	1000	53
2	1190	90	950	43
3	1190	120	920	40
4	1100	75	744	37
5	1100	75	820	48
6	1100	75	800	44
7	1100	75	790	33
8	1100	90	793	40
9	1100	100	816	41
10	1100	105	750	32
11	1050	85	690	24
12	1050	85	696	24.5
13	1050	90	690	23
14	1050	90	682	16

15	1050	90	695	23
16	1050	110	720	33
17	1050	110	708	34
18	1050	110	712	30
19	1050	110	708	28
20	1050	110	696	26
21	1050	110	685	18
22	1050	110	704	27
23	1050	110	691	24
24	1050	110	680	17
25	1050	120	740	35
26	1035	70	646	13
27	1035	70	640	13
28	1035	70	637	11
29	1035	70	627	7
30	1025	90	610	7
31	1025	100	630	9
32	1015	85	670	21
33	1015	100	708	22

Fig.2-12 illustrates the correlation between the PL peak wavelength and thermal disproportionation temperature. From the figure, it can be observed that as the thermal disproportionation temperature increases, there is an increase in the grain growth of SiQDs and a corresponding increase in the PL peak wavelength. Furthermore, at the same temperature of thermal disproportionation, an increment in the etching duration results in a shift towards shorter wavelengths in the PL peak wavelength, owing to the diminution in the size of the SiQDs.

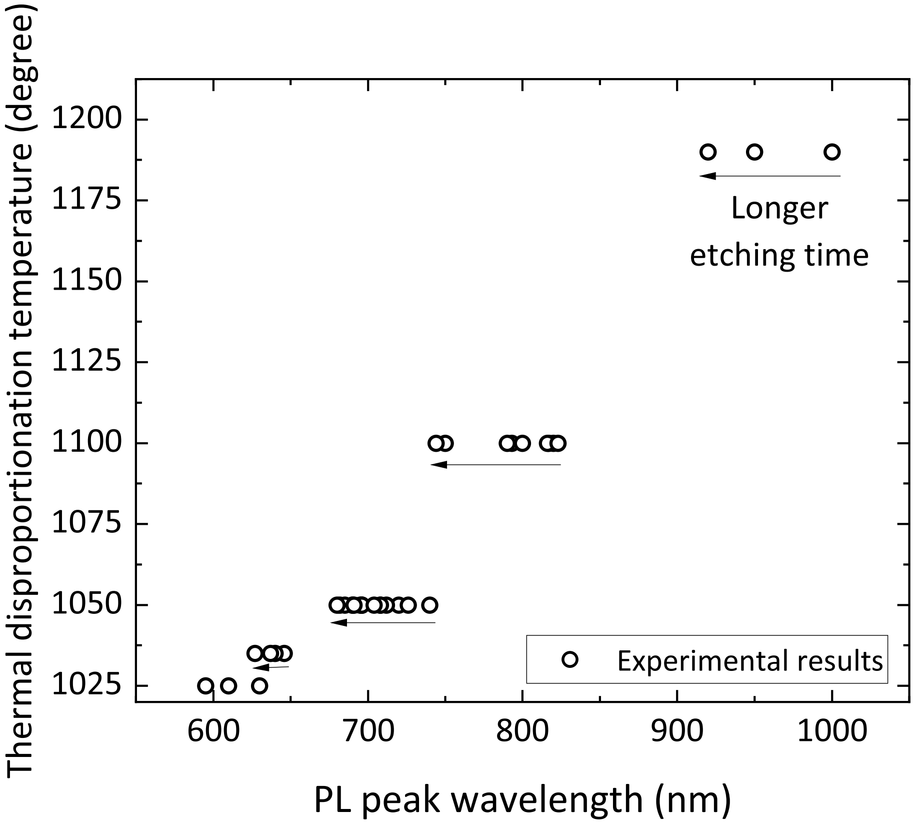

Fig.2-12 The correlation between the peak wavelength of PL and the thermal disproportionation temperature. The direction indicated by the black arrow corresponds to an increased etching duration.

Fig.2-13 illustrates the correlation between the PL peak wavelength and PLQY in this study. From this figure, it can be observed that as the PL peak wavelength increases (*i.e.*, the particle size becomes larger), the PLQY also increases. Conversely, as the PL peak wavelength decreases (*i.e.*, the particle size becomes smaller), the PLQY decreases. This correlation can be attributed to the surface-to-volume ratio. As the particle size increases, the ratio of the surface to the volume decreases, thus the light can be emitted without being affected by surface defects. Conversely, as the particle size decreases, the surface-to-volume ratio increases, resulting in an increased effect of surface defects and inefficient radiative recombination.

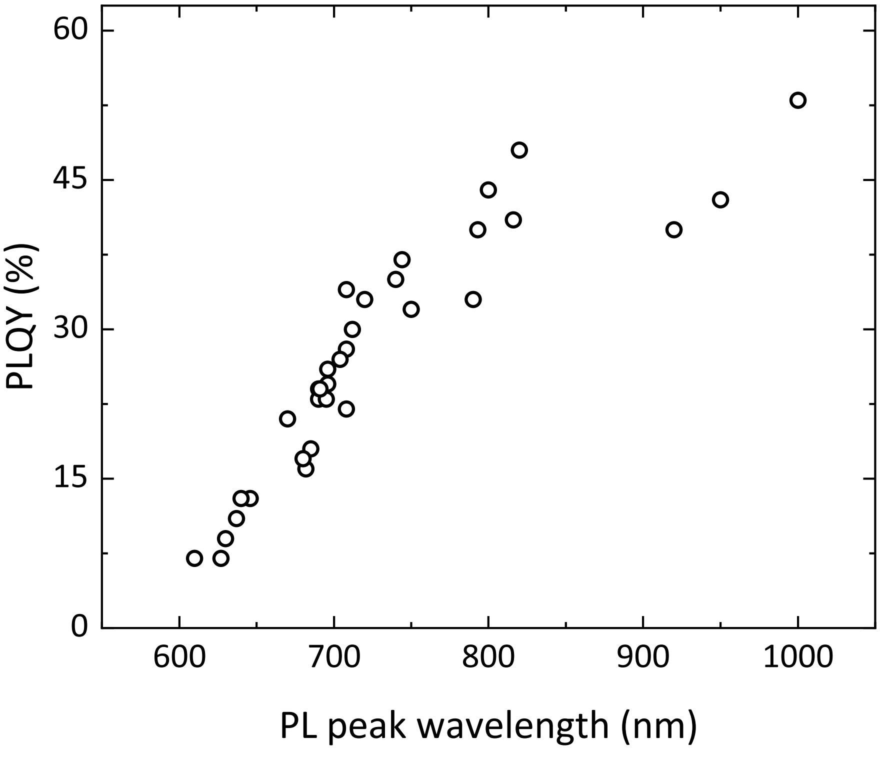

Fig.2-13 The correlation between the peak wavelength of PL and the PLQY in this study.

2.3.3 Investigation of the Impact of Hydrolysis Techniques on Photoluminescence Quantum Yield in Triethoxysilane-based SiQDs

In this section, the effect of different injection methods of acidic solutions on PLQY during the hydrolysis of TES was investigated. Herein, two distinct injection methods, manual injection and automatic injection, were adopted. In the manual injection method, the rate of injection is notoriously challenging to regulate as the injection is conducted manually (Fig.2-14). Conversely, the automatic injection method enables precise control of the injection rate as the injection is executed via a syringe pump (Fig.2-15). For the automatic injection method, the injection rate was set at 1.92 mL/min. As shown in Fig.2-16, the photograph illustrates the HSQs synthesized through manual (left) and automatic (right) injection methods following drying. Despite a disparity in yield, there was no discernible alteration in the appearance of the white powder resulting from the differing injection methods (Fig.2-16).

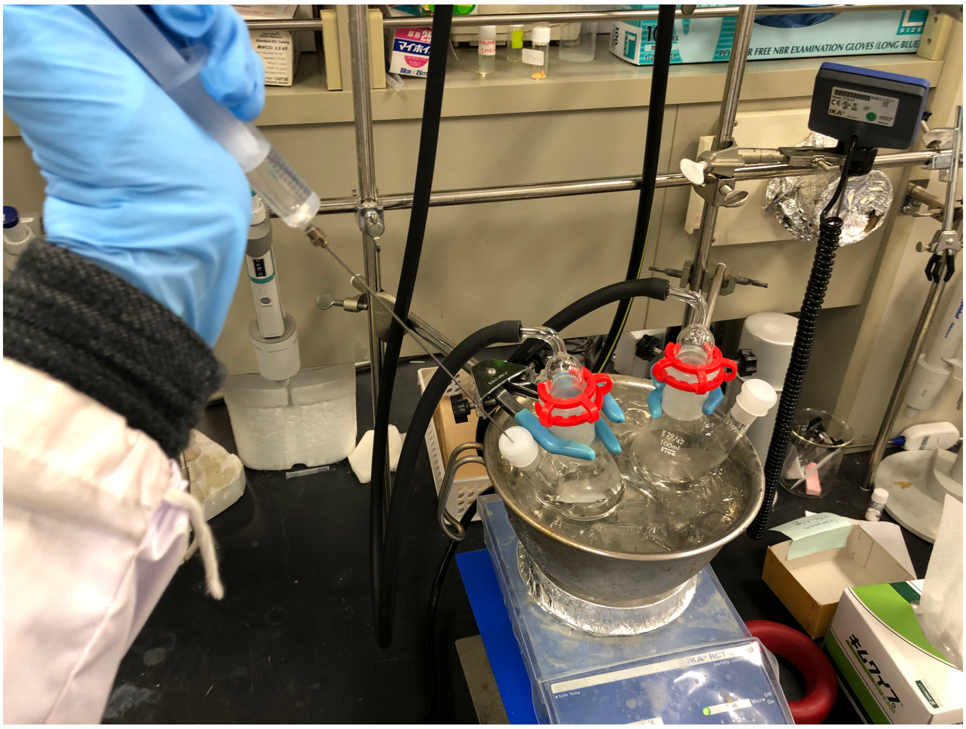

Fig.2-14 A photograph taken during the process of manual injection administered by human hands.

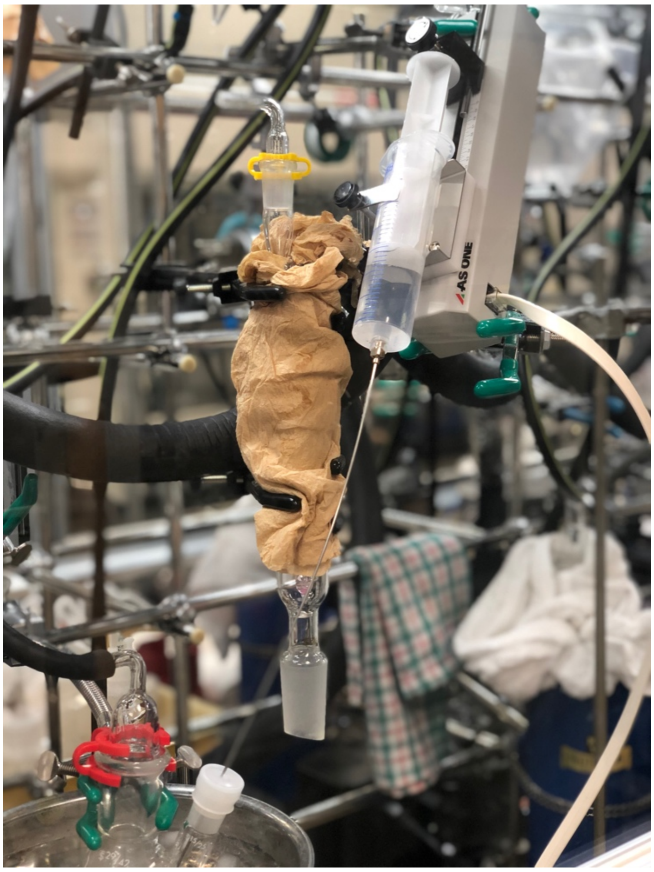

Fig.2-15 A photograph taken during the process of automatic injection utilizing a syringe pump.

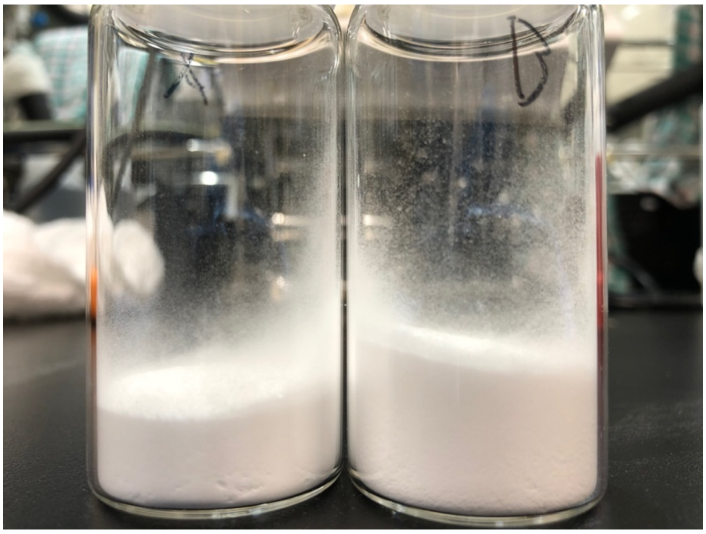

Fig.2-16 A photograph of HSQ after drying: (left) HSQ synthesized via manual injection method and (right) HSQ synthesized via automatic injection method.

Subsequently, X-ray photoelectron spectroscopy (XPS) measurements were conducted. Fig.2-17 illustrates the XPS spectrum of HSQ synthesized via the manual injection method, and the fitting results are summarized in Table.2-2. Conversely, Fig.2-18 presents the XPS spectrum of HSQ synthesized through the automatic injection method, and the fitting results are outlined in Table.2-3. The automatic injection method resulted in an elevation of the ratio of Si 3^+ and a marked decrease in the ratio of Si 2^+ in comparison to the manual injection method. This indicates that $HSiO_{1.5}$ can be efficiently synthesized during hydrolysis. However, the ratio of Si 0^+ also increased with the automatic injection method, which necessitates further investigation.

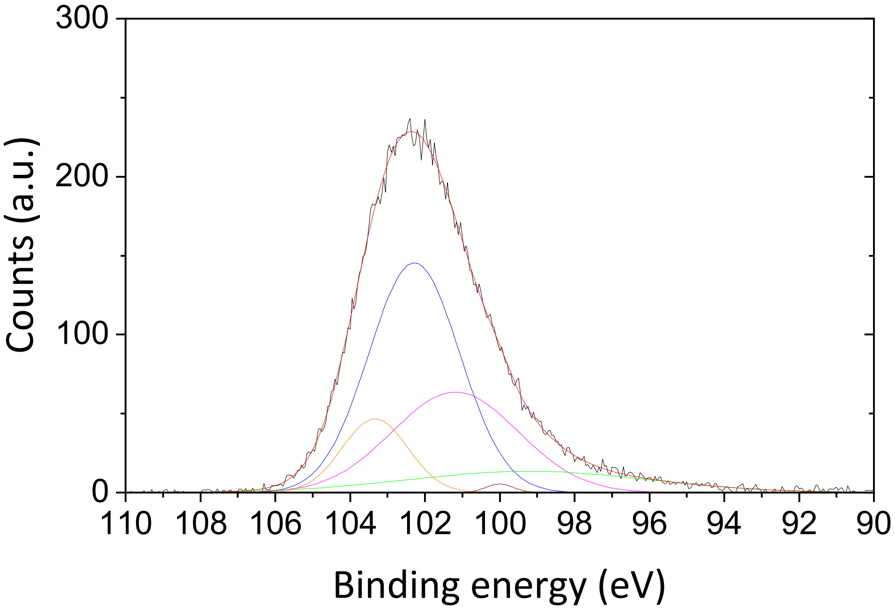

Fig.2-17 The XPS spectrum of HSQ synthesized via manual injection method.

Table.2-2 A fitting results of Fig.2-17.

Peak index	Peak energy (eV)	Peak data area ratio (%)
Si 4^+ (orange)	103.3	11.06
Si 3^+ (blue)	102.2	47.8
Si 2^+ (pink)	101.2	28.97
Si 1^+ (brown)	100	0.53
Si 0^+ (green)	99.2	11.62

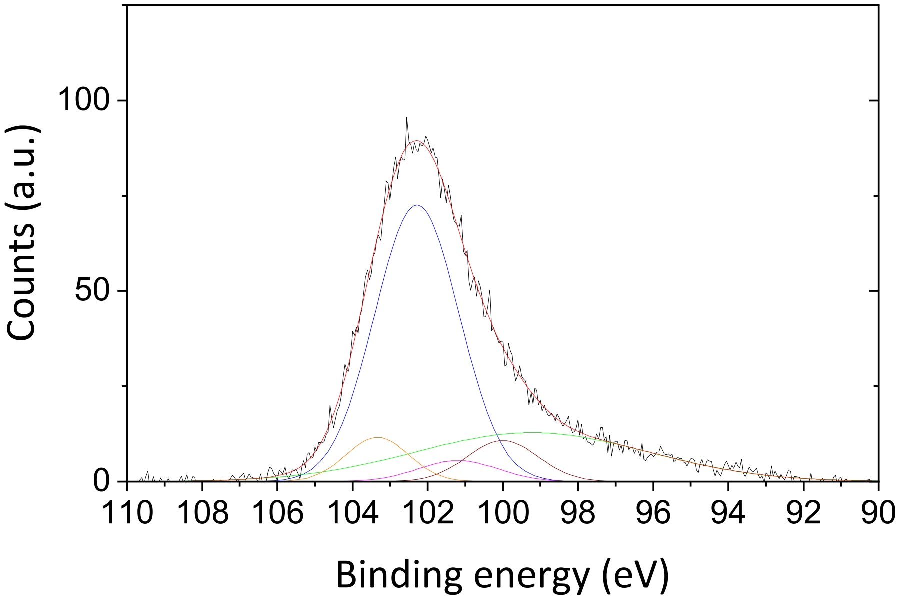

Fig.2-18 The XPS spectrum of HSQ synthesized via automatic injection method.

Table.2-3 A fitting results of Fig.2-18.

Peak index	Peak energy (eV)	Peak data area ratio (%)
Si 4^+ (orange)	103.3	6.58
Si 3^+ (blue)	102.2	55.44
Si 2^+ (pink)	101.2	3.99
Si 1^+ (brown)	100	6.92
Si 0^+ (green)	99.2	27.04

Next, the PLQY of decane-terminated SiQDs synthesized utilizing HSQ synthesized via the automatic injection method is summarized in Table.2-4. Interestingly, a PLQY of up to 50.2% was achieved at a PL peak wavelength of 704 nm. Such a high PLQY is innovative in red region emission SiQDs, as it has traditionally been limited to NIR region emission SiQDs.

Table.2-4 A comparison of the PLQY properties of SiQDs synthesized with HSQ prepared via different injection methods.

Method	Thermal disproportionation temperature (°C)	HF etching time (min)	PL peak wavelength (nm)	PLQY (%)
Automatic	1075	120	704	50.2
Automatic	1075	120	727	45.8
Automatic	1075	120	687	38
Automatic	1075	125	701	31
Automatic	1075	125	696	31.7
Automatic	1075	125	684	28
Automatic	1075	125	664	20
Automatic	1075	125	712	33
Automatic	1075	125	693	34
Automatic	1075	125	670	27
Automatic	1075	125	644	18

Fig.2-19 shows a comparison of PLQY of decane-terminated SiQDs synthesized with HSQ prepared by manual and automatic injection methods. Evidently, the automatic injection method results in a superior PLQY value when compared to the manual injection method. Consequently, the utilization of the automatic injection method for HSQ synthesis holds promise for innovating SiQDs synthesis with elevated PLQY.

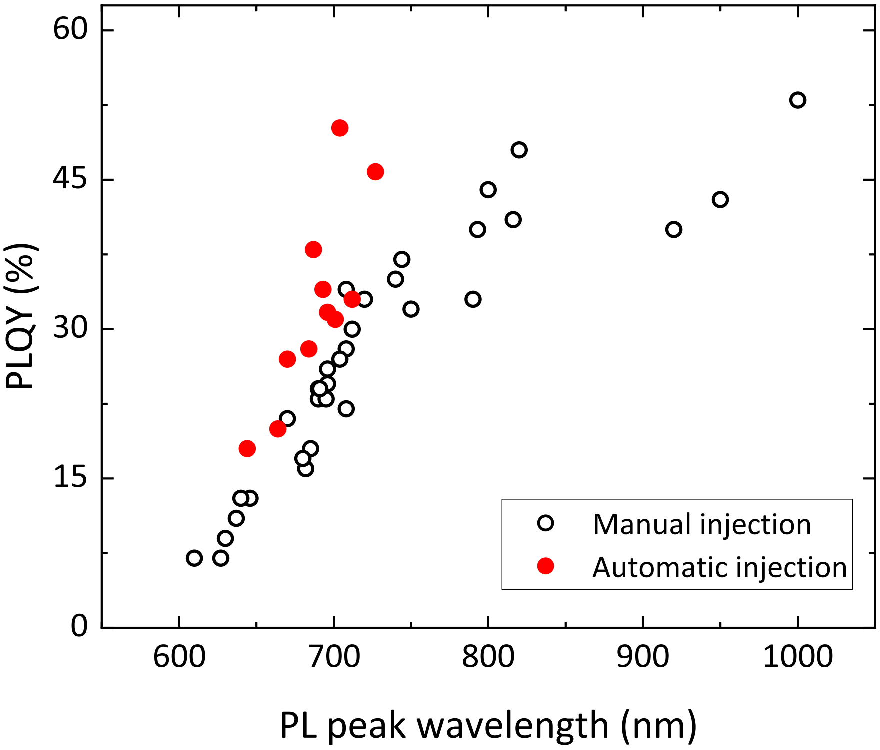

Fig.2-19 A comparison of the PLQY obtained through different injection methods.

2.4 Conclusion

In this chapter, SiQDs were synthesized via thermal disproportionation reaction. The synthesized SiQDs were found to have a diamond structure from XRD pattern diagrams. Furthermore, the HR-TEM measurement of SiQDs found out that the diameter of SiQDs corresponded well with the Scherrer equation. In addition, the PL peak wavelength can be controlled by thermal disproportionation temperature and hydrofluoric acid etching time. Finally, it was found that SiQDs synthesized with HSQ, which was hydrolyzed and synthesized via the automatic injection method, generally had high PLQY. The XPS measurements of HSQ showed that the peak area ratio of Si 2^+ drastically decreased in HSQ synthesized via the automatic injection method compared with HSQ synthesized via the manual injection method. Therefore, the results suggested that $HSiO_{1.5}$ could be synthesized efficiently, which led to PLQY enhancement.

2.5 References

[1] Cullis, A. G. & Canham, L. T. Visible light emission due to quantum size effects in highly porous crystalline silicon. *Nature* **353**, 335–338 (1991)

[2] Wang, J. *et al.* Efficient infrared-upconversion luminescence in porous silicon: A quantum-confinement-induced effect. *Phys. Rev. Lett.* **69**, 3252–3255 (1992)

[3] Trupke, T., Zhao, J., Wang, A., Corkish, R. & Green, M. A. Very efficient light emission from bulk crystalline silicon. *Appl. Phys. Lett.* **82**, 2996–2998 (2003)

[4] Lockwood, D. J. Quantum confined luminescence in Si/SiO2 superlattices. *Phase Transitions* **68**, 151–168 (1999)

[5] Vinciguerra, V., Franzò, G., Priolo, F., Iacona, F. & Spinella, C. Quantum confinement and recombination dynamics in silicon nanocrystals embedded in Si/SiO2 superlattices. *J. Appl. Phys.* **87**, 8165–8173 (2000)

[6] Zacharias, M. *et al.* Size-controlled highly luminescent silicon nanocrystals: A SiO/SiO 2 superlattice approach. *Appl. Phys. Lett.* **80**, 661–663 (2002)

[7] GARRIDO, B. *et al.* Optical and electrical properties of Si-nanocrystals ion beam synthesized in SiO2. *Nucl. Instruments Methods Phys. Res. Sect. B Beam Interact. with Mater. Atoms* **216**, 213–221 (2004)

[8] Nesbit, L. A. Annealing characteristics of Si-rich SiO2 films. *Appl. Phys. Lett.* **46**, 38–40 (1985)

[9] Shirahata, N. Colloidal Si nanocrystals: a controlled organic–inorganic interface and its implications of color-tuning and chemical design toward sophisticated architectures. *Phys. Chem. Chem. Phys.* **13**, 7284 (2011)

[10] Veinot, J. G. C. Synthesis, surface functionalization, and properties of freestanding silicon nanocrystals. *Chem. Commun.* 4160–4168 (2006) doi:10.1039/b607476f

[11] Fan, J. & Chu, P. K. Group IV Nanoparticles: Synthesis, Properties, and Biological Applications. *Small* **6**, 2080–2098 (2010)

[12] Mastronardi, M. L., Henderson, E. J., Puzzo, D. P. & Ozin, G. A. Small Silicon, Big Opportunities: The Development and Future of Colloidally-Stable Monodisperse Silicon Nanocrystals. *Adv. Mater.* **24**, 5890–5898 (2012)

[13] Henderson, E. J. *et al.* Colloidally Stable Silicon Nanocrystals with Near-Infrared Photoluminescence for Biological Fluorescence Imaging. *Small* **7**, 2507–2516 (2011)

[14] Hessel, C. M. *et al.* Synthesis of Ligand-Stabilized Silicon Nanocrystals with Size-Dependent Photoluminescence Spanning Visible to Near-Infrared Wavelengths. *Chem. Mater.* **24**, 393–401 (2012)

[15] English, D. S., Pell, L. E., Yu, Z., Barbara, P. F. & Korgel, B. A. Size Tunable Visible Luminescence from Individual Organic Monolayer Stabilized Silicon Nanocrystal Quantum Dots. *Nano Lett.* **2**, 681–685 (2002)

[16] Gupta, A., Swihart, M. T. & Wiggers, H. Luminescent Colloidal Dispersion of Silicon Quantum Dots from Microwave Plasma Synthesis: Exploring the Photoluminescence Behavior Across the Visible Spectrum. *Adv. Funct. Mater.* **19**, 696–703 (2009)

[17] Shirahata, N., Hasegawa, T., Sakka, Y. & Tsuruoka, T. Size-Tunable UV-Luminescent Silicon Nanocrystals. *Small* **6**, 915–921 (2010)

[18] Morozova, S., Alikina, M., Vinogradov, A. & Pagliaro, M. Silicon Quantum Dots: Synthesis, Encapsulation, and Application in Light-Emitting Diodes. *Front. Chem.* **8**, 1–8 (2020)

[19] Botas, A. M. P. *et al.* Influence of the surface termination on the light emission of crystalline silicon nanoparticles. *Nanotechnology* **27**, 325703 (2016)

[20] Dong, Y., Bapat, A., Hilchie, S., Kortshagen, U. & Campbell, S. A. Generation of nano-sized free standing single crystal silicon particles. *J. Vac. Sci. Technol. B Microelectron. Nanom. Struct.* **22**, 1923–1930 (2004)

[21] Bapat, A., Perrey, C. R., Campbell, S. A., Carter, C. B. & Kortshagen, U. Synthesis of highly oriented, single-crystal silicon nanoparticles in a low-pressure, inductively coupled plasma. *J. Appl. Phys.* **94**, 1969–1974 (2003)

[22] Mangolini, L., Thimsen, E. & Kortshagen, U. High-yield plasma synthesis of luminescent silicon nanocrystals. *Nano Lett.* **5**, 655–659 (2005)

[23] Jurbergs, D., Rogojina, E., Mangolini, L. & Kortshagen, U. Silicon nanocrystals with ensemble quantum yields exceeding 60%. *Appl. Phys. Lett.* **88**, 233116 (2006)

[24] Pi, X. D. *et al.* Air-stable full-visible-spectrum emission from silicon nanocrystals synthesized by an all-gas-phase plasma approach. *Nanotechnology* **19**, 245603 (2008)

[25] Mangolini, L. & Kortshagen, U. Plasma-Assisted Synthesis of Silicon Nanocrystal Inks. *Adv. Mater.* **19**, 2513–2519 (2007)

[26] Sorarù, G. D. *et al.* Si nanocrystals obtained through polymer pyrolysis. *Appl. Phys. Lett.* **83**, 749–751 (2003)

[27] Liu, S. M., Yang, Y., Sato, S. & Kimura, K. Enhanced photoluminescence from Si nano-organosols by functionalization with alkenes and their size evolution. *Chem. Mater.* **18**, 637–642 (2006)

[28] Hessel, C. M., Henderson, E. J. & Veinot, J. G. C. Hydrogen silsesquioxane: A molecular precursor for nanocrystalline Si-SiO2 composites and freestanding hydride-surface-terminated silicon nanoparticles. *Chem. Mater.* **18**, 6139–6146 (2006)

[29] Kelly, J. A., Henderson, E. J. & Veinot, J. G. C. Sol-gel precursors for group 14 nanocrystals. *Chemical Communications* vol. 46 8704–8718 (2010)

[30] Henderson, E. J., Kelly, J. A. & Veinot, J. G. C. Influence of HSiO1.5 sol-gel polymer structure and composition on the size and luminescent properties of silicon nanocrystals. *Chem. Mater.* **21**, 5426–5434 (2009)

[31] Kelly, J. A., Shukaliak, A. M., Fleischauer, M. D. & Veinot, J. G. C. Size-dependent reactivity in hydrosilylation of silicon nanocrystals. *J. Am. Chem. Soc.* **133**, 9564–9571 (2011)

[32] Rodríguez Núñez, J. R., Kelly, J. A., Henderson, E. J. & Veinot, J. G. C. Wavelength-controlled etching of silicon nanocrystals. *Chem. Mater.* **24**, 346–352 (2012)

[33] Shirahata, N. *et al.* Emerging Atomic Energy Levels in Zero-Dimensional Silicon Quantum Dots. *Nano Lett.* **20**, 1491–1498 (2020)

[34] Ghosh, B. *et al.* Hybrid White Light Emitting Diode Based on Silicon Nanocrystals. *Adv. Funct. Mater.* **24**, 7151–7160 (2014)

[35] Ghosh, B., Hamaoka, T., Nemoto, Y., Takeguchi, M. & Shirahata, N. Impact of Anchoring Monolayers on the Enhancement of Radiative Recombination in Light-Emitting Diodes Based on Silicon Nanocrystals. *J. Phys. Chem. C* **122**, 6422–6430 (2018)

[36] Ke, W., Feng, X. & Huang, Y. The effect of Si-nanocrystal size distribution on Raman spectrum. *J. Appl. Phys.* **109**, 083526 (2011)

[37] Fauchet, P. M. & Campbell, I. H. Raman spectroscopy of low-dimensional semiconductors. *Crit. Rev. Solid State Mater. Sci.* **14**, s79–s101 (1988)

[38] Zi, J. *et al.* Raman shifts in Si nanocrystals. *Appl. Phys. Lett.* **69**, 200–202 (1996)

[39] Holm, J. & Roberts, J. T. Surface Chemistry of Aerosolized Silicon Nanoparticles: Evolution and Desorption of Hydrogen from 6-nm Diameter Particles. *J. Am. Chem. Soc.* **129**, 2496–2503 (2007)

[40] Shirahata, N., Hirakawa, D. & Sakka, Y. Interfacial-related color tuning of colloidal Si nanocrystals. *Green Chem.* **12**, 2139 (2010)

[41] Wilcoxon, J. P., Samara, G. A. & Provencio, P. N. Optical and electronic properties of Si nanoclusters synthesized in inverse micelles. *Phys. Rev. B - Condens. Matter Mater. Phys.* **60**, 2704–2714 (1999)

Chapter 3 Inverted Device Architecture for Silicon Quantum Dots Light-Emitting Diodes

3.1 Introduction

Flexible display technologies have been gaining increased market attention due to their potential applications in portable, foldable, and wearable photoelectronics [1–3]. Organic light-emitting diodes (OLEDs) feature a multilayer architecture, with the luminescent properties emanating from the self-luminescent organic layers within the multilayer structure. Reducing the overall thickness of the device results in mechanical flexibility, such as bending, stretching, and folding. However, device instabilities that arise from the insulating nature of organics, when exposed to air, impede operations at high applied voltages [4]. As a result, the flexibility of current commercialized OLEDs is restricted by the need for an encapsulation layer to protect them from air.

Colloidal quantum dots (QDs), which are three-dimensionally nanostructured semiconductor crystals, offer advantageous photoluminescence (PL) properties such as color purity, narrower spectra for emission (full-width at half-maximum, fwhm < 30 nm), and spectral tunability of efficient emissions over a broad wavelength range. Additionally, QDs possess superior thermal and air stability when compared to common organics [4,5]. As a result, LEDs that incorporate an optically active layer of QDs (QLEDs) can achieve exceptional device performance characteristics, such as an electroluminescence (EL) spectrum as narrow as 30 nm, a high luminance (~200,000 cd/m^2), a low turn-on voltage of 2 V, stable emission under long-term usage and high-current-density conditions, and solution-based processability [6–9].

In most cases, QLEDs adopt a conventional device structure in which indium tin oxide (ITO) and aluminum (Al) function as the anode and cathode, respectively. These QLEDs possess a multilayer architecture that comprises an electron injection layer (EIL), an electron transport layer (ETL), an optically active layer, a hole transport layer (HTL), and a hole injection layer (HIL). In contrast to the conventional structure, the inverted device structure of QLEDs (iQLEDs) employs ITO as the cathode. Recently, the inverted structure has garnered significant attention due to (i) its high compatibility with n-channel field-effect transistors for pixel driver backplanes in active-matrix displays [10,11], (ii) the availability of a transparent bottom cathode and a high work function (*i.e.,* air stable) top anode, (iii) a broad range of inorganic crystals that can function as the ETL (*e.g.*, ZrO_2, TiO_2, and ZnO) [12,13] or HTL (*e.g.*, V_2O_5, WO_3, and MoO_3) [14,15], which shield organic interlayers from air, and (iv) the availability for EIL/ETL use of ZnO, which provides a deep energy level of the highest occupied molecular orbital (HOMO) and serves as an efficient hole blocker. Furthermore, iQLEDs offer advantages from a processing perspective, leading to improved device performance. For instance, (v) the combination of ZnO/QD creates a robust platform for consecutive deposition of the HTL/HIL and anode, resulting in efficient hole injection and high hole mobility from a vacuum, and avoiding damage or solvent penetration to the underlying layer.

Baigent *et al.*, were the pioneers in exploiting the inverted structure for the fabrication of OLEDs, referring to it as the "upside-down" structure [16]. While various material combinations have been proposed to improve the performance of inverted OLEDs [17–19], the conventional architecture continues to dominate the device structure of QLEDs. However, in recent years, there has been a significant increase in the use of inverted device structures in the field [11,20–26]. Currently, the external quantum efficiencies (EQEs) of red, green, and blue (RGB) QLEDs with conventional structures are 20.5%, 21%, and 19.8%, respectively, while those of inverted QLEDs (iQLEDs) are 18.0%, 15.6%, and 4.0% [27–33]. The high EQEs are achieved through the use of optically active Cd-based QD layers, such as CdSe and CdS. However, the usage of these toxic elements, including Cd, is restricted by the RoHS regulations, which calls for the development of heavy-metal-free QLEDs in the future [21,34].

Silicon (Si), which is abundant and non-toxic, has the potential to be used as an alternative to Cd-based QDs. Studies have shown that Si is environmentally and biologically safe, making it an ideal material for SiQDs [35–39]. The EL spectra of Si-QLED devices have been reported over a wavelength range from 630 to 850 nm, with EQE values as high as 8.6% for near-infrared (NIR) [40], 6.2% for red [41], 0.03% for orange [42], and 0.03% for white EL emissions [43]. However, a major challenge in the development of such devices is their lack of stability during operation. To advance the development of non-toxic QLEDs, it is essential to identify an appropriate device architecture that can effectively utilize the optically active layer of SiQDs.

In this chapter, a new device architecture for Si-iQLEDs was reported. It was found that a combination of MoO_3/4,4′-Bis(9*H*-carbazol-9-yl)biphenyl (CBP) HIL/HTL and ZnO EIL/ETL adapted for Si-iQLEDs results in favorable band alignment, allowing for efficient charge injection and balance, as well as overcoming previous drawbacks. It was noted that the energy level of the HOMO of the MoO_3 film was highly dependent on the deposition conditions, which was a significant finding.

3.2 Experimental Methods

Reagents and Materials: Triethoxysilane (TES) was purchased from TCI chemicals. 1-Decene, zinc acetate dihydrate, PEDOT:PSS solution and molybdenum (VI) oxide (99.97% trace metals basis) were purchased from Sigma-Aldrich, and used as received. 2,2′,2"-(1,3,5-Benzinetriyl)-tris(1-phenyl-1-H-benzimidazole) (TPBi), Poly-TPD and 4,4′-Bis(9*H*-carbazol-9-yl)biphenyl (CBP, 99.9% trace metals basis) were purchased from Luminescence Technology Corp., and used as received. Electronic grade hydrofluoric acid (49% aqueous solution, Kanto Chemical), HPLC grade toluene, dichlorobenzene, ethanol, and methanol were purchased from Wako chemical. Water was purified and deionized using Sartorius (arium 611 UV) water purification system.

Preparation of SiQD: Preparation was performed in a two-step process. In a typical, Triethoxysilane (TES) was employed as a starting precursor. The hydrolysis product, (*i.e.*, $HSiO_{1.5})_n$, of TES was disproportionated at 1,100 °C for 1 hour in 5%/95% H_2/Ar atmosphere to produce SiQD dispersed in SiO_2 matrix. After cooling to room temperature, the dark-brown solid (*i.e.*, Si/SiO_2 composite) as powder was mechanically ground in an agate mortar with a pestle. The fine powder thus obtained was stirred in a mixture of ethanol and 48% HF (aq) to liberate SiQD from the oxide. The resultant QD was terminated with hydrogen atoms. Thermal hydrosilylation was carried out in 1-decene at 200 °C to yield decane-capped SiQD (*i.e.*, De-SiQD).

Preparation of ZnO nanocrystals: ZnO was prepared from zinc acetate dihydrate. In a typical synthesis, 312 mg $Zn(OAc)_2$ was dissolved in 15 mL of methanol and stirred. 30 mL methanol of 0.1N KOH was added slowly with continuous stirring. After refluxing 2 hours at 60 °C, ZnO nanocrystals was collected and washed with methanol.

Device Fabrication: Devices were fabricated on indium tin oxide (ITO)-coated polyethylene terephthalate (PET) substrates. A 150 nm thin film of ITO, uniformly sputtered on a sheet of PET, yields a resistivity of 10-14 Ω/sq, which is an optimal value for the fabrication of EL devices.

Conventional device structure: The ITO-coated substrates were first etched using HCl and Zn dust in a narrow strip. Then, they were cleaned by ultrasonic agitation with a nonionic detergent, followed by washing with ethanol, acetone, and isopropanol and finally rinsed with distilled water (resistivity= 18.2 MΩ·cm). After drying, the substrates were subjected to VUV lamp (Ushio Corp.) for oxidation for 30 min under a pressure of 10^3 Pa air. Then PEDOT:PSS solution was first spin-coated onto plasma-treated substrates at a speed of 5,000 rpm for 45 s. Afterward, the PEDOT:PSS-coated substrates were loaded into an Ar-filled homemade chamber and baked at 140 °C for 30 min to eradicate any remaining solvent before the deposition of subsequent organic and SiQD layers. Poly-TPD was spun from chlorobenzene solution 10 mg/mL at a speed of 1,800 rpm. The films were dried at 110 °C for 1 hour in Ar environment. A ~20 nm of the De-SiQD layer was coated on the Poly-TPD surface by spin-coating the De-SiQDs solution (10 mg/mL) for 1 min at 800 rpm. The films were dried in an Ar atmosphere at 100 °C for 1.5 hours. TPBi and aluminum (Al) were deposited as an electron transportation layer (ETL) and a top electrode cathode from vacuum evaporation.

Inverted device structure: ITO-coated polyethylene terephthalate (PET) substrates were prepared using a fabrication method similar to that employed in conventional device fabrication. Subsequently, colloidal ZnO nanocrystals were spin-coated onto the substrate from a solution of concentration 20 mg/mL in isopropanol, using a rotation speed of 2,000 rpm. After baking the film at 120 °C in air, the emission layer of De-SiQDs was spin-coated with a concentration of 10 mg/mL in chlorobenzene, using a speed of 1,500 rpm. A 40-nm-thick organic layer of CBP was then thermally evaporated onto the substrate. A 30-nm-thick layer of MoO_3 was deposited by thermal evaporation, under a vacuum level of 10^{-4} Pa. Finally, a 150-nm-thick aluminum (Al) top electrode was deposited using a mask over the film.

Characterization: The morphology of the De-SiQD was analyzed using high-resolution transmission electron microscope (HR-TEM, JEOL JEM-2100) operated at 200 kV. Major crystalline planes of the product were evaluated with X-ray powder diffraction (HT-XRD, RINT-TTR II and Reactor X, Rigaku, Japan). Surface roughness and morphology were observed at ambient conditions by atomic force microscope (AFM; Seiko Instruments Inc., SPA-400, SPI-3800N) in dynamic force mode (DFM) using a Si probe (Seiko Instruments Inc., cantilever; force constant = 0.12 N/m). Optical absorbance spectra were recorded by UV–VIS spectrophotometer (JASCO V-650, Japan) with integrated sphere. PL measurements at room temperature were carried out with a spectrofluorometer (NanoLog, Horiba Jovin Yvon, Japan). Absolute PLQYs were measured by with an absolute PLQY measurement system (C9920-02, Hamamatsu Photonics, Japan). Time-resolved fluorescence decay profiles were recorded at room temperature on a TTL trigger from the DeltaHub time-correlated single photon counting (TCSPC) electronic module, operating in the MCS mode lifetime spectroscopy system in phosphorous mode with pulse laser diodes of λ_{em} = 370 nm (NanoLog, Horiba Jovin Ybon, Japan). The quality of the fit has been judged by the fitting parameters such as χ^2 (<1.2) as well as the visual inspection of the residuals. Photoelectron yield spectra (PYS) were measured by a model AC-3 (RIKEN KEIKI Co. Ltd., Japan).

Calculation of EQE: EQE and optical power density were calculated assuming that EL has a Lambertian emission profile. EQE is expressed as the ratio of the number of radiated photons to the number of injected electrons per unit time $I_d(V)/|e|$, where $I_d(V)$ is current through device when applied voltage V, e is the electron charge. EQE is represented by the following equation,

$$\mathrm{EQE}\ (\%) = \frac{N_p(V) \times |e| \times g}{I_d(V)} \times 100 \qquad \mathrm{Eq.}\,3-1$$

where $N_p(V)$ is the number of photons collected by photodiode. Geometry factor g expresses when EL profile assumed to be Lambertian the ratio of the luminous flux emitted from LED to the luminous flux measured by photodiode, given by the following equation,

$$g = \frac{a^2 + L^2}{a^2} \qquad \text{Eq. } 3-2$$

where a indicates the radius of aperture of photodiode, L is distance between the light emitting surface of LED and photodiode. Here, the geometry factor was calculated as 4.59. $N_p(V)$ based on the actual observed EL spectrum $EL(\lambda)$ and photodiode current I_p^m is given by the following equation,

$$N_p(V) = \int_{\lambda_i}^{\lambda_f} EL(\lambda) \times \frac{I_p^m}{I_p'(\lambda)} d\lambda \qquad \text{Eq. } 3-3$$

where $I_p'(\lambda)$ is expressed using Planck constant h, the speed of light in vacuum c, EL emission wavelength λ and photodiode responsivity $R(\lambda)$,

$$I_p'(\lambda) = \int_{\lambda_i}^{\lambda_f} EL(\lambda) \times \frac{hc}{\lambda} \times R(\lambda)\, d\lambda \qquad \text{Eq. } 3-4$$

By calculating $N_p(V)$ for all applied voltages and substituting it into $\text{Eq. } 3-1$ gives voltage or current density dependent EQE characteristics.

Optical power density was calculated as follows. The emitted power $P(V)$ is calculated by following equation

$$P(V) = \int_{\lambda_i}^{\lambda_f} EL(\lambda) \times \frac{I_p^m}{I_p'(\lambda)} \times \frac{hc}{\lambda} d\lambda \qquad \text{Eq. } 3-5$$

Then optical power density is expressed using $P(V)$

$$\text{Optical power density } (\mathrm{W/cm^2}) = \frac{P(V)}{A} \qquad \text{Eq. } 3-6$$

where A is the area of the light emitting surface.

3.3 Experimental Results

Fig.3-1 illustrates schematically the conventional and inverted QLEDs, as well as their flat energy band diagrams. The conventional QLED, which serves as a standard, was prepared using PEDOT:PSS (10 nm) as the HIL and HTL, Poly-TPD (10 nm) as the HTL, and TPBi (20 nm) as the EIL and ETL. The device was constructed on a 150-nm-thick layer of ITO anode, with a resistivity of 10-14 Ω/sq. The cathode of the conventional QLED consisted of a 150-nm-thick Al layer that was deposited under a vacuum. This type of multilayer structure is commonly seen in the literature [42,47,50]. The De-SiQD exhibited an average diameter of 2.1 nm, which corresponds to a PL band peak at 720 nm and a PLQY of 40%. The estimated PL lifetime was 105 μs, which aligns with previously reported values [48,51]. The De-SiQD film, which was spin-coated, presented a smooth and uniform surface with a root-mean-square roughness of less than 1.2 nm, as depicted in Fig.3-2. In the conventional QLED structure, electrons are injected from the Al electrode, and holes are injected from the ITO electrode (as shown in Fig.3-1 (b)). The inverted QLED structure presented here features the following layer sequence: ITO (150 nm)/ZnO (20 nm)/De-SiQD (20 nm)/CBP (40 nm)/MoO_3 (30 nm)/Al (150 nm), as depicted in Fig.3-1(c). In contrast to the conventional QLED, electrons and holes are injected from the ITO cathode and the Al anode, as illustrated in Fig.3-1(d). The procedure for synthesizing ZnO nanocrystals was modified [52] to produce nanocrystals with an average diameter of 5.4 ± 0.7 nm, as illustrated in Fig.3-3. The spin-coated ZnO film presents a flat substrate for the deposition of QDs. The utilization of a ZnO film as the EIL and ETL leverages its advantageous properties, including high transparency in the visible spectrum, high electron mobility, a valence band (VB) edge energy level that is significantly lower than that of the QD to prevent hole leakage from the neighboring optical layer, robustness for repeated spin-coating of the QD film, and a low conduction band (CB) edge energy level for efficient electron injection and transport. The incorporation of a MoO_3 film as the HIL and HTL provides a shallow work function for efficient hole injection. The surface of MoO_3

exhibited exceptional smoothness on an atomic scale, with a minimal quantity of grain boundaries (Fig.3-4). The CBP film, deposited under a vacuum via thermal evaporation, presents a noteworthy advantage. As depicted in Fig.3-1 (d), the shallow HOMO level of CBP facilitates hole transportation between the MoO_3 and QD layers, while the LUMO level, responsible for generating a significant barrier height between the QD and MoO_3 layers, effectively suppresses electron leakage from the QD to the MoO_3 films.

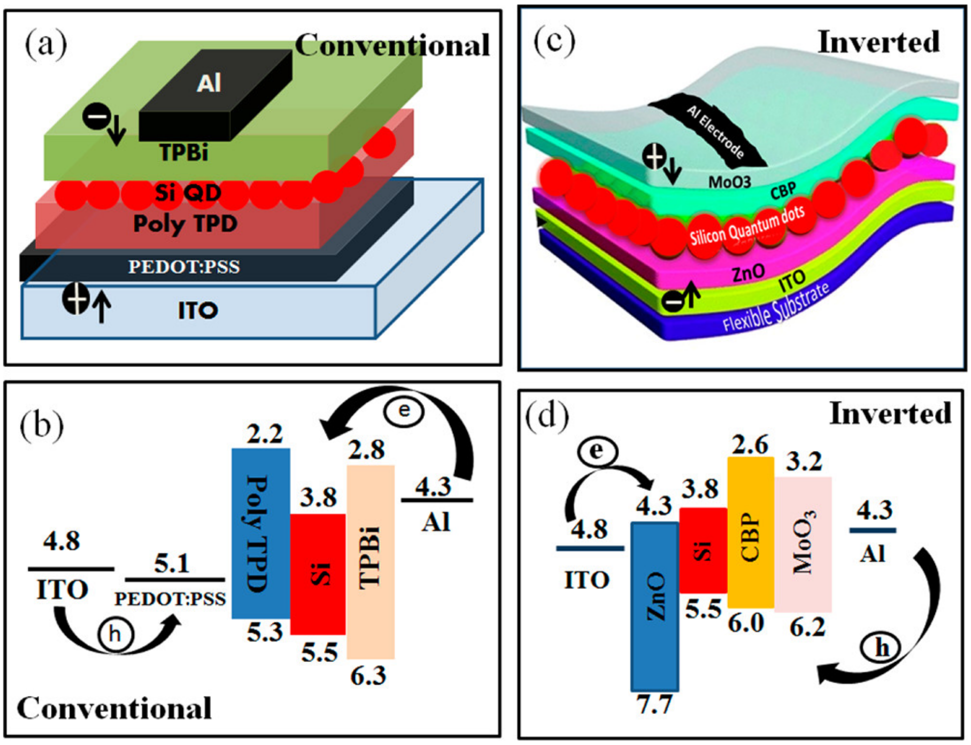

Fig.3-1 Schematic representations (upper) and flat band diagrams (lower) of the conventional (a, b) and inverted (c, d) device structures of the flexible, red-light emitting Si-QLED.

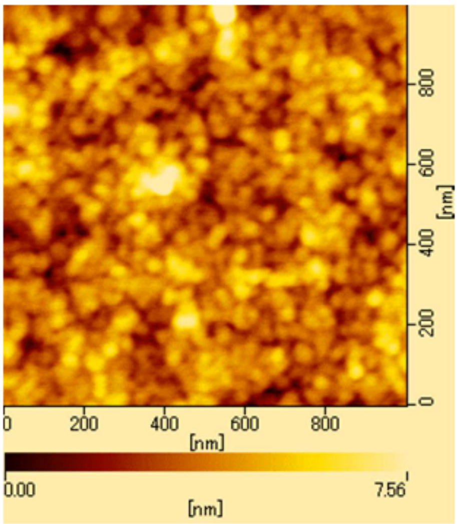

Fig.3-2 AFM image taken by DFM operation mode for De-SiQD film.

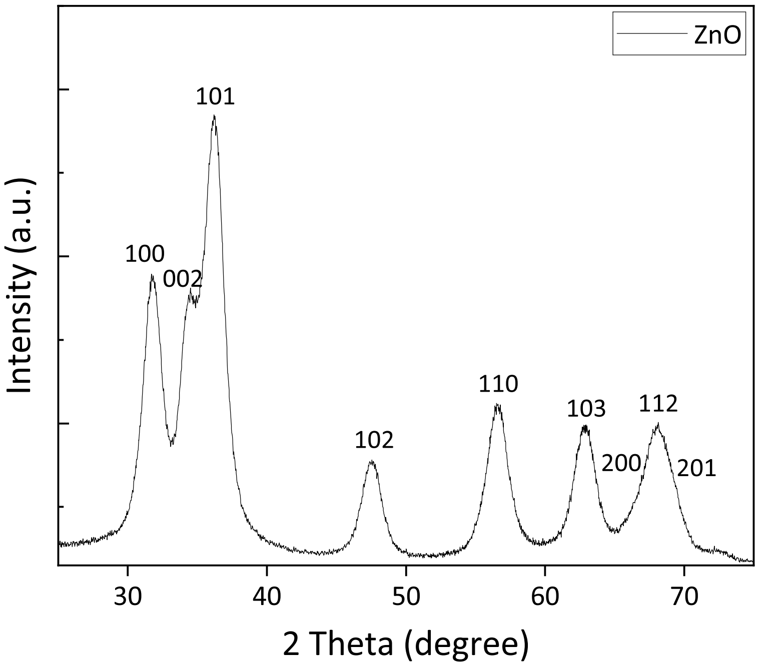

Fig.3-3 XRD pattern of ZnO nanocrystals. The pattern (red) experimentally measured is fitted with calculated curve for analysis. Clearly, the product was composed of high crystalline and single phase of ZnO. An average diameter of the ZnO nanocrystals were calculated from Scherrer equation to be 5.4±0.7 nm.

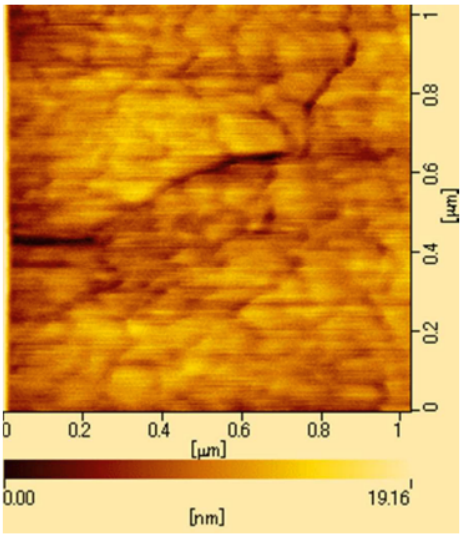

Fig.3-4 AFM image taken by DFM operation mode for the MoO_3 film.

The photoelectron yield spectroscopy (PYS) was employed to experimentally measure the local surface work functions of the QD and MoO_3 films. The films were prepared using a deposition process similar to the device fabrication process. Fig.3-5 illustrates the work function regions derived from the PYS measurements for the VB maximum of the QD (Fig.3-5(a)) and the MoO_3 film (Fig.3-5(b)). Each line was defined as a pair consisting of the base and the rise in order to calculate the onset. It is worth noting that the electronic structure of MoO_3 is strongly influenced by the stoichiometric oxygen composition in the film [53,54]. Yao *et al.*, have previously reported that a MoO_3 film deposited under high-vacuum conditions exhibits deep HOMO and LUMO levels at 9.5 and 6.7 eV, respectively [25]. However, upon exposure to air, the HOMO and LUMO levels decrease to 5.3 and 2.3 eV, respectively [55]. To enhance hole injection from the Al anode to the QD layer via MoO_3, it is optimal to use a vacuum condition of approximately 10^{-4} Pa to deposit a 30 nm thick MoO_3 film, which provides a work function as low as approximately 6.2 eV.

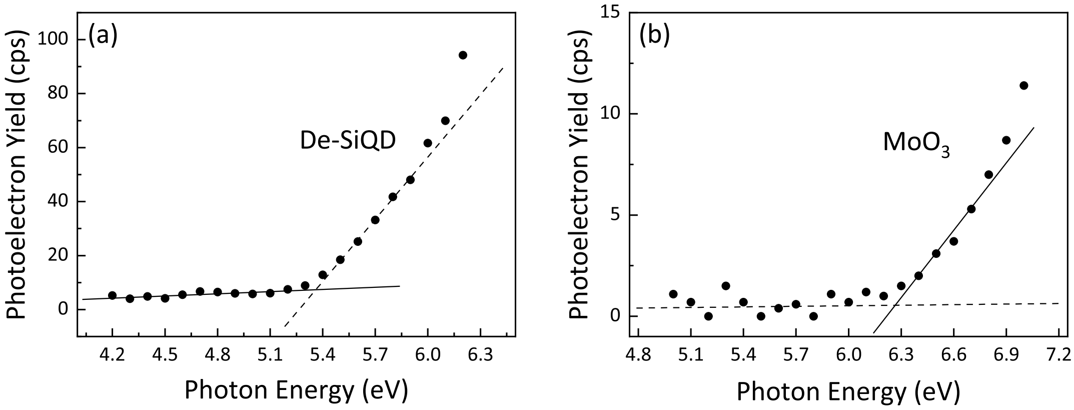

Fig.3-5 Photoelectron yield spectra of (a) De-SiQD and (b) MoO$_3$ films on a quartz glass substrate. The values depicted in the figure indicate the experimentally determined negative values of the HOMO energy.

Fig.3-6 illustrates the current–voltage (*I–V*) characteristics of Si-iQLED, along with the photodiode *J–V* characteristics. The measurement utilized a calibrated Si photodetector (Hamamatsu S1336 8BQ) coupled with a Keithley 2425. The count of photons emitted from the ITO side and directly collected by the photodetector increases with the current. The turn-on voltage, defined as the minimum applied bias at which the iQLED begins to emit light, was determined from the photodiode *J–V* characteristics. The estimated turn-on voltage for Si-iQLED was 3.5 V, with a corresponding minimum optical power density of 0.01 μW/cm^2 as determined from the calibrated photodiode current. It should be noted that a value of 0.01 μW/cm^2 represents the lower limit of optical detection for the employed optical setup.

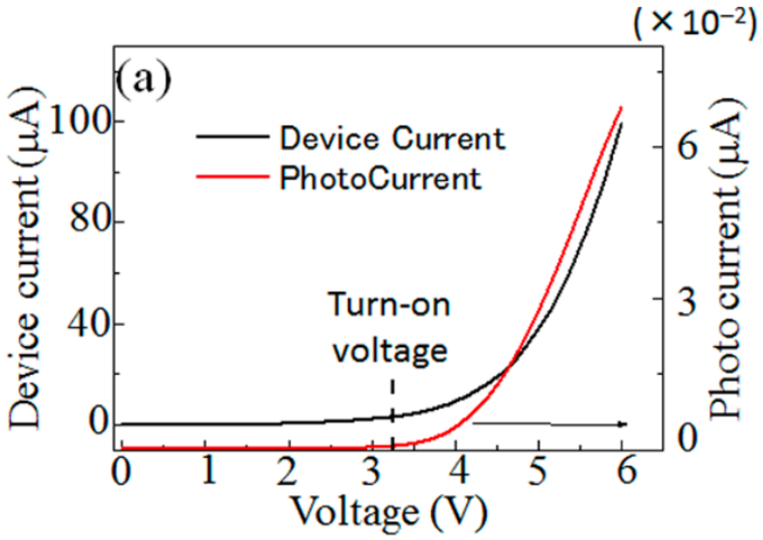

Fig.3-6 Device *I-V* characteristics (black line) and photodiode *J-V* characteristics (red line).

Xue *et al*., have recently reported blue-violet ZnCdS/ZnS QLEDs with a low turn-on voltage of 2.5 V [56]. Regarding Si-QLEDs, Maier-Flaig *et al*., reported a turn-on voltage of approximately 4 V [42], while Mastronardi *et al*., reported a slightly higher value of about 4.6 V [57]. Liu *et al*., have reported a recent finding of a low turn-on voltage of 3 V using a conventional device structure [41]. The detection of a low turn-on voltage implies the existence of a small barrier height for charge injection from the electrodes into the QD layer. The provision of a decent deep HOMO level by the well-controlled MoO_3 layer results in a reduced operation applied voltage. Further reduction in the turn-on voltage for device operation can be achieved by decreasing the energy barrier between ITO and ZnO. One possible technique involves modifying the surface of ITO to make its work function shallow.

Fig.3-7 displays the typical optical power density curves as a function of the device current density, showing an optical power density reaching as high as 6.13 μW/cm^2 at 5 V. The EL spectrum exhibited a peak at 720 nm and a narrow fwhm of 150 nm (Fig.3-8). These spectral characteristics resemble the PL characteristics of the corresponding De-SiQD specimen. These spectral characteristics closely resembled the PL characteristics of the corresponding De-SiQD specimen. Although the EL spectrum was slightly narrower than the PL spectrum, further study is needed to clarify the mechanism behind this. Notably, the adoption of a thin polyethylene terephthalate (PET) sheet as a substrate enables mechanical flexibility, as illustrated in the inset of Fig.3-8. Additionally, the emitted light from the iQLED was vibrant and luminous enough to be visible to the naked eye, even in a well-lit room (Fig.3-8, inset). This achievement marks the first time a Si-QLED has been successfully fabricated with sufficient flexibility to be worn or attached to a curved 3D surface, as the device structure is also constructed on a thin PET sheet. This novel development represents a significant advancement towards wearable display technologies.

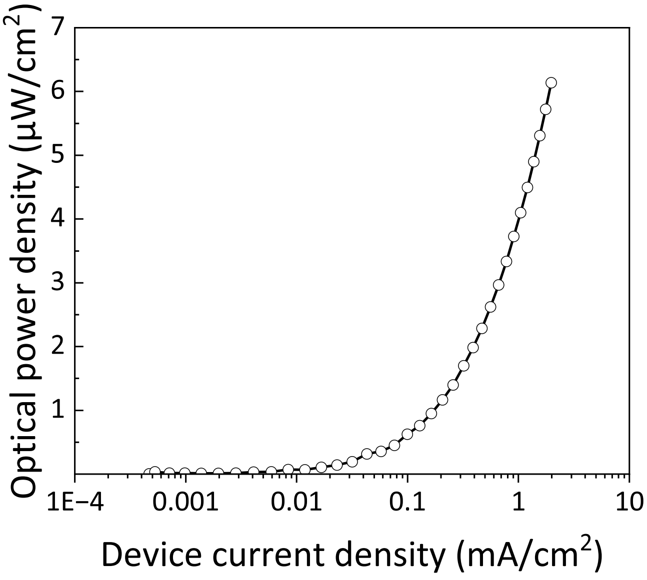

Fig.3-7 Optical power density characteristic plotted with device current density.

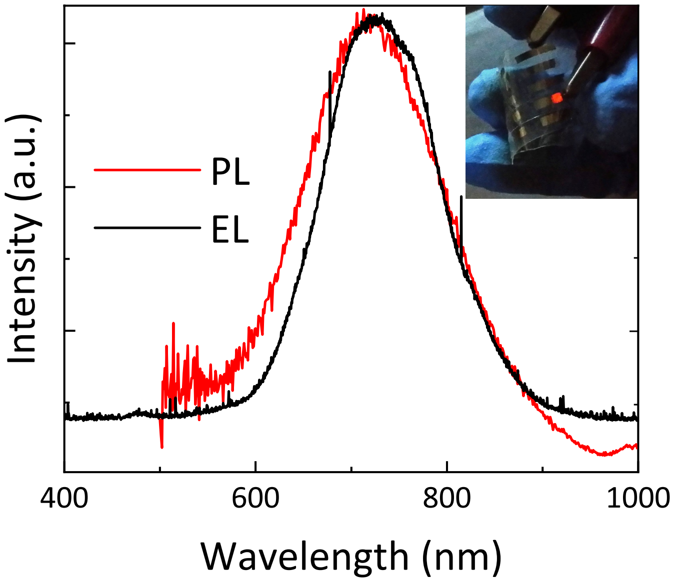

Fig.3-8 A typical EL spectrum at the operation voltage of 4 V (PL spectrum of the corresponding De-SiQD dispersed in chloroform). A photograph demonstrates a representative red-light emitting QLED folded in hand during operation.

Although there has been recent progress in the development of Si-QLEDs, a comprehensive investigation into the stability of their performance during device operation is currently lacking in the literature. Specifically, there has been no examination of the stability of the EL color under high operation voltage regimes, the operational lifetime of the device, the potential for parasitic emission from neighboring compositional layers or the QD surface states over the entire range of driving voltages, or the leveling off of the EQE during device operation. It is important to note that the inverted device structure has the potential to overcome issues commonly observed in conventional QLEDs.

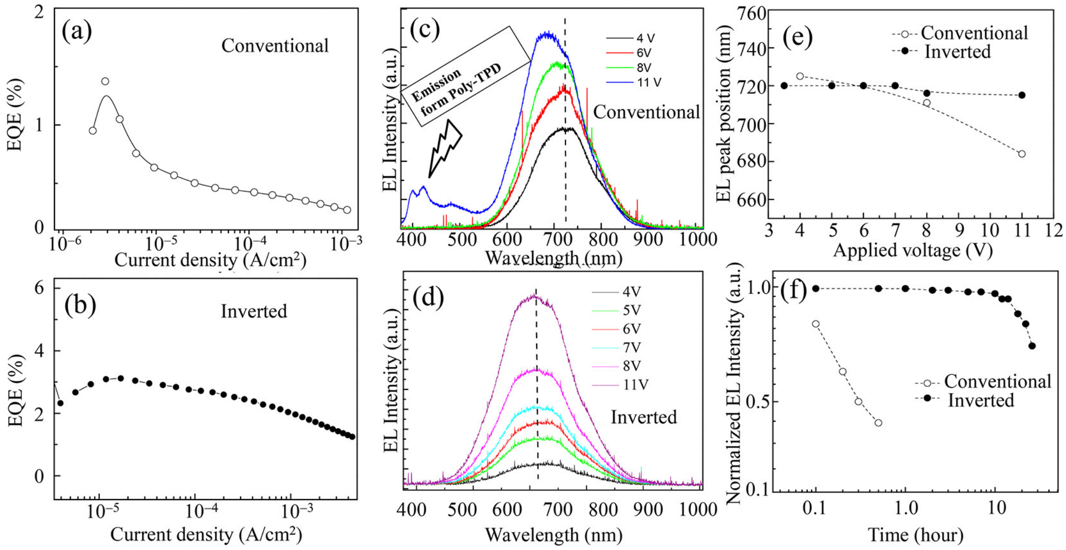

Fig.3-9 Summary of different optical performance between the conventional and the inverted QLEDs in terms of (a, b) EQE-current density (c, d) voltage variance of the EL spectra at different applied bias, (e) EL peak positions as a function of driving voltage, and (f) operational device lifetime depicted by EL intensities at each time normalized with respect to the initial EL intensity.

A Si-QLED with a conventional device structure was fabricated and its optical characteristics were compared with those of an iQLED (refer to Fig.3-1 for device schematics). Fig.3-9 illustrates the optical performance comparison between the conventional and inverted device structures. The EQE values of the conventional and inverted structures are plotted as a function of the applied voltage in Fig.3-9(a,b), respectively. For the conventional device structure, the maximum EQE value (~1.4%) significantly decreases as the current density increases. The critical current density, at which the EQE is reduced to half its maximum value, was approximately 0.01 mA/cm^2. There was an 80% reduction from the peak value at 0.1 mA/cm^2. The iQLED exhibited a slow and steady decrease in EQE as the current density increases, with a maximum EQE performance of 3.1%. Unlike the conventional structure, there was no rapid decline in EQE across the entire range of current density. In contrast, the EQE for the QLED plateaued in the range of 10^{-4}-10^{-5} A/cm^2, with a noticeable decrease observed at $J = 0.03$ mA/cm^2, and a critical current density of approximately 0.3 mA/cm^2, which is 30 times larger than that for a conventional device. The observed EQE stability may be attributed to improved charge balance and reduced exciton quenching, as suggested by previous research [58]. Figures (c) and (d) in Fig.3-9 present a comparison of the EL spectra obtained at various voltages. In the case of the conventional structure, the EL peak shifts towards the blue by 50 nm at 11 V, as illustrated in Fig.3-9(e). The blue shift of the EL peak with an increase in driving voltage is a common observation in Si-QLEDs with conventional structures. Maier-Flaig *et al.*, reported a blue shift of the EL peak of approximately 15 nm by increasing the operation voltage from 3.5 to 10 V [42]. Similarly, Liu *et al.*, observed a blue shift of approximately 50 nm in the EL peak with an increase in driving voltage from 3.5 to 6.5 V, despite achieving a high EQE of 6.2% [41]. The EL peak position of an NIR-emitting Si-QLED also experienced a blue shift of similar magnitude, as reported in previous studies [40,59]. This blue shift may be attributed to the quantum confined Stark effect and/or band filling at higher current density, among other factors [60]. Another possibility for the observed blue shift in the EL spectrum is the parasitic emission from the neighboring compositional layers of the QD, as shown in the EL spectrum at 11 V in Fig.3-9(c). In contrast, the EL spectrum of the inverted structure, as shown in Fig.3-9(d), exhibited no undesirable emission other than that of the QDs and the EL spectral shape was independent of the driving voltage. As evidenced in Fig.3-9(e), the shift in the EL peak was negligible, indicating that the EL emission originated solely from the QD layer even at high applied voltages. Additional research is required to provide definitive evidence of the very small spectral shift. It should be noted that a high conductivity and good band alignment of the HTL make it difficult to build up band-filling, resulting in a decrease in the amplitude of the high-photon-energy component of the EL spectrum. Furthermore, the lack of parasitic emissions from neighboring layers in the iQLEDs, where only electrons and holes injected from the electrodes recombine within the optically active layer for efficient EL, results in a smaller spectral shift.

In this study, the operational lifetime of the Si-QLEDs with continuous light emission was investigated for each device structure under ambient conditions, without any protective sealing, encapsulation, or packaging to prevent reactions with oxygen and water molecules. The device was subjected to a constant bias, and the photodiode was used to measure the photocurrent generated by the emitted photons concurrently. The EL intensity values, normalized by the initial intensity, are presented in Fig.3-9(f) as a function of operational time. The results indicate that the iQLED exhibited no noticeable reduction in intensity until 12 hours, but after 26 hours, the initial intensity was reduced by approximately 30%. In contrast, the conventional device exhibited a rapid reduction in EL intensity, with only 40% of the initial intensity remaining after a time scale of 1 hour. Device degradation during operation is a common issue in OLED studies. In many cases, the failure of the device is attributed to unwanted damage to the device components during operation, including (i) the migration or diffusion of elements from neighboring layers, leading to the formation of a nonconductive barrier in the multilayer stack, and (ii) the oxidation of the Al cathode.

Current investigations into device failure for QLEDs are still limited. Maier-Flaig *et al.*, recently attempted to clarify the degradation process of Si-QLEDs during device operation by utilizing advanced TEM observations of a conventional Si-QLED before and after operation, as well as energy dispersive X-ray spectroscopic (EDX) analysis [61]. Their findings suggest that a shorter operational lifetime in a conventional QLED may be due to (i) the presence of a defective and/or poorly surface-functionalized SiQD in the active layer at a low voltage, (ii) significant morphological changes, such as electromigration of the SiQD to the ETL (*i.e.*, TPBi) for layer-intermixing, and (iii) microscopic defects that remain after the atomic migration at a high voltage, which can ultimately lead to rapid device degradation.

The longer device lifetime observed for the iQLED, even under high-voltage conditions, suggests that most of the issues observed in the conventional structure can be addressed. However, a detailed microscopic analysis is needed to provide further clarification. The utilization of two metal oxide layers, such as ZnO and MoO_3, for the ETL/EIL and HTL/HIL, respectively, provides inherent robustness and protection of the interlayers against oxidation. Additionally, reducing the degree of charged QDs, which leads to carrier loss due to Auger recombination, is expected to enhance the EQE [62].

Subsequently, the inverted device was compared to previously reported Si-QLEDs in terms of both the EQE and the stability of the EL peak with increasing operation voltage. Fig.3-10(a) illustrates the EQE values plotted against the EL peak wavelength. The majority of the device EQEs still remain in the 1% range. While a few papers reported EQE values exceeding 6% for red-EL and 8% for NIR-EL [40,41], they lack the EL spectral stability observed in both QLEDs. This may be attributed to the use of a normal device structure in the previous reports. The iQLED demonstrated a maximum EQE of 3.1%, yet exhibited high EQE stability across a wide range of operating voltages. Fig.3-10(b) depicts the EL peak wavelengths of the iQLED and various other devices at different operation voltages. The EL spectral peak of the Si-iQLEDs in this study demonstrated a minimal blue shift of only 4 nm as the voltage was increased from the turn-on voltage to 11 V. Conversely, the reported devices experienced a larger blue shift of the EL peak wavelength (up to 50 nm) with increasing applied voltage, indicating the advantages of the inverted device structure.

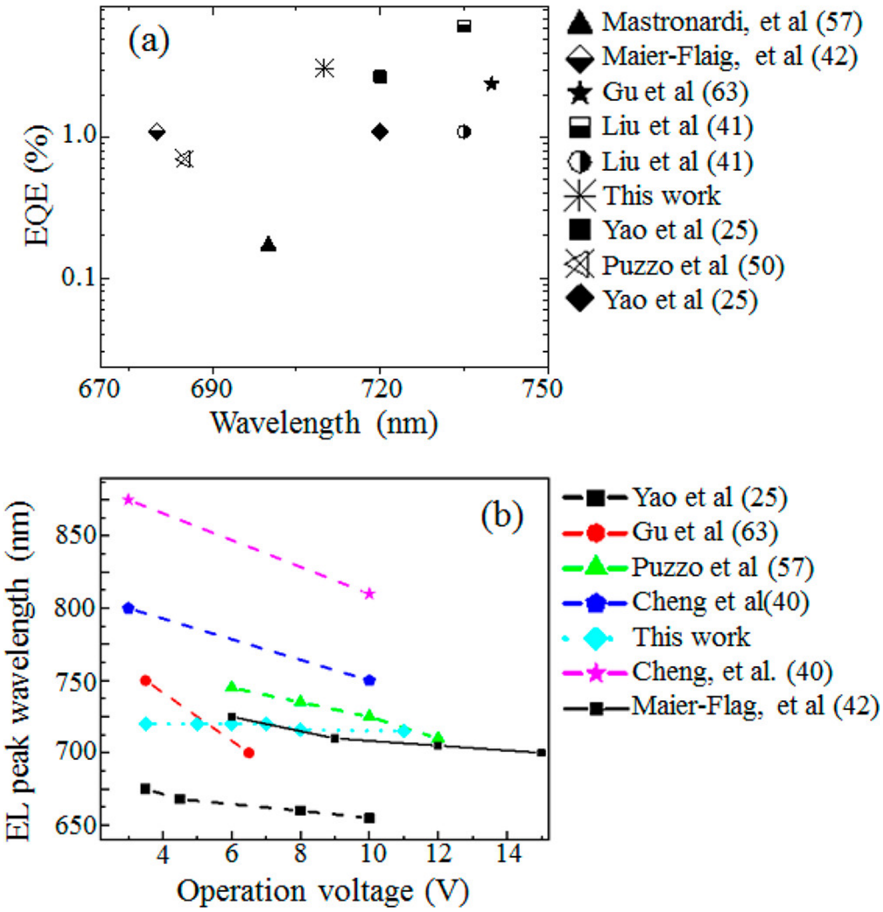

Fig.3-10 (a) Peak values of EQE versus EL peak wavelengths and (b) the spectral blue shift of EL peaks with increasing driving voltage for this study and a number of literature reports of Si-QLED. In (b), the EL peak wavelengths are estimated by eye.

3.4 Conclusion

In summary, the first investigation of the benefits of the inverted device structure for Si-QLEDs through a comparison with the optical performance of traditional device structures has been reported. The implementation of optimal CBP/MoO_3 HTL/HIL layers yielded a drastic improvement in the optical performance of Si-iQLED. Notably, the following observations were made: (i) low turn-on voltage for light emission, (ii) EQE leveling off over a wide driving-voltage range, (iii) EL spectral shape and position remaining unchanged even at high driving voltage (∼11 V), and (iv) extended device lifetimes. The Si-iQLEDs in this study outperform previous Si-QLEDs in various optical performances, to the best of available knowledge. Furthermore, this study presented a highly flexible Si-QLED for the first time through the adoption of a PET sheet substrate, instead of a glass substrate, towards the widespread and convenient use of Si-QLEDs in flexible technologies.

3.5 References

[1] Choi, M. K., Yang, J., Hyeon, T. & Kim, D. H. Flexible quantum dot light-emitting diodes for next-generation displays. *npj Flexible Electronics* vol. 2 10 (2018)

[2] Kim, T. H. *et al.* Full-colour quantum dot displays fabricated by transfer printing. *Nat. Photonics* **5**, 176–182 (2011)

[3] Tan, Z. *et al.* Colloidal nanocrystal-based light-emitting diodes fabricated on plastic toward flexible quantum dot optoelectronics. *J. Appl. Phys.* **105**, 034312 (2009)

[4] Shirasaki, Y., Supran, G. J., Bawendi, M. G. & Bulović, V. Emergence of colloidal quantum-dot light-emitting technologies. *Nat. Photonics* **7**, 13–23 (2013)

[5] Tyan, Y.-S. Organic light-emitting-diode lighting overview. *J. Photonics Energy* **1**, 011009 (2011)

[6] Caruge, J. M., Halpert, J. E., Wood, V., Buloví, V. & Bawendi, M. G. Colloidal quantum-dot light-emitting diodes with metal-oxide charge transport layers. *Nat. Photonics* **2**, 247–250 (2008)

[7] Bendall, J. S. *et al.* Layer-by-Layer All-Inorganic Quantum-Dot-Based LEDs: A Simple Procedure with Robust Performance. *Adv. Funct. Mater.* **20**, 3298–3302 (2010)

[8] Yang, J., Choi, M. K., Kim, D. H. & Hyeon, T. Designed Assembly and Integration of Colloidal Nanocrystals for Device Applications. *Adv. Mater.* **28**, 1176–1207 (2016)

[9] Dai, X., Deng, Y., Peng, X. & Jin, Y. Quantum-Dot Light-Emitting Diodes for Large-Area Displays: Towards the Dawn of Commercialization. *Adv. Mater.* **29**, 1607022 (2017)

[10] Zhang, H., Li, H., Sun, X. & Chen, S. Inverted Quantum-Dot Light-Emitting Diodes Fabricated by All-Solution Processing. *ACS Appl. Mater. Interfaces* **8**, 5493–5498 (2016)

[11] Pan, J. *et al.* Boosting the efficiency of inverted quantum dot light-emitting diodes by balancing charge densities and suppressing exciton quenching through band alignment. *Nanoscale* **10**, 592–602 (2018)

[12] Kim, J. H. & Park, J. W. Designing an electron-transport layer for highly efficient, reliable, and solution-processed organic light-emitting diodes. *J. Mater. Chem. C* **5**, 3097–3106 (2017)

[13] Yang, G., Tao, H., Qin, P., Ke, W. & Fang, G. Recent progress in electron transport layers for efficient perovskite solar cells. *Journal of Materials Chemistry A* vol. 4 3970–3990 (2016)

[14] Wang, G. *et al.* Preparation and characterization of MoO3 hole-injection layer for organic solar cell fabrication and optimization. *Sol. Energy Mater. Sol. Cells* **120**, 603–609 (2014)

[15] Li, X., Xie, F., Zhang, S., Hou, J. & Choy, W. C. H. MoOx and V2Ox as hole and electron

transport layers through functionalized intercalation in normal and inverted organic optoelectronic devices. *Light Sci. Appl.* **4**, e273–e273 (2015)

[16] Baigent, D. R. *et al.* Conjugated polymer light-emitting diodes on silicon substrates. *Appl. Phys. Lett.* **65**, 2636–2638 (1994)

[17] Zhou, X. *et al.* Low-voltage inverted transparent vacuum deposited organic light-emitting diodes using electrical doping. *Appl. Phys. Lett.* **81**, 922–924 (2002)

[18] Kaçar, R., Mucur, S. P., Yıldız, F., Dabak, S. & Tekin, E. Highly efficient inverted organic light emitting diodes by inserting a zinc oxide/polyethyleneimine (ZnO:PEI) nano-composite interfacial layer. *Nanotechnology* **28**, 245204 (2017)

[19] Zhao, X. D. *et al.* Efficient color-stable inverted white organic light-emitting diodes with outcoupling-enhanced ZnO layer. *ACS Appl. Mater. Interfaces* **9**, 2767–2775 (2017)

[20] Liu, S. *et al.* Top-emitting quantum dots light-emitting devices employing microcontact printing with electricfield-independent emission. *Sci. Rep.* **6**, 22530 (2016)

[21] Jang, I. *et al.* Inverted InP quantum dot light-emitting diodes using low-temperature solution-processed metal-oxide as an electron transport layer. *Jpn. J. Appl. Phys.* **54**, (2015)

[22] Castan, A., Kim, H.-M. & Jang, J. All-Solution-Processed Inverted Quantum-Dot Light-Emitting Diodes. *ACS Appl. Mater. Interfaces* **6**, 2508–2515 (2014)

[23] Liu, Y. *et al.* Highly Efficient All-Solution Processed Inverted Quantum Dots Based Light Emitting Diodes. *ACS Nano* **12**, 1564–1570 (2018)

[24] Son, D. I. *et al.* Carrier transport of inverted quantum dot LED with PEIE polymer. *Org. Electron.* **15**, 886–892 (2014)

[25] Yao, L. *et al.* Efficient silicon quantum dots light emitting diodes with an inverted device structure. *J. Mater. Chem. C* **4**, 673–677 (2015)

[26] Kwak, J. *et al.* Bright and Efficient Full-Color Colloidal Quantum Dot Light-Emitting Diodes Using an Inverted Device Structure. *Nano Lett.* **12**, 2362–2366 (2012)

[27] Kim, D. *et al.* Polyethylenimine Ethoxylated-Mediated All-Solution-Processed High-Performance Flexible Inverted Quantum Dot-Light-Emitting Device. *ACS Nano* **11**, 1982–1990 (2017)

[28] Dai, X. *et al.* Solution-processed, high-performance light-emitting diodes based on quantum dots. *Nature* **515**, 96–99 (2014)

[29] Yang, Y. *et al.* High-efficiency light-emitting devices based on quantum dots with tailored nanostructures. *Nat. Photonics* **9**, 259–265 (2015)

[30] Jiang, C. *et al.* Improved performance of inverted quantum dots light emitting devices by

introducing double hole transport layers. *Org. Electron.* **31**, 82–89 (2016)

[31] Mashford, B. S. *et al.* High-efficiency quantum-dot light-emitting devices with enhanced charge injection. *Nat. Photonics* **7**, 407–412 (2013)

[32] Zou, Y. *et al.* A General Solvent Selection Strategy for Solution Processed Quantum Dots Targeting High Performance Light-Emitting Diode. *Adv. Funct. Mater.* **27**, 1603325 (2017)

[33] Wang, L. *et al.* Blue Quantum Dot Light-Emitting Diodes with High Electroluminescent Efficiency. *ACS Appl. Mater. Interfaces* **9**, 38755–38760 (2017)

[34] Gelloz, B. & Koshida, N. Electroluminescence with high and stable quantum efficiency and low threshold voltage from anodically oxidized thin porous silicon diode. *J. Appl. Phys.* **88**, 4319–4324 (2000)

[35] Dasog, M., Kehrle, J., Rieger, B. & Veinot, J. G. C. Silicon Nanocrystals and Silicon-Polymer Hybrids: Synthesis, Surface Engineering, and Applications. *Angew. Chemie Int. Ed.* **55**, 2322–2339 (2016)

[36] Ruizendaal, L. *et al.* Synthesis and cytotoxicity of silicon nanoparticles with covalently attached organic monolayers. *Nanotoxicology* **3**, 339–347 (2009)

[37] Shirahata, N. Colloidal Si nanocrystals: a controlled organic–inorganic interface and its implications of color-tuning and chemical design toward sophisticated architectures. *Phys. Chem. Chem. Phys.* **13**, 7284 (2011)

[38] Su, Y., Ji, X. & He, Y. Water-Dispersible Fluorescent Silicon Nanoparticles and their Optical Applications. *Adv. Mater.* **28**, 10567–10574 (2016)

[39] Tu, C., Ma, X., Pantazis, P., Kauzlarich, S. M. & Louie, A. Y. Paramagnetic, silicon quantum dots for magnetic resonance and two-photon imaging of macrophages. *J. Am. Chem. Soc.* **132**, 2016–2023 (2010)

[40] Cheng, K.-Y., Anthony, R., Kortshagen, U. R. & Holmes, R. J. High-Efficiency Silicon Nanocrystal Light-Emitting Devices. *Nano Lett.* **11**, 1952–1956 (2011)

[41] Liu, X. *et al.* Light-Emitting Diodes Based on Colloidal Silicon Quantum Dots with Octyl and Phenylpropyl Ligands. *ACS Appl. Mater. Interfaces* **10**, 5959–5966 (2018)

[42] Maier-Flaig, F. *et al.* Multicolor Silicon Light-Emitting Diodes (SiLEDs). *Nano Lett.* **13**, 475–480 (2013)

[43] Ghosh, B. *et al.* Hybrid white light emitting diode based on silicon nanocrystals. *Adv. Funct. Mater.* **24**, 7151–7160 (2014)

[44] Ghosh, B., Hamaoka, T., Nemoto, Y., Takeguchi, M. & Shirahata, N. Impact of Anchoring

Monolayers on the Enhancement of Radiative Recombination in Light-Emitting Diodes Based on Silicon Nanocrystals. *J. Phys. Chem. C* **122**, 6422–6430 (2018)

[45] Puzzo, D. P. *et al.* Visible Colloidal Nanocrystal Silicon Light-Emitting Diode. *Nano Lett.* **11**, 1585–1590 (2011)

[46] Chandra, S., Masuda, Y., Shirahata, N. & Winnik, F. M. Transition-Metal-Doped NIR-Emitting Silicon Nanocrystals. *Angew. Chemie Int. Ed.* **56**, 6157–6160 (2017)

[47] Ghosh, B. *et al.* Origin of the Photoluminescence Quantum Yields Enhanced by Alkane-Termination of Freestanding Silicon Nanocrystals: Temperature-Dependence of Optical Properties. *Sci. Rep.* **6**, 36951 (2016)

[48] Mashford, B. S., Nguyen, T. L., Wilson, G. J. & Mulvaney, P. All-inorganic quantum-dot light-emitting devices formed via low-cost, wet-chemical processing. *J. Mater. Chem.* **20**, 167–172 (2010)

[49] Hu, X., Chen, L. & Chen, Y. Universal and versatile MoO3-based hole transport layers for efficient and stable polymer solar cells. *J. Phys. Chem. C* **118**, 9930–9938 (2014)

[50] Guo, Y. & Robertson, J. Origin of the high work function and high conductivity of MoO3. *Appl. Phys. Lett.* **105**, 222110 (2014)

[51] Zhao, Y., Chen, J., Chen, W. & Ma, D. Poly(3,4-ethylenedioxythiophene):Poly(styrenesulfonate)/MoO 3 composite layer for efficient and stable hole injection in organic semiconductors. *J. Appl. Phys.* **111**, 043716 (2012)

[52] Shen, H. *et al.* High-efficiency, Low turn-on voltage blue-violet quantum-dot-based light-emitting diodes. *Nano Lett.* **15**, 1211–1216 (2015)

[53] Mastronardi, M. L. *et al.* Silicon nanocrystal OLEDs: Effect of organic capping group on performance. *Small* **8**, 3647–3654 (2012)

[54] Giebink, N. C. & Forrest, S. R. Quantum efficiency roll-off at high brightness in fluorescent and phosphorescent organic light emitting diodes. *Phys. Rev. B - Condens. Matter Mater. Phys.* **77**, 1–9 (2008)

[55] Cheng, K. Y., Anthony, R., Kortshagen, U. R. & Holmes, R. J. Hybrid silicon nanocrystal?organic light-emitting devices for infrared electroluminescence. *Nano Lett.* **10**, 1154–1157 (2010)

[56] Wang, D. C., Chen, J. R., Zhu, J., Lu, C. T. & Lu, M. On the spectral difference between electroluminescence and photoluminescence of Si nanocrystals: A mechanism study of electroluminescence. *J. Nanoparticle Res.* **15**, (2013)

[57] Maier-Flaig, F. *et al.* Looking inside a working SiLED. *Nano Lett.* **13**, 3539–3545 (2013)

[58] Bae, W. K. *et al.* Controlling the influence of Auger recombination on the performance of quantum-dot light-emitting diodes. *Nat. Commun.* **4**, 2661 (2013)

Chapter 4 Color-Tunable Silicon Quantum Dots Light-Emitting Diodes

4.1 Introduction

Quantum dot light-emitting diodes (QLEDs) have garnered significant interest in optoelectronics due to their distinctive optical characteristics, such as color purity, high luminance, narrow spectral emission (full-width at half-maximum, fwhm), and spectral tunability of electroluminescence (EL) emissions that span the entire visible region [1–4]. Currently, the external quantum efficiencies (EQEs) of QLEDs emitting in the red, green, and blue regions stand at record values of 21.6%, 22.9%, and 19.8%, respectively, as reported in the literature [1,4]. These EQE values are comparable to the energy conversion efficiency of a mercury lamp, which is considered the benchmark for commercialization. High EQEs have been attained using state-of-the-art QLEDs containing optically active layers composed of cadmium (Cd) based quantum dots (QDs) [1–7]. Notwithstanding the unique optical properties of heavy-metal QDs, such as Cd-based QDs, their industrial utilization is hampered by their intrinsic toxicity. Indeed, regulatory agencies, such as RoHS (Restriction of Hazardous Substances Directive), have imposed stringent restrictions on Cd- and Pb-based materials in electronic devices. Therefore, research on heavy-metal-free QLEDs, utilizing optically active layers of materials such as indium phosphide (InP) [8–12], copper indium sulfide ($CuInS_2$) [13,14], silicon (Si) [15–25], and lead-free perovskite QDs [26], has experienced a remarkable growth.

Since the groundbreaking work of Holmes and colleagues, such high PLQY values have been utilized as optically active layers in solution-processed Si-QLEDs [15]. Currently, the EL spectral peaks can cover a wide wavelength range from 620 to 850 nm [27,28]. The highest EQE values to date are 8.6% for NIR EL [16], 6.2% for red EL [18], 0.03% for orange EL [21], and 0.03% for white EL spectra [29]. The shortest emission wavelength achieved so far for a Si-QLED is approximately 625 nm, but its EQE is as low as 0.0006% [21]. Improving the EQE of a pale-orange-light emitter (*i.e.*, 600–630 nm range) for achieving superior color rendering is a challenging task. These values are superior to most heavy-metal-free QLEDs [10,13,26], with the exception of the InP-QLEDs that set a new record in late 2019 [8].

A significant limitation of Si-QLEDs is their lack of device stability at high operating voltages, which impairs their luminance output. Maier-Flaig *et al.*, have shed light on the underlying mechanism by investigating the morphological and chemical compositional changes in Si-QLEDs with conventional device architecture during operation [21,30]. Their use of a scanning transmission electron microscope (STEM) revealed the generation of large macroscopic defects under high applied electric fields, which ultimately degrade the multilayer structure and lead to short circuits [30].

In this chapter, it is demonstrated that bright, high EQE, and color-tunable Si-QLEDs can be achieved over an EL peak wavelength range from 590 to 1,000 nm by tailoring their size. The QLEDs consisted of a multilayer sandwiched between a cathode and an anode, with an inverted device architecture in which indium tin oxide (ITO) and aluminum (Al) serve as the cathode and anode, respectively. These QLEDs exhibited good optical performance even at high driving voltages of up to 10 V. A detailed study using the STEM and elemental mapping demonstrated that the morphologies and compositions of the multilayers remained stable in the working QLEDs at high operation voltages, resulting in high luminance values and improved device lifetimes.

4.2 Experimental Methods

Regents and Materials: Triethoxysilane (TES) was purchased from TCI chemicals. The colloidal ink of ZnO, 1-Decene and molybdenum (VI) oxide (99.97% trace metals basis) were purchased from Sigma-Aldrich and used as received. 4,4′-Bis(9*H*-carbazol-9-yl)biphenyl (CBP, 99.9% trace metals basis) was purchased from Luminescence Technology Corp. Electronic grade hydrofluoric acid (49% aqueous solution, Kanto Chemical), HPLC grade toluene, chloroform, ethanol, methanol and Zn powder were purchased from Wako chemical. Water was purified and deionized by Sartorius (arium 611 UV) water purification system.

Preparation of Colloidal SiQD Ink: The SiQDs were synthesized via two-step process reported in previous papers [29,31]. In a typical, TES was employed as a starting precursor. The hydrolysis product, (*i.e.*, $(HSiO_{1.5})_n$), of TES was disproportionated at 1,050 °C for 2 hour in 5%/95% H_2/Ar atmosphere, which produce SiQDs dispersed in SiO_2 matrix. After cooling down to room temperature, 300 mg of the dark-brown solid (*i.e.*, Si/SiO_2 composite) as powder was mechanically ground in an agate mortar with a pestle. The fine powder thus obtained was stirred for ~1 h 30 min in a mixture of ethanol and 48% HF (aq) to liberate SiQDs from the oxide. The surface of resultant SiQDs was terminated with hydrogen atoms. Then, thermal hydrosilylation was carried out in 1-decene at 180 °C to yield decane-capped SiQDs.

Device Fabrication: Si-QLEDs were fabricated on a glass substrate. A thin film of indium tin oxide (ITO) uniformly sputtered on the glass with 150 nm thickness gives a resistivity of 10–14 Ω/sq, which is an optimal value for EL device fabrication. The ITO-coated substrates were first etched using HCl and Zn powder in a narrow strip. Then, the substrates were cleaned by ultrasonic agitation with a nonionic detergent diluted by distilled water (resistivity=18.2 MΩ·cm), followed by washing with acetone, ethanol, and isopropanol at room temperature. After drying, the substrates were exposed to

VUV lamp (Ushio Corp.) for oxidation for 30 min under a pressure of 10^3 Pa air. Next, the colloidal ink of ZnO was spin-coated with a rotation speed of 2,000 rpm for 30 s. After drying the film at 120 ℃ under vacuum, the active layer of the SiQDs was spin-coated with a concentration of 10 mg/mL in toluene with a speed of 1,000 rpm for 30 s. Especially, the SiQDs inks with a concentration of 10, 5, 2.5, 1 mg/mL were used respectively for investigation of SiQDs thickness dependance. Then an organic layer of CBP with a thickness of ~90 nm was thermally evaporated. A 30 nm MoO_3 layer was deposited with a vacuum level of 10^{-5} Pa by thermal evaporation. Finally, the 200 nm of Al top electrode was deposited with mask over the film.

Characterization: Major crystalline planes of the SiQDs were evaluated with X-ray powder diffraction (MiniFlex600, Rigaku, Japan). Optical absorbance spectra were measured by UV–VIS spectrophotometer (JASCO V-650, Japan) with integrated sphere. PL measurement was carried out using a modular double grating Czerny–Turner monochromator and an iHR 320 emission monochromator (1,200 lines/mm of gratings) coupled to a photomultiplier tube (PMT) on a NanoLog Horiba Jovin Yvon spectrofluorometer with 450W xenon arc lamp. The spectral resolution of the system was around 0.3 nm. To avoid scattered excitation lights, cut filters for 495-nm-light was placed in the front of monochrometer-PMT setup. The absolute PLQYs were measured at room temperature using the QY measurement system C9920-02 from Hamamatsu Photonics Co. Ltd with a 150 W xenon lamp coupled to a monochromator for wavelength discrimination, an integrating sphere as a sample chamber, and a multichannel analyzer for signal detection. The film form specimens of SiQD were used for the estimation of PLQYs. Photoelectron yield spectra (PYS) were measured by a model AC-3 (RIKEN KEIKI Co. Ltd., Japan).

Observation and Analysis of Microstructures: Before FIB processing with a Ga^+ ion source (FB-2100, Hitachi, Japan), the substrates were coated with a chromium (Cr)-containing oil-based ink to protect the surface. Then, FIB processing was performed for tungsten (W) protection coating (deposited from $W(CO)_6$ gas) and subsequent preparation of the cross-sectional samples. Each sample was then mounted on a copper (Cu) FIB lift-out grid, and thinned to approximately 100 nm. The prepared cross-sectional ultra-thin samples were analyzed using an analytical transmission electron microscope (TEM; Tecnai Osiris, FEI, USA) operating at 200 kV. The TEM was equipped with an EDS analyzer (Super-X system, FEI, USA) and a high-angle annular dark field (HAADF) scanning transmission electron microscopy (STEM) system with a probe diameter of less than 1 nm.

Calculation of EQE and optical power density: EQE and optical power density were calculated assuming that EL has a Lambertian emission profile. EQE is expressed as the ratio of the number of radiated photons to the number of injected electrons per unit time $I_d(V)/|e|$, where $I_d(V)$ is current through device when applied voltage V, e is the electron charge. EQE is represented by the following equation,

$$\text{EQE}\ (\%) = \frac{N_p(V) \times |e| \times g}{I_d(V)} \times 100 \qquad \text{Eq. } 4-1$$

where $N_p(V)$ is the number of photons collected by photodiode. Geometry factor g expresses when EL profile assumed to be Lambertian the ratio of the luminous flux emitted from LED to the luminous flux measured by photodiode, given by the following equation,

$$g = \frac{a^2 + L^2}{a^2} \qquad \text{Eq. } 4-2$$

where a indicates the radius of aperture of photodiode, L is distance between the light emitting surface of LED and photodiode. Here, the geometry factor was calculated as 4.59. $N_p(V)$ based on the actual observed EL spectrum $EL(\lambda)$ and photodiode current I_p^m is given by the following equation,

$$N_p(V) = \int_{\lambda_i}^{\lambda_f} EL(\lambda) \times \frac{I_p^m}{I_p'(\lambda)} d\lambda \qquad \text{Eq. } 4-3$$

where $I_p'(\lambda)$ is expressed using Planck constant h, the speed of light in vacuum c, EL emission wavelength λ and photodiode responsivity $R(\lambda)$,

$$I_p'(\lambda) = \int_{\lambda_i}^{\lambda_f} EL(\lambda) \times \frac{hc}{\lambda} \times R(\lambda)\, d\lambda \qquad \mathrm{Eq.}\,4-4$$

By calculating $N_p(V)$ for all applied voltages and substituting it into $\mathrm{Eq.}\,4-1$ gives voltage or current density dependent EQE characteristics.

Optical power density was calculated as follows. The emitted power $P(V)$ is calculated by following equation

$$P(V) = \int_{\lambda_i}^{\lambda_f} EL(\lambda) \times \frac{I_p^m}{I_p'(\lambda)} \times \frac{hc}{\lambda}\, d\lambda \qquad \mathrm{Eq.}\,4-5$$

Then optical power density is expressed using $P(V)$

$$\text{Optical power density } (\mathrm{W/cm^2}) = \frac{P(V)}{A} \qquad \mathrm{Eq.}\,4-6$$

where A is the area of the light emitting surface.

4.3 Experimental Results

4.3.1 Impact of QD Layer Thickness on Device Performance in Si-QLEDs

First, the film thickness dependence of the SiQDs layer in the EL spectrum was investigated. Because Maier-flaig *et al*., fabricated conventional Si-QLEDs and reported that the parasitic EL emissions from the neighboring compositional layer appeared when the QD-layer thickness is as thin as 11 nm whereas 31 nm QD layer was thick enough to disappear parasitic emission and improve luminance [21]. Therefore, this section also investigated the device performance dependance on SiQDs thickness as shown in Fig.4-1 and Table.4-1. Fig.4-1(a) and (b) illustrate device current density characteristics. From Fig.4-1(a), the *I-V* characteristics strongly depended on the thickness of the SiQDs. It was found that the device current density increases with decreasing SiQDs film thickness (Fig.4-1(b)). Furthermore, the maximum device current densities were 0.54 mA/cm^2 for 46 nm, 3.3 mA/cm^2 for 21 nm, 6.8 mA/cm^2 for 10 nm and 112 mA/cm^2 for 6 nm, respectively. This trend is mainly due to a decrease in device resistance caused by a decrease in the thickness of SiQDs acting as an insulator. Fig.4-1(c) illustrates optical power density plotted with device current density. The 6 nm device exhibited 27.8 μW/cm^2 at 112 mA/cm^2. The 10 nm device and 21 nm device exhibited similar optical power density of 21.5 μW/cm^2 at 6.8 mA/cm^2 and 22.5 μW/cm^2 at 3.3 mA/cm^2, respectively. Finally, the 46 nm device exhibited only 5.77 μW/cm^2 at 0.54 mA/cm^2. This decrease in optical power density was caused by a decrease in the device current density, which reduces the total amount of radiatively recombined carriers. But that doesn't mean increasing the device current density to gain optical power density. Fig.4-1(d) illustrates EQE plotted with optical power density. The EQE exhibited less than 0.01% in the 6 nm device, while it tended to increase as the thickness of the SiQD layer increased. The maximum EQE exhibited 1.9% for 46 nm device.

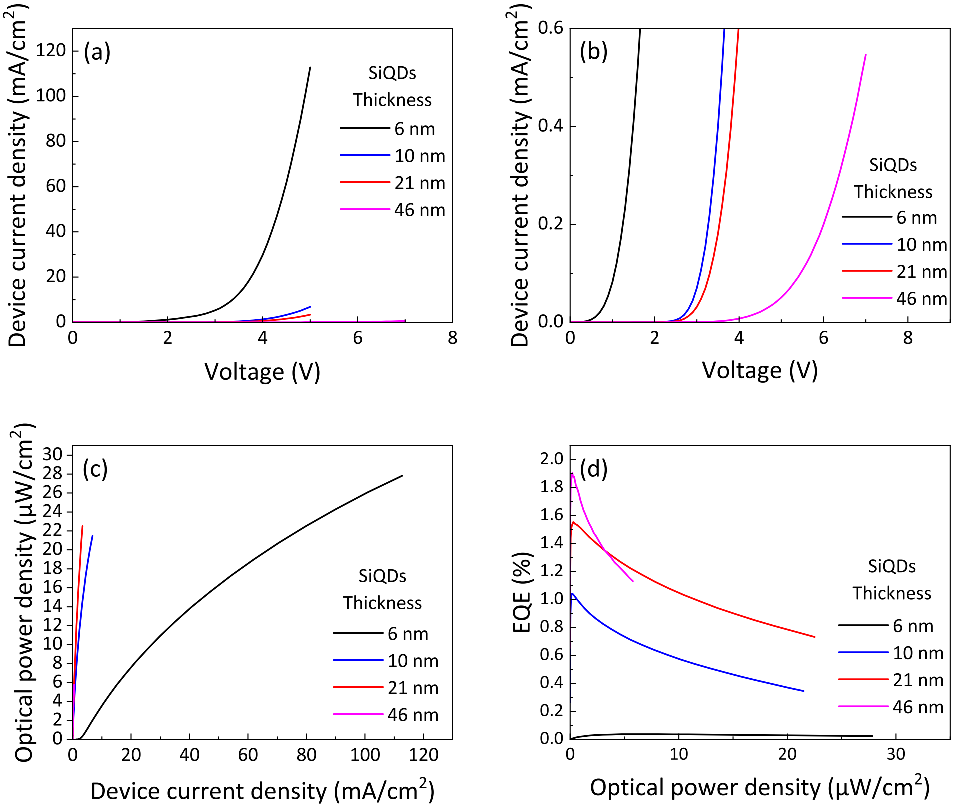

Fig.4-1 The thickness dependence of SiQDs layer on (a, b) device current density, (c) optical power density and (d) EQE performance.

Subsequently, the EL spectra of Si-iQLEDs with varying film thicknesses of SiQDs were investigated and presented in Fig.4-2. The devices were operated at a constant voltage of 5 V, and the corresponding EL peak wavelengths were summarized in Table.4-1. It was observed that the 46 nm and 21 nm devices exhibited no parasitic emission (as seen in Fig.4-2(a) and (b)), while slight parasitic emission from the ZnO layer began to appear in the 10 nm device (Fig.4-2(c)). Additionally, stronger parasitic emission was observed in the 6 nm device (Fig.4-2(d)). The poor EQE for the 6 nm device was attributed to the parasitic emission from the ZnO layer, which resulted in inefficient carrier recombination in the SiQDs layer. However, it was noted that EQE could potentially be improved by suppressing parasitic emission. This was evident in devices that exhibited reduced or completely extinguished parasitic emissions, as shown in Table.4-1.

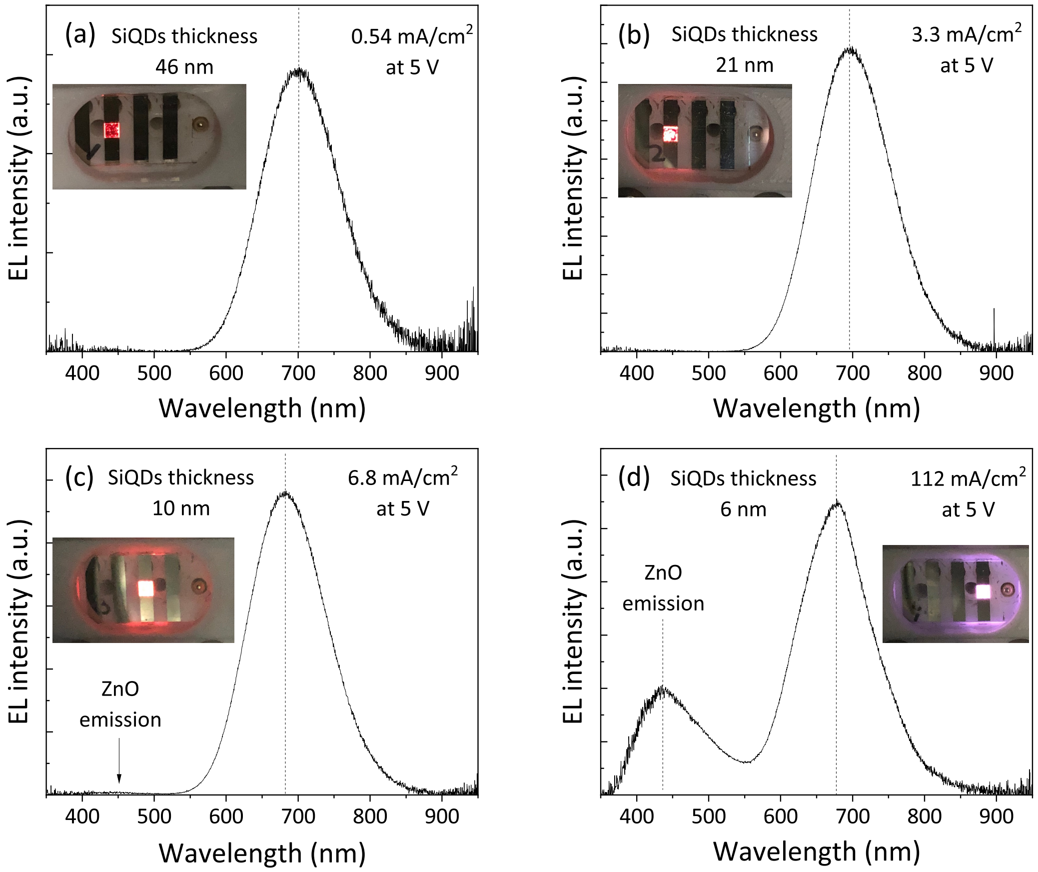

Fig.4-2 The EL spectra with different thickness operated at 5 V.

Table.4-1 A summary of Si-iQLEDs with different SiQDs thickness.

SiQDs thickness (nm)	Maximum device current density (mA/cm^2)	Maximum optical power density (μW/cm^2)	Maximum EQE (%)	EL peak wavelength at 5 V (nm)	Parasitic emission
46	0.54	5.77	1.9	700	no
21	3.3	22.5	1.54	695	no
10	6.8	21.5	1.04	682	slightly
6	112	27.8	0.37	677	largely

4.3.2 Pale-Orange Region Emission from Si-QLEDs

Fig.4-3 illustrates a device architecture and its corresponding flat energy band diagram for a Si-QLED, which displays an EL spectrum peaking at 620 nm. The device was constructed on a 150 nm thick layer of ITO cathode with a resistivity of 10-14 Ω/sq, while the anode was a 150 nm thick Al film deposited in a vacuum. As shown in the diagram, the QLED employed an inverted device architecture with a multilayer structure, as reported in the literature [24,32]. Unlike the conventional device structure, the inverted device structure facilitated electron injection from the ITO electrode and hole injection from the Al electrode. The multilayered structure utilized in this study comprises the following layers, in order: ITO/ZnO/De-SiQD/CBP/MoO_3/Al. The local surface work function of the MoO_3 layer was determined to be -6.2 eV using photoelectron yield spectroscopy (PYS). Previous research has shown that the work function values of MoO_3 films can be affected by the chemical composition of the films [24]. This study employed a 30 nm thick MoO_3 film that was deposited in a vacuum of 10^{-5} Pa, resulting in a local surface work function of -6.2 eV. The ZnO nanocrystal layer acted as the electron injection and transportation layers (EIL/ETL), through which the electrons were transported to the SiQD layer. In contrast, the holes are transported to the SiQD layer through the hole injection and transportation layers (HIL/HTL) of the MoO_3 and CBP layers. As illustrated in the energy diagram, the ZnO nanocrystal layer exhibited a low electron affinity (-4.3 eV), which was close to the value of the ITO, facilitating the injection of electrons and leading to a low turn-on voltage. It is believed that the first ionization potential of the ZnO layer (-7.7 eV) may also have played a role in reducing hole leakage current.

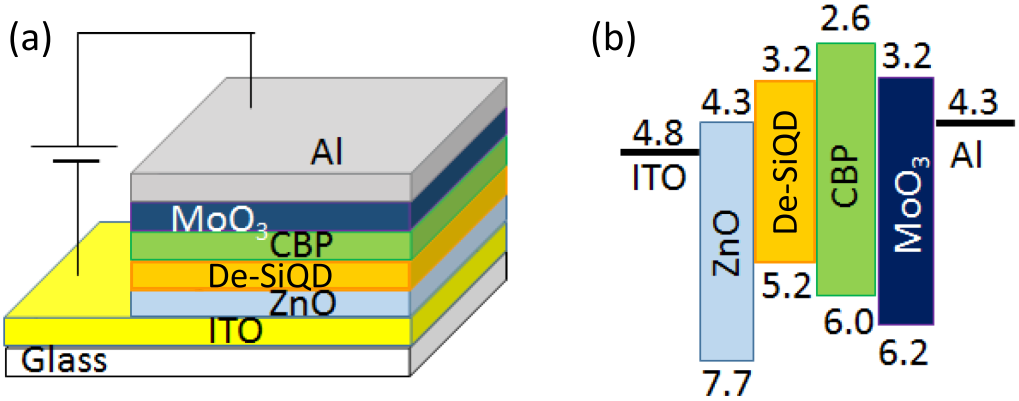

Fig.4-3 (a) Schematic representation and (b) flat energy band diagram of the pale-orange-light-emitting silicon quantum dot light emitting diode (Si-QLED) with an inverted device structure.

Fig.4-4 depicts a standard performance of the Si-iQLED, including the device current-voltage, photocurrent-voltage, luminance-voltage, and electroluminescence (EL) spectrum compared to the photoluminescence (PL) spectrum. Fig.4-4(a) illustrates the current-voltage (*I-V*) characteristics alongside the photodiode *J-V* characteristics. To obtain these results, a calibrated Si photodetector (S1336 8BQ, Hamamatsu Photonics) was employed in conjunction with a Keithley 2425. The quantity of photons collected directly by the photodetector and emitted from the ITO side was observed to increase with current. The turn-on voltage, defined as the minimum applied bias at which the iQLED starts to emit light, was estimated from the photodiode *J-V* characteristics. The calculated turn-on voltage was found to be 2.8 V, a value comparable to that of a normal Si-iQLED emitting light peaking at 625 nm [21]. The composition of the device, rather than the QD size, has been reported to influence the turn-on voltage. Therefore, the low turn-on voltage observed in this study confirms the presence of a small barrier height for charge injection into the photoactive layer from the electrodes. Fig.4-4(b) depicts the typical luminance curves as a function of the applied voltage. The luminance reaches a high value of 17.6 cd/m^2 at 5 V. The EL spectrum was characterized by a peak at 620 nm, which exhibited a red shift of 3 nm in comparison to the corresponding PL spectrum, as shown in Fig.4-4(c). The EL spectrum exhibited a narrow fwhm of approximately 95 nm (~283 meV), as shown in Fig.4-

4(c), which is slightly narrower than the corresponding PL spectrum. The negligible spectral shift of approximately 3 nm and the fwhm value smaller than the PL linewidth suggest effective suppression of the quantum-confined Stark effect, although further research is required to clarify the mechanism. The inset of Fig.4-4(c) displays a photograph of the QLED operating at 5 V, thereby providing evidence that the emitted light was bright and vivid enough to be perceptible to the naked eye, even in a room with ample illumination. However, the color purity of the pale orange light emitted from the iQLED was lower than anticipated, despite the narrow linewidth of the spectrum with no emission tail. The reduced color purity may be attributed to the appearance of an additional EL spectrum peaking around 420 nm, which is not present in the PL spectrum. The EL spectra displayed a voltage dependence, as illustrated in Fig.4-4(d). At a bias voltage of 4 V, the spectral profile exhibited an EL peak at 620 nm, with a minor luminance contribution (λ_{EL}= ~420 nm) emanating from one of the layers in the multilayer structure, resulting in a reduced purity of the pale-orange color. The presence of the parasitic emission at 420 nm may potentially arise from the neighboring compositional layer of ZnO, with the intensity of this emission increasing as the voltage is raised. Simultaneously, the EL intensity stemming from the De-SiQD layers also intensifies under increasing bias voltage. There exist two possible reasons to account for the emergence of the parasitic emission. Firstly, in accordance with the flat energy band diagram, there is a discernable energy gap of 0.9 eV between the ZnO and De-SiQD layers. As a result of the energy barrier impeding carrier transport, certain electrons injected from the ITO electrode were retained within the conduction minimum of ZnO, thereby enabling recombination for blue EL. Another plausible explanation is that the occurrence of this undesirable blue emission may be attributed to inadequate thickness of De-SiQDs [29]. Further elevation of voltage is required to explore the fundamental physics underlying the parasitic emission. In Fig.4-4(d), the inverted device structure exhibits two advantages. Firstly, there is no shift in the EL peak as the operating voltage is increased, indicating that the emission at 620 nm originates solely from the QD layer even at high voltages. This contrasts with conventional semiconductor QLEDs that include Si, which are known to exhibit a shift towards the blue in the EL peak [23,33,34]. Secondly, the spectral shape of the EL emission is independent of the driving voltage. It should be emphasized that the presence of the parasitic emission spectrum does not affect the emission spectral characteristics, such as the EL peak position and shape. Hence, the observed stability of the EL characteristics might be attributed to an optimal conductivity in the band alignment of the HTL, which impedes the buildup of the band-filling. Furthermore, the use of metal oxide layers (such as ZnO and MoO_3) for the EIL/ETL and the HTL/HIL provides inherent robustness and protection of the interlayers against oxidation, thereby contributing to the EL stability under increasing operation voltage.

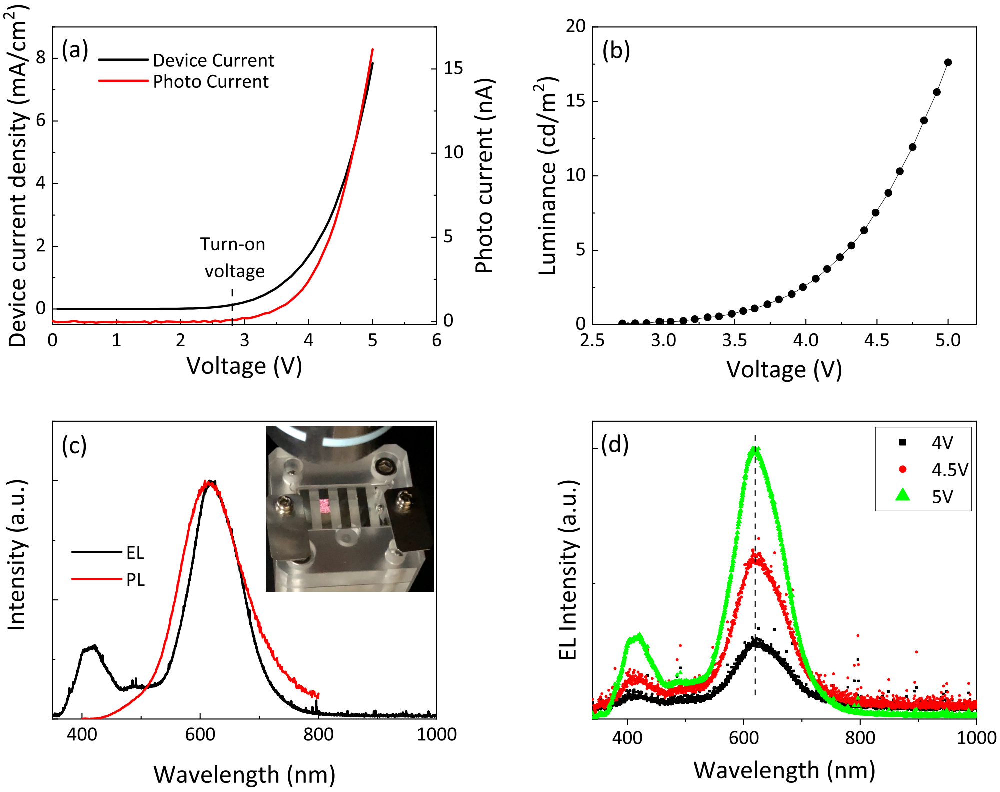

Fig.4-4 (a) Device *I-V* characteristics (black line) and photodiode *I-V* characteristics (red line), (b) luminance-voltage characteristics, and (c) an EL spectrum at the operation voltage of 5 V (PL spectrum of the corresponding De-SiQD dispersed in chloroform), (d) EL spectra at different bias voltage. A photograph demonstrates a representative pale-orange emitting QLED.

The EQE was determined by measuring the photocurrent as the EL output using a photodetector and plotting the results as a function of the injected current density in Fig.4-5. The peak EQE was found to be 0.036%, which is presently the highest reported value for a Si-QLED operating in the pale-orange emission range. The favorable band alignment of the inverted device structure utilized in this study may lead to an enhancement of the EQE. A reduction in the degree of the charged QDs, which results in carrier loss due to Auger recombination, could also contribute to the improvement of the EQE [35].

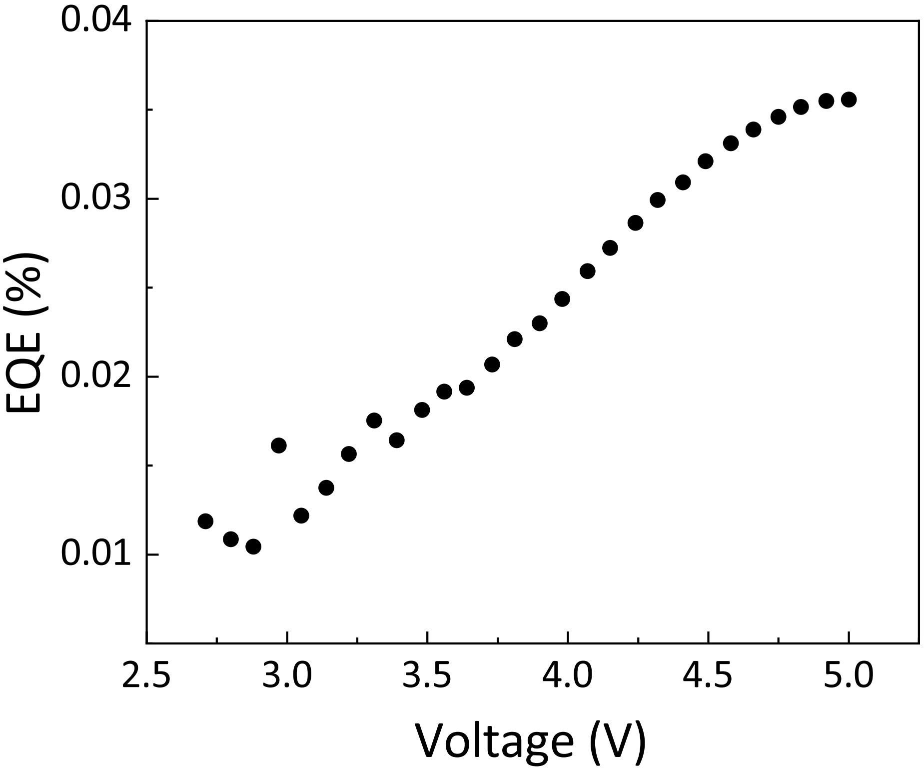

Fig.4-5 External quantum efficiency (EQE) versus device current density.

4.3.3 Control of EL Peak Wavelength through the 590-755 nm Range

Fig.4-6 illustrates the device architecture and a representative cross-sectional transmission electron microscopic (TEM) image with energy-dispersive X-ray spectroscopy (EDS) maps for a pristine device of Si-QLEDs fabricated in this study. The Si-QLED featured an inverted device architecture, comprising a hybrid organic-inorganic multilayer stack (Fig.4-6(a)). Unlike the conventional structure, electrons and holes are injected from ITO and Al electrode sides, respectively. The device was fabricated on soda-lime glass coated with a 150-nm-thick ITO film (resistivity = 10-14 Ω/sq). The cross-sectional TEM image with EDS mapping indicated that the individual layers were distinct and exhibited smooth interfaces between the stacked layers (Fig.4-6(b)). A comprehensive cross-sectional analysis of the multilayer structure was conducted over a region larger than 1 mm to ensure precision. No significant morphological or compositional changes were observed (as shown in Fig.4-7). The active emissive layer was a 50-nm-thick ZnO film, which functioned as the electron injection and transportation layers (EIL/ETL), spin-coated in air on the top of the structured ITO surface, followed by a thin layer of SiQDs (~15 nm). Both thin layers of 4,4′-Bis(9*H*-carbazol-9-yl)biphenyl (CBP, ~100 nm) and molybdenum (VI) oxide (MoO_3, ~15 nm) functioned as hole injection and transportation layers (HIL/HTL) and were deposited by thermal evaporation under vacuum. Finally, the top Al electrode (~220 nm) was fabricated by vacuum deposition under 5×10^{-5} Pa. The layer sequence corresponded to the stack shown schematically in Panel (a), except for a ~32 nm-thick weak material contrast, which was evident between the CBP and the MoO_3 layers, as previously reported elsewhere [35].

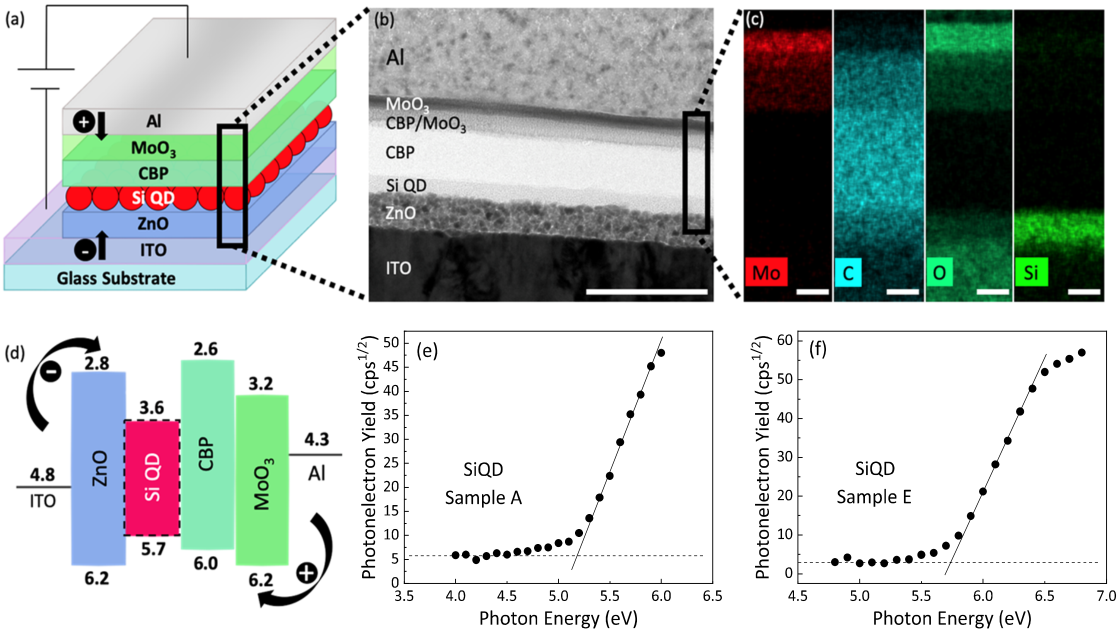

Fig.4-6 (a) A schematic representation, (b) a cross-sectional TEM image with (c) EDS maps of the area indicated in the image, and (d) the energy band diagram in the unbiased conditions. Scale bars are 200 nm for the image (b) and 20 nm for the image (c). In the illustration (d), the energy range is shown with dotted lines because of QD-size dependent of the magnitude of valence band. PYS spectra of (e) samples A and (f) E.

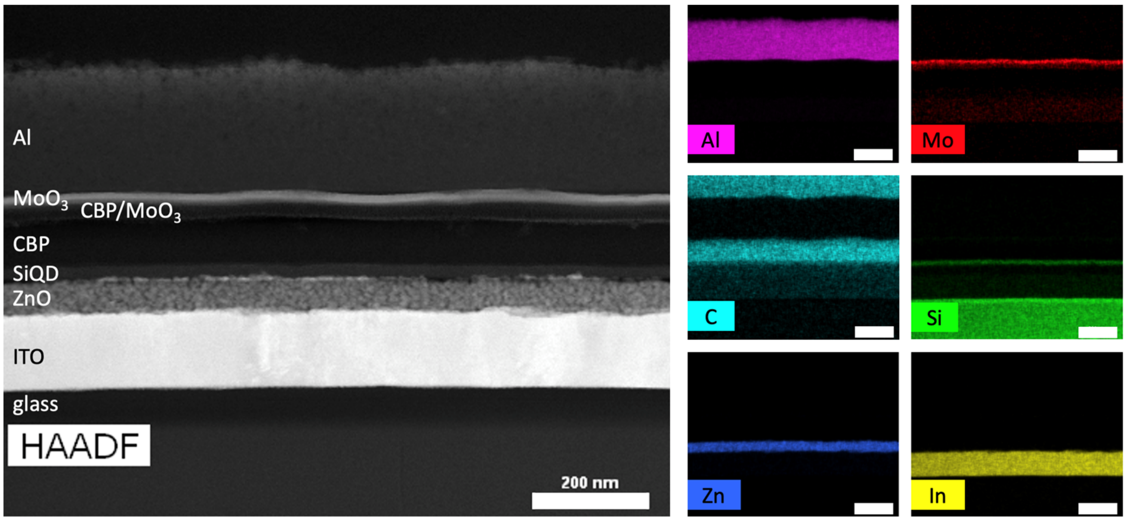

Fig.4-7 A typical cross-sectional HAADF-STEM image of a pristine Si-QLED (left) and EDS maps (right). The scale bars are 200 nm for all images.

The chemical composition analysis depicted in Fig.4-6(c) evinces the coalescence of Mo and oxygen ions with a segment of the underlying CBP stratum, indicating that the translocation and dispersion of MoO_3 clusters during thermal deposition led to the intermingling of MoO_3 and CBP. This supposition is buttressed by the findings of White *et al.*, who expounded that an intensely heated MoO_3 cluster, utilized for thermal deposition, possesses sufficient kinetic energy to infiltrate and diffuse within the organic stratum [36]. The EDS map representing oxygen corroborated the lack of signals within the CBP layer. The formation of a well-defined boundary between the CBP and SiQD strata was evident, and the component QDs exhibited slight oxidation, as substantiated by attenuated total reflection Fourier transform infrared spectroscopy (ATR-FTIR; data not presented). To elucidate the impact of carbon content in the zinc oxide layer, additional data is necessary since the ZnO ink was purchased.

Fig.4-6(d) illustrates a flat energy band diagram based on valence band values obtained through photoelectron yield spectroscopy (PYS). To carry out PYS measurements, each material was deposited onto an ITO-coated glass substrate to prevent electrostatic charge, employing a method comparable to that utilized in the device fabrication process. The magnitudes of the lowest unoccupied molecular orbital (LUMO) were estimated via the optical band gap values derived from absorption spectra. The PYS spectra acquired for the samples with the largest QDs (for Device A) and the smallest QDs (for Device E) manifest that the valence band magnitude is contingent on the QD size, and the value fluctuates between 5.2 eV and 5.7 eV, as illustrated in Fig.4-6(e) and (f).

The valence band magnitude of the ZnO film was determined to be approximately 6.2 eV (as depicted in Fig.4-8), which serves as a substantial potential energy barrier for holes traversing from the QD to the neighboring ETL. In prior studies, experimental values for the valence band of the CBP and MoO_3 layers have been reported [24]. A relatively elevated energy barrier of ~2 eV was identified for electron injection into the conduction-band energy level of ZnO from the ITO electrode. This energy barrier obstructs electron injection at low applied voltage, potentially resulting in a high turn-on voltage for device operation. Nevertheless, the potential barrier for hole injection from the Al electrode was also approximately 2 eV, promoting charge balance for electrons and holes from the electrodes and facilitating efficient recombination at the active layer.

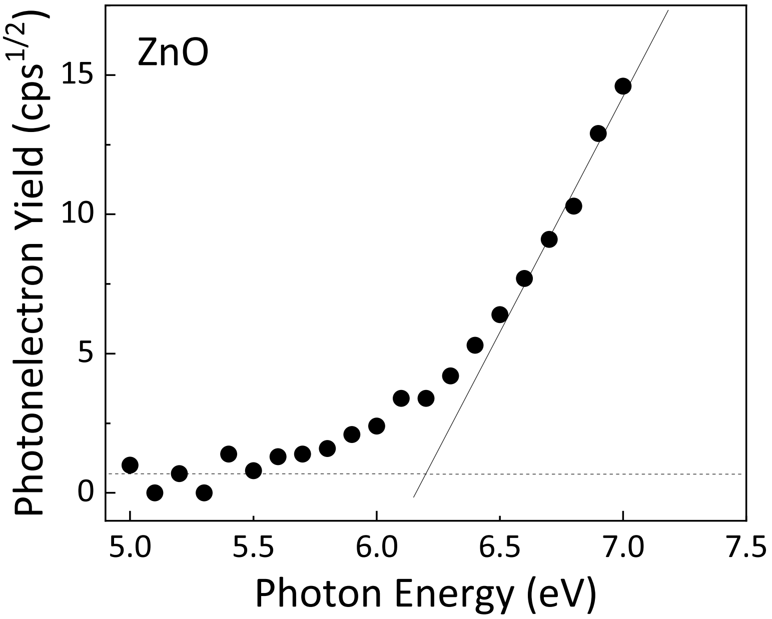

Fig.4-8 Photoelectron yield spectrum (PYS) of a film form of ZnO spin-coated on ITO-coated glass substrates. Each line was determined as a pair consisting of the base and the rise to calculate the onset. The photon energy values show the negative of the experimental valence band energy level.

In this study, five classes of Si-QLEDs (Devices A-E) were prepared, each with a distinct emission color, utilizing SiQDs. The details of the devices are summarized in Table.4-2. Fig.4-9 presents a summary of the QLED device performance, including the current-voltage characteristics, luminance-voltage characteristics, photographs of operational QLEDs, and typical EL spectra compared to the corresponding PL spectra of the QDs. The *I-V* characteristics were investigated using a source meter (Keithley 2425) and a calibrated Si photodetector (Hamamatsu Photonics S1336 8BQ) for Devices A–

E. Panels (a)-(e) reveal that the number of photons emitted from the ITO side directly collected by the photodetector increases with the current. All of the *I-V* characteristics were plotted on a double-logarithmic scale. The devices exhibited the power law behavior (*i.e.*, $J \propto V^n$). The values of exponent "*n*" were obtained from the slopes of the straight lines for each *I-V* characteristic. In the low applied voltage region, the conduction can be described by Ohmic conductance behavior ($n \approx 1$), while charge-trapped space-charge-limited conduction appears in the higher applied voltage region (>5 V). These results are consistent with common *I-V* characteristics for semiconductors [37]. The values of the turn-on voltage, which represent the minimum applied bias at which light emission begins, were determined from the luminance-voltage characteristics. Specifically, the estimated turn-on voltages were 6.0 V for Device A, 3.4 V for Device B, 4.0 V for Device C, 5.8 V for Device D, and 3.5 V for Device E. The observed high turn-on voltages for Devices A and D may be attributed to contamination of the SiQDs ink, as supported by the lower turn-on voltage of a device fabricated with purified SiQDs (as shown in Fig.4-10). Further investigation is necessary to fully comprehend the mechanism by which contamination affects the surface morphology and electronic energy levels of the SiQDs, resulting in the observed increase in turn-on voltage. Specifically, in Fig.4-10, a device with a similar structure as Device D but with purified SiQDs in the active layer exhibited a relatively low turn-on voltage of approximately 4 V. In contrast, Device D, whose active layer comprised Sample D that had been purified one week prior, showed a high turn-on voltage of approximately 6 V. This difference in turn-on voltage is likely attributed to the contamination of the SiQDs ink, which can adversely affect the film quality, hampering efficient carrier injection and leading to a high turn-on voltage in Device D.

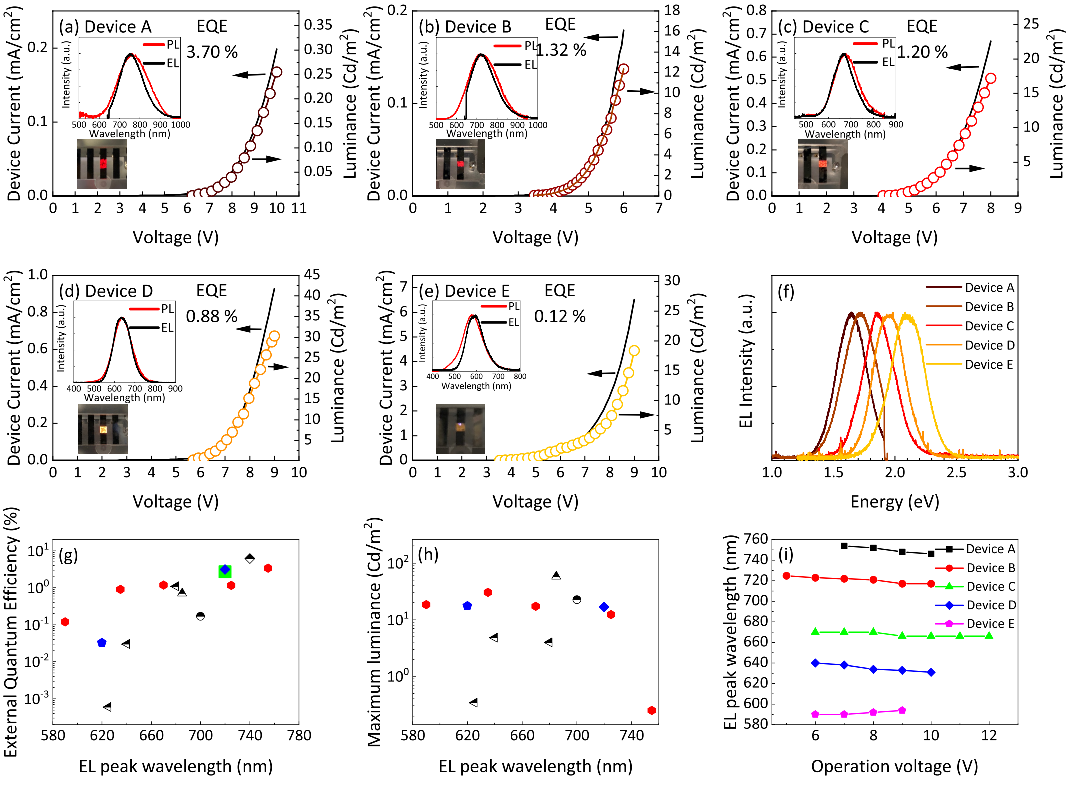

Fig.4-9 (a-e) Device current-voltage and luminance-voltage characteristics for each device. Inset figure shows comparison of EL and PL spectra and photograph demonstrates a representative EL emission during operation. (f) EL spectra of Device A-E during operating at 8 V. A photograph demonstrates a representative EL emission during operation. (g,h) EL peak wavelength versus (g) maximum EQE and (h) maximum luminance values with this study and the literature reports of Si-QLEDs: ⬣ This study; ◆ Ghosh *et al.*[24]; ⬟ Yamada *et al.*[17]; ⬘ Liu *et al.*[18]; ▲ Puzzo *et al.*[19]; ◓ Mastronardi *et al.*[20]; ◀ Maier-Flaig *et al.*[21]; 🟩 Yao *et al.*[22] (i) EL peak positions for each device as a function of applying voltage.

Table.4-2 A summary of PL properties for QD samples with different average size.

Sample	QD diameter (nm)	PL peak energy (eV)	PL peak wavelength (nm)	FWHM (meV)	FWHM (nm)	PLQY (%)
A	2.7	1.623	764	368	170	37
B	2.2	1.710	725	395	169	26
C	1.9	1.837	675	339	120	23
D	1.7	1.937	640	324	106	10
E	1.3	2.137	580	387	107	5

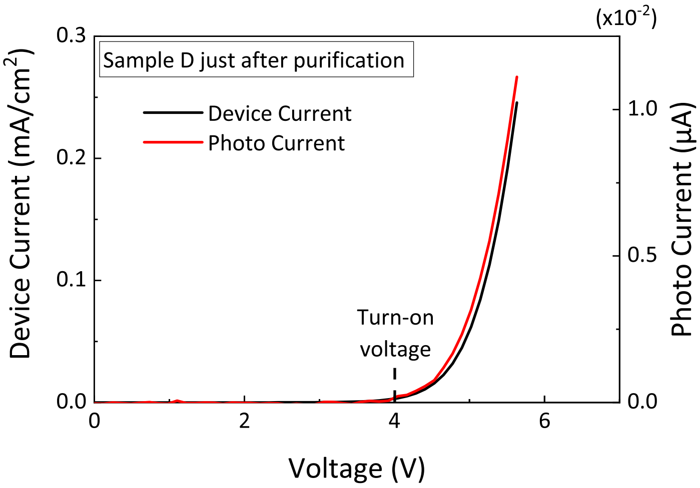

Fig.4-10 The *I-V* characteristic of Si-QLED whose active layer consisted of Sample D just after purification.

As anticipated from the substantial potential barrier between ITO and ZnO, the recorded values are comparatively greater than those achieved by conventional Si-QLEDs, which exhibit turn-on voltages of approximately 3 V or below [16,18,21]. This line of reasoning is consistent with the proposition by Maier-Flaig *et al.*, who postulated that the device structure of QLEDs has a greater impact on the turn-on voltage than the size of the QDs [21]. Upon activation of the devices, the luminance improved substantially with distinct rates observed among the devices. As displayed in Table.4-3, the maximum luminance values were 0.25 cd/m^2 at 10 V for Device A, 12.34 cd/m^2 at 6 V for Device B, 17.2 cd/m^2 at 8 V for Device C, 30.28 cd/m^2 at 9 V for Device D, and 18.4 cd/m^2 at 9 V for Device E. Notably, extraneous EL emissions from neighboring compositional layers or surface states of QDs were absent, even at voltages exceeding 10 V.

Table.4-3 A summary of EL performances for the five Si-QLEDs.

Device	SiQDs	EL peak energy (eV)	EL peak wavelength (nm)	FWHM (meV)	FWHM (nm)	Luminance (cd/m^2)	Turn-on voltage (V)	EQE (%)
A	Sample A	1.642	755	289	132	0.25	6.0	3.70
B	Sample B	1.717	722	327	147	12.34	3.4	1.32
C	Sample C	1.850	670	305	111	17.2	4.0	1.20
D	Sample D	1.952	635	309	104	30.28	5.8	0.88
E	Sample E	2.101	590	335	94.4	18.4	3.5	0.12

As anticipated, the EL emissions were strong enough to be distinguished by the naked eye even in ambient lighting conditions. The EL peak positions were observed to be at 755 nm for Device A, 722 nm for Device B, 670 nm for Device C, 635 nm for Device D, and 590 nm for Device E, indicating a size-dependent wavelength tunability of the EL spectral peaks (as depicted in Fig.4-9(f)).

In this study, the stability of the EL spectra of five classes of Si-QLEDs (Devices A-E) with different emission colors using SiQDs as summarized in Table.4-2 was investigated. Fig.4-11 illustrates the changes in the peak position of the EL spectra with increasing operation voltage for Devices A-E. As the applied voltage increased, the EL spectra were monitored to assess their stabilities.

The results indicated that the stability of the EL spectra was superior for the inverted device architecture of the Si-QLEDs. For example, Device A had a turn-on voltage of 6 V, and the EL peak position did not shift even at 9 V while a 14 nm blue shift was observed at 10 V. Similarly, Device B had a turn-on voltage of 3.4 V, with no shift in the spectral peak position of the EL spectra between 4 and 8 V. However, a 10 nm shift of the EL peak to the blue was observed at 9 and 10 V. Device C had a turn-on voltage of 4 V, with no difference in the spectral position of the EL spectra between 4 V and

12 V. Device D had a turn-on voltage of 5.8 V, with an EL spectrum shift to blue by 4 nm at 10 V while no change between 6 and 9 V. Device E had a turn-on voltage of 4.5 V, with no difference in the spectral peak position between 5 and 9 V.

In contrast, previous reports have shown that the EL peaks of conventional structures for Si-QLEDs shift to the blue by a much greater degree (~50 nm) [24]. This comparative study underscores the superiority of the inverted device architecture in enabling Si-QLEDs to operate even at high voltages, resulting in robust stability and strong luminance.

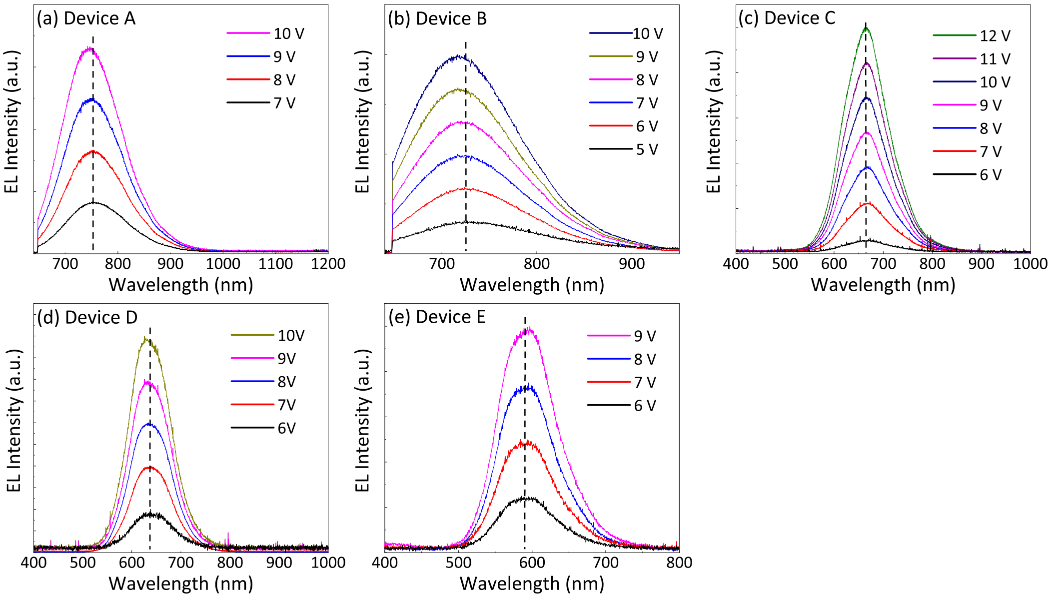

Fig.4-11 EL spectra measured at room temperature in the air for (a) the Device A, (b) the Device B, (c) the Device C, (d) the Device D and (e) the Device E. Applied voltage varies between 5 and 12 V for operation of the Devices A-E.

In comparison to the PL spectra of the corresponding QDs, a subtle blue shift was observed in the EL peaks. Specifically, the blue shift was 9 nm for Device A, 3 nm for Device B, 5 nm for Device C, and 5 nm for Device D. Conversely, Device E exhibited a 10 nm red shift. The spectral shape remained largely unchanged between the PL and EL spectra, indicating that the EL emissions originated from the recombination of electrons and holes across the fundamental energy-gaps in SiQDs. Notably, the

EL spectral linewidths were slightly narrower than those in the PL spectra (as seen in Table.4-2 and Table.4-3), suggesting that the quantum-confined Stark effect was suppressed [39]. Fig.4-9(g) compares the peak values of the EQE to previous records reported in the literature for different visible-EL peak wavelengths. The blue diamond, blue pentagon and green square indicate the EQE value of Si-QLEDs with an inverted device structure in other studies [17,22,24]. Fig.4-12 illustrates the EL spectra of the Devices A-E as a function of applied voltage. EL intensities at each applied voltage are normalized with respect to the initial EL intensity for each device. No change in the shape of EL spectra was observed with increasing voltages for all the devices.

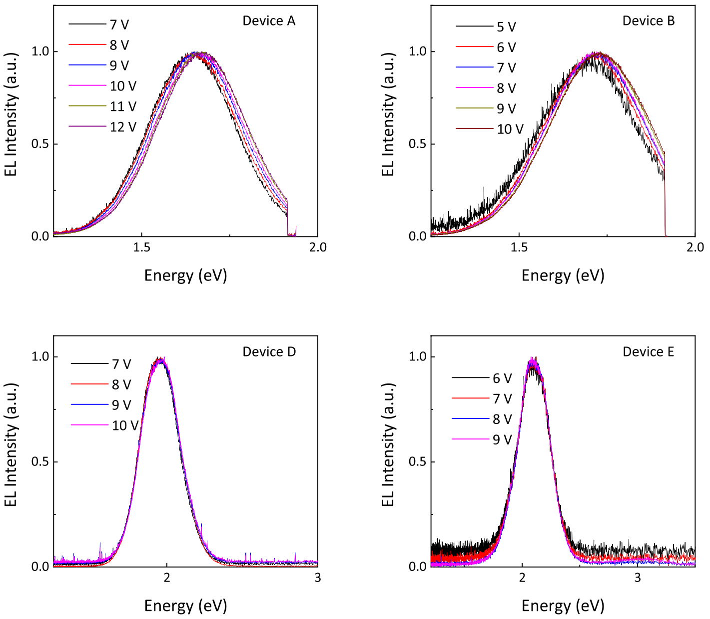

Fig.4-12 Normalized EL intensity as a function of operation voltage for the Devices A-E.

The decreasing trend of EQE with shorter EL emission wavelengths is a typical characteristic of Si-QLEDs due to the lower PLQYs of smaller QDs. Notably, the PLQY values of the samples in this study are comparable to those reported elsewhere [40], yet the EQE values recorded herein exceed those of prior Si-QLEDs. Moreover, other research on Si-QLEDs with inverted device structure (Fig.4-9(g), blue diamond, blue pentagon and green square) also manifested superior EQE values over the conventional structure. These results suggest that carrier recombination is more efficient in the inverted device architecture compared to previous device structures, leading to higher EQE values. Moreover, the EL peak is broadened and extended by 590 nm into the yellow range of the visible spectrum rather than the orange or red regions. It is noteworthy that Si-QLEDs have suffered from poor stability at high applied voltages, which has limited the magnitude of luminance. Fig.4-9(h) illustrates a comparison of the maximum luminance and EL peak wavelength between the current study and previous literature. The results reveal that the luminance displayed higher luminous intensity than the literature in the range of 590-670 nm. Conversely, poor luminance was observed for the 755 nm device. This is primarily attributed to the fact that the International Commission on Illumination (CIE) optical radiation efficiency function, which is used to convert radiant energy to luminance, has almost no visible sensitivity curve at EL peak wavelengths beyond 700 nm.

Fig.4-9(i) summarizes the change in the EL peak wavelengths as a function of increasing device operation voltage for each QLED. It is well-established that the EL peaks of Si-QLEDs tend to blue shift as the driving voltage increases, with a magnitude of ~50 nm at 6.5 V [18]. However, the positions of the EL peaks do not shift even at an applied voltage above 6 V, indicating that the driving voltage does not influence the EL peak position for devices in this study. Despite the superior EL performances reported in many papers, which may be attributed to the use of inverted device structures [5,6,24,41], there is a dearth of research on the underlying mechanism in the literature. This study endeavors to provide a plausible mechanism for the improvement by comparing morphological and compositional changes between a functioning Si-QLED and a Si-QLED that has exceeded its device lifetime. For the sake of reliability in the comparison, 1 mg of De-SiQDs was prepared in a single batch for hydrosilylation and then purified using GPC, with the sample then divided into two portions to produce the two QLEDs. The functioning Si-QLED was prepared by operating it for 10 min at 6 V, while the Si-QLED beyond its service life was prepared by operating it for 10 min at 20 V.

Shown in Fig.4-13 is a representative cross-sectional TEM image of a functioning Si-QLED. Despite being subjected to a high applied voltage of up to 6 V, the device's multilayer structure is well-maintained, as evidenced by the elemental maps showing smooth interfaces between each layer. Notably, the SiQDs in the optically active layer remained intact and did not diffuse or migrate towards the adjacent compositional layers, as demonstrated in the silicon EDS map. The SiQDs had a visible diameter of approximately 2.0 nm and were uniformly dispersed without any aggregation, as shown in Fig.4-14. The CBP layer appeared to be dominated by carbon, with a uniform and densely-contrasted image suggesting the absence of defects such as voids or cracks. The QD layer, on the other hand, exhibited a very weak carbon contrast, likely due to covalent binding with the Si in the decane monolayers. Oxygen was observed in the ITO/glass, ZnO, MoO_3, SiQD, and MoO_3/CBP layers, but not in the CBP layer, indicating that applying voltage to the electrodes did not induce further migration of MoO_3 in the CBP layer. Taken together, the layer sequence appeared to correspond well to the multilayers of the pristine Si-QLED.

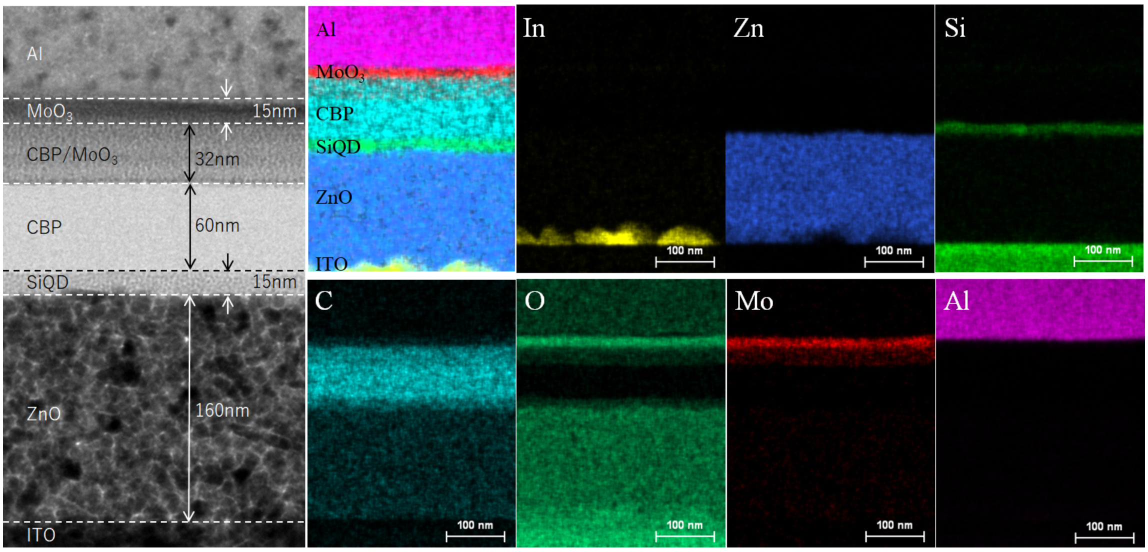

Fig.4-13 Cross-sectional TEM image and EDS maps of the working Si-QLED operated at 6V for 10 min. The TEM view (left) shows the well-defined structure of a multilayer. In the EDS maps (right), the individual layers can be clearly distinguished based on their elemental composition.

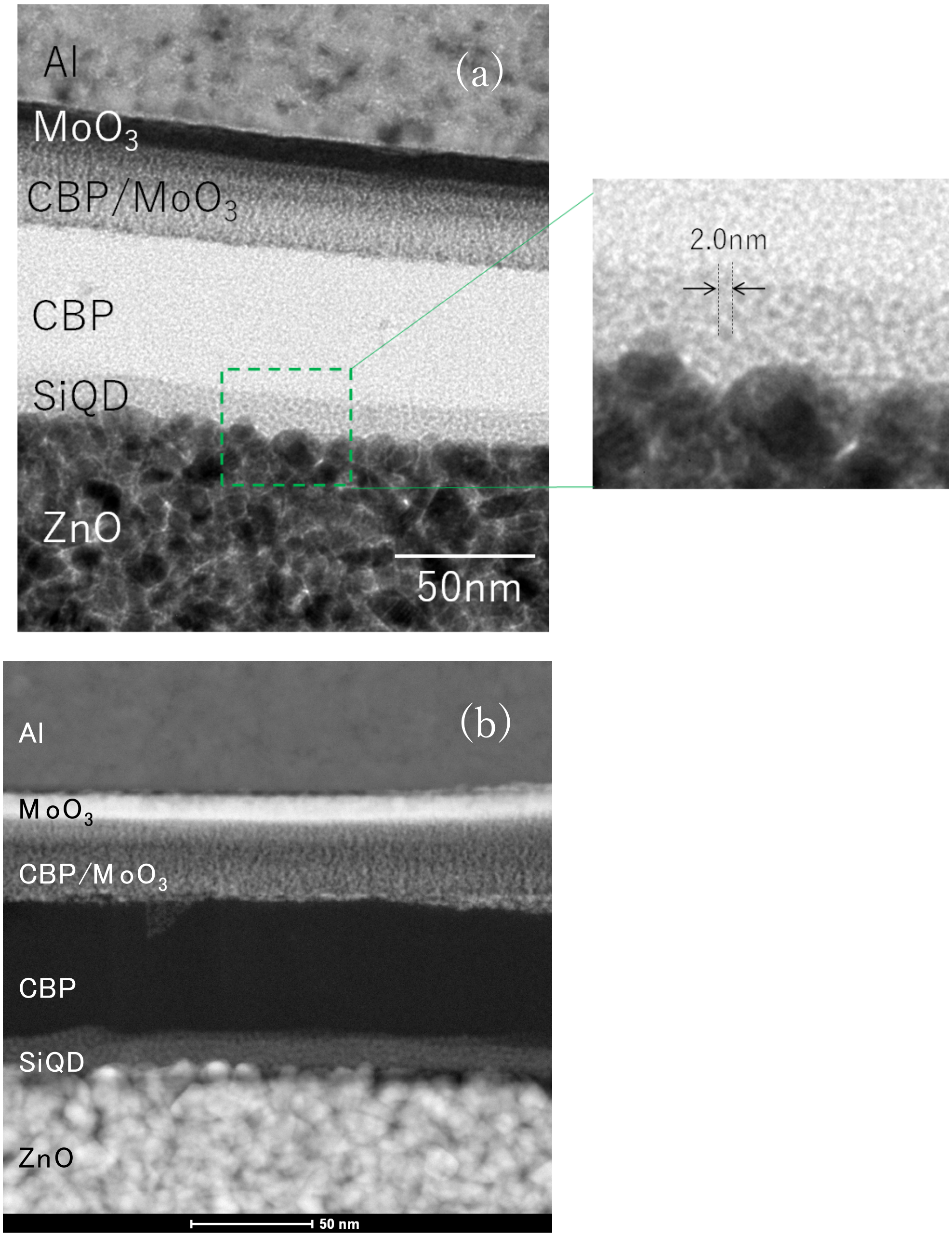

Fig.4-14 Cross-sectional (a) TEM and (b) HAADF-STEM images of a working Si-QLED operated for 10 min at 6V. (a) Both images show the well-defined layer structures as well as individual SiQDs in the SiQD layers. In the Panel (a), the enlarged image (right) of the area indicated with slashed rectangle in the TEM image (left) shows that SiQDs are clearly distinguished by contrast of a gray scale. The round shaped dots correspond to SiQDs. The optically active layer consists of 7~8 monolayers of SiQDs.

Considering the minimal decay of the EL for a duration of 10 minutes at 6 V (refer to Fig.4-15), the well-defined multilayer structure, as evidenced by TEM, HAADF-STEM, and STEM-EDS analyses, can be deemed rational. Nevertheless, a meticulous examination of a wide range (~12 μm) with TEM revealed a few small macroscopic defects that might have formed during the operation of the device (see Fig.4-16). The elemental mapping presented in Fig.4-17 provides further evidence that the defects were voids rather than a segregated material, with sizes ranging from 50–100 nm. The observations suggest that the defects arise at the interface between the CBP and intermixing MoO_3/CBP layers, and they propagate towards the lower-lying HTL (*i.e.*, CBP), leading to the formation of triangle-shaped voids. As anticipated, QLEDs that have exceeded their lifetime displayed a greater number of voids.

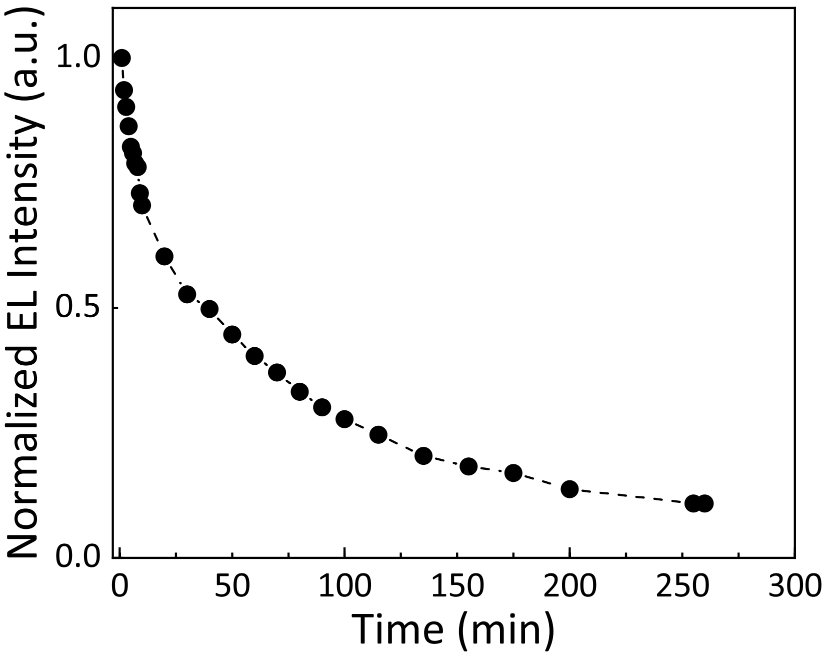

Fig.4-15 Decreasing behavior of EL intensity of orange-light emitting Si-QLED with increasing operation time at 6 V in ambient air. All the values of EL intensity at each time were normalized to the value recorded just after applying a power source voltage.

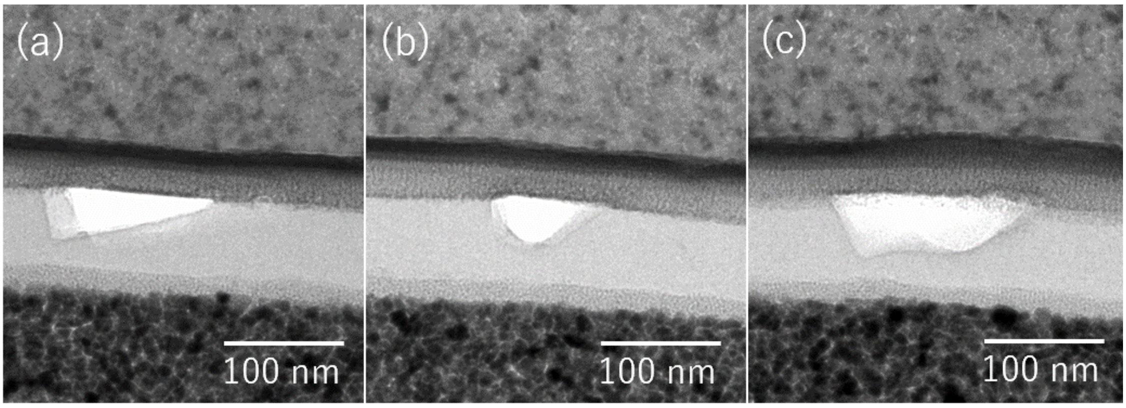

Fig.4-16 Typical shapes of voids observed in a cross-sectional TEM image of Si-QLED driven for 10 min at 6 V.

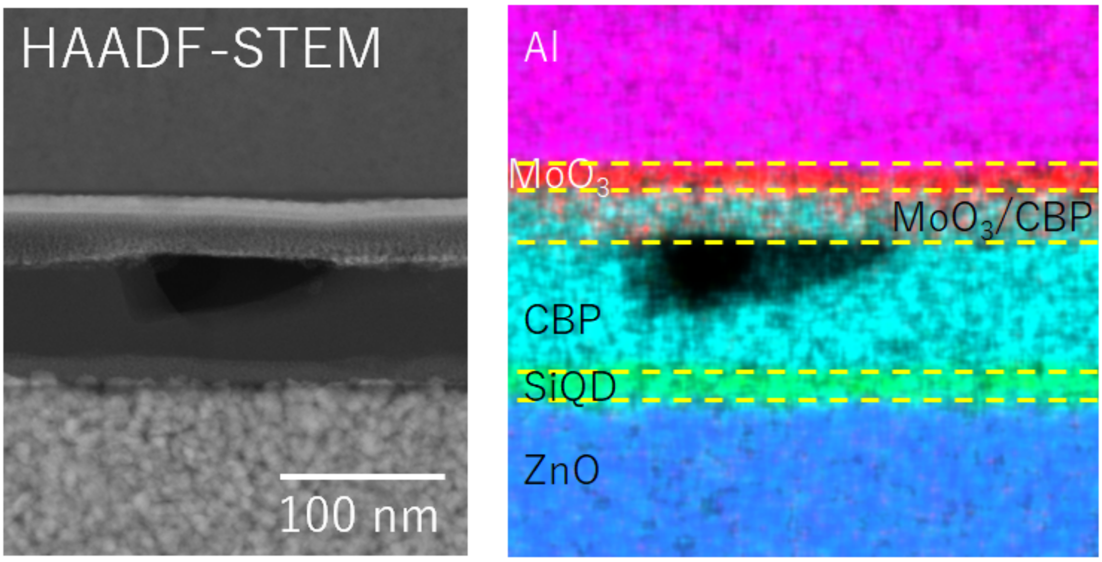

Fig.4-17 HAADF-STEM and EDS mapping images of the area shown in Fig.4-16(a).

To make observations, another Si-QLED with a comparable EL performance was prepared. The device exhibited noteworthy EL performance even under extreme operational conditions, such as a high operation voltage of 13 V. However, the duration of the operation must be limited to 10 minutes or less to maintain stable performance. This harsh electrical excitation resulted in a high density of injected carriers and an elevated electrical field. Photocurrent measurements combined with spectroscopic observations revealed that the orange-EL emission faded away after 10 minutes of operation.

Fig.4-18 depicts a cross-sectional view of the Si-QLED that has surpassed its lifetime. Notably, the CBP layers exhibited defective structures (Panel (a), dashed and open rectangles). Panels (b) and (c) present the TEM and STEM-EDS maps of the region. It is evident that voids, which initially appeared in the CBP layer under a lower magnitude of the operation voltage, propagated downwards and completely penetrated the underlying 200-nm-wide CBP layer. Interestingly, the growing voids ceased at the interface between the CBP and the SiQD layers, which is consistent with other voids (see Fig.4-19, Fig.4-20). As the observation area is limited, the lower-lying SiQD layer remains unaffected by the growing voids. Despite the entire CBP layer being damaged by the growing void, a smooth interface between the CBP and SiQD layers was retained.

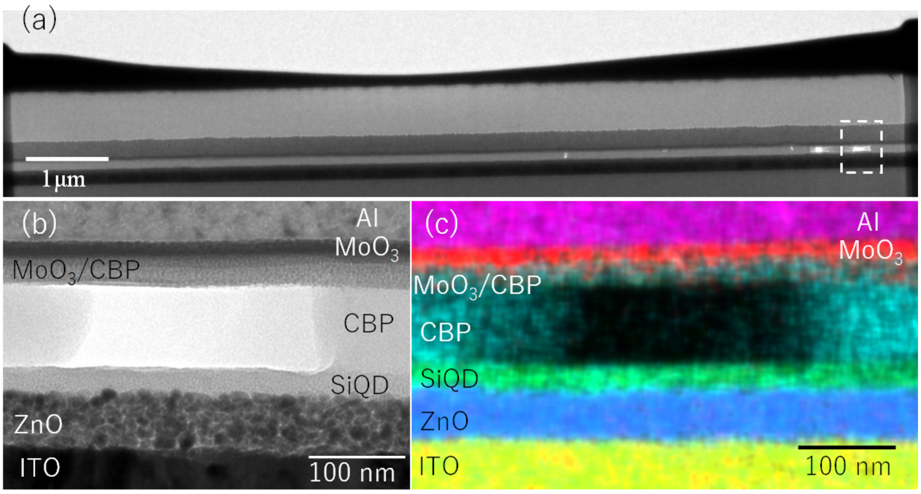

Fig.4-18 Morphological and compositional changes of Si-QLED operated 20V. (a) TEM overview cross-sectional image of the QLED. (b) Cross-section HAADF-STEM image of the area indicated in topmost image. (c) EDS mapping image of the area shown in the Panel (b).

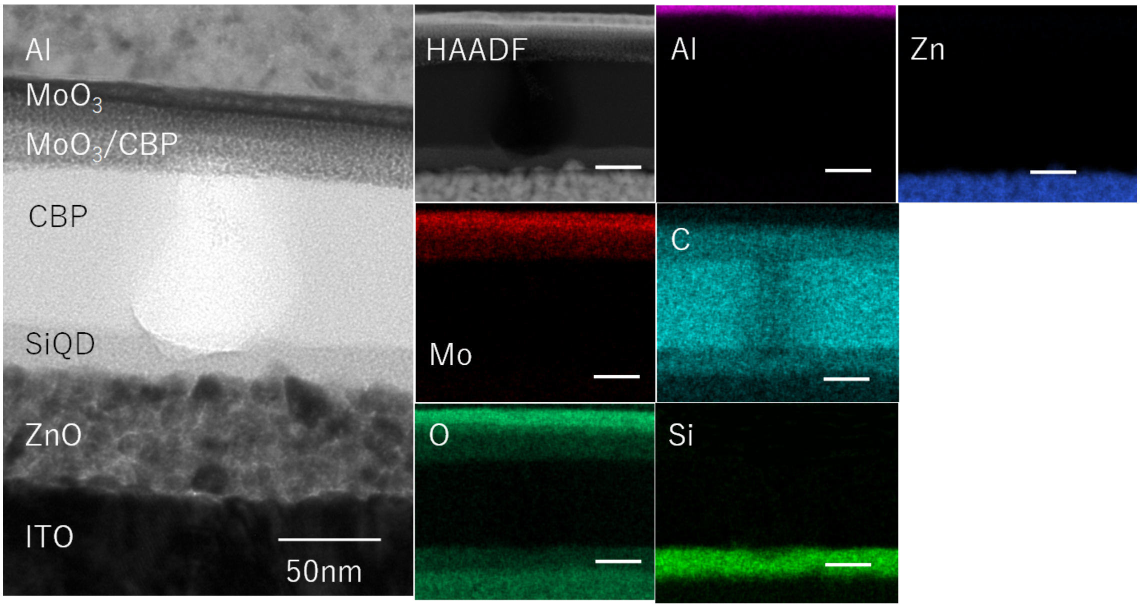

Fig.4-19 Cross-section of Si-QLED operated for 10 min at 20 V. The TEM image (left) shows the well-defined layer structure. In the EDS maps (right) the individual layers can be clearly distinguished based on their elemental composition. The scale bars are 40 nm for all elemental maps.

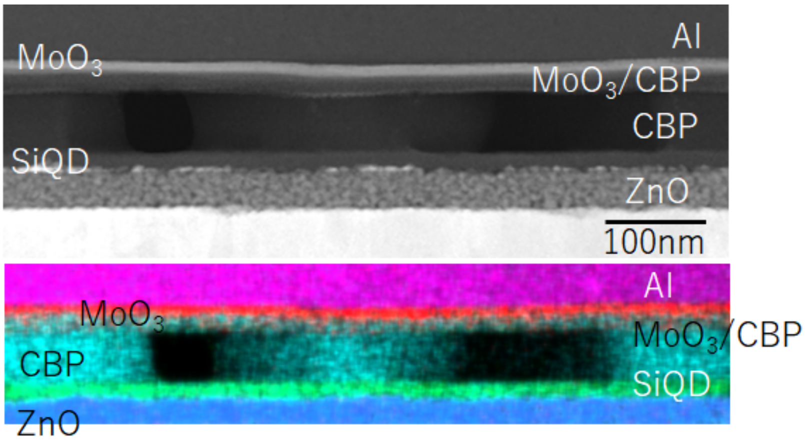

Fig.4-20 Cross-sectional HAADF-STEM and EDS mapping images of Si-QLED driven at 20 V for 10 min under air.

In Fig.4-18(a), with the exception of the sub-micrometer scale voids present in certain parts of the CBP layer, the majority of the stacking sequence appears to have maintained its initially defined multilayer structure. As shown in Fig.4-21, the thickness of the MoO_3/CBP layer was approximately 30 nm, which aligns with that of the pristine QLED. Although a small quantity of SiQDs within the optically active layer appeared to have diffused into the upper CBP layer according to the silicon map, its impact on carrier transportation and radiative recombination was negligible. In summary, the inverted device structure employed in this investigation preserved the initially designed multilayer stacking sequence even when subjected to high current/voltage operations, resulting in enhanced device stability for strong luminance under high operation voltage. This stands in contrast to the conventional structure of Si-QLEDs.

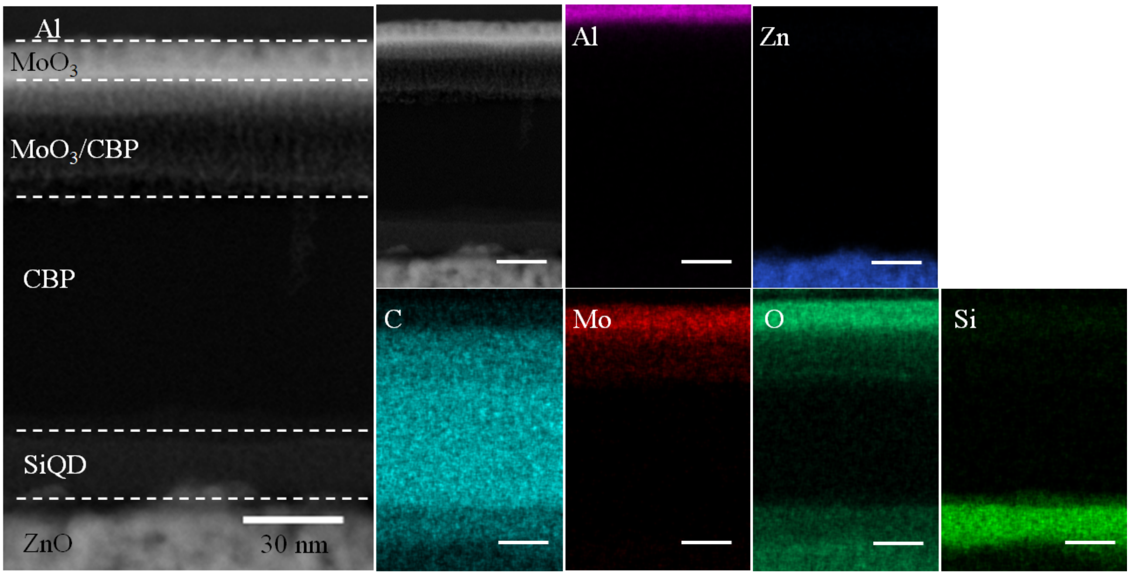

Fig.4-21 Cross-section of Si-QLED operated for 10 min at 20 V. The HAADF-STEM image (left) shows the well-defined layer structure. In the EDS maps (right) of the area corresponding to the HAADF image (right), the individual layers can be clearly distinguished based on their elemental composition. The scale bars are 20 nm for all elemental maps.

4.3.4 Si-QLEDs Operating in the Near-Infrared II Spectral Window

Schematic representation of the device architecture of the Si-QLED and a typical cross-sectional SEM image are presented in Fig.4-22(a). The device features an organic/inorganic hybrid multilayer stack consisting of ITO/ZnO/De-SiQDs/CBP/MoO_3/Al. The cathode and anode roles are served by ITO and Al, respectively. An electron injection/transportation layer (EIL/ETL) of 37 nm thickness made of ZnO was spin-coated onto the ITO-coated substrate. Following this, an optically active layer consisting of 28-nm-thick De-SiQDs was spin-coated. Vacuum evaporation was used to deposit the hole injection and transportation (HIL/HTL) layers of CBP and MoO_3 at a pressure of approximately 10^{-5} Pa. The CBP and MoO_3 layers have measured thicknesses of 68 nm and 25 nm, respectively. In Fig.4-22(b), the proposed energy level diagram is presented under zero applied bias. The work function, ionization energy, and electron affinity values of ITO, ZnO, CBP, and MoO_3/Al were obtained from the literature [42]. The ionization energy value for the De-SiQDs layer, measured by PYS, was -5.15 eV (refer to Fig.4-23). Assuming that the PL emission originates from the fundamental optical gap of De-SiQD, the calculated electron affinity value was -3.9 eV.

Fig.4-22(c) depicts the UV-VIS transmittance spectrum of the glass substrate coated with ITO and the PL spectrum of De-SiQDs. The ITO-coated glass exhibits approximately 90% transparency for the PL peak wavelength, suggesting that the outcoupling efficiency of the EL-emitting light may be diminished, which could lead to a decreased EQE. Fig.4-22(d) depicts the current density-voltage and irradiance-voltage characteristics of the Si-QLED. The turn-on voltage, defined as the minimum applied bias voltage required for the emission of photons, was measured to be 2.0 V. Subsequently, the current density and irradiance increased steeply once the voltage reached ~2.0 V. Under 9 V, the maximum current density was observed to be 0.13 mA/cm^2. It is noteworthy that the current density of a CdSe QLED with the same structure reached almost 1,000 mA/cm^2 at an applied voltage of 9 V [42]. The low current density observed in this study was attributed to a low carrier mobility of SiQDs.

To support this, an electron-only device with a device architecture "ITO/ZnO/De-SiQDs/ZnO/Al" was prepared and its *I-V* characteristics were measured (see Fig.4-24). The estimated value of electron mobility using the equation reported in the literature [43] was $\mu_{\mathrm{e,Si}} = 2.01 \times 10^{-7}\ [\mathrm{cm^2/V \cdot s}]$. On the other hand, the reported value of electron mobility of the CdSe-based device was $\mu_{\mathrm{e,CdSe}} = 2.91 \times 10^{-3}\ [\mathrm{cm^2/V \cdot s}]$, which was 10,000 times larger than this study. As a result, it was discussed that the current density of the device in this study was low. Irradiance began to saturate at 9 V and was anticipated to decrease at higher voltages. As shown in Fig.4-25, another NIR Si-QLED exhibited that the irradiance saturated under high voltage and then decreased with increasing voltage. This is a typical characteristic of QLEDs and has been reported previously [16]. The maximum irradiance of 0.43 μW/cm^2 was attained at an applied voltage of 9 V.

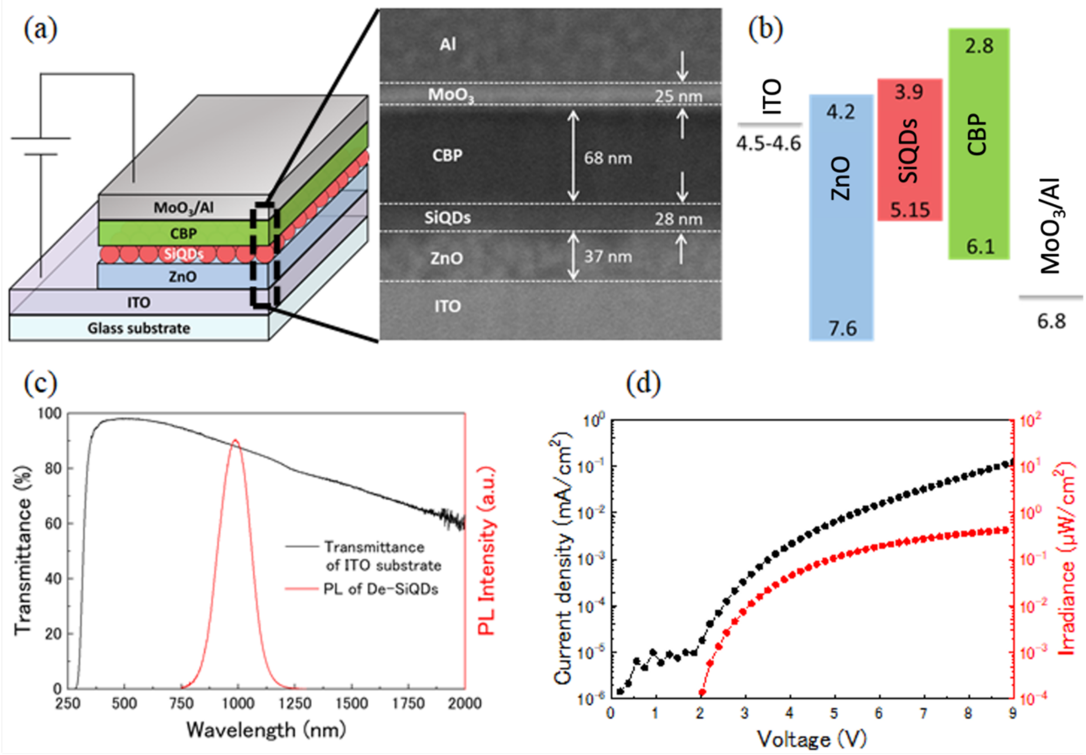

Fig.4-22 (a) Schematic illustration of Si-QLED with inverted device structure and a cross-sectional SEM image of the device structure with a hybrid organic/inorganic multilayer stack, (b) the energy band diagram in the unbiased conditions, (c) UV-VIS-NIR transmittance spectrum of ITO-coated soda-lime glass substrate and PL spectrum of De-SiQD, and (d) Current density and irradiance versus voltage characteristics of the device.

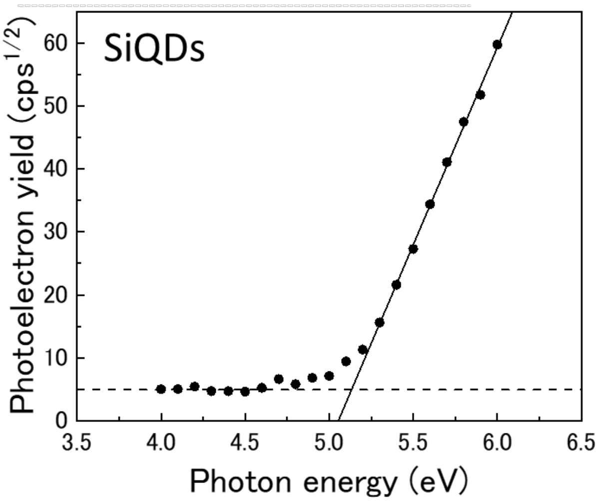

Fig.4-23 Photoelectron yield spectroscopic (PYS) spectrum of a film form of the 990-nm emitting De-SiQD sample.

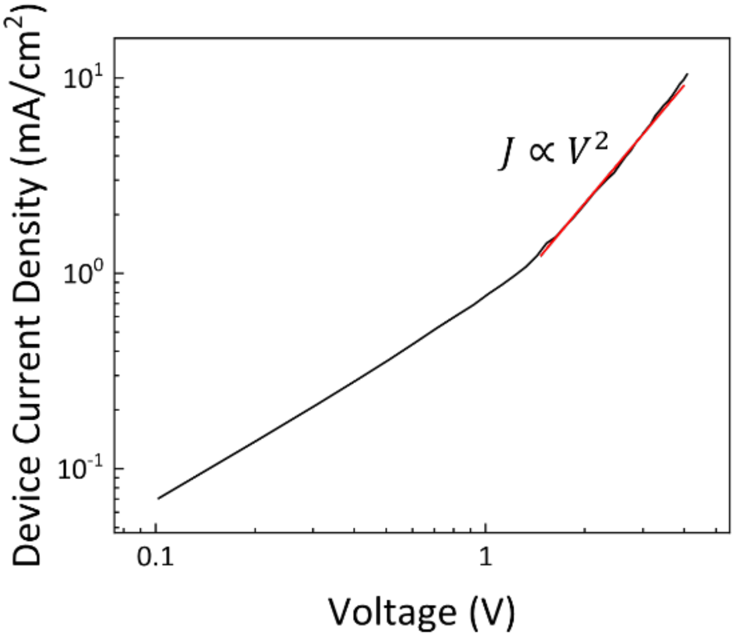

Fig.4-24 Device current density-voltage characteristics of electron only device.

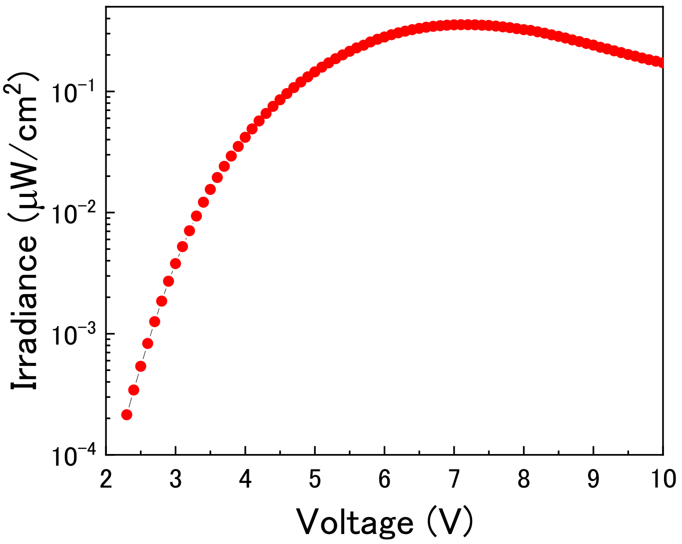

Fig.4-25 Irradiance-voltage characteristics of another NIR Si-QLED.

Subsequently, the EL performances of the Si-QLEDs were analyzed. Fig.4-26(a) presents a comparison of a typical EL spectrum, operated at 7 V, and the PL spectrum of the corresponding QDs. The EL spectrum exhibited a single peak centered at 1,000 nm. Fig.4-26(b) illustrates the EL spectra of the same device as the driving voltage varied between 4 V and 7 V. Evidently, the EL radiation intensity increased as the applied bias increased, while the spectral peak photon energy remained independent of the applied voltage. Additionally, no parasitic emission was observed from the neighboring compositional layers, even under a high bias. These observations suggest that the electrons and holes injected from each electrode recombined solely within the De-SiQD layer for EL, thus not inducing a spectral shift. Such a stable EL spectrum may be a feature of the inverted device structure, as the EL spectral peak is known to shift towards the shorter wavelength side as the applied voltage increases in conventional device architectures of Si-QLEDs [16,18,22]. Fig.4-26(c) plots the estimated EQE values as a function of current density. The highest EQE of 4.84% was achieved at a current density of 4.85×10^{-4} mA/cm^2. This EQE is comparable to the record value among reported NIR-II EL devices as seen in Table.4-4. As the current density increased, the EQE showed a decreasing trend, however, the rate was minimal. This implies that relatively high EQE values were maintained over a wide voltage range. Furthermore, EQE values of more than 3% were observed at current densities as high as 0.01 mA/cm^2. Additionally, five NIR Si-QLEDs were fabricated utilizing the same procedure. The maximum EQE reproducibility was confirmed to be more than 3.5% (as seen in Fig.4-27). The observation of such high EQE values might be attributed to the high PLQY of more than 50%, resulting from GPC-based separation of the QDs, as well as favorable band alignment, allowing for efficient charge injection and charge balance, and ~2.4 eV of hole-blocking barrier and ~1.1 eV of electron-blocking barrier.

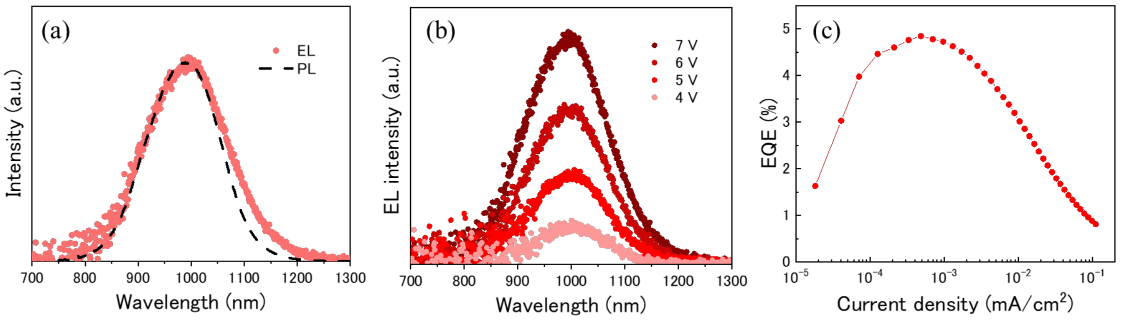

Fig.4-26 Optoelectronic performance of Si-QLEDs exhibiting NIR-II EL spectra. (a) PL spectrum of De-SiQD to compare its peak position and shape with EL spectrum of the device containing a same batch of De-SiQD, (b) changes in intensity of EL spectra at four different bias voltages, and (c) Current density-dependence of external quantum efficiency (EQE) of the NIR-II emitting Si-QLED.

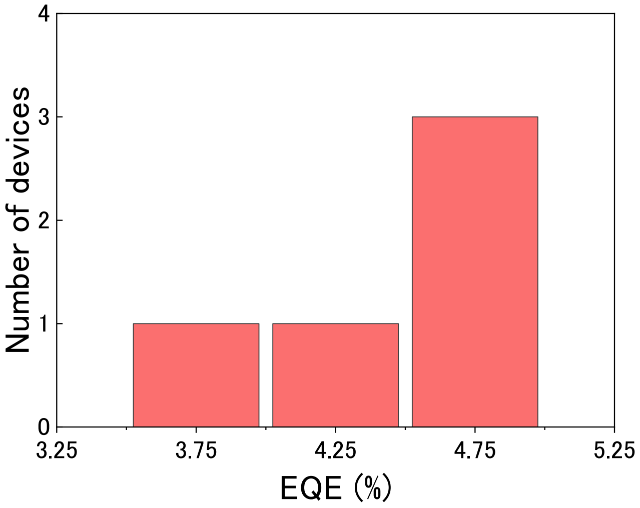

Fig.4-27 Histograms of maximum EQEs of five NIR Si-QLEDs.

Table.4-4 A summary of the EL performances for NIR-LEDs operating in the 900-1,100 nm spectral wavelength. The device performance data in this study was compared with EQE values reported in literatures.

	Emission layer	PLQY [%]	EL peak [nm]	Max EQE [%]	Reference
QD	Si	53	1000	4.84	This study
	HgCdTe	31	940	N/A	[44]
	PbS	N/A	1054	2.0	[45]
Perovskite	$MAPb_{0.6}Sn_{0.4}I_{2.6}Br_{0.4}$	N/A	900	2.6	[46]
	$MASnI_3$	N/A	901	0.9	[46]
	$MAPb_{0.6}Sn_{0.4}I_{2.8}Br_{0.2}$	N/A	909	3.3	[46]
	$MAPb_{0.6}Sn_{0.4}I_3$	N/A	917	5.0	[46]
	$MAPb_{0.6}Sn_{0.4}I_3$	N/A	928	2.7	[46]
	$MAPb_{0.2}Sn_{0.8}I_3$	N/A	943	0.6	[46]
	$MASnI_3$	N/A	945	0.72	[47]
	$CsSnI_3$	N/A	950	3.8	[48]
	Yb^{3+}:$CsPbCl_3$	62.3	984	5.9	[49]
Complex	Pt-TPTNP	22	900	3.8	[50]
	Pt-Ar_4TAP	8	1005	0.12	[51]
Polymer	D-A-D	N/A	939	0.006	[52]
	D-A	0.3	970	0.1	[53]
	D-A-D	N/A	970	0.05	[54]
	D-A-D	N/A	990	0.018	[52]
	D-A-D	6.3	1050	0.12	[55]
	D-A-D	5.8	1080	0.28	[55]
	D-A	0.3	1100	0.03	[53]

4.3.5 Manipulating the Spectral Characteristics of Electroluminescence

The tailoring of a spectral shape in the NIR-EL is of significant interest in the advancement of noninvasive clinical diagnoses. This is because various blood components possess distinct absorption coefficients for NIR light. In this section, the emphasis is placed on the substantial Stokes shift between optical absorption and emission, as illustrated in Fig.4-28. It is anticipated that, with a large window available for other EL components, the efficient superimposition of the EL spectra will effectively tailor the spectral shape and its NIR-color rendering, thereby minimizing unexpected energy transfer between differently-sized QDs.

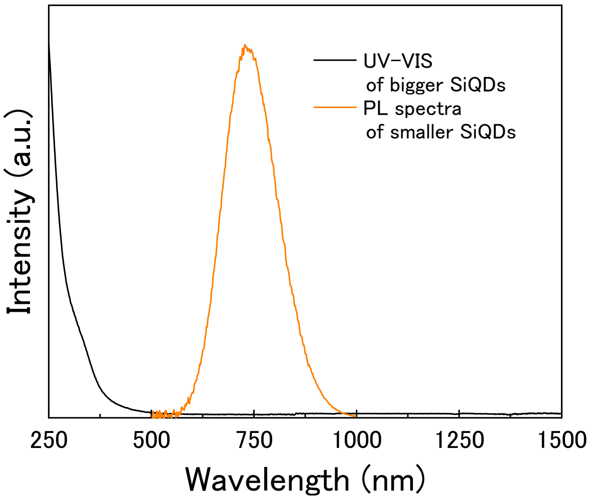

Fig.4-28 UV-VIS spectra of bigger SiQDs and PL spectra of smaller SiQDs.

Fig.4-29(a) illustrates a device fabrication scheme for spectral superimposition. Initially, De-SiQDs with a PL peak around 730 nm was prepared using a protocol similar to that previously described [24], and was combined with an equal weight of a 990 nm emitting counterpart. The absolute PLQY of the 730 nm emitting De-SiQDs is 38%, which is 15% lower than the value of the other QD sample. Subsequently, ZnO was spin-coated onto the patterned ITO surface, and the QD mixture was spin-coated and dried. Materials for the HTL/HIL and the electrode were then deposited under vacuum. Fig.4-29(b) plots the current density and irradiance versus voltage characteristics of the corresponding

Si-QLED. The turn-on voltage was increased by mixing SiQD with a large band gap in the emitting layer, as previously confirmed in studies [56]. In Fig.4-29(c), the dotted lines depict the normalized PL spectra centered at 730 nm (1.698 eV) and 990 nm (1.252 eV). The EL spectrum, represented by the red color-coded, was obtained at 13 V and had a FWHM of 382 nm (~625 meV). According to the curve fitting of the spectrum with a Gaussian function (see Fig.4-30), the integrated intensity of the 786 nm EL peak was 21% lower than that of the 972 nm EL peak. This closely corresponded to the PLQY ratio, suggesting that the observed broad-spectrum results from the 786 nm emission peak superimposed upon the 972 nm emission peak without energy transfer between different-sized QDs via sequential reabsorption of emitting light. This phenomenon is attributed to the fact that the photon energy emitted from small-sized SiQDs (with a PL peak at 1.698 eV) is not absorbed by neighboring large-sized SiQDs (with a PL peak at 1.252 eV), thereby preventing the transfer of photon energy from small-sized QDs to large-sized QDs. The results of the curve-fitting indicate that the values of EL-FWHM are 168 nm (~400 meV) and 210 nm (~279 meV) for the 786 nm and 972 nm emission spectra, respectively. The estimated turn-on voltage was 7.1 V. Fig.4-29(d) illustrates the EL spectra as the applied bias varied in the range of 13-16 V. Both peaks remained at consistent spectral positions within this range. Nevertheless, the intensity ratio of the 786 nm peak to the 972 nm peak exhibited an increase as the applied voltage increased, as evidenced in Fig.4-31. There are two possible mechanisms that could account for this. Firstly, the contribution of the smaller QD with a larger band gap to the entire EL spectrum increases with the driving voltage, thereby growing the EL peak centered at a shorter wavelength at a higher bias. The other mechanism could be the saturation of the emissions from the larger QDs due to a low efficiency of the carrier injection into the 972 nm luminescent QD layers. A similar phenomenon has been reported in previous studies [56].

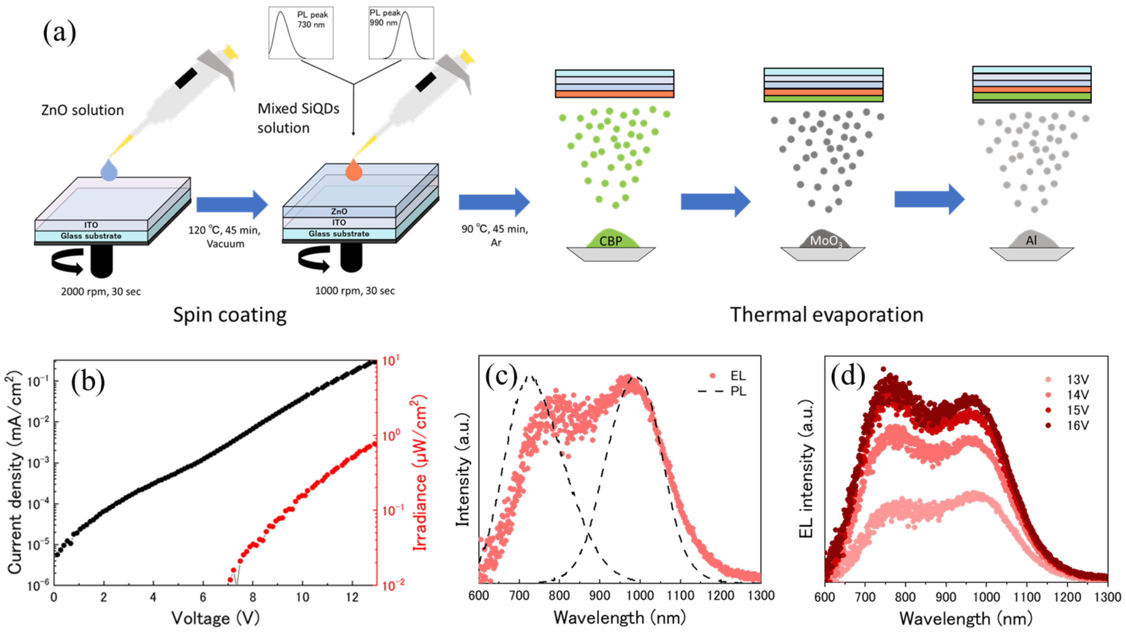

Fig.4-29 (a) Schematic fabrication process of spectral-shape tailored Si-QLED, (b) Current density and irradiance versus voltage characteristics of the device, (c) a typical EL spectrum of the device where an optically active layer consists of both the red-visible and the NIR light emitting QDs with PL spectra shown by broken lines, and (d) Changes in intensity and shape of EL spectra with increasing operating voltage.

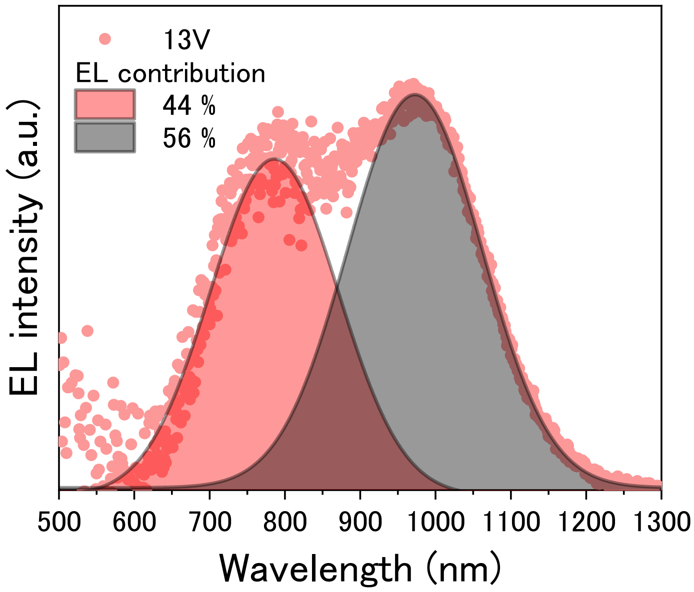

Fig.4-30 EL spectrum of Si-QLED, in which the red- light emitting QDs mixed with the NIR-light emitting QDs serves as optically active layer, operated at 13V and its deconvolution.

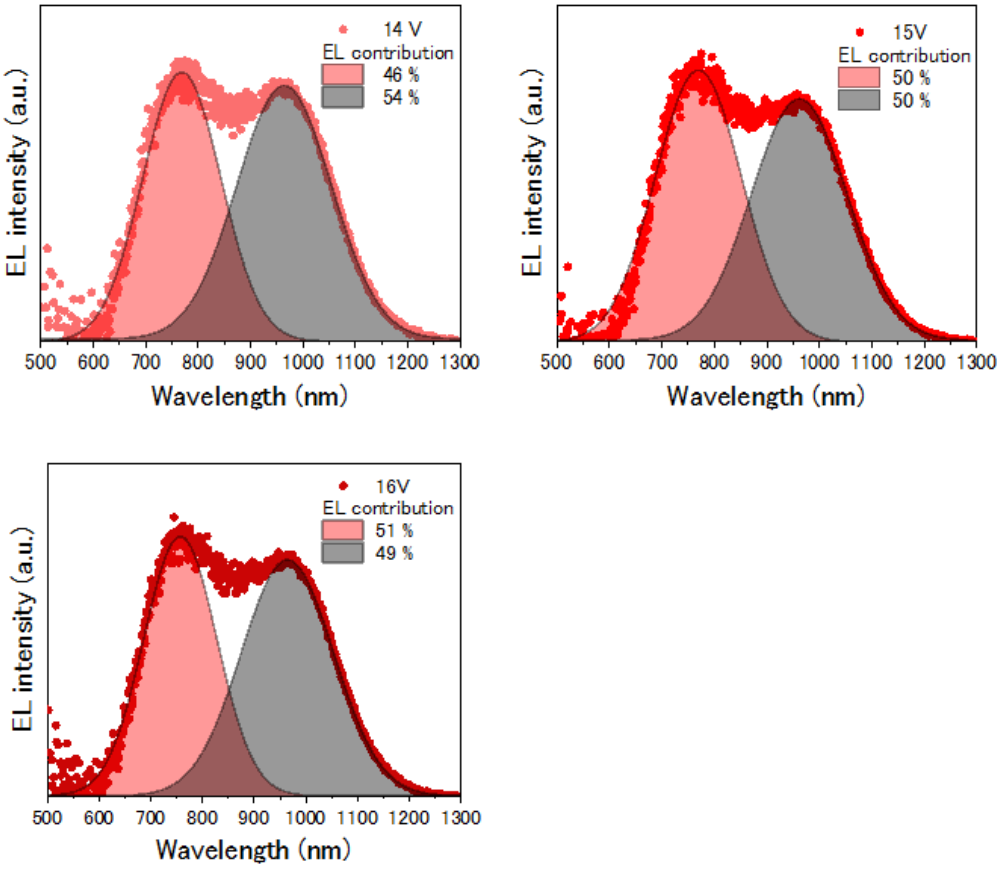

Fig.4-31 EL spectra of a same Si-QLED, in which the red-emitting QDs mixed with the NIR-emitting QDs serves as optically active layer, operated at different applied biases and their deconvolutions.

In general, as QDs of direct band gap semiconductors exhibit band-edge emissions, most of the emissions from smaller QDs are optically reabsorbed by larger counterparts, making it challenging to tailor the emission spectrum using band gap engineering. However, the large Stokes shift between the absorption and emission enables spectral tailoring as the energy transfer between adjacent differently-sized QDs is minimal and can be disregarded. This could be beneficial for the optical utilization of QDs made of indirect band gap semiconductor.

4.4 Conclusion

In this chapter, the influence of SiQD film thickness on EL spectra was initially investigated. When the SiQD film thicknesses were 46 nm and 21 nm, only EL emission from SiQDs was observed, however, when the film thicknesses were 10 nm and 6 nm, parasitic emission from ZnO also emerged. Additionally, as the SiQD film thickness decreased, the device current density and optical power density increased. Subsequently, a SiQD-based QLED was produced through a solution-processed method, featuring a narrow EL spectrum peaking at 620 nm. A pale-orange luminescent sample of SiQD with 8% PLQY was utilized as the active layer of the QLED. The device, consisting of multiple layers of an inverted device structure, emitted a pale-orange emission with 0.03% EQE, which was visible to the naked eye even in an illuminated room. This study expanded the tunable emission range, which is currently limited to between 640 nm and 850 nm. Furthermore, five Si-QLEDs with an inverted structure were prepared, with the optically active layers consisting of SiQDs of varying diameters. The EL spectral peaks appeared at 755 nm for Device A, 722 nm for Device B, 670 nm for Device C, 635 nm for Device D, and 590 nm for Device E. These EL peak positions corresponded with those in the PL spectra, indicating the presence of quantum confinement effects in SiQDs. The peak EQE and luminance were 3.34% and 0.25 cd/m^2 for Device A, 1.15% and 12.34 cd/m^2 for Device B, 1.18% and 17.2 cd/m^2 for Device C, 0.89% and 30.28 cd/m^2 for Device D, 0.12% and 18.4 cd/m^2 for Device E. No parasitic emission from the neighboring compositional layer was detected. The shortest wavelength of the EL spectral peak was updated to 590 nm, which is shorter than the previous study. The improved EQE may be attributed to the improved PLQYs of SiQDs and well-aligned energy diagrams of the inverted device architecture. Cross-sectional TEM imaging revealed that device-structural degradation of Si-QLED was promoted by the growth of sub-microscopic voids, which were initially created at the interface between CBP and MoO$_3$/CBP layers. Finally, a NIR-II LED based on SiQD as an optically active layer was developed for the first time. The 4.84% EQE was the record value for heavy-metal-free QLEDs operating in the 900-1,100-nm spectral range. Such a high EQE was obtained using SiQD with a PLQY of 53%, which was fractionated separately from the QD sample via a chromatographic technique. The Si-QLED displayed a turn-on voltage as low as 2.0 V, and neither a peak at 1,000 nm in the EL spectrum nor parasitic emissions of the adjacent layer were observed at high driving voltage. The wavelength tuning range of the current Si-QLEDs (590-868 nm) was greatly expanded to the longer wavelength side, and by leveraging the substantial Stokes shift between the absorption and emission spectra, it was demonstrated that utilizing spectral superimposition with minimized energy transfer from reabsorption of light emitted by a smaller QD results in a significantly broadened NIR EL spectrum.

4.5 References

[1] Shen, H. *et al.* Supporting Information :Visible quantum dot light-emitting diodes with simultaneous high brightness and efficiency. *Nat. Photonics* **13**, 192–197 (2019)

[2] Cao, W. *et al.* Highly stable QLEDs with improved hole injection via quantum dot structure tailoring. *Nat. Commun.* **9**, 2608 (2018)

[3] Sun, Q. *et al.* Bright, multicoloured light-emitting diodes based on quantum dots. *Nat. Photonics* **1**, 717–722 (2007)

[4] Wang, L. *et al.* Blue Quantum Dot Light-Emitting Diodes with High Electroluminescent Efficiency. *ACS Appl. Mater. Interfaces* **9**, 38755–38760 (2017)

[5] Yang, Y. *et al.* High-efficiency light-emitting devices based on quantum dots with tailored nanostructures. *Nat. Photonics* **9**, 259–266 (2015)

[6] Mashford, B. S. *et al.* High-efficiency quantum-dot light-emitting devices with enhanced charge injection. *Nat. Photonics* **7**, 407–412 (2013)

[7] Dai, X. *et al.* Solution-processed, high-performance light-emitting diodes based on quantum dots. *Nature* **515**, 96–99 (2014)

[8] Won, Y.-H. *et al.* Highly efficient and stable InP/ZnSe/ZnS quantum dot light-emitting diodes. *Nature* **575**, 634–638 (2019)

[9] Li, Y. *et al.* Stoichiometry-Controlled InP-Based Quantum Dots: Synthesis, Photoluminescence, and Electroluminescence. *J. Am. Chem. Soc.* **141**, 6448–6452 (2019)

[10] Cao, F. *et al.* A Layer-by-Layer Growth Strategy for Large-Size InP/ZnSe/ZnS Core–Shell Quantum Dots Enabling High-Efficiency Light-Emitting Diodes. *Chem. Mater.* **30**, 8002–8007 (2018)

[11] Ramasamy, P., Ko, K.-J., Kang, J.-W. & Lee, J.-S. Two-Step "Seed-Mediated" Synthetic Approach to Colloidal Indium Phosphide Quantum Dots with High-Purity Photo- and Electroluminescence. *Chem. Mater.* **30**, 3643–3647 (2018)

[12] Kim, H. Y. *et al.* Transparent InP Quantum Dot Light-Emitting Diodes with ZrO 2 Electron Transport Layer and Indium Zinc Oxide Top Electrode. *Adv. Funct. Mater.* **26**, 3454–3461 (2016)

[13] Pons, T. *et al.* Cadmium-Free CuInS 2 /ZnS Quantum Dots for Sentinel Lymph Node Imaging with Reduced Toxicity. *ACS Nano* **4**, 2531–2538 (2010)

[14] Tan, Z. *et al.* Near-Band-Edge Electroluminescence from Heavy-Metal-Free Colloidal Quantum Dots. *Adv. Mater.* **23**, 3553–3558 (2011)

[15] Cheng, K.-Y., Anthony, R., Kortshagen, U. R. & Holmes, R. J. Hybrid Silicon Nanocrystal−Organic Light-Emitting Devices for Infrared Electroluminescence. *Nano Lett.* **10**, 1154–1157 (2010)

[16] Cheng, K.-Y., Anthony, R., Kortshagen, U. R. & Holmes, R. J. High-Efficiency Silicon Nanocrystal Light-Emitting Devices. *Nano Lett.* **11**, 1952–1956 (2011)

[17] Yamada, H. & Shirahata, N. Silicon Quantum Dot Light Emitting Diode at 620 nm. *Micromachines* **10**, 318 (2019)

[18] Liu, X. *et al.* Light-Emitting Diodes Based on Colloidal Silicon Quantum Dots with Octyl and Phenylpropyl Ligands. *ACS Appl. Mater. Interfaces* **10**, 5959–5966 (2018)

[19] Puzzo, D. P. *et al.* Visible Colloidal Nanocrystal Silicon Light-Emitting Diode. *Nano Lett.* **11**, 1585–1590 (2011)

[20] Mastronardi, M. L. *et al.* Silicon Nanocrystal OLEDs: Effect of Organic Capping Group on Performance. *Small* **8**, 3647–3654 (2012)

[21] Maier-Flaig, F. *et al.* Multicolor Silicon Light-Emitting Diodes (SiLEDs). *Nano Lett.* **13**, 475–480 (2013)

[22] Yao, L. *et al.* Efficient silicon quantum dots light emitting diodes with an inverted device structure. *J. Mater. Chem. C* **4**, 673–677 (2016)

[23] Gu, W. *et al.* Silicon-Quantum-Dot Light-Emitting Diodes With Interlayer-Enhanced Hole Transport. *IEEE Photonics J.* **9**, 1–10 (2017)

[24] Ghosh, B., Yamada, H., Chinnathambi, S., Özbilgin, İ. N. G. & Shirahata, N. Inverted Device Architecture for Enhanced Performance of Flexible Silicon Quantum Dot Light-Emitting Diode. *J. Phys. Chem. Lett.* **9**, 5400–5407 (2018)

[25] Ghosh, B. & Shirahata, N. All-Inorganic Red-Light Emitting Diodes Based on Silicon Quantum Dots. *Crystals* **9**, 385 (2019)

[26] Liang, H. *et al.* High Color Purity Lead-Free Perovskite Light-Emitting Diodes via Sn Stabilization. *Adv. Sci.* **7**, 1903213 (2020)

[27] Morozova, S., Alikina, M., Vinogradov, A. & Pagliaro, M. Silicon Quantum Dots: Synthesis, Encapsulation, and Application in Light-Emitting Diodes. *Front. Chem.* **8**, 1–8 (2020)

[28] Zhao, S., Liu, X., Pi, X. & Yang, D. Light-emitting diodes based on colloidal silicon quantum dots. *J. Semicond.* **39**, 061008 (2018)

[29] Ghosh, B. *et al.* Hybrid White Light Emitting Diode Based on Silicon Nanocrystals. *Adv. Funct. Mater.* **24**, 7151–7160 (2014)

[30] Maier-Flaig, F. *et al.* Looking Inside a Working SiLED. *Nano Lett.* **13**, 3539–3545 (2013)

[31] Chandra, S., Masuda, Y., Shirahata, N. & Winnik, F. M. Transition-Metal-Doped NIR-Emitting Silicon Nanocrystals. *Angew. Chemie Int. Ed.* **56**, 6157–6160 (2017)

[32] Yao, L. *et al.* Efficient silicon quantum dots light emitting diodes with an inverted device structure. *J. Mater. Chem. C* **4**, 673–677 (2015)

[33] Cheng, K. Y., Anthony, R., Kortshagen, U. R. & Holmes, R. J. High-efficiency silicon nanocrystal light-emitting devices. *Nano Lett.* **11**, 1952–1956 (2011)

[34] Liu, X. *et al.* Light-Emitting Diodes Based on Colloidal Silicon Quantum Dots with Octyl and Phenylpropyl Ligands. *ACS Appl. Mater. Interfaces* **10**, 5959–5966 (2018)

[35] Bae, W. K. *et al.* Controlling the influence of Auger recombination on the performance of quantum-dot light-emitting diodes. *Nat. Commun.* **4**, 2661 (2013)

[36] White, R. T., Thibau, E. S. & Lu, Z.-H. Interface Structure of MoO3 on Organic Semiconductors. *Sci. Rep.* **6**, 21109 (2016)

[37] Lampert, M. A. Simplified Theory of Space-Charge-Limited Currents in an Insulator with Traps. *Phys. Rev.* **103**, 1648–1656 (1956)

[38] Kahn, A. Fermi level, work function and vacuum level. *Mater. Horizons* **3**, 7–10 (2016)

[39] Miller, D. A. B. *et al.* Electric field dependence of optical absorption near the band gap of quantum-well structures. *Phys. Rev. B* **32**, 1043–1060 (1985)

[40] Mastronardi, M. L. *et al.* Size-Dependent Absolute Quantum Yields for Size-Separated Colloidally-Stable Silicon Nanocrystals. *Nano Lett.* **12**, 337–342 (2012)

[41] Kwak, J. *et al.* Bright and Efficient Full-Color Colloidal Quantum Dot Light-Emitting Diodes Using an Inverted Device Structure. *Nano Lett.* **12**, 2362–2366 (2012)

[42] Li, X. *et al.* Bright colloidal quantum dot light-emitting diodes enabled by efficient chlorination. *Nat. Photonics* **12**, 159–164 (2018)

[43] Wan, Q. *et al.* Surface Oxidation of Quantum Dots to Improve the Device Performance of Quantum Dot Light-Emitting Diodes. *J. Phys. Chem. C* **124**, 28424–28430 (2020)

[44] Kalytchuk, S. *et al.* Sodium Chloride Protected CdHgTe Quantum Dot Based Solid-State Near-Infrared Luminophore for Light-Emitting Devices and Luminescence Thermometry. *ACS Photonics* **4**, 1459–1465 (2017)

[45] Sun, L. *et al.* Bright infrared quantum-dot light-emitting diodes through inter-dot spacing control. *Nat. Nanotechnol.* **7**, 369–373 (2012)

[46] Qiu, W. *et al.* Mixed Lead–Tin Halide Perovskites for Efficient and Wavelength-Tunable Near-Infrared Light-Emitting Diodes. *Adv. Mater.* **31**, 1806105 (2019)

[47] Lai, M. L. *et al.* Tunable Near-Infrared Luminescence in Tin Halide Perovskite Devices. *J. Phys. Chem. Lett.* **7**, 2653–2658 (2016)

[48] Hong, W. *et al.* Efficient Low-Temperature Solution-Processed Lead-Free Perovskite Infrared Light-Emitting Diodes. *Adv. Mater.* **28**, 8029–8036 (2016)

[49] Ishii, A. & Miyasaka, T. Sensitized Yb 3+ Luminescence in CsPbCl 3 Film for Highly Efficient Near-Infrared Light-Emitting Diodes. *Adv. Sci.* **7**, 1903142 (2020)

[50] Sommer, J. R. *et al.* Efficient Near-Infrared Polymer and Organic Light-Emitting Diodes Based on Electrophosphorescence from (Tetraphenyltetranaphtho[2,3]porphyrin)platinum(II). *ACS Appl. Mater. Interfaces* **1**, 274–278 (2009)

[51] Graham, K. R. *et al.* Extended Conjugation Platinum(II) Porphyrins for use in Near-Infrared Emitting Organic Light Emitting Diodes. *Chem. Mater.* **23**, 5305–5312 (2011)

[52] Tregnago, G., Steckler, T. T., Fenwick, O., Andersson, M. R. & Cacialli, F. Thia- and selena-

diazole containing polymers for near-infrared light-emitting diodes. *J. Mater. Chem. C* **3**, 2792–2797 (2015)

[53] Nagata, R., Nakanotani, H. & Adachi, C. Near-Infrared Electrophosphorescence up to 1.1 µm using a Thermally Activated Delayed Fluorescence Molecule as Triplet Sensitizer. *Adv. Mater.* **29**, 1604265 (2017)

[54] Chen, M. X. *et al.* Low band gap donor–acceptor–donor polymers for infra-red electroluminescence and transistors. *Synth. Met.* **146**, 233–236 (2004)

[55] Qian, G. *et al.* Simple and Efficient Near-Infrared Organic Chromophores for Light-Emitting Diodes with Single Electroluminescent Emission above 1000 nm. *Adv. Mater.* **21**, 111–116 (2009)

[56] Bae, W. K. *et al.* R/G/B/Natural White Light Thin Colloidal Quantum Dot-Based Light-Emitting Devices. *Adv. Mater.* **26**, 6387–6393 (2014)

Chapter 5 Manipulation of Carrier Transport Layer and Interparticle Distance in the Active Layer for Improved Performance in Si-QLEDs

5.1 Introduction

Heavy-metal-free quantum dots light-emitting diodes (QLEDs) incorporating indium phosphide (InP) [1], zinc selenide (ZnSe) [2], copper indium sulfide ($CuInS_2$) [3], carbon dots [4], $(AgIn)_xZn_{2(1-x)}S_2$ (ZAIS) [5], lead (Pb)-free perovskite [6], double perovskite [7] or silicon (Si) [8–22] quantum dots (QDs) as active layers are expected to represent an environmentally friendly and sustainable option for the next-generation of QLEDs. In particular, InP or ZnSe-based QLEDs exhibit remarkable device performance, such as high external quantum efficiency (EQE) that exceeds 20%, a brightness of up to 100,000 cd m^{-2}, and a low turn-on voltage of approximately 2 V [1,2]. Despite significant advances, alternative heavy-metal-free QLEDs still exhibit poor EQE characteristics. For instance, $CuInS_2$ achieved only 7.8% EQE [3], while ZAIS attained 2.2% [5], carbon achieved 0.083% [4], Pb-free perovskite achieved 0.3% [6] and Pb-free double perovskite achieved 0.064% [7]. Researchers have encountered challenges in realizing high EQE values for these QLEDs, particularly exceeding 7%.

Achieving a balanced electron-hole (*e-h*) injection into the QD layer is a critical parameter for enhancing EQE. Imbalanced *e-h* injection, as reported, hinders radiative carrier recombination in the QD layer, ultimately resulting in lower EQE [23]. The imbalance of charge carriers is commonly attributed to two factors: (i) a larger potential energy barrier for hole injection into the emissive layer in comparison to electron injection and (ii) a relatively higher electron mobility in the electron transport layer (ETL) than the hole mobility in the hole transport layer (HTL) [24]. One effective approach to addressing this issue involves the insertion of an electron blocking layer (EBL) between the ETL and emissive layer, which helps to suppress electron injection and improve charge injection balance. Various materials have been reported as EBLs, such as alumina [24], tert-butyldimethylsilyl chloride-modified poly(p-phenylene benzobisoxazole) [25], 1,3,5-tri(m-pyrid-3-yl-phenyl)benzene [26], and poly(methyl methacrylate) (PMMA) [27–31].

Si is the second most abundant element on Earth and has not been reported to be toxic to the environment or living organisms [32]. The effects of quantum confinement (QC) become evident in Si nanocrystals with diameters smaller than 5 nm [33]. By varying the diameter of SiQDs between 1.1 nm and 11.8 nm, the photoluminescence (PL) peak can be adjusted across a broad spectral range from 535 nm to 1,050 nm [34,35]. The covalent attachment of hydrocarbon chains to the surface atoms of QDs via Si-C linkages is crucial in rendering nonradiative channels inactive and dramatically enhancing the radiative recombination rate, leading to a significant increase in the PL quantum yield (PLQY) of up to 60%. However, SiQDs are not well-suited for use as emissive layers in phosphor-type LEDs owing to their low optical absorbance in the visible wavelength range. In contrast, SiQDs may be well-suited for use in a current-driven device architecture because the EQE is theoretically dominated by the PLQY, given that the charge carriers are injected from the electrodes. As expected, the first Si-QLED demonstrated near-infrared (NIR) electroluminescence (EL) spectrum centered at 853 nm and achieved 8.6% EQE [19]. Since then, considerable efforts have been invested in the advancement of visible-light-emitting Si-QLEDs, resulting in 6.2% EQE for red EL [13], 0.12% for pale-orange EL (*i.e.*, 590-630 nm) [15], and 0.03% for white EL spectra [36]. Generally, the colloidal stability of QDs is conferred by organic ligands possessing a long molecular chain, such as octadecane or oleyl amine. Conversely, shorter ligands are preferred for promoting carrier mobility in the optically active layer of QLEDs. As such, a common technique in the device fabrication process is to perform a ligand exchange that replaces the longer ligand with a shorter counterpart. However, in the case of SiQDs, the surface ligands, namely decane or hexadecane, are covalently bound to the outermost Si atoms, thereby hindering the ligand engineering process. As a result, alternative techniques are limited to employing ligands with shorter molecular lengths initially. Liu *et al.,* synthesized SiQDs terminated with octyl monolayers, despite the common use of 1-decene or 1-octadecene as precursors for thermal hydrosilylation of alkene. Through a reduction of the interparticle distance, they were able to achieve an EQE of 6.2%, which is a record value for red-light emitting Si-QLEDs [13]. Since the linear hydrocarbons used as ligands have low electrical conductivity, the use of shorter ligands is thought to result in more efficient charge injection into the optically active layer and improved EQE compared to long ligands. In essence, decreasing the interparticle distance between QDs in the active layer is expected to enhance the efficiency of the charge injection process, leading to an improvement in EQE.

In this section, a novel and facile method referred to as "post-electric-annealing" is presented for enhancing the EQE of red-emitting Si-QLEDs by applying a continuous voltage bias. After 9 hours of voltage application, the device exhibited an EQE of 12.2%. Microscopic examination revealed that this improvement was due to a reduction in the interparticle distance within the emissive layer of the device, resulting in enhanced charge carrier injection into the QD layer. In addition, the utilization of a PMMA layer as an EBL was observed to boost the EQE by rectifying charge injection equilibrium. Furthermore, Si-iQLEDs featuring $Zn_{0.86}Mg_{0.14}O$ as the electron transport layer (ETL) and Tris(4-carbazoyl-9-ylphenyl)amine (TCTA) as the hole transport layer (HTL) displayed a 12-fold amplification in light output intensity as opposed to ZnO/CBP ETL/HTL configurations. The long-term drive stability of the device provides a steppingstone for practical applications in lighting and display, as the device structure demonstrated stability even without encapsulation in air.

5.2 Experimental Methods

Reagents and Materials: Triethoxysilane (TES) was purchased from Tokyo Chemical Industry Co., LTD. Colloidal ink of zinc oxide (ZnO), 1-decene, hydrochloric acid (HCl) and molybdenum (IV) oxide (MoO_3, 99.97% trace metal basis), zinc acetate dihydrate (reagent grade), magnesium acetate tetrahydrate (ACS reagent, 98%), tetramethylammonium hydroxide pentahydrate (TMAH, 97%), dimethyl sulfoxide (DMSO, HPLC grade, 99.9%), Tris(4-carbazoyl-9-ylphenyl)amine (TCTA, 97%) were purchased from Sigma-Aldrich and used as received. 4,4′-Bis(9*H*-carbazol-9-yl)biphenyl (CBP, 99.9% trace metals basis) was purchased from Luminescence Technology Corp. Electronic-grade hydrofluoric acid (HF, 48% aqueous solution) was purchased from Kanto Chemical Co., INC. Toluene (HPLC-grade), chloroform, ethanol (99.5), methanol, and Zn powder were purchased from Wako Chemical. Milli-Q water (resistivity= 18.2 MΩ·cm) was obtained by Sartorius water purification system (arium 611 UV).

Preparation of ZnMgO Nanoparticle Ink: ZnMgO ETL NPs were synthesized at ambient condition using a solution based hydrolysis reaction [37]. For ZnMgO, Mg acetate was added to the Zn acetate solution at 15.0 mol% of the total metal precursor in DMSO were stirred for 1 hour at ambient condition. 10 mL of 0.5 M TMAH solution in ethanol were added dropwise into the Zn acetate solution at 0.5 mL/min and the mixture was vigorously stirred for 1 h. The mixture was then washed with acetone and centrifuged at 10,000 rpm for 10 min. The resulting white precipitation was dispersed in ethanol at a concentration of 30 mg/mL.

Preparation of SiQD Ink: SiQDs were synthesized via a two-step process reported in previous papers [36,38]. In a typical process, TES was hydrolyzed at pH 3. The hydrolysis product, that is, $(HSiO_{1.5})_n$, was heated to 1,050°C in 95%/5% Ar/H_2 atmosphere and kept for 2 hours for thermal disproportionation, yielding SiQDs dispersed in the oxidized silicon matrix. After cooling down to room temperature, 300 mg of the dark-brown powder (*i.e.*, Si/SiO_2 composite) was mechanically ground using an agate mortar with a pestle. The resultant fine powder was stirred for 90 min in acidic solution containing 8 mL of ethanol and 16 mL of 48%-HF aqueous solution. The surface of the resultant SiQDs was terminated with hydrogen atoms (H-SiQD). The H-SiQDs were centrifugated with 15,000 rpm at 10°C for collection. Next, the H-SiQDs were subjected to thermal hydrosilylation of 1-decene at 175°C to yield decane-terminated SiQDs (De-SiQDs).

Device Fabrication: Si-QLEDs were fabricated on a soda-lime glass substrate. A thin film of ITO uniformly sputtered on the glass with 130 nm thickness gave a resistivity of 10-14 Ω/sq. Etching was performed using HCl and Zn powder to process the ITO thin film into narrow strips of 2×20 mm. Then, the substrates were ultrasonicated with Milli-Q water, acetone, ethanol, and isopropanol in that order. After drying, the samples were oxidized using a VUV lamp (Ushio Inc.) at a pressure of 10^3 Pa for 30 min under N_2 flow. Next, the colloidal ink of ZnO was spin-coated with a rotation speed of 2,000 rpm for 60 s. After drying the film at 120°C under vacuum, PMMA as EBL, whose concentration was adjusted to 1.8 mg/mL in acetone, was spin-coated with a rotation speed of 2,000 rpm for 60 s and dried at 70°C. Next, the emissive layer of De-SiQDs was spin-coated with a concentration of 10 mg/mL in toluene with a speed of 1,000 rpm for 60 s. Then, an organic layer of CBP or TCTA and an inorganic layer of MoO_3 with a thickness of 30 nm were thermally evaporated in that order. Finally, the sample substrate with mask was transferred into the thermal evaporation chamber and a 200 nm of Al thin film as a top electrode was deposited under a vacuum level of 2×10^{-5} Pa.

Characterization: The major crystalline planes of the samples were characterized with X-ray powder diffraction (MiniFlex600, Rigaku, Japan). The high-resolution transmission electron microscopy (HR-TEM) images were obtained using a JEOL JEM-2100F microscope, operating at 200 kV. Optical absorbance spectra were measured by UV-VIS spectrophotometer (JASCO V-650, Japan) with an integrated sphere. PL spectra were measured by a modular double grating Czerny-Turner monochromator and iHR 320 emission monochromator (1,200 lines/mm of gratings) coupled to a photomultiplier tube (PMT) on a NanoLog Horiba Jovin Yvon spectrofluorometer with a 450 W xenon arc lamp. The spectral resolution of the system was around 0.3 nm. A cut filter of 495 nm-light was placed in front of the monochromator-PMT setup. The absolute PLQYs were measured at room temperature using the QY measurement system C9920-02 from Hamamatsu Photonics Co., Ltd. with a 150 W xenon lamp coupled to a monochromator for wavelength discrimination, an integrating sphere as a sample chamber, and a multichannel analyzer for signal detection. SiQDs dispersed in toluene were used for measurement of PLQYs. Ultraviolet photoelectron spectroscopy (UPS) measurements were performed by SigmaProbe (Thermo Fisher Scientific, USA). Photoelectron yield spectra (PYS) were measured by a model AC-3 (RIKEN KEIKI Co. Ltd., Japan). For UPS and PYS measurements, the thin film was prepared on an ITO-coated glass substrate for antistatic electricity by a manner similar to the device fabrication process. For device characterization, a calibrated Si photodetector (Hamamatsu S1336 8BQ) coupled with a Keithley 2400 was used.

Observation and Analysis: Cross-sectional scanning electron microscopic (SEM) images of the multilayer structure were obtained by ZEISS Auriga Laser (Carl Zeiss, Germany) combined with a focused ion beam (FIB) with a Ga^+ ion source. The FIB processing was performed for the carbon protection coating (deposited from carbon gas) and subsequent making of crevices to reveal the cross-sectional observation surface. Then, the microstructure was observed by SEM operated at 1 kV under a 54° gradient condition. Cross-sectional TEM images were obtained by Tecnai Osiris (FEI, USA). Before FIB processing with a Ga^+ ion source (FB-2100, Hitachi, Japan), the substrates were coated with a chromium (Cr)-containing oil-based ink to protect the surface. Then, FIB processing was performed for the tungsten (W) protection coating (deposited from $W(CO)_6$ gas) and subsequent preparation of the cross-sectional samples. Each sample was then mounted on a copper (Cu) FIB lift-out grid and thinned to approximately 100 nm. The prepared cross-sectional ultrathin samples were analyzed using TEM operated at 200 kV.

Calculation of EQE and Optical Power Density: EQE and optical power density were calculated assuming that EL has a Lambertian emission profile. EQE is expressed as the ratio of the number of radiated photons to the number of injected electrons per unit time $I_d(V)/|e|$, where $I_d(V)$ is current through device when applied voltage V, e is the electron charge. EQE is represented by the following equation [39],

$$\mathrm{EQE}\ (\%) = \frac{N_p(V) \times |e| \times g}{I_d(V)} \times 100 \qquad \mathrm{Eq.}\,5-1$$

where $N_p(V)$ is the number of photons collected by photodiode. Geometry factor g expresses when EL profile assumed to be Lambertian the ratio of the luminous flux emitted from LED to the luminous flux measured by photodiode, given by the following equation,

$$g = \frac{a^2 + L^2}{a^2} \qquad \mathrm{Eq.}\,5-2$$

where a indicates the radius of aperture of photodiode, L is distance between the light emitting surface of LED and photodiode. Here, the geometry factor was calculated as 2.49. $N_p(V)$ based on the actual observed EL spectrum $EL(\lambda)$ and photodiode current I_p^m is given by the following equation,

$$N_p(V) = \int_{\lambda_i}^{\lambda_f} EL(\lambda) \times \frac{I_p^m}{I_p'(\lambda)} d\lambda \qquad \mathrm{Eq.}\,5-3$$

where $I_p'(\lambda)$ is expressed using Planck constant h, the speed of light in vacuum c, EL emission wavelength λ and photodiode responsivity $R(\lambda)$,

$$I_p'(\lambda) = \int_{\lambda_i}^{\lambda_f} EL(\lambda) \times \frac{hc}{\lambda} \times R(\lambda)\, d\lambda \qquad \mathrm{Eq.}\,5-4$$

By calculating $N_p(V)$ for all applied voltages and substituting it into $\mathrm{Eq.}\,5-1$ gives voltage or current density dependent EQE characteristics.

Optical power density was calculated as follows. The emitted power $P(V)$ is calculated by following equation

$$P(V) = \int_{\lambda_i}^{\lambda_f} EL(\lambda) \times \frac{I_p^m}{I_p'(\lambda)} \times \frac{hc}{\lambda} d\lambda \qquad \text{Eq. } 5-5$$

Then optical power density is expressed using $P(V)$

$$\text{Optical power density } (\mathrm{W/cm^2}) = \frac{P(V)}{A} \qquad \text{Eq. } 5-6$$

where A is the area of the light emitting surface.

5.3 Experimental Results and Discussion

5.3.1 Manipulation of Carrier Transport Layer for Improved Performance in Si-QLEDs

An attempt was made to regulate the balance of charge injection by incorporating PMMA as an EBL between the ETL and the SiQDs layer. In order to assess the balance of electron and hole injection in the SiQDs layer, two electron-only devices (EODs) and a hole-only device (HOD) were fabricated using the same method as Si-QLEDs. The device consisted of ITO/ZnO/SiQDs/Al (as a reference EOD), ITO/ZnO/PMMA/SiQDs/Al (as an EBL-inserted EOD) and ITO/SiQDs/CBP/MoO_3/Al (as a HOD). The carrier mobilities of both electrons and holes were estimated using the Space-Charge-Limited-Current (SCLC) model [40], as shown in Fig.5-1. The calculation equation is as follows:

$$J = \frac{9}{8}\varepsilon_r\varepsilon_0\mu\frac{V^2}{d^3} \qquad \text{Eq. } 5-7$$

Where J is the device current density, ε_r and ε_0 are the relative and vacuum dielectric constants, respectively. μ represents the field-independent carrier mobility, and d represents the thickness of the QD layer. In this study, ε_r and ε_0 are assumed to be 5.8 and 8.85×10^{-14} F cm^{-1}, respectively, based on the literature [41]. It is assumed that the thicknesses of the QD films are 40 nm.

The calculated charge injection ratios are presented in Table.5-1. The EBL inserted EOD displayed a decreased electron carrier mobility when compared to the reference EOD. Furthermore, the electron and hole injection ratios of the EBL inserted EOD were found to be lower than those of the reference EOD. A point of note is that a charge injection ratio approaching 1 is desirable. Based on these results, it is anticipated that the incorporation of the EBL in the device structure will result in an enhanced EQE relative to the device without an EBL.

Table.5-1 Electron and hole mobilities estimated by the SCLC model.

EOD structure	μ_e (cm^2 V^{-1} s^{-1})	μ_h (cm^2 V^{-1} s^{-1})	μ_e / μ_h
ITO/ZnO/SiQD/Al	5.95×10^{-4}	1.42×10^{-4}	4.19
ITO/PMMA/SiQD/Al	4.39×10^{-4}		3.09

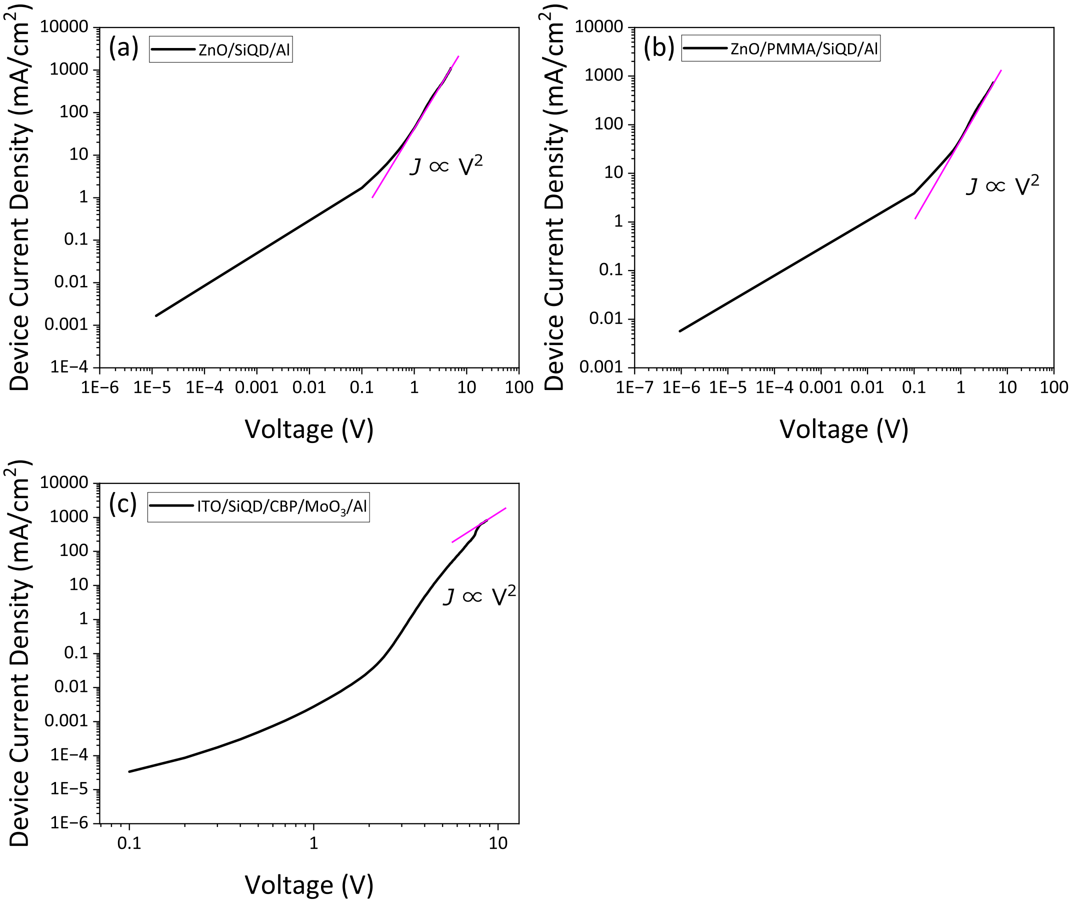

Fig.5-1 ***J-V*** **characteristics of electron only device (EOD) with device structure of (a) ITO/ZnO/SiQD/Al and (b) ITO/ZnO/PMMA/SiQD/Al and (c) hole only device (HOD) with device structure of ITO/SiQD/CBP/MoO$_3$/Al.**

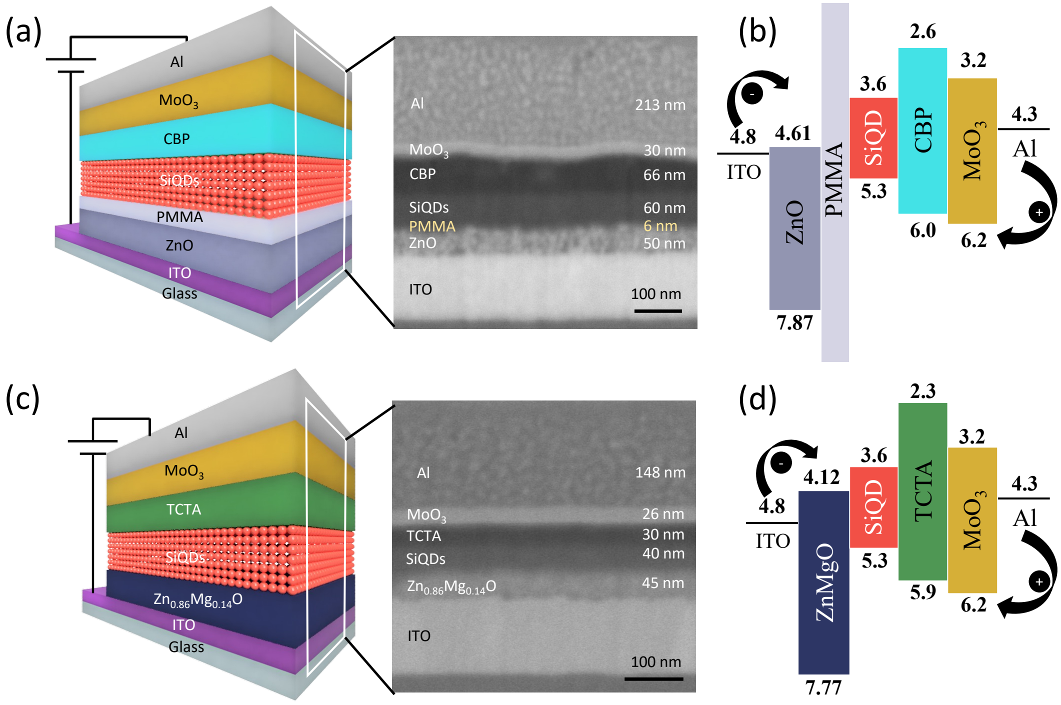

Fig.5-2 (a),(c) Schematic illustration of Si-QLEDs with an inverted device structure and a cross-sectional SEM image of the device structure with a hybrid organic/inorganic multilayer stack, (b),(d) flat energy band diagram in the unbiased conditions.

In this study, the fabrication of EBL inserted Si-iQLEDs (PMMA-device) and ZnMgO-device, which consists of ITO/$Zn_{0.86}Mg_{0.14}O$/SiQDs/TCTA/MoO_3/Al, were conducted to address the charge injection balance. The device architectures of PMMA- and ZnMgO-device, and their cross-sectional SEM images are presented in Fig.5-2(a) and (c), respectively. The proposed energy level diagram under zero applied bias voltage is illustrated in Fig.5-2(b) and (d), where the energy structures of ZnO, ZnMgO and De-SiQD were characterized by UPS and PYS, respectively.

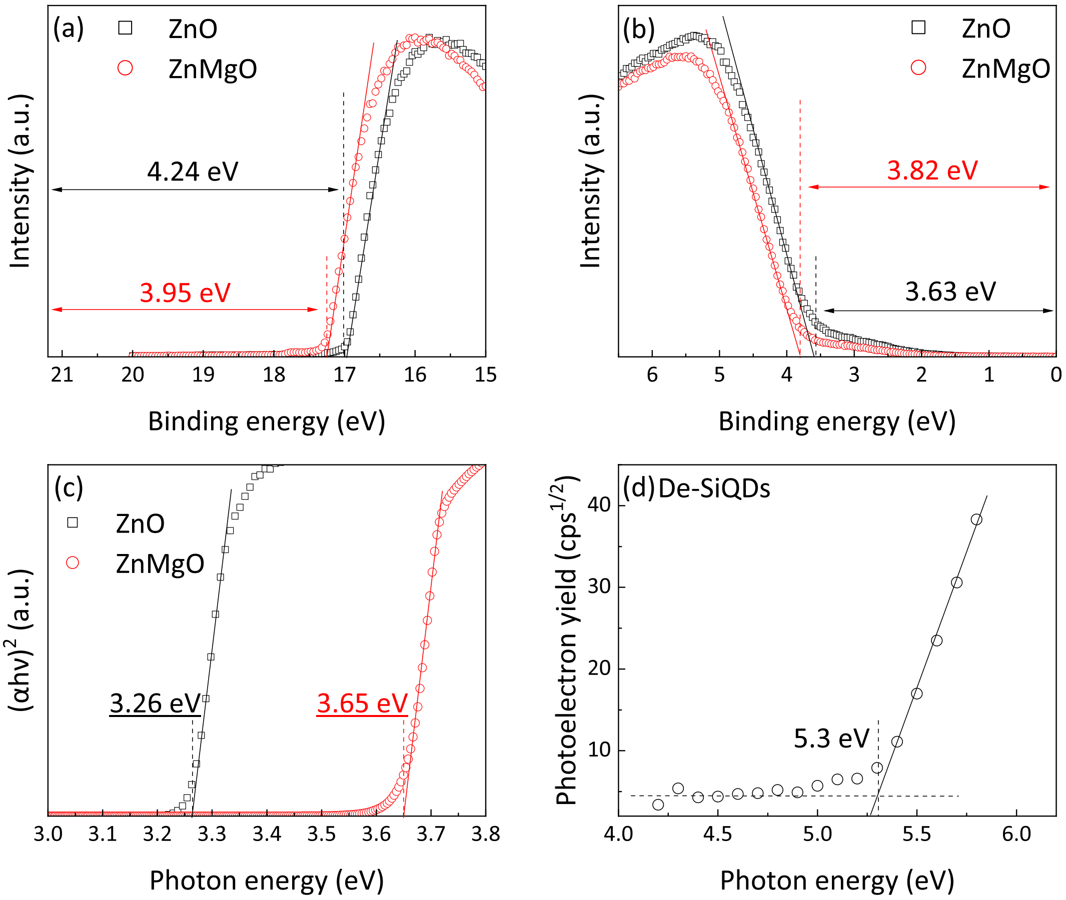

Fig.5-3 Ultraviolet photoelectron spectroscopic (UPS) spectra of (a) secondary-electron cutoff and (b) valence-band edge regions of ZnO and ZnMgO thin film. (c) $(\alpha hv)^2$ - hv plots converted from the absorption spectra of ZnO and ZnMgO nanoparticles. (d) Photoelectron yield spectroscopic (PYS) spectrum of thin film of De-SiQDs.

Fig.5-3(a) and (b) illustrate the UPS spectra of the secondary electron cut-off and valence band edge regions of ZnO and ZnMgO thin films, respectively. The determination of the work function involved computing the energy disparity between the incident light (21.2 eV) and the secondary-electron cutoff, which was 4.24 eV for ZnO and 3.95 eV for ZnMgO, as indicated in Fig.5-3(a). The estimation of the disparity in energy between the Fermi level and valence band maximum (VBM) was conducted through the examination of the valence band edge region, as shown in Fig.5-3(b), and the results were 3.63 eV for ZnO and 3.82 eV for ZnMgO. Consequently, the calculated VBM levels for ZnO and

ZnMgO, relative to the vacuum level, were approximately 7.87 eV and 7.77 eV, respectively. The optical band gap of ZnO and ZnMgO thin films was deduced by analyzing their UV-VIS spectra, as presented in Fig.5-3(c), via the plotting of $(\alpha h\nu)^2$ against photon energy ($h\nu$). The band gap values were determined to be 3.26 eV for ZnO and 3.65 eV for ZnMgO. From these values, it was feasible to estimate the conduction band minimum (CBM) levels of ZnO and ZnMgO to be 4.61 eV and 4.12 eV, respectively, as illustrated in Fig.5-2(b) and (d). Additionally, the PYS spectrum presented in Fig.5-3(d) allowed for the determination of a VBM level of 5.3 eV for the De-SiQD film. Assuming that the PL photon energy (1.7 eV) is equivalent to the magnitude of the optical band gap, the CBM level was estimated to be 3.6 eV. The highest occupied molecular orbital (HOMO) and lowest unoccupied molecular orbital (LUMO) values of the CBP and TCTA layers, as well as the VBM and CBM of the MoO_3 layer, were obtained from previous literature [9]. Fig.5-2(b) and (d) depict the favorable condition for effective electron injection from the electrode at a low applied bias voltage owing to the low energy barrier between ITO and ZnO or ZnMgO. Additionally, the deep HOMO energy level of ZnO and ZnMgO acted as a hole blocking barrier, confining holes within the De-SiQD layer. Moreover, the high LUMO energy barrier of CBP and TCTA layers prevented the leakage of electrons to the adjacent anode, leading to enhanced radiative electron-hole recombination in the De-SiQD layer for light emission.

Fig.5-4 presents the device characteristics of the PMMA- and ZnMgO-devices. Fig.5-4(a) displays the current-voltage characteristics, while Fig.5-4(b) illustrates the optical power density characteristics with voltage. The turn-on voltage, defined as the voltage at which the optical power density is greater than 0.1 nW/cm^2, for the PMMA-device and ZnMgO-device were found to be 2.25 V and 2 V, respectively, which are consistent with their *I-V* characteristics. The PMMA-device and ZnMgO-device demonstrated maximum optical power densities of 5.9 μW/cm^2 at 15 V and 75 μW/cm^2 at 10 V, respectively, as shown in Fig.5-4(a) and (b). The estimated EQE values plotted as a function of device current density and optical power density in Fig.5-4(c) and (d) showed the best EQE values of 7.44% at 0.11 μW/cm^2 for the PMMA-device and 3.77% at 0.72 μW/cm^2 for the ZnMgO-device. Consistent with the expectations based on the charge injection balances, the PMMA-device exhibited higher EQE than the non-EBL inserted device. The EQE of the PMMA-device showed a decline in regions above 0.2 μW/cm^2, but remained above 3% at 5.9 μW/cm^2. In contrast, the ZnMgO-device exhibited higher optical power density and EQE stability compared to the PMMA-device. These results suggest that the ZnMgO-device structure is more favorable, possibly due to the lower energy barrier between the ZnMgO and SiQDs layer, and the higher energy barrier between the SiQDs and TCTA layer, which promotes carrier injection into the SiQDs layer and confines the injected carrier within the SiQDs layer.

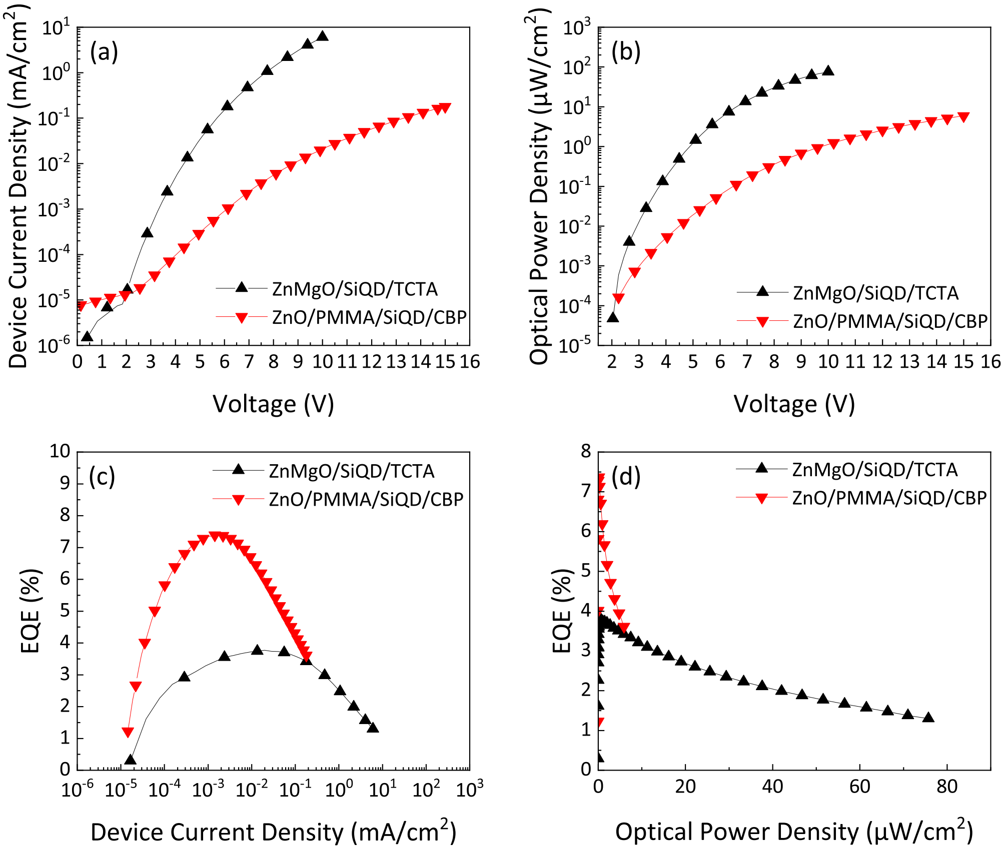

Fig.5-4 The device characteristics of Si-iQLEDs of (a) *I-V* characteristics, (b) optical power density plotted by voltage, EQE performance with (c) device current density and (d) optical power density.

Fig.5-5 depicts the raw data of the EL spectra for (a) the PMMA-device and (b) the ZnMgO-device measured at various applied voltages ranging from 8 V to 15 V for the PMMA-device and from 6 V to 10 V for the ZnMgO-device. It is evident from the data that the EL emission intensity increases with an increase in the applied voltage. The PMMA-device exhibited EL peak wavelengths of 751 nm at 8 V and 732 nm at 15 V, while the ZnMgO-device exhibited EL peak wavelengths of 715 nm at 6 V and 700 nm at 10 V. The blue shift of the EL peak wavelength in the high applied voltage region was observed to be 19 nm for the PMMA-device and 15 nm for the ZnMgO-device. The observed magnitudes of peak shift in the PMMA-device and ZnMgO-device were lower than those typically observed in conventional devices, which exhibit a shift of approximately 50 nm. These blue shifts are likely due to the quantum confined Stark effect and/or band-filling effect at high device current density regions. Additionally, there was no parasitic emission from neighboring layers, as observed in conventional devices, indicating that the EL emission originates from efficient recombination between electrons and holes in the SiQDs layer. The insets in Fig.5-5(a) and (b) show photographs of the PMMA-device and ZnMgO-device operated at 15 V and 10 V, respectively. It is apparent that the ZnMgO-device exhibits brighter emission than the PMMA-device to the naked eye.

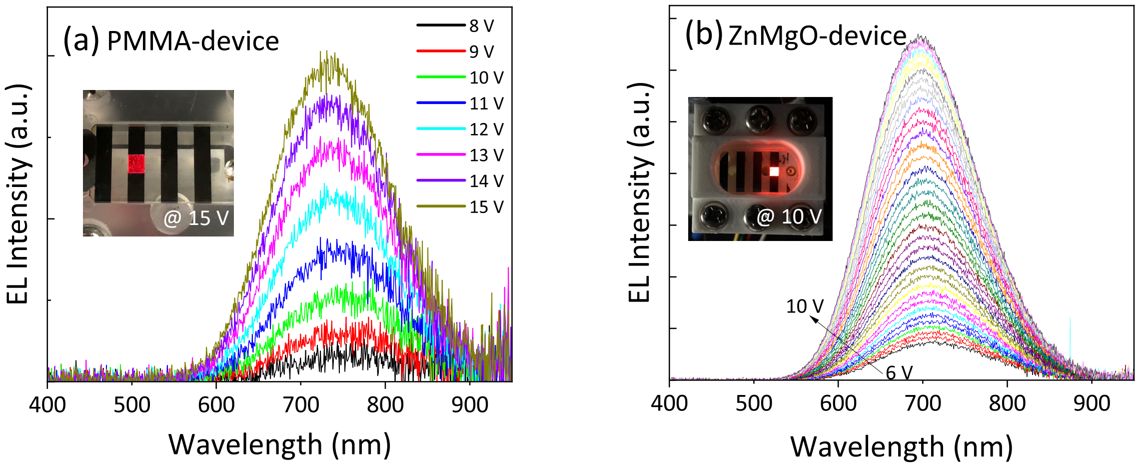

Fig.5-5 Electroluminescence spectra of (a) the PMMA-device and (b) the ZnMgO-device. The insets show the photo operating at (a) 15 V and (b) 10 V.

5.3.2 Post-Production Techniques for Enhancing EQE in Si-QLEDs

5.3.2.1 Device Performance Results

Instead of applying short ligands to the surface of the QDs during the hydrosilylation process, it was discovered that subjecting the pristine Si-QLEDs to a constant bias voltage of 5 V for a specified duration (*e.g.*, 9 hours) resulted in a reduction of the interparticle distance between adjacent QDs in the emitting layer. This post-production treatment was coined "post-electric-annealing". To demonstrate the efficacy of this technique, Si-QLEDs with a device structure of ITO/ZnO/SiQDs/CBP/MoO_3/Al were fabricated.

Fig.5-6(a) and Fig.5-7(a) exhibit the current-voltage characteristics prior to and post electric annealing, respectively. The estimated turn-on voltage before electric annealing was 3.47 V. However, after electric annealing, the turn-on voltage was reduced to 2.45 V. Fig.5-7(b) illustrates the optical power density characteristic as a function of the device current density. The use of optical power density instead of luminance is due to the lack of a discernible sensitivity curve at EL peak wavelengths exceeding 700 nm in the International Commission on Illumination (CIE) optical radiation efficiency function, which is utilized to transform radiant energy to luminance.

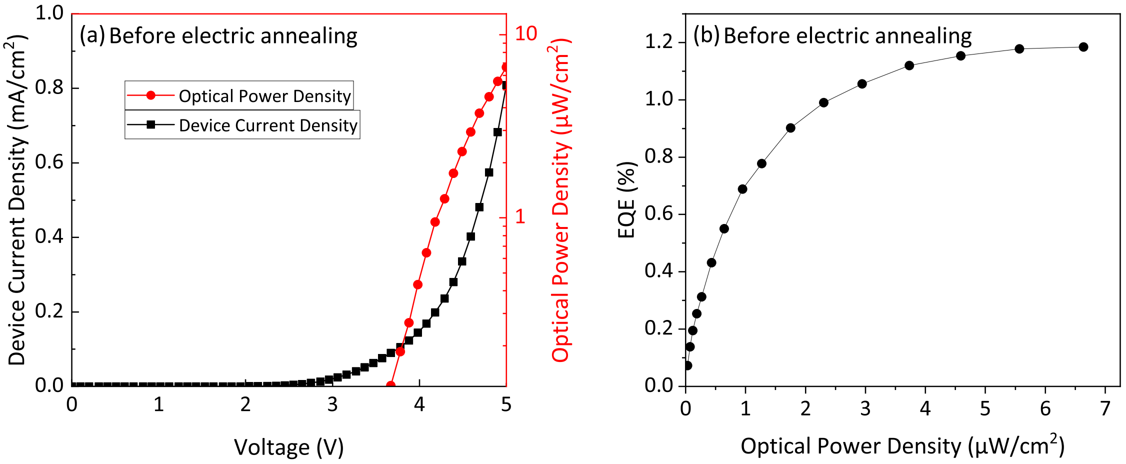

Fig.5-6 (a) The device current density and optical power density versus applied voltage, and (b) the EQE performance before electric annealing.

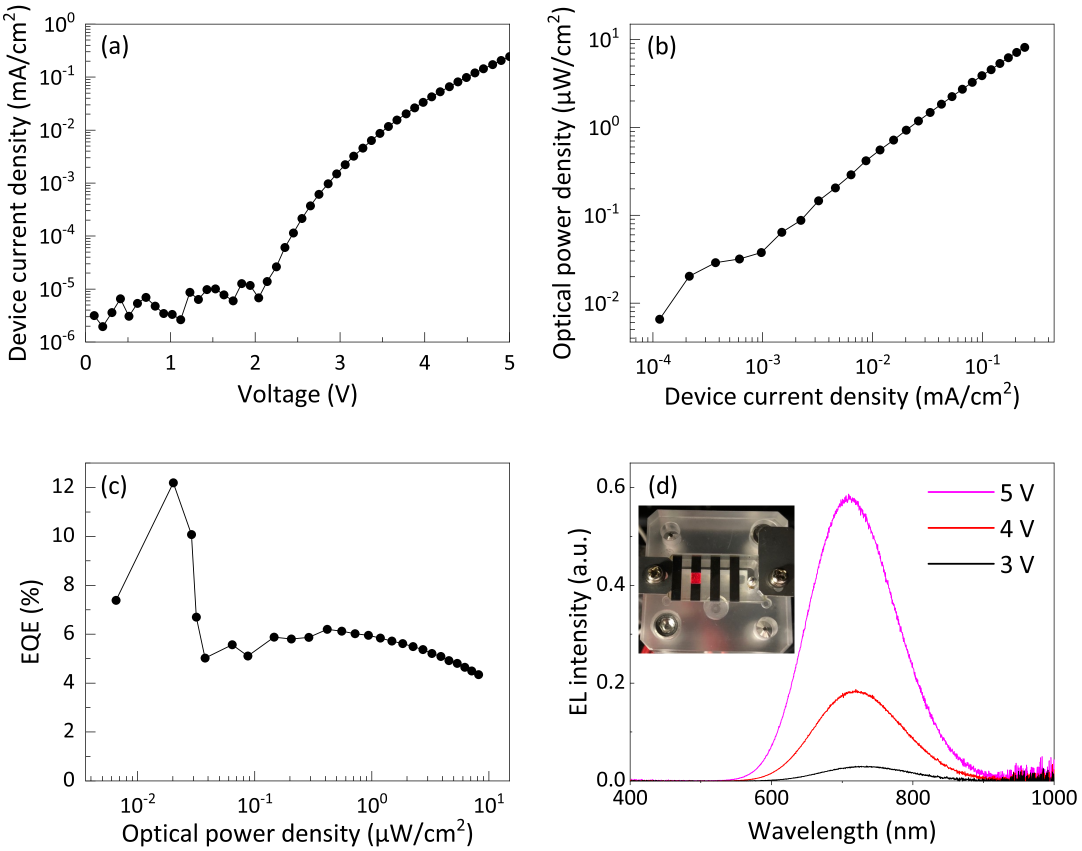

Fig.5-7 The device characteristics of Si-QLEDs of (a) *I-V* characteristics, (b) optical power density plotted by device current density, (c) EQE performance with optical power density and (d) electroluminescence (EL) spectra operated at different voltages with an inset of device photograph operating at 5 V.

The optical power density was observed to increase substantially within the narrow range of 0.1-0.4 μA/cm^2, with marginal enhancements in the range of 0.4-1.0 μA/cm^2, and gradual amplifications in the device current density beyond 1 μA/cm^2. The device manifested an optical power density of up to 8.16 μW/cm^2 at 5 V. In contrast, the device prior to electric annealing demonstrated a peak optical power density of 6.63 μW/cm^2 at 5 V (refer to Fig.5-6(a)). Fig.5-6(b) and Fig.5-7(c) depict the estimated EQE values before and after electric annealing as a function of the optical power density. The maximum EQE prior to electric annealing was 1.18%. As anticipated from the optical power plot, the highest EQE value post electric annealing was 12.2% at 0.02 μW/cm^2, corresponding to the device current density range of 0.1-0.3 μA/cm^2 in Fig.5-7(b). Additionally, reproducible EQE values exceeding 10% were achieved (refer to Fig.5-8). Thereafter, similar to the other instance, the EQE declined, but remained above 4% even at 8.16 μW/cm^2. Fig.5-9 compares the optical power density of Si-iQLEDs with other reported values [8,13,42,43].

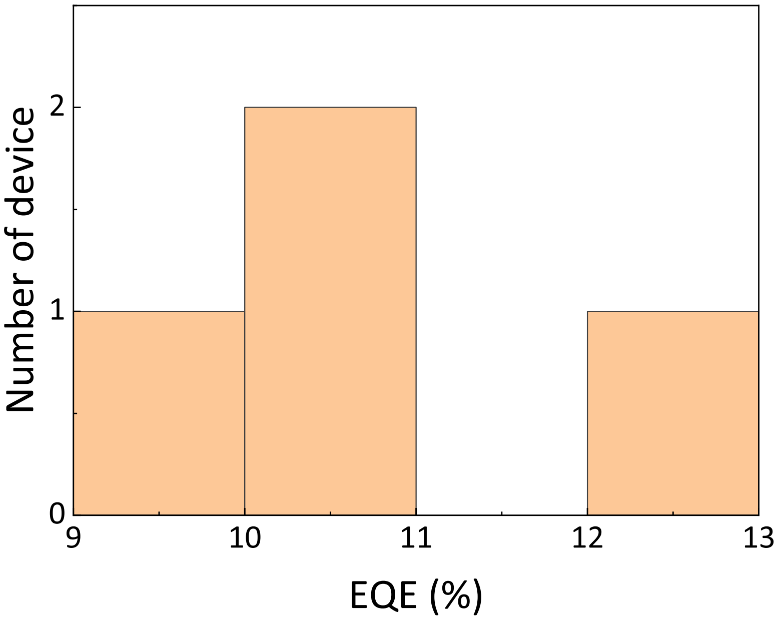

Fig.5-8 Histograms of maximum EQEs of four Si-QLEDs. The respective EQEs were 9.27%, 10.13%, 10.19%, and 12.2%.

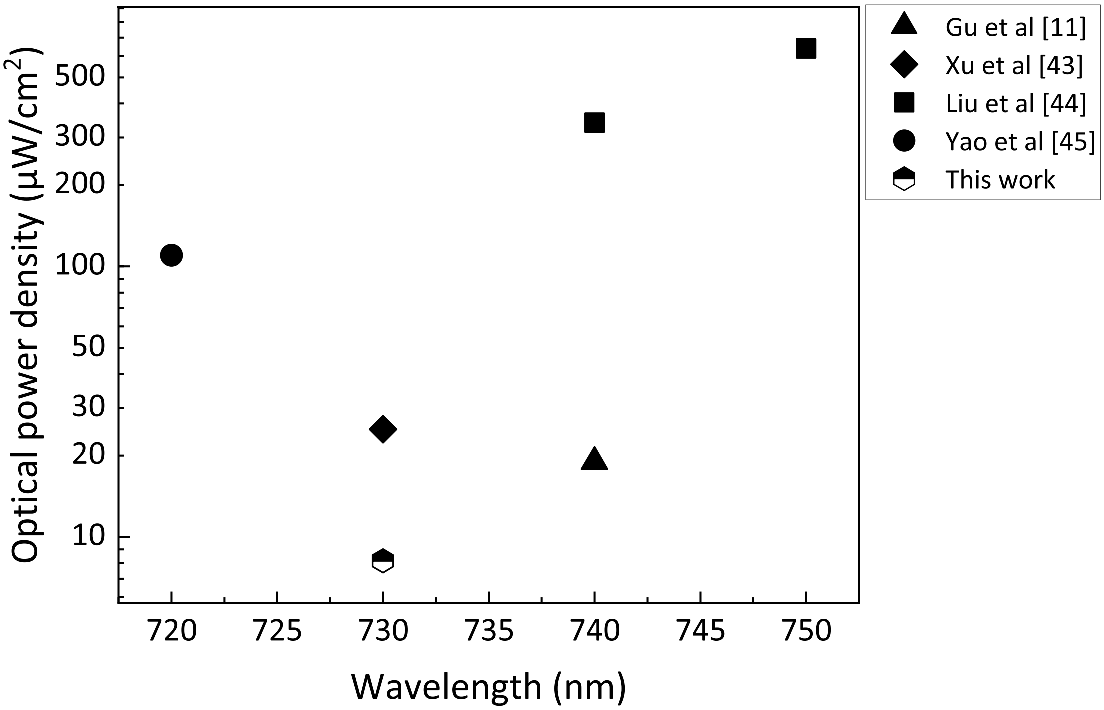

Fig.5-9 A summary of the optical power density of Si-QLEDs emitting in the same wavelength range as in this study [11,43–45].

The optical power density (*i.e.*, 8.16 μW/cm^2) was comparatively lower than the reported values. Nonetheless, it was sufficiently bright to perceive the luminescent color with unaided vision under room illumination (refer to Fig.5-7(d), inset). The lower optical power density might be attributed to a lower device current density in comparison to the reported devices, although the mechanism behind this observation is still being investigated. Fig.5-7(d) illustrates the EL spectra at varying applied bias voltage levels ranging from 3 V to 5 V. High signal-to-noise ratio EL spectra were observed for all devices. The EL intensity showed a noticeable increase with the applied voltage, and the center of the EL spectrum shifted from 730 nm at 3 V to 710 nm at 5 V. The spectral blueshift observed was about 20 nm, which is approximately 30 nm smaller than the conventional Si-QLEDs [8,42,46–48]. This blueshift is likely attributed to the quantum confinement Stark effect and band-filling effect at higher applied bias voltage [49]. The absence of parasitic emission from the adjacent ZnO layer indicates that the carriers did not leak from the QD layer to the adjacent ZnO and CBP layers, even during high-voltage operation that enhances electron-hole recombination in the emitting layer for EL. Moreover, as shown in Fig.5-10, the PL and EL spectra were found to overlap exactly, suggesting that the luminous characteristics were not influenced by the distance between SiQDs, owing to a large Stokes shift between the optical absorption and PL emission spectra, as demonstrated in Fig.5-11.

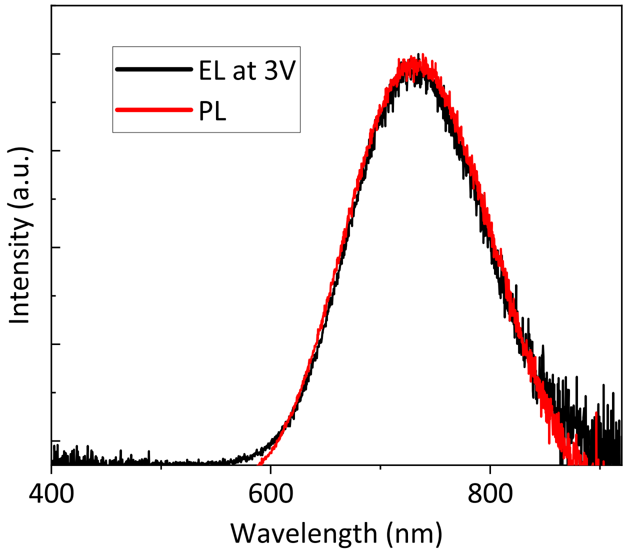

Fig.5-10 The comparison of PL and EL spectra operated at 3 V.

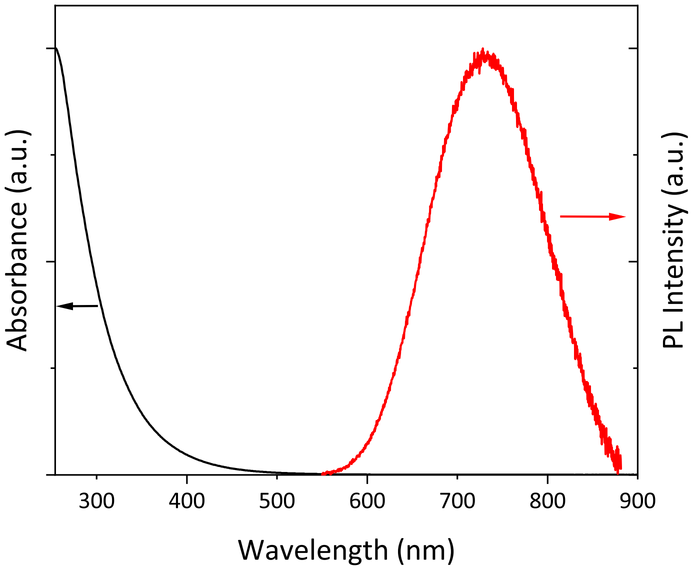

Fig.5-11 Optical absorption and photoluminescence (PL) spectra of De-SiQDs dispersed in toluene.

5.3.2.2 Analysis of the "Post-Electric-Annealing" Mechanism

To elucidate the phenomena occurring within the device subsequent to electric annealing, a red-emitting Si-iQLED was fabricated and scrutinized using electron microscopes. Cross-sectional TEM images of the device before and after 22 hours of voltage application are depicted in Fig.5-12(a) and (b), respectively. Notably, Fig.5-12(c) and (d) present histograms of interparticle distances within the SiQDs layer, inferred from the cross-sectional views. Although the SiQDs stacks were denser in both images, the average distance between SiQDs was estimated to be 1.54 nm and 0.95 nm before and after electric annealing, respectively. On the basis of these findings, the plausible mechanism underlying the shortening of interparticle distance is demonstrated in Fig.5-13.

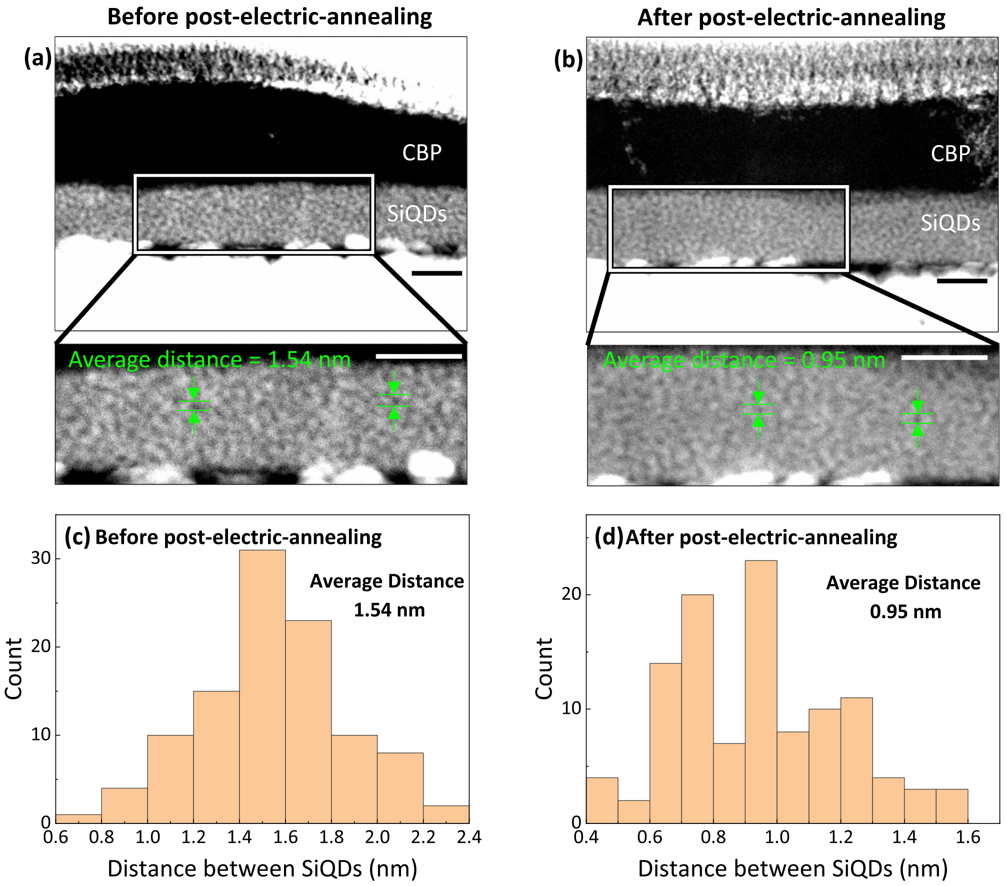

Fig.5-12 Cross-sectional TEM images of Si-QLEDs and histogram of distance between SiQDs in the active layer (a,c) before and (b,d) after post-electric-annealing. For post-electric-annealing, the device was applied voltage for 22 hours at 5 V. Each scale bar is 20 nm.

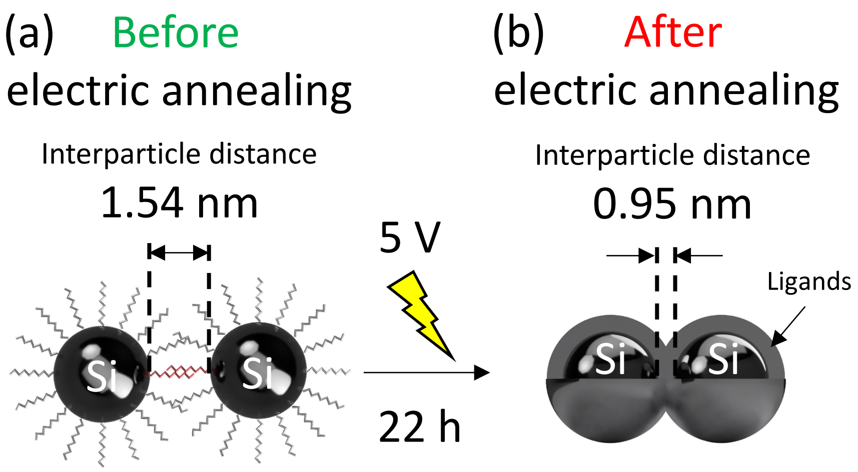

Fig.5-13 Schematic representation of electric-annealing mechanism in SiQDs layer at (a) before, (b) after electric-annealing state.

(1) Prior to voltage application, SiQDs assemble to constitute an active layer. However, the capping ligands of adjacent QDs engender steric hindrance and do not enhance packing density, as depicted in Fig.5-13(a). (2) Upon application of a voltage of 5 V to the device, Joule heat is generated, which leads to thermal degradation of the capping ligands with increased duration of voltage application. The carbonization of ligands due to thermal degradation diminishes steric hindrance, thereby shortening the interparticle distance between QDs, as depicted in Fig.5-13(b). The carbonized ligands and reduced interparticle distance result in decreased device resistance, thereby inducing a high current density. Consequently, the radiative recombination rate within the SiQDs is heightened. (3) With an increase in the duration of voltage application, the reduction in distance between SiQDs approaches a saturation point, along with the current density and optical power density of the device. (4) Ultimately, the ligands undergo additional degradation, and may act as energy barriers within the SiQD layer, which might necessitate further investigation. Consequently, the current density and optical power density of the device are reduced. One of the critical concerns during electric annealing was the potential reduction in QD diameter owing to oxidation or carbonization of the Si surface. To investigate the impact of applied voltage on QD size, EL spectra were recorded at 5 V, with increments of 1 hour. Fig.5-14

indicates that there were no alterations in the spectral shape or position of EL peaks. Additionally, the abbreviated interparticle distance did not affect the shape or position of EL spectra, possibly due to a reduced or non-existent energy transfer between adjacent QDs in the emitting layer, as indicated by the significant Stokes shift between absorption and PL spectra that are characteristic of SiQD.

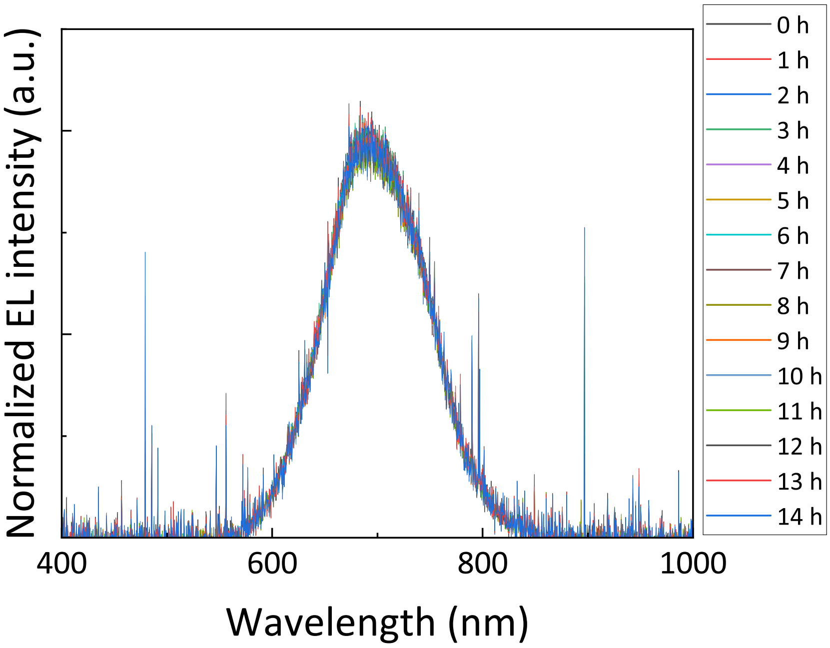

Fig.5-14 Normalized EL spectra during annealing plotted in 1-hour increments at 5 V.

Subsequently, the device performance during electric annealing was evaluated. Fig.5-15 provides an overview of the device performance variations during electric annealing at a constant applied voltage of 5 V. The alterations in both device current density and resistance over the duration of the annealing process are illustrated in Fig.5-15(a). In the first 6 hours, the device resistance experienced a significant reduction, and from 6 to 9 hours, the current density increased, eventually reaching near-saturation levels for both current density and resistance. However, after 10 hours, resistance started to increase, and current density began to decrease. As shown in Fig.5-15(b), the optical power density increased during the initial 9 hours, reached a state of near saturation between 10 and 21 hours, and then started to decrease after 22 hours. During the electric annealing process, there was no noticeable alteration in the spectral shape or peak position of the EL spectra (as illustrated in Fig.5-14). The variations in EQE of the Si-iQLED are depicted in Fig.5-15(c). The EQE values increased in the first 21 hours but started to decrease thereafter. Fig.5-15(d) illustrates the changes in EQE and optical power density over time in relation to current density. As demonstrated in Fig.5-15(d), the EQE exhibited an increase with increasing current density up to 9 hours. From 10 to 21 hours, although the current density decreased, the EQE continued to rise. In contrast, the optical power density showed an increase with increasing current density up to 9 hours. Notably, despite the decline in current density from 10 to 21 hours, the optical power density remained nearly constant, resulting in an increase in the EQE.

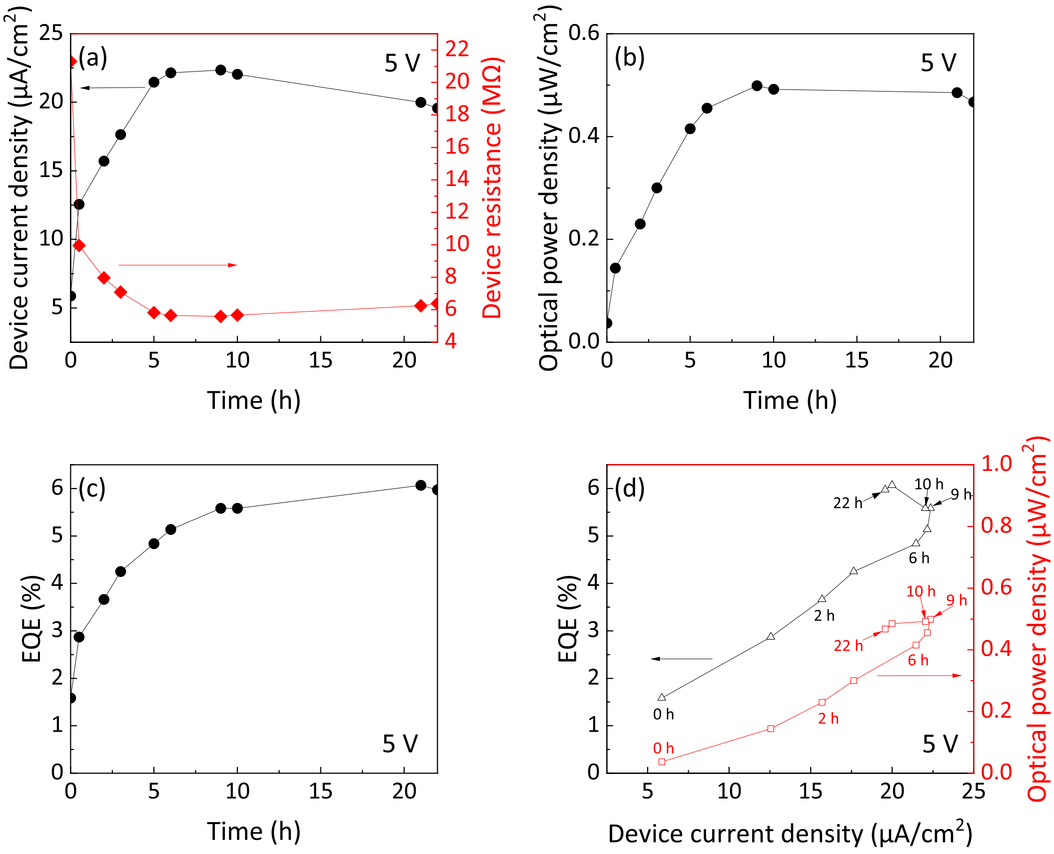

Fig.5-15 Device characteristics of (a) device current density and device resistance, (b) optical power and (c) external quantum efficiency (EQE) plotted with time of voltage application. (d) The EQE and optical power plots with device current density during voltage application up to 22 hours. Here, a constant voltage of 5 V was applied into the device.

Finally, the stability of light emission before and after cooling of the device was assessed via repeated application of 5 V during electric annealing. Fig.5-16 depicts the changes in device current density and optical power density prior to and following cooling, with details provided in the figure caption. Subsequent to cooling, the initial measurements of optical power density for all cycles (indicated by red arrows in Fig.5-16) experienced a more pronounced decline in comparison to the pre-cooling measurements (indicated by black arrows in Fig.5-16). Although the optical power density subsequently increased with rising applied voltage, it failed to reach the level of optical power density observed prior to cooling. The device current density exhibited analogous behavior. Hence, it is plausible to conclude that the reduction in optical power density was mainly due to augmented device resistance arising from device degradation. Consequently, it can be surmised that the most favorable utilization of post-electric-annealing should be concluded when the device resistance is minimal, and luminance is maximal. Prolonging the annealing process beyond this point will yield an elevation in EQE, but a reduction in luminance, ultimately resulting in the impairment of the device's functionality as a light-emitting component.

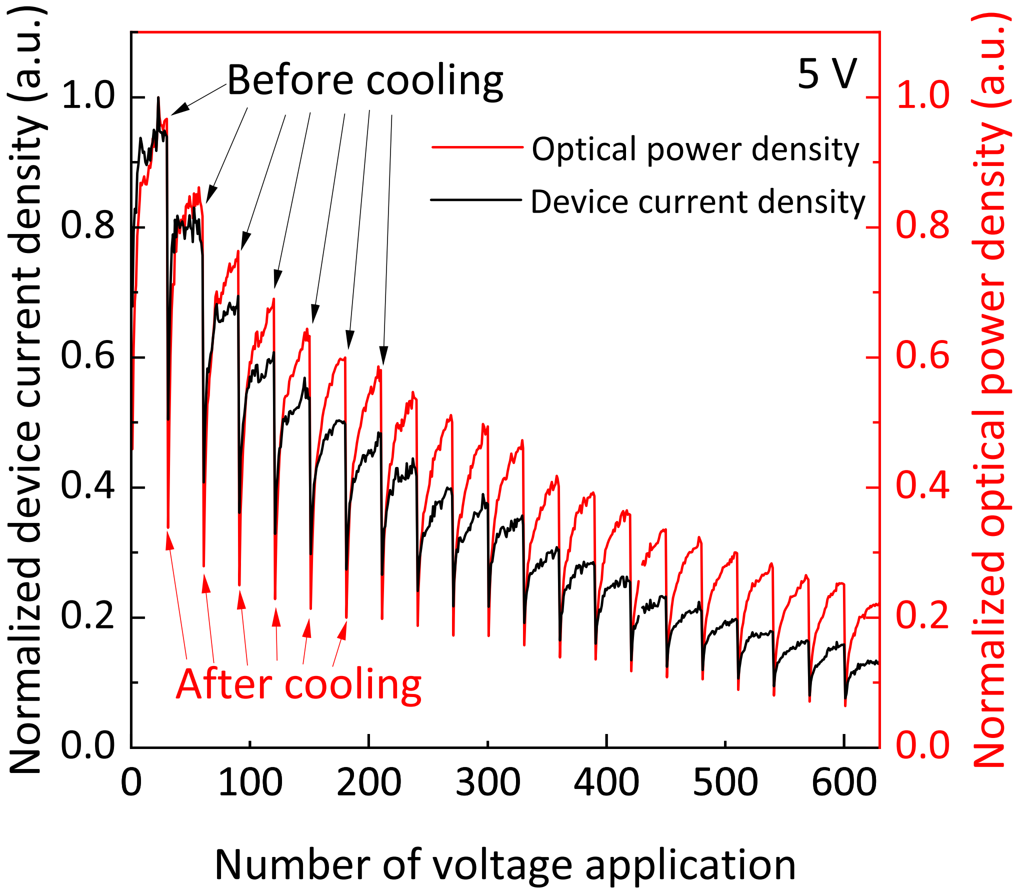

Fig.5-16 Stability of the device current density and the optical power density before and after cooling the device. Here, the bias voltage was increased to 5 V in 51 steps, kept for 0.5 sec, and then returned to 0 V. This was repeated 30 times. Intervals between each repetition were 5 sec. After 30 times of measurement, turn off the power for 1 hour to cooling down the device. After 1 hour, the device is subjected to another 30 times of repetitive voltage applications again. This series of cycles was performed 21 times.

5.4 Conclusion

In this chapter, it was demonstrated that Si-QLEDs with PMMA inserted as an EBL between the ETL and the active layer exhibited an EL peak wavelength of 732 nm at 15 V, a maximum optical power density of 5.9 μW/cm^2 and EQE characteristics with a peak EQE value of 7.44%. It was concluded that this enhancement in EQE was realized by improving the charge injection balance by inhibiting electron injection via the PMMA thin film as an EBL. Furthermore, the device using $Zn_{0.86}Mg_{0.14}O$ as an ETL and TCTA as a HTL exhibited as high as 3.77% of EQE and 75 μW/cm^2 of optical power density. This enhancement in optical power density is likely due to the lower energy barrier between the $Zn_{0.86}Mg_{0.14}O$ and SiQDs layer and the higher energy barrier between the SiQDs and TCTA layer, which promotes carrier injection into the SiQDs layer and confines the injected carriers in the SiQDs layer. In addition, a novel method named as "post-electric-annealing" was reported as a means to enhance the EQE of red-emitting Si-iQLEDs. In this study, post-electric-annealing was performed by applying a constant voltage of 5 V to the Si-iQLEDs for a duration of 9 hours, resulting in an increase of the EQE up to 12.2%. Alternatively, the EQE could also be increased to approximately 12% by repeatedly applying a voltage from 0 V to 5 V over a similar time period. Detailed transmission microscopy studies revealed that the interparticle distance between adjacent De-SiQDs shortened in the emitting layer, which facilitated charge carrier injection into the QDs layer, thus improving the optical power density and EQE. It is believed that this phenomenon of interparticle distance shortening was caused by ligand damage due to Joule heat generated during voltage application. To prevent degradation as a light-emitting device, it is crucial to terminate the post-production treatment at the point where the device resistance is the lowest and luminance is at its maximum. While this process may be difficult to implement in an industrial setting, the findings suggest that both shortening the interparticle distance between adjacent SiQDs in the optically active layer and improving the packing density of QDs have the potential to improve the EQE by at least 12.2%.

5.5 References

[1] Won, Y.-H. *et al.* Highly efficient and stable InP/ZnSe/ZnS quantum dot light-emitting diodes. *Nature* **575**, 634–638 (2019)

[2] Kim, T. *et al.* Efficient and stable blue quantum dot light-emitting diode. *Nature* **586**, 385–389 (2020)

[3] Wang, Z. *et al.* Facile Synthesis of Cu–In–S/ZnS Core/Shell Quantum Dots in 1-Dodecanethiol for Efficient Light-Emitting Diodes with an External Quantum Efficiency of 7.8%. *Chem. Mater.* **30**, 8939–8947 (2018)

[4] Zhao, B. & Tan, Z. Fluorescent Carbon Dots: Fantastic Electroluminescent Materials for Light-Emitting Diodes. *Adv. Sci.* **8**, 2001977 (2021)

[5] Motomura, G. *et al.* Efficient quantum-dot light-emitting diodes using ZnS–AgInS 2 solid-solution quantum dots in combination with organic charge-transport materials. *Appl. Phys. Lett.* **116**, 093302 (2020)

[6] Liang, H. *et al.* High Color Purity Lead-Free Perovskite Light-Emitting Diodes via Sn Stabilization. *Adv. Sci.* **7**, 1903213 (2020)

[7] Zhang, Y. *et al.* Lead-free Double Perovskite Cs2AgIn0.9Bi0.1Cl6 Quantum Dots for White Light-Emitting Diodes. *Adv. Sci.* **9**, 2102895 (2022)

[8] Yao, L. *et al.* Efficient silicon quantum dots light emitting diodes with an inverted device structure. *J. Mater. Chem. C* **4**, 673–677 (2016)

[9] Ghosh, B., Yamada, H., Chinnathambi, S., Özbilgin, İ. N. G. & Shirahata, N. Inverted Device Architecture for Enhanced Performance of Flexible Silicon Quantum Dot Light-Emitting Diode. *J. Phys. Chem. Lett.* **9**, 5400–5407 (2018)

[10] Wei Gu, Xiangkai Liu, Shuangyi Zhao, Xiaodong Pi & Deren Yang. Silicon-quantum-dot light-emitting diodes with varying emission layer thickness. in *2016 13th IEEE International Conference on Solid-State and Integrated Circuit Technology (ICSICT)* 157–159 (IEEE, 2016). doi:10.1109/ICSICT.2016.7998866

[11] Gu, W. *et al.* Silicon-Quantum-Dot Light-Emitting Diodes With Interlayer-Enhanced Hole Transport. *IEEE Photonics J.* **9**, 1–10 (2017)

[12] Zhao, S. *et al.* Al 2 O 3 -Interlayer-Enhanced Performance of All-Inorganic Silicon-Quantum-Dot Near-Infrared Light-Emitting Diodes. *IEEE Trans. Electron Devices* **65**, 577–583 (2018)

[13] Liu, X. *et al.* Light-Emitting Diodes Based on Colloidal Silicon Quantum Dots with Octyl and Phenylpropyl Ligands. *ACS Appl. Mater. Interfaces* **10**, 5959–5966 (2018)

[14] Mock, J., Groß, E., Kloberg, M. J., Rieger, B. & Becherer, M. Surface Engineering of Silicon Quantum Dots: Does the Ligand Length Impact the Optoelectronic Properties of Light-Emitting Diodes? *Adv. Photonics Res.* **2**, 2100083 (2021)

[15] Yamada, H. *et al.* Improved Brightness and Color Tunability of Solution-Processed Silicon

Quantum Dot Light-Emitting Diodes. *J. Phys. Chem. C* **124**, 23333–23342 (2020)

[16] Watanabe, J. *et al.* Silicon Quantum Dots for Light-Emitting Diodes Extending to the NIR-II Window. *ACS Appl. Nano Mater.* **4**, 11651–11660 (2021)

[17] Cheng, K.-Y., Anthony, R., Kortshagen, U. R. & Holmes, R. J. Hybrid Silicon Nanocrystal─Organic Light-Emitting Devices for Infrared Electroluminescence. *Nano Lett.* **10**, 1154–1157 (2010)

[18] Tu, C.-C., Tang, L., Huang, J., Voutsas, A. & Lin, L. Y. Visible electroluminescence from hybrid colloidal silicon quantum dot-organic light-emitting diodes. *Appl. Phys. Lett.* **98**, 213102 (2011)

[19] Cheng, K.-Y., Anthony, R., Kortshagen, U. R. & Holmes, R. J. High-Efficiency Silicon Nanocrystal Light-Emitting Devices. *Nano Lett.* **11**, 1952–1956 (2011)

[20] Puzzo, D. P. *et al.* Visible Colloidal Nanocrystal Silicon Light-Emitting Diode. *Nano Lett.* **11**, 1585–1590 (2011)

[21] Mastronardi, M. L. *et al.* Silicon Nanocrystal OLEDs: Effect of Organic Capping Group on Performance. *Small* **8**, 3647–3654 (2012)

[22] Maier-Flaig, F. *et al.* Multicolor Silicon Light-Emitting Diodes (SiLEDs). *Nano Lett.* **13**, 475–480 (2013)

[23] Anikeeva, P. O., Madigan, C. F., Halpert, J. E., Bawendi, M. G. & Bulović, V. Electronic and excitonic processes in light-emitting devices based on organic materials and colloidal quantum dots. *Phys. Rev. B* **78**, 085434 (2008)

[24] Jia, H., Wang, F. & Tan, Z. Material and device engineering for high-performance blue quantum dot light-emitting diodes. *Nanoscale* vol. 12 13186–13224 (2020)

[25] Jin, X. *et al.* Balancing the Electron and Hole Transfer for Efficient Quantum Dot Light-Emitting Diodes by Employing a Versatile Organic Electron-Blocking Layer. *ACS Appl. Mater. Interfaces* **10**, 15803–15811 (2018)

[26] Zheng, W. *et al.* Performance improvements in all-solution processed inverted QLEDs realized by inserting an electron blocking layer. *Nanotechnology* **32**, 335204 (2021)

[27] Dai, X. *et al.* Solution-processed, high-performance light-emitting diodes based on quantum dots. *Nature* **515**, 96–99 (2014)

[28] Lin, Q. *et al.* Nonblinking Quantum-Dot-Based Blue Light-Emitting Diodes with High Efficiency and a Balanced Charge-Injection Process. *ACS Photonics* **5**, 939–946 (2018)

[29] Rahmati, M., Dayneko, S., Pahlevani, M. & Shi, Y. Highly Efficient Quantum Dot Light-Emitting Diodes by Inserting Multiple Poly(methyl methacrylate) as Electron-Blocking Layers. *Adv. Funct. Mater.* **29**, 1–10 (2019)

[30] Liu, M., Luan, W., Huang, Y. & Zhang, S. Efficiency Enhancement of Perovskite CsPbBr 3 Quantum Dot Light-emitting Diodes by Doped Hole Transport Layer. *IOP Conf. Ser. Mater. Sci. Eng.* **729**, 012098 (2020)

[31] Zvaigzne, M. *et al.* Optimizing the PMMA Electron-Blocking Layer of Quantum Dot Light-Emitting Diodes. *Nanomaterials* **11**, 2014 (2021)

[32] Ghosh, B. & Shirahata, N. Colloidal silicon quantum dots: synthesis and luminescence tuning from the near-UV to the near-IR range. *Sci. Technol. Adv. Mater.* **15**, 014207 (2014)

[33] Canham, L. Introductory lecture: Origins and applications of efficient visible photoluminescence from silicon-based nanostructures. *Faraday Discuss.* **222**, 10–81 (2020)

[34] Hessel, C. M. *et al.* Synthesis of Ligand-Stabilized Silicon Nanocrystals with Size-Dependent Photoluminescence Spanning Visible to Near-Infrared Wavelengths. *Chem. Mater.* **24**, 393–401 (2012)

[35] Shirahata, N. *et al.* Emerging Atomic Energy Levels in Zero-Dimensional Silicon Quantum Dots. *Nano Lett.* **20**, 1491–1498 (2020)

[36] Ghosh, B. *et al.* Hybrid White Light Emitting Diode Based on Silicon Nanocrystals. *Adv. Funct. Mater.* **24**, 7151–7160 (2014)

[37] Kim, J.-H. *et al.* Performance Improvement of Quantum Dot-Light-Emitting Diodes Enabled by an Alloyed ZnMgO Nanoparticle Electron Transport Layer. *Chem. Mater.* **27**, 197–204 (2015)

[38] Chandra, S., Masuda, Y., Shirahata, N. & Winnik, F. M. Transition-Metal-Doped NIR-Emitting Silicon Nanocrystals. *Angew. Chemie Int. Ed.* **56**, 6157–6160 (2017)

[39] Supran, G. J. S. Enhancing quantum-dot luminescence in visible and infrared light emitting devices. (2016)

[40] Lampert, M. A. Simplified Theory of Space-Charge-Limited Currents in an Insulator with Traps. *Phys. Rev.* **103**, 1648–1656 (1956)

[41] Wan, Q. *et al.* Surface Oxidation of Quantum Dots to Improve the Device Performance of Quantum Dot Light-Emitting Diodes. *J. Phys. Chem. C* **124**, 28424–28430 (2020)

[42] Gu, W. *et al.* Silicon-Quantum-Dot Light-Emitting Diodes with Interlayer-Enhanced Hole Transport. *IEEE Photonics J.* **9**, (2017)

[43] Xu, Y., Terada, S., Xin, Y., Ueda, H. & Saitow, K. Ligand Effects on Photoluminescence and Electroluminescence of Silicon Quantum Dots for Light-Emitting Diodes. *ACS Appl. Nano Mater.* **5**, 7787–7797 (2022)

[44] Liu, X. *et al.* Light-Emitting Diodes Based on Colloidal Silicon Quantum Dots with Octyl and Phenylpropyl Ligands. *ACS Appl. Mater. Interfaces* **10**, 5959–5966 (2018)

[45] Yao, L. *et al.* Efficient silicon quantum dots light emitting diodes with an inverted device structure. *J. Mater. Chem. C* **4**, 673–677 (2015)

[46] Mastronardi, M. L. *et al.* Silicon nanocrystal OLEDs: Effect of organic capping group on performance. *Small* **8**, 3647–3654 (2012)

[47] Cheng, K. Y., Anthony, R., Kortshagen, U. R. & Holmes, R. J. High-efficiency silicon nanocrystal light-emitting devices. *Nano Lett.* **11**, 1952–1956 (2011)

[48] Maier-Flaig, F. *et al.* Multicolor silicon light-emitting diodes (SiLEDs). *Nano Lett.* **13**, 475–480 (2013)

[49] Wang, D. C., Chen, J. R., Zhu, J., Lu, C. T. & Lu, M. On the spectral difference between electroluminescence and photoluminescence of Si nanocrystals: A mechanism study of electroluminescence. *J. Nanoparticle Res.* **15**, (2013)

Chapter 6 Summary and Future Prospects

Summary

This paper aims to examine the correlation between luminescence properties and QDs or QLEDs structures in order to determine the optimal elemental technologies required for the fabrication of Si-QLEDs with superior EL properties. Specifically, the focus is on SiQDs with high PLQY, device structures with high stability, and carrier transport layers that enhance the EQE of EL.

In Chapter 2, SiQDs were synthesized via thermal disproportionation reaction. The synthesized SiQDs were found to have a diamond structure from XRD pattern diagrams. Furthermore, the HRTEM measurement of SiQDs found out that the diameter of SiQDs corresponded well with the Scherrer equation. In addition, the PL peak wavelength can be controlled by thermal disproportionation temperature and HF etching time. Finally, it was found that SiQDs synthesized with HSQ, which was hydrolyzed and synthesized via the automatic injection method, generally had high PLQY. The XPS measurements of HSQ showed that the peak area ratio of Si 2^+ drastically decreased in HSQ synthesized via the automatic injection method compared with HSQ synthesized via the manual injection method. Therefore, the results suggested that $HSiO_{1.5}$ could be synthesized efficiently, which led to PLQY enhancement.

In Chapter 3, a study was conducted to investigate the advantages of an inverted device structure for Si-QLEDs in comparison to traditional device structures with respect to optical performance. The utilization of optimal CBP/MoO_3 HTL/HIL layers led to a significant enhancement in the optical performance of Si-iQLED, resulting in several notable improvements such as (i) a low turn-on voltage for light emission, (ii) EQE leveling off over a wide driving-voltage regime, (iii) the spectral shape and position of EL remaining unchanged even at a high driving voltage (~11 V), and (iv) extended device lifetimes. Notably, the optical performance of the Si-iQLED in this study surpassed that of previous Si-QLEDs. Furthermore, this study represents the first demonstration of a highly flexible Si-QLED through the adoption of a sheet of PET as a substrate, in lieu of a glass substrate, facilitating the widespread and convenient use of Si-QLEDs in flexible technologies.

In Chapter 4, the influence of SiQD film thickness on EL spectra was initially investigated. When the SiQD film thicknesses were 46 nm and 21 nm, only EL emission from SiQDs was observed, however, when the film thicknesses were 10 nm and 6 nm, parasitic emission from ZnO also emerged. Additionally, as the SiQD film thickness decreased, the device current density and optical power density increased. Subsequently, a SiQD-based QLED was produced through a solution-processed method, featuring a narrow EL spectrum peaking at 620 nm. A pale-orange luminescent sample of SiQD with 8% PLQY was utilized as the active layer of the QLED. The device, consisting of multiple layers of an inverted device structure, emitted a pale-orange emission with 0.036% EQE, which was visible to the naked eye even in an illuminated room. This study expanded the tunable emission range, which is currently limited to between 640 nm and 850 nm. Furthermore, five Si-QLEDs with an inverted structure were prepared, with the optically active layers consisting of SiQDs of varying diameters. The EL spectral peaks appeared at 755 nm for Device A, 722 nm for Device B, 670 nm for Device C, 635 nm for Device D, and 590 nm for Device E. These EL peak positions corresponded with those in the PL spectra, indicating the presence of quantum confinement effects in SiQDs. The peak EQE and maximum luminance were 3.70% and 0.25 cd/m^2 for Device A, 1.32% and 12.34 cd/m^2 for Device B, 1.20% and 17.2 cd/m^2 for Device C, 0.88% and 30.28 cd/m^2 for Device D, 0.12% and 18.4 cd/m^2 for Device E. No parasitic emission from the neighboring compositional layer was detected. The shortest wavelength of the EL spectral peak was updated to 590 nm, which is shorter than the previous study. The improved EQE may be attributed to the improved PLQYs of SiQDs and well-aligned energy diagrams of the inverted device architecture. Cross-sectional TEM imaging revealed that device-structural degradation of Si-QLED was promoted by the growth of sub-microscopic voids, which were initially created at the interface between CBP and MoO_3/CBP layers. Finally, a NIR-II LED based on SiQD as an optically active layer was developed for the first time. The 4.84% EQE was the record value for heavy-metal free QLEDs operating in the 900-1,100-nm spectral range. Such a high EQE was obtained using SiQD with a PLQY of 53%, which was fractionated separately from the QD sample via a chromatographic technique. The Si-QLED displayed a turn-on voltage as low as 2.0 V, and neither a peak at 1,000 nm in the EL spectrum nor parasitic emissions of the adjacent layer were observed at high driving voltage. The wavelength tuning range of the current Si-QLEDs (590-868 nm) was greatly expanded to the longer wavelength side, and by leveraging the substantial Stokes shift between the absorption and emission spectra, it was demonstrated that utilizing spectral superimposition with minimized energy transfer from reabsorption of light emitted by a smaller QD results in a significantly broadened NIR EL spectrum.

In Chapter 5, it was demonstrated that Si-QLEDs with PMMA inserted as EBL between ETL and active layer showed EL peak wavelength of 732 nm at 15 V, the maximum optical power density of 5.9 $\mu W/cm^2$ and EQE characteristics with a peak EQE value of 7.44%. It was concluded that this enhanced EQE was realized by improving the charge injection balance by inhibiting electron injection by PMMA thin film which work as an EBL. Furthermore, the device using $Zn_{0.86}Mg_{0.14}O$ as an ETL and TCTA as a HTL exhibited as high as 3.77% of EQE and 75 $\mu W/cm^2$ of optical power density. This enhanced optical power density is possibly due to lower energy barrier between $Zn_{0.86}Mg_{0.14}O$ and SiQDs layer and higher energy barrier between SiQDs and TCTA layer, which promotes the carrier injection into SiQDs layer and confine the injected carrier in the SiQDs layer. In addition, a novel method named as "post-electric-annealing" was reported as a means to enhance the EQE of red-emitting Si-iQLEDs. In this study, post-electric-annealing was performed by applying a constant voltage of 5 V to the Si-iQLEDs for a duration of 9 hours, resulting in an increase of the EQE up to

12.2%. Alternatively, the EQE could also be increased to approximately 12% by repeatedly applying a voltage from 0 V to 5 V over a similar time period. Detailed transmission microscopy studies revealed that the interparticle distance between adjacent De-SiQDs shortened in the emitting layer, which facilitated charge carrier injection into the QDs layer, thus improving the optical power density and EQE. It is believed that this phenomenon of interparticle distance shortening was caused by ligand damage due to Joule heat generated during voltage application. To prevent degradation as a light-emitting device, it is crucial to terminate the post-production treatment at the point where the device resistance is the lowest and luminance is at its maximum. While this process may be difficult to implement in an industrial setting, the findings suggest that both shortening the interparticle distance between adjacent SiQDs in the optically active layer and improving the packing density of QDs have the potential to improve the EQE by at least 12.2%.

Future Prospects

In this study, SiQDs with high PLQY of approximately 50% were synthesized through the use of an automatic injection method for the hydrolysis of HSQ. XPS measurements of the HSQ revealed that the peak area ratio of Si 2^+ significantly decreased in HSQ synthesized by the automatic injection method in comparison to HSQ synthesized by manual injection method. Consequently, it was inferred that efficient synthesis of pure $HSiO_{1.5}$ can consistently yield PLQY of more than 50% even in liquid-phase synthesis.

This study also demonstrated that Si-QLEDs with an inverted structure (Si-iQLEDs) exhibit high EL stability in high voltage regions. In a device where the thickness of the SiQDs layer was reduced to 6 nm, light emission was observed from the adjacent layer, indicating the potential for color rendering. This device has potential application in environmentally friendly lighting. Additionally, the EL peak wavelength was found to be controllable in the range of 590-1,000 nm. Furthermore, by incorporating SiQDs with different EL peaks, the EL spectra in the NIR region could be tailored. This has the potential to enable the development of NIR devices that emit light at the windows of living organisms in a wide band and could prove valuable in the field of bioimaging.

The "post-electric-annealing" process overcame the barrier for EQE of approximately 10% in Si-QLEDs. Although the process may prove challenging to implement in industry, the findings suggest that both reducing the interparticle distance between adjacent SiQDs in the optically active layer and increasing the packing density of QDs have the potential to improve EQE by at least 12.2%.

謝辞

本研究は、北海道大学大学院総合化学院後期課程在籍中、連携大学院制度により国立研究開発法人物質・材料研究機構(NIMS)で得られた研究内容をまとめたものです。本博士論文研究の遂行にあたり、北海道大学総合化学院客員教授 兼 NIMS 国際ナノアーキテクトニクス研究拠点 ナノ粒子グループ、グループリーダーの白幡 直人博士には研究の方向性、得られたデータの議論、論文投稿、常に研究に集中できる環境に至るまで、多大なるご指導ご鞭撻を賜りました。ここに心より深く感謝を申し上げます。

ご多忙の中、本論文をまとめるにあたり有益なご助言、ご指導賜りました北海道大学総合化学院・村越 敬教授、長谷川 靖哉教授、野口 秀典客員教授、打越 哲郎客員教授、島田 敏宏教授に厚く感謝申し上げます。また本研究に関する数々のご教授賜りました NIMS・スンホンタオ博士、鈴木 達博士に深く感謝申し上げます。

ナノ粒子グループに所属すべての皆様から、研究を進めるにあたっての様々な支援を頂きました。同研究室・根本 一宏博士と研究業務員・高澤 史枝氏には実験的な助言と支援を頂きました。事務業務員・曽我 まさみ氏とグローバル連携室・横田 詠子氏には NIMS での学生生活を支えていただきました。同後期課程在籍・CHATTERJEE Subhashri 氏、HUANG Xiaoyu 氏、CHEN Jiakai 氏、ZHANG Binbin 氏、ZHANG Cong 氏および中央大学・渡邊 純平氏には実験の手法に関して助言をいただきました。ここに深く感謝申し上げます。また NIMS 内の石井 健斗博士、İrem Nur Gamze ÖZBİLGİN 博士からのご協力賜りましたこと厚く御礼申し上げます。さらに本学で学ぶにあたり研究奨励金及び科研費を賜りました日本学術振興会様に深く感謝申し上げます。

最後に、本学で学ぶ機会を与えて頂くとともに、常に暖かく励まし応援して下さった家族にこの場を借りて深謝の意を表します。

令和 5 年 3 月

山田　博之